

Multi-instrument study of the hourly pulsations in Saturn's magnetosphere

Dissertation

zur Erlangung des mathematisch-naturwissenschaftlichen Doktorgrades

“Doctor rerum naturalium”

der Georg-August-Universität Göttingen

im Promotionsprogramm PROPHYS

der Georg-August University School of Science (GAUSS)

vorgelegt von

Benjamin Palmaerts

aus Wavre, Belgien

Göttingen, 2017

Betreuungsausschuss

Prof. Dr. Andreas Tilgner

Institut für Geophysik, Georg-August-Universität Göttingen, Göttingen, Deutschland

Prof. Dr. Denis Grodent

Institut STAR, Université de Liège, Lüttich, Belgien

Dr. Norbert Krupp

Max-Planck-Institut für Sonnensystemforschung, Göttingen, Deutschland

Mitglieder der Prüfungskommission

Referent: Prof. Dr. Andreas Tilgner

Institut für Geophysik, Georg-August-Universität Göttingen, Göttingen, Deutschland

Korreferent: Prof. Dr. Denis Grodent

Institut STAR, Université de Liège, Lüttich, Belgien

Weitere Mitglieder der Prüfungskommission:

Prof. Dr. Gregor Rauw

Institut STAR, Université de Liège, Lüttich, Belgien

Dr. Norbert Krupp

Max-Planck-Institut für Sonnensystemforschung, Göttingen, Deutschland

Dr. Aikaterini Radioti

Institut STAR, Université de Liège, Lüttich, Belgien

Dr. Elias Roussos

Max-Planck-Institut für Sonnensystemforschung, Göttingen, Deutschland

Tag der mündlichen Prüfung: 31.05.2017

Bibliografische Information der Deutschen Nationalbibliothek

Die Deutsche Nationalbibliothek verzeichnet diese Publikation in der Deutschen Nationalbibliografie; detaillierte bibliografische Daten sind im Internet über <http://dnb.d-nb.de> abrufbar.

ISBN 978-3-944072-56-2

uni-edition GmbH 2017

<http://www.uni-edition.de>

© Benjamin Palmaerts



This work is distributed under a
Creative Commons Attribution 3.0 License

Printed in Germany

Contents

Summary	15
Résumé	17
Zusammenfassung	19
1 Saturn and its magnetosphere	21
1.1 The planet Saturn	21
1.2 The magnetosphere of Saturn	22
1.2.1 Saturn's magnetic field	23
1.2.2 Magnetospheric configuration	23
1.2.3 Particle environment in Saturn's magnetosphere	26
1.2.4 Magnetospheric dynamics	32
1.3 Auroral processes at Saturn	40
1.3.1 The main auroral emission	41
1.3.2 Auroral signatures of dayside reconnection	42
1.3.3 Auroral signatures of tail reconnection	43
1.3.4 Auroral signatures of injections	44
1.3.5 Auroral hiss	44
1.4 Periodicities in Saturn's magnetosphere	45
1.4.1 Planetary period oscillations	46
1.4.2 Hourly periodicities	46
2 The Cassini mission	51
2.1 Missions at Saturn before Cassini	51
2.2 The Cassini-Huygens mission	51
2.3 The Magnetosphere Imaging Instrument (MIMI)	52
2.3.1 LEMMS	54
2.4 The Ultraviolet Imaging Spectrograph (UVIS)	58
2.5 The Radio and Plasma Wave Science (RPWS) instrument	59
2.6 The Magnetometer (MAG)	59
2.7 The Cassini Plasma Spectrometer (CAPS)	59
3 Quasi-periodic hourly pulsations in the energetic electron fluxes	61
3.1 Example of a quasi-periodic electron pulsed event	61
3.2 Initial survey	64
3.3 New survey of the hourly electron pulsations	64

3.4	Spatial distribution of the quasi-periodic electron injections	66
3.5	Morphological properties of the hourly electron pulsations	70
3.5.1	Interpulse period	70
3.5.2	Number of pulses	71
3.5.3	Morphology of the pulsations	74
3.5.4	Pitch angle distribution of the pulsations	77
3.6	Discussion	82
4	Coincident pulsations in the plasma wave and magnetic field	87
4.1	Pulsed signatures in plasma wave data	87
4.1.1	Presence of pulsed signal in the radio emissions	88
4.1.2	Characteristics of the signatures in the radio emissions	88
4.2	Pulsed signatures in the magnetic field	92
4.3	Discussion	92
5	Pulsations in the polar cusp aurora	97
5.1	Observation of an isolated polar auroral emission	97
5.2	In-situ measurements during auroral observations	102
5.3	Discussion	104
5.3.1	Polar cusp aurora	104
5.3.2	Pulsations of the high-latitude magnetopause reconnection	105
6	Electron pulsation triggering process at the magnetopause	109
6.1	Survey of the magnetospheric environment during the energetic electron pulsations	109
6.1.1	Spatial distribution of the plasma environment	110
6.1.2	Evidence of electron events in the close vicinity of the magnetopause	111
6.2	Study of the solar wind influence	113
6.2.1	Magnetopause crossings	113
6.2.2	The mSWiM model	116
6.3	Discussion	119
7	Conclusions and Perspectives	123
7.1	Conclusions	123
7.2	Perspectives	124
7.2.1	Pulsed oscillation of the main auroral emission	124
7.2.2	Other perspectives	128
A	List of quasi-periodic hourly electron pulsed events	133
A.1	List of events used in this thesis: 1 st July 2004 - 30 rd June 2014	133
A.2	Preliminary list of events from July 2014 to April 2017	149
B	Magnetospheric environment containing energetic electron pulsations	153
	Bibliography	157

Publications	181
Acknowledgements	185
Curriculum vitae	187

List of Figures

1.1	Artist view of the location of the rings and the major moons around Saturn	22
1.2	Sketch of Saturn's magnetosphere	24
1.3	Warping of the current sheet illustrated in the noon-midnight plane	25
1.4	Image of plumes at Enceladus	26
1.5	Magnetospheric ion composition at Saturn measured during Saturn Orbit Insertion	28
1.6	Differential flux map of the stable belts of the 25-60 MeV/nuc ions inside Tethys' L-shell	30
1.7	Long-term average of differential intensities of electrons as a function of L-shell	31
1.8	Schematic illustrating classical plasma motion along magnetic field lines around Saturn	33
1.9	Schematic of an interchange motion and example of interchange motion signatures in the charged particle data	36
1.10	Sketch of the Dungey cycle	38
1.11	Schematic showing the Vasyliūnas cycle	39
1.12	MHD simulation of Kelvin-Helmholtz vortices propagating along the magnetopause	40
1.13	Sketch of the main UV auroral components at Saturn	41
1.14	Typical Cassini/RPWS electric field spectrogram showing the auroral hiss emission and the Saturn Kilometric Radiation	45
1.15	First observation of quasi-periodic injections of energetic electron fluxes in Saturn's magnetosphere	47
1.16	Cassini observations of a pulsed particle acceleration event on day 269 of 2006	48
1.17	Ulysses observations of quasi-periodic 40-min pulsations and correlation with the solar wind velocity	50
2.1	Trajectories of Pioneer 11, Voyager 1, Voyager 2 and Cassini Saturn orbit insertion through Saturn's magnetosphere	52
2.2	Trajectories of Cassini during the "Grand Finale" phase of the mission	53
2.3	Sketch of the Cassini spacecraft with the instruments on board and the Huygens probe	53
2.4	Flight model of the MIMI/LEMMS sensor	55
2.5	Simulated trajectories of electrons and ions in the MIMI/LEMMS Low-Energy Telescope	56

2.6	Sketch of the MIMI/LEMMS double-ended detector	57
2.7	Optical design of the UVIS FUV telescope-spectrograph	58
3.1	Example of a quasi-periodic pulsed event	63
3.2	Lomb-Scargle periodogram of a quasi-periodic pulsed electron event . . .	66
3.3	Spatial distribution of the quasi-periodic pulsed events at low latitude . .	67
3.4	Distribution of the quasi-periodic electron pulsed events as a function of local time	68
3.5	Average number of days between two quasi-periodic electron pulsed events as a function of local time	69
3.6	Spatial distribution of the quasi-periodic pulsed events in a latitude-local time diagram	69
3.7	Distribution of the interpulse period for each LEMMS E-channel	71
3.8	Averaged interpulse period as a function of local time	72
3.9	Example of a 19h-long quasi-periodic pulsed event	72
3.10	Distribution of the number of pulsations per event	73
3.11	Averaged number of pulses per event as a function of local time	74
3.12	Normalized occurrence rate of each individual pulsation within a quasi- periodic pulsed event	75
3.13	Distribution of the ratio between the rise time and the decay time of the pulses	77
3.14	Spatial distribution of the rise and decay rates of the pulses	78
3.15	Correlation between the peak intensity of the pulses and their rise and decay rates	79
3.16	Quasi-periodic pulsed event with a good pitch angle distribution	80
3.17	Quasi-periodic pulsed event mixed with a field-aligned electron beam population	81
3.18	Illustration of the method to identify if Cassini is on open or closed field lines using Cassini/LEMMS instrument	82
3.19	Pitch angle distribution of the rise, the peak and the decay of the pulses .	83
3.20	Strong acceleration event in the magnetotail	84
4.1	Examples of quasi-periodic electron events for each category of coinci- dent signature in the plasma wave data	89
4.2	Spatial distribution of each category of coincident signature in the plasma wave data and relation with the electron cyclotron frequency	90
4.3	Example of two quasi-periodic electron events connected by their coinci- dent pulsed radio signatures	91
4.4	Spatial distribution of the coincident signatures in the magnetic field . . .	93
4.5	Sketch representing two observation situations of Cassini with and with- out auroral hiss pulsed signature	94
5.1	Sequence of polar projections of UVIS pseudoimages of the south FUV aurora on day 128 of 2013	99
5.2	Aurora brightness variation during the UVIS sequence on day 128 of 2013	100
5.3	Four examples of UVIS observations of pulsating isolated polar emissions	101
5.4	Cassini in-situ observations on days 127 and 128 of 2013	102

5.5	Cassini in-situ observations on days 237 and 238 of 2008	104
5.6	Example of quasi-periodic electron event located on open field lines	108
6.1	Spatial distribution of the plasma environments where quasi-periodic hourly electron pulsations are observed	111
6.2	Evidence of quasi-periodic energetic electron injections close to the magnetopause	112
6.3	Distribution of the Cassini magnetopause crossings and estimation of the solar wind dynamic pressure	114
6.4	Comparison between the estimation of the solar wind dynamic pressure at the magnetopause crossings given by two different methods	115
6.5	Cassini orbits considered in the investigation of the solar wind dependence	115
6.6	Daily number of hourly electron injections within 2 days from the magnetopause compared to the estimation of the solar wind dynamic pressure	116
6.7	Daily number of hourly electron injections compared to the mSWiM propagated solar wind velocity	117
6.8	Correlation coefficient between the daily number of hourly electron injections and the mSWiM propagated solar wind velocity for variable time lag	118
6.9	Daily number of hourly electron injections compared to the differential intensity in the LEMMS ion P2 channel	119
6.10	Sketch of Kelvin-Helmholtz-induced reconnection of flux tubes at the magnetospheric flanks	121
7.1	Motion of the main auroral oval during the Cassini/UVIS imaging sequence on day 129 of 2008	126
7.2	Latitudinal displacement of the main emission at 12 LT and 0 LT during the UVIS imaging sequence on day 129 of 2008	127
7.3	Pulsed electron injection exhibiting energy dispersion	128
B.1	Quasi-periodic hourly electron event observed in the central region of the plasma sheet	154
B.2	Quasi-periodic hourly electron event observed in the plasma sheet	154
B.3	Quasi-periodic hourly electron event observed in the southern lobe	155
B.4	Quasi-periodic hourly electron event observed in the low-latitude boundary layer	155
B.5	Quasi-periodic hourly electron event observed in a bimodal plasma environment	156

List of Tables

1.1	Physical properties of Saturn and its orbit	21
1.2	Properties of Saturn's magnetic field and magnetosphere	23
2.1	Instruments on board the Cassini spacecraft	54
2.2	Energy passbands for the ion and electron channels of MIMI/LEMMS used in this thesis	57
2.3	Cassini instruments used in this thesis	60
3.1	Percentage of events with the foreground pulsed signal in each LEMMS E-channel	67
3.2	Number of pulses and percentage of sawtooth pulses in each LEMMS E-channel	75
5.1	Occurrence probability of the polar cusp auroral emission and the dawn- side high-latitude ~1-h electron pulsations	107
6.1	Distribution of the quasi-periodic hourly electron injections in the differ- ent magnetospheric environments	110
B.1	Characteristics of the different magnetospheric environments	153

Summary

The exploration of the magnetospheres of Jupiter and Saturn has revealed various periodic processes. Some periodicities are related to the planetary rotation while some others are characterized by a short period. In Saturn's magnetosphere, periodicities of about one hour have been reported in the measurements of charged particle fluxes, plasma wave emissions, magnetic field strength and auroral emission brightness. The frequency, the spatial distribution and the magnetospheric process generating these hourly periodicities are still unknown. Similar short-period pulsations have been also observed in Jupiter's magnetosphere, suggesting that these 1-hour periodicities are the signature of a fundamental process in the magnetospheres of these two giant planets.

In this thesis, I performed a thorough analysis of these hourly periodicities at Saturn using the data sets of several instruments on board the Cassini spacecraft in orbit around the giant planet since 2004. First I made a survey of the quasi-periodic 1-hour energetic electron pulsations observed in Saturn's magnetosphere between 2004 and 2014 by the Cassini particle instrumentation. These pulsations appear in the electron fluxes at energies between a hundred keV up to several MeV. The survey includes 720 pulsed electron events observed in the outer magnetosphere over a wide range of latitudes and local times, revealing that this phenomenon is common and frequent in Saturn's magnetosphere. A statistical analysis on the morphological properties of the pulsed events suggests a high-latitude source for the pulsed energetic electrons.

I also investigated the simultaneous signatures of the electron pulsations in the radio emissions and the magnetic field measured by Cassini. The results of the multi-instrument study support the scenario of a high-latitude electron source and suggest a possible relation with the auroral processes. Images of Saturn's auroral emissions, which display the ionospheric response to magnetospheric dynamics, have been investigated to highlight any hourly pulsations. A high-latitude auroral spot exhibits quasi-periodic brightening with a periodicity of around 60 minutes. This auroral spot is associated with the magnetospheric cusp and high-latitude magnetopause reconnection in the lobes. Pulsed dayside magnetopause reconnection is likely a common triggering process for the cusp auroral brightening and for the high-latitude energetic electron pulsations.

Finally, analysis of the plasma environment with low-energy electron measurements provided evidence of the presence of energetic electron pulsed events in the close vicinity of the magnetopause. Therefore it is suggested that processes at the magnetopause, most likely magnetic reconnection induced by instabilities, generate the hourly electron pulsations located at low latitude.

The multi-instrument study achieved in my thesis sets constraints on the origin of the pulsed electron events and bring forward our current understanding on the hourly pulsations in Saturn's magnetosphere.

Résumé

L'exploration des magnétosphères de Jupiter et de Saturne a mis en évidence de nombreux phénomènes périodiques. Certaines périodicités sont liées à la rotation planétaire tandis que d'autres sont caractérisées par une courte période. Dans la magnétosphère de Saturne, des périodicités proches d'une heure ont été rapportées dans le flux de particules chargées, les émissions radio, l'intensité du champ magnétique et la brillance des émissions aurorales. La fréquence, la distribution spatiale et le mécanisme magnétosphérique produisant ces périodicités d'une heure restent inconnus. De semblables pulsations à courtes périodes ont également été observées dans la magnétosphère de Jupiter, ce qui semble indiquer que ces périodicités sont la signature d'un processus fondamental se produisant dans les magnétosphères de ces deux planètes géantes.

Dans le cadre de cette thèse, j'ai analysé de manière approfondie ces périodicités d'une heure mesurées dans l'environnement de Saturne, en utilisant les données de plusieurs instruments embarqués sur la sonde Cassini, en orbite autour de cette planète depuis 2004. J'ai tout d'abord répertorié toutes les injections quasi-périodiques d'électrons énergétiques détectées entre 2004 et 2014 par l'instrumentation de Cassini. Ces injections se traduisent par des pulsations dans le flux d'électrons à des énergies comprises entre une centaine de keV et plusieurs MeV. L'étude contient 720 événements d'électrons pulsés recensés dans la magnétosphère externe à différentes latitudes et différents temps locaux, ce qui montre que ce phénomène est commun et fréquent dans la magnétosphère de Saturne. Une analyse statistique des propriétés morphologiques des événements pulsés indique que la source des électrons se situe aux hautes latitudes.

J'ai aussi étudié les signatures des pulsations électroniques qui apparaissent simultanément dans les émissions radio et dans le champ magnétique mesurés par Cassini. Les résultats de cette observation multi-instrument renforcent le scénario d'une source d'électrons aux hautes latitudes et suggèrent un possible lien avec les processus auroraux. Des images des émissions aurorales sur Saturne, qui sont la réponse ionosphérique à la dynamique magnétosphérique, ont été analysées afin de mettre en évidence d'éventuelles pulsations d'une heure. Une structure aurorale isolée observée aux hautes latitudes montre une luminosité variable marquée par une période d'environ 60 minutes. Ce spot auroral est associé au cornet polaire et à de la reconnexion magnétique à la magnétopause aux hautes latitudes dans les lobes de la magnétosphère. Une reconnexion pulsée à la magnétopause est probablement un processus déclencheur commun pour l'embrillancement périodique de l'aurore du cornet polaire ainsi que pour les pulsations d'électrons énergétiques situées aux hautes latitudes.

Enfin, l'analyse de l'environnement de plasma réalisée à l'aide des mesures d'électrons aux basses énergies a révélé la présence d'électrons énergétiques pulsés dans le proche voisinage de la magnétopause. Il est dès lors avancé que des processus à la magnétopause,

probablement de la reconnexion magnétique produite par des instabilités, génèrent les pulsations électroniques d'une heure situées aux basses latitudes.

L'étude multi-instrument menée dans le cadre de ma thèse apporte de nouveaux éléments sur l'origine des électrons pulsés et accroît notre compréhension actuelle des pulsations d'une heure dans la magnétosphère de Saturne.

Zusammenfassung

Die Erforschung der Magnetosphären von Jupiter und Saturn zeigte viele periodische Prozesse. Einige davon sind verknüpft mit der Rotation des Planeten, andere sind durch kürzere Perioden charakterisiert. In der Saturnmagnetosphäre wurden periodische Variationen in Messungen von geladenen Teilchen, Plasmawellen, Magnetfeld und Auroraemissionen mit einer Periode von etwa einer Stunde nachgewiesen. Die Häufigkeit, die räumliche Verteilung sowie der zu Grunde liegende magnetosphärische Prozess dieser 60-Minuten Variationen sind nach wie vor unbekannt. Ähnliche Pulsationen in der Jupitermagnetosphäre deuten allerdings auf einen fundamentalen Prozess in den Magnetosphären bei beiden Gasplaneten hin.

In dieser Doktorarbeit führte ich eine detaillierte Analyse der 60-Minuten-Variationen in der Saturnmagnetosphäre durch. Dabei benutzte ich die Daten von mehreren Instrumenten an Bord der Raumsonde Cassini, die sich seit 2004 in einer Umlaufbahn um Saturn befindet. Zunächst wurde eine statistische Erhebung der Daten zwischen 2004 und 2014 in der äußeren Magnetosphäre durchgeführt. Dabei wurden quasi-periodische 60-Minuten-Variationen in den gemessenen Intensitäten von energiereichen Elektronen mit Energien von 100 keV bis zu einigen MeV untersucht. Insgesamt wurden 720 Elektronen-Pulsationen registriert, die sich über einen weiten Bereich von Breiten und Lokalzeiten in der Magnetosphäre verteilen. Dies deutet auf ein weit verbreitetes und häufiges Phänomen in der Saturnmagnetosphäre hin. Eine detaillierte Analyse der morphologischen Eigenschaften der Elektronen-Pulsationen lässt auf eine Quellregion in hohen Breiten schließen.

Zusätzlich führte ich im Rahmen dieser Arbeit eine Untersuchung von Plasmawellen- und Magnetfelddaten gemessen an Bord von Cassini zu Zeiten der Elektronen-Pulsationen durch. Dabei konnte die Annahme einer Quellregion dieser Elektronen-Pulsationen auf hohen Breiten und eine Korrelation zu Auroraemissionen unterstützt werden. Aufnahmen der Saturnaurora, die die Dynamik der magnetosphärischen Aktivität in der polaren Ionosphäre des Planeten abbildet, wurden auf Helligkeitsvariationen untersucht. Dabei konnte eine Emission auf hohen Breiten identifiziert werden deren Helligkeit mit etwa einer Stunde variierte. Diese Emission ist mit der Cusp-Region und mit Rekonnexionprozessen der Magnetopause auf hohen Breiten verknüpft. Gepulste Rekonnexion an der tagseitigen Magnetopause ist vermutlich ein häufiger Triggerprozess sowohl für diese Variation der Helligkeit der Cusp-Aurora als auch für die Elektronen-Pulsationen auf hohen Breiten.

Abschließend konnte auch eine Analyse der Plasmaumgebung mit Hilfe von Daten niederenergetischer Elektronen zeigen, dass Elektronen-Pulsationen ganz in der Nähe der Magnetopause beobachtet wurden. Daher ergibt sich die Schlussfolgerung, dass Rekonnexionprozesse an der Magnetopause, induziert durch Plasmainstabilitäten, zur Generierung von 60-Minuten-Variationen in Elektronenintensitäten auf niedrigen Breiten

führen.

Diese Multi-Instrument-Analyse im Rahmen meiner Doktorarbeit grenzt den Ursprung von beobachteten Elektronen-Pulsationen ein und erweitert das Verständnis von 60-Minuten Variationen in der Saturnmagnetosphäre.

1 Saturn and its magnetosphere

1.1 The planet Saturn

From all the planets of the solar system, Saturn holds a particular place in people's minds because of its striking rings, observed for the first time by Galileo Galilei in 1610. Saturn got its name in ancient times from the Roman god of agriculture *Saturnus*. The equivalent Greek god is called *Kronos*, explaining why both “Saturnian” and “Kronian” are adjectives relative to the planet Saturn.

Saturn is also the second largest planet in the solar system after Jupiter. Its equatorial radius of 60 268 km, which corresponds, by definition, to 1 Saturnian radius (R_S), is almost 10 times larger than the Earth's radius. Due to its fast rotation, around 10.7 h, and its low density, Saturn is particularly oblate with an equatorial radius 10% larger than its polar radius. Starting from the Sun, it is the sixth planet, orbiting at a distance of 9.6 AU¹. It takes about 29.5 years for Saturn to accomplish one revolution around the Sun. Its obliquity, similar to the Earth's obliquity, implies that different seasons exist at Saturn. Table 1.1 lists some physical properties of Saturn and its magnetosphere, facing the same information for the Earth.

Saturn is a gas giant since it is primarily composed of an atmosphere of molecular hydrogen (96.3%) and helium (3.25%). Traces of methane, ammonia and several other heavier species have been also detected in the different atmospheric layers (Fouchet et al. 2009). Hence, unlike the Earth, Saturn has no physical rocky surface. Its surface is defined as the level where the pressure reaches 1 bar. Saturn is the only planet with a density lower than the water density. The knowledge of the interior structure of Saturn is still imperfect. In the deep layers of the atmosphere, high pressure and temperature induce a liquefaction and an ionization of the hydrogen which becomes metallic at around 0.5 R_S (Hubbard

1. 1 Astronomical Unit (AU) is defined by the semimajor axis of the Earth which is 149 597 870 km.

	Saturn	Earth
Semimajor axis [AU]	9.58	1
Sidereal orbital period [years]	29.46	1
Equatorial radius (1 bar) [km]	60 268	6 378
Polar radius (1 bar) [km]	54 364	6 357
Sidereal rotation period [h]	~10.7	23.93
Mean density [g/cm ³]	0.687	5.514
Obliquity [°]	26.73	23.44

Table 1.1: Physical properties of Saturn and its orbit, compared to the Earth's values.

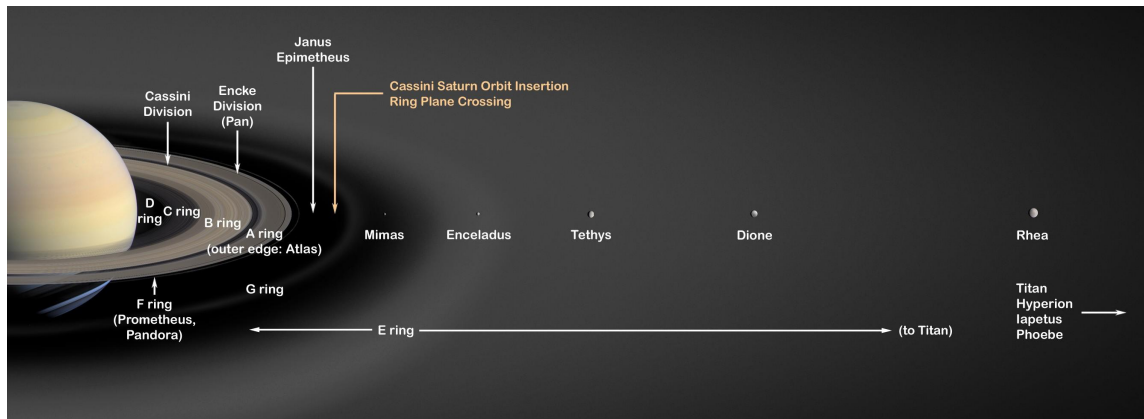


Figure 1.1: Artist view of the location of the rings and the major moons around Saturn. Image courtesy of NASA/JPL.

et al. 2002, Guillot 2005, Fortney and Nettelmann 2010). The center of the planet hosts probably a dense core composed of rock, iron and ice and has a mass of 15-20 Earth masses (Guillot et al. 2009, Hubbard et al. 2009).

In the Saturnian system, at least 62 moons are orbiting around the ringed planet. Ten of them have a diameter larger than 100 km. The major moons are Janus and Epimetheus (located at $2.5 R_S$ from Saturn, see Figure 1.1), Mimas ($3.1 R_S$), Enceladus ($3.9 R_S$), Tethys ($4.9 R_S$), Dione ($6.3 R_S$), Rhea ($8.7 R_S$), Titan ($20.3 R_S$) and Iapetus ($59.1 R_S$). These satellites are primarily composed of ice. Titan is the second largest moon in the solar system, after Jupiter's moon Ganymede, and the only one with a thick atmosphere. Its atmosphere is constituted of molecular nitrogen (97%) and methane (<3%).

Saturn's ring system includes seven rings in the equatorial plane, noted from A to G (see Figure 1.1). They can be grouped into two categories: the main rings (A, B, C) and the tenuous rings (D, E, G). The F ring is somewhat intermediate. The main rings are dense, bright and are located between 1.2 and $2.3 R_S$. They are made up of water ice particles of size in the order of centimeters or tens of centimeters. The A and B rings are separated by a darker band, the so-called Cassini division. The tenuous rings contain micrometer icy dust particles probably originating from the moons. The broad and faint E ring is mainly concentrated in the vicinity of Enceladus' orbit but extends out to the orbit of Titan. The E ring is thought to be populated by the ejecta from Enceladus (see Section 1.2.3.1). Reviews on Saturn ring investigations are given by Colwell et al. (2009) and Cuzzi et al. (2009).

1.2 The magnetosphere of Saturn

The magnetosphere of a magnetized planet is the region around the planet where the plasma² dynamics are mainly controlled by the planetary magnetic field. Three ingredients are necessary to form a planetary magnetosphere: a magnetic field strong enough to counter the solar wind, i.e. the plasma coming from the Sun, a source of magnetospheric

2. A plasma is an ionized state of matter made up of charged particles, namely ions and electrons.

	Saturn	Earth	Jupiter
Magnetic moment [Gauss.cm ³]	4.6×10^{28}	7.9×10^{25}	1.6×10^{30}
Surface magnetic field at equator [Gauss]	~0.2	0.31	4.28
Dipole tilt [°]	~ 0.0	9.9	9.4
Northward offset	~0.04 R _S	0.076 R _E	0.12 R _J
Typical magnetopause distance	22-27 R _S	8-12 R _E	63-92 R _J

Table 1.2: Properties of Saturn’s magnetic field and magnetosphere (Gombosi et al. (2009), Bagenal (2013)).

plasma and a source of energy. In this section, these ingredients are described for the particular case of the Saturnian magnetosphere.

1.2.1 Saturn’s magnetic field

Saturn has an intrinsic magnetic field produced by a dynamo process, like the Earth and Jupiter. Contrary to these two planets, Saturn’s magnetic field has the particularity to have a dipole axis nearly aligned with the rotation axis, implying an axisymmetry of the internal magnetic field (Smith et al. 1980, Connerney et al. 1982). The dipole tilt has been found to not exceed 0.06° (Cao et al. 2011). This axisymmetry is contradictory with Cowling’s theorem which states that axisymmetric magnetic field cannot be sustained by a dynamo (Cowling 1933). However, the field produced by the dynamo could be symmetrized by differentially rotating thermal winds in a stably stratified electrically conducting layer surrounding the dynamo, in the transition region between molecular and metallic hydrogen (Stevenson 1982, Stanley 2010).

Saturn’s magnetic dipole has been revealed to be offset northward by about 0.04 R_S from the planet center. Unlike the Earth which has a reversed magnetic field, the northern magnetic pole at Saturn corresponds to the northern geographic pole. The surface magnetic field at the equator is around 0.2 Gauss³, slightly smaller than the Earth’s equatorial magnetic field intensity (see Table 1.2).

1.2.2 Magnetospheric configuration

The planetary magnetic field is an obstacle for the solar wind flow. The deviation of the solar plasma around the planet forms an elongated cavity called magnetosphere. The solar wind compresses the magnetosphere on the dayside and stretches the magnetic field lines in the nightside, shaping the so-called magnetotail. This cavity is composed of different regions and particle populations described below and indicated on a sketch representing Saturn’s magnetosphere in Figure 1.2.

On the dayside, the magnetosphere is delimited by the magnetopause. This boundary is the surface where the dynamic pressure of the solar wind balances the total pressure inside the magnetosphere, namely the magnetic pressure and the plasma pressure (Kanani et al. 2010). The magnetopause location is in constant motion and is influenced by the solar wind dynamics. The relation between the magnetopause stand-off distance (R_{MP})

3. 1 Gauss = 10⁻⁴ Tesla

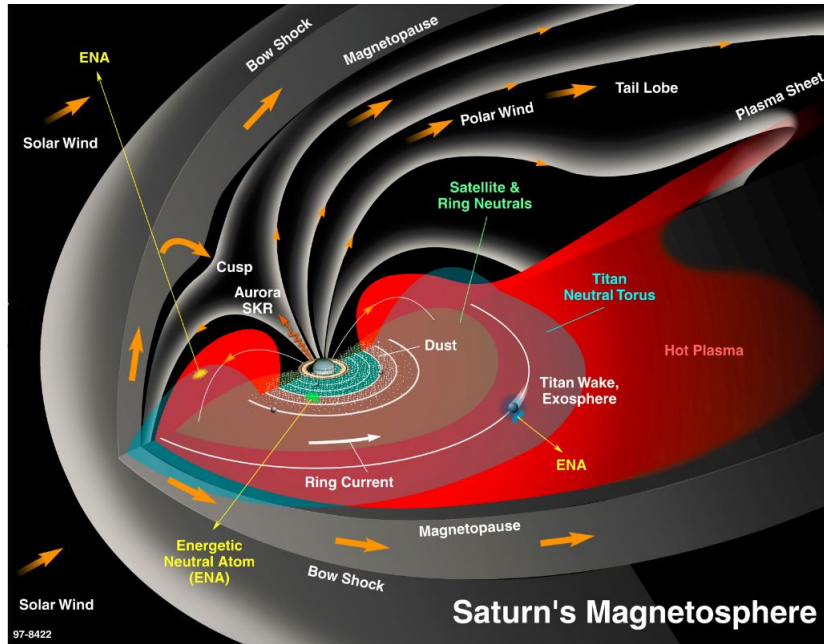


Figure 1.2: Sketch of Saturn’s magnetosphere. From Krimigis et al. (2004).

and the upstream dynamic pressure (P_{SW}) can be expressed by the following power law

$$R_{MP} \propto P_{SW}^{-\frac{1}{\alpha}} \quad (1.1)$$

The value of the parameter α equals 6 in the case of the Earth’s magnetosphere (Shue et al. 1997) and ranges between 4 and 5 for the Jovian magnetosphere which is hence more compressible (Huddleston et al. 1998). The Kronian case is intermediate with an $\alpha = 5.7 \pm 0.1$ according to the latest model of Saturn’s magnetopause based on seven years of Cassini⁴ measurements (Pilkington et al. 2015). Typically, the magnetopause stand-off distance at Saturn is between $22 R_S$ and $27 R_S$ from the planet, but can be as close as $18 R_S$ when the magnetosphere is compressed or at $29 R_S$ in the case of an expanded magnetosphere (Achilleos et al. 2008).

The magnetosphere being an obstacle for the supersonic solar wind flow, a shock wave, called bow shock, is formed upstream the obstacle, in front of the magnetopause (Burgess 1995). At the bow shock, the solar wind particles are slowed down to subsonic velocities and heated. The bow shock at Saturn is typically located between 24 and $32 R_S$ (Sulaiman et al. 2016). The magnetosheath is the region extending from the bow shock to the magnetopause and is populated by solar wind particles.

Due to the fast rotation of Saturn, a strong centrifugal force acts on the large amount of plasma coming from the moon Enceladus (see Section 1.2.3.1) and corotating with the planet. The centrifugal force confined the plasma to the equatorial region and drive it outwards, forming a plasma sheet. Since the magnetic field is “frozen” to the plasma, the magnetic field lines are stretched in a disc-like configuration by the outward plasma flow, creating the so-called magnetodisc (Arridge et al. 2007). The oppositely directed stretched field lines of the magnetodisc generate electric currents through the plasma sheet

4. Cassini is a spacecraft orbiting around Saturn (see Chapter 2).

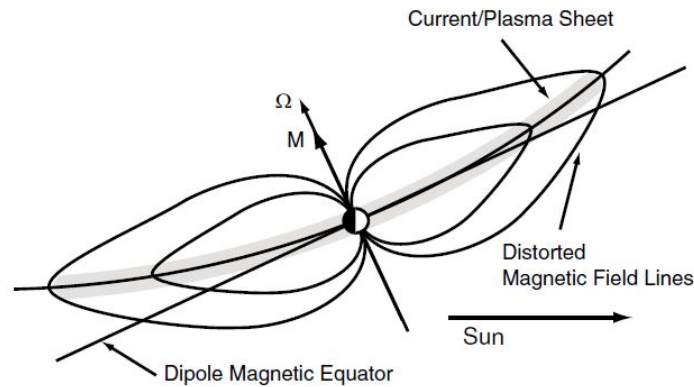


Figure 1.3: Warping of the current sheet illustrated in the noon-midnight plane. From Arridge et al. (2008b).

so that it is also referred to as the current sheet. Cassini observations have revealed that the plasma sheet has a typical thickness of $4 R_S$ (Arridge et al. 2008b) but it undergoes periodic thickening and thinning in the magnetotail (Thomsen et al. 2017, Cowley et al. 2017). The plasma sheet can extend out to the magnetopause in the dayside and at much larger distances in the nightside (Krupp et al. 2005). However, the dayside magnetodisc is more extended when the magnetosphere is expanded, and thus when the solar wind dynamic pressure is low (Arridge et al. 2008a). A seasonal effect acting on the current sheet has been also identified by Arridge et al. (2008b): the current sheet is warped into a bowl-shape whose orientation, northward or southward, depends on the solar wind direction (Figure 1.3).

Closer to the planet, the opposite drift of negative and positive magnetospheric particles (see Section 1.2.4.1) in an inhomogeneous planetary magnetic field creates an electric current around the planet, called ring current. An eastward ring current has been detected around Saturn during the Voyager 1 and 2 flybys (Connerney et al. 1981). The ring current has an averaged half-thickness of $1.5 R_S$ (Kellett et al. 2009) and extends from around 7 to $15 R_S$ from the planet (Gombosi et al. 2009, Kellett et al. 2011, Sergis et al. 2017). However, the ring current and its outer boundary are significantly influenced by the magnetopause position (Bunce et al. 2007, Gombosi et al. 2009). Furthermore, this current produces a perturbation in the magnetic field by depressing the field close to the planet and strengthening it in the outer magnetosphere.

The magnetotail regions above and below the plasma sheet are called the lobes. They host tailward elongated open flux tubes connecting the high-latitude ionosphere to the interplanetary magnetic field (IMF). The Saturnian northern and southern lobes are characterized by a much stronger and quieter (i.e. without fast fluctuations) magnetic field than in the current sheet and by a very low plasma density (Jackman and Arridge 2011).

Above the poles of the planet, the topology of the magnetic field forms a funnel-shaped region inclined toward the Sun. This high-latitude region is known as the cusp and it constitutes the main entry into the magnetosphere for the solar wind particles (Smith and Lockwood 1996, Cargill et al. 2005).

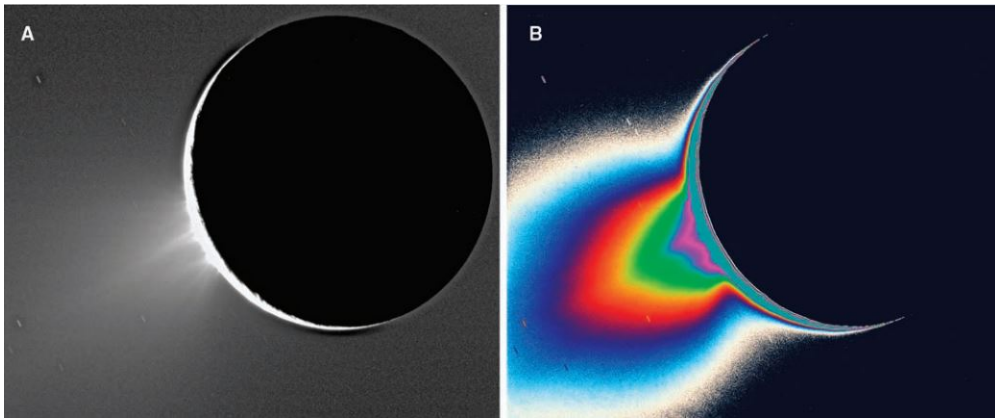


Figure 1.4: Panel A: Image of plumes at Enceladus, acquired with the Cassini/ISS NAC camera. Panel B: the same image color-coded to enhance the visibility of the plumes. From Porco et al. (2006).

1.2.3 Particle environment in Saturn's magnetosphere

1.2.3.1 Enceladus: the primary source

Like at Jupiter, internal plasma sources are very important in the magnetosphere of Saturn. While the volcanic moon Io is the main plasma source in the Jovian magnetosphere, the little icy moon Enceladus (radius of 252 km) plays the same role in the Kronian magnetosphere. Before the Cassini mission, nitrogen, supplied by Titan's dense atmosphere, was thought to be the main constituent of Saturn's magnetosphere. Surprisingly, Cassini discovered a magnetosphere containing mainly water molecules and its derived species, revealing Enceladus as the primary source of matter for Saturn's magnetosphere (Dougherty et al. 2006). The active volcanism on Enceladus, caused by internal tidal heating, results in eruption of a hundred of geysers along icy surface fractures in the southern polar region (see Figure 1.4, Porco et al. (2006, 2014)). These geyser plumes, which can extend over 500 km above the surface, are mainly composed of water vapor and ice grains (Hansen et al. 2006, Waite et al. 2006). The source rate of water molecules ejected from Enceladus is variable as revealed by the different Enceladus flybys by Cassini and ranges from less than 100 kg/s to 750 kg/s (Smith et al. 2010). A production rate as high as 1 600 kg/s has been even claimed by Saur et al. (2008) on the basis of an atmospheric model constrained by Cassini data. The geological activity of Enceladus and the quantity of material ejected is controlled by the tidal stresses inside the moon (Hedman et al. 2013, Porco et al. 2014).

Hence, the Enceladus' plumes are made up of neutral particles which escape the icy moon and populate a neutral torus, also known as the Enceladus torus, which is located in the vicinity of the moon's orbit, at around $4 R_S$ (Johnson et al. 2006b). This narrow torus provides neutrals to a larger torus containing O, OH and H_2O molecules (Shemansky et al. 1993) through charge-exchange processes and collisions with corotating ions, collisions between neutrals and molecular dissociation (Johnson et al. 2006b, Jurac and Richardson 2005, Cassidy and Johnson 2010). This large toroidal neutral cloud extends from $2 R_S$ to beyond Titan's orbit, at $20 R_S$ (Melin et al. 2009, Persoon et al. 2013). Additionally, the grains of Enceladus' plume, provided that they have a sufficient velocity to escape,

populate the E Ring which mainly lies from $3 R_S$ to at least $8 R_S$ (Kempf et al. 2010).

The Saturnian magnetosphere has the particularity to be dominated by neutral atoms and molecules, mainly due to Enceladus' cryovolcanism which provides 10^{28} molecules of water per second (Hansen et al. 2006, Burger et al. 2007). Therefore, neutral H_2O , H and their dissociative products (which constitutes the so-called water group) are the dominant species in the magnetosphere (Mauk et al. 2009). The neutral density exceeds the plasma density by at least one order of magnitude (André et al. 2008) and the neutral-to-ion number density ratio is three orders of magnitude larger at Saturn than at Jupiter (Delamere et al. 2007). In addition to the water group species coming from Enceladus, atomic hydrogen arises out of Saturn's thermosphere⁵ (Shemansky et al. 2009), the rings are source of molecular hydrogen and molecular oxygen (Johnson et al. 2006a, Tseng et al. 2010) and Titan's atmosphere supplies the magnetosphere with molecular hydrogen, molecular nitrogen and, to a lesser extent, methane (De La Haye et al. 2007, Cui et al. 2008).

1.2.3.2 The plasma sources

As explained above, the moon Enceladus is the primary source of neutrals in Saturn's magnetosphere. It is also indirectly the dominant source of plasma, given that roughly 30% of the particles in the neutral water cloud are expected to be ionized (Cassidy and Johnson 2010). The ionization can occur via an impact with an electron or a solar ultraviolet (UV) photon (photoionization). Charge exchange is another important process which does not increase the ion population but adds fresh ions in the magnetosphere and change the overall plasma momentum (Fleshman et al. 2010, Blanc et al. 2015). Saturn's and Titan's ionosphere, as well as the rings and the solar wind, are other sources of plasma, but minor compared to Enceladus.

The primary ions encountered in Saturn's magnetosphere are H^+ , H_2^+ and the water group ions W^+ (O^+ , OH^+ , H_2O^+ , H_3O^+) which are the most abundant (DiFabio et al. 2011). The magnetospheric ion composition measured by the Cassini MIMI/CHEMS instrument (Section 2.3) during Saturn Orbit Insertion is given in Figure 1.5. The water ions are produced from the Enceladus plume material (Burger et al. 2007). Most of the protons result of the ionization of the H cloud arising from the atmosphere of Saturn (Shemansky et al. 2009, Melin et al. 2009). They can also come from the neutral cloud or be supplied by the solar wind. The dominant source of the H_2^+ ions is Titan's atmosphere (Cui et al. 2008). Other minor species have been detected in Saturn's magnetosphere such as He^+ and He^{++} originating from the solar wind (DiFabio et al. 2011), O^{++} produced by the ionization of O^+ , O_2^+ whose sources are the rings and Enceladus (Christon et al. 2013), N^+ likely originating from Enceladus too (Smith et al. 2007), the Mass-28 ion group (including $C_2H_5^+$, $HCNH^+$, N_2^+ and CO^+) from the rings and the moons (Christon et al. 2013, 2014), and Fe^+ produced in the ionosphere and/or in the main rings (Christon et al. 2015).

5. The thermosphere is the upper layer of Saturn's atmosphere.

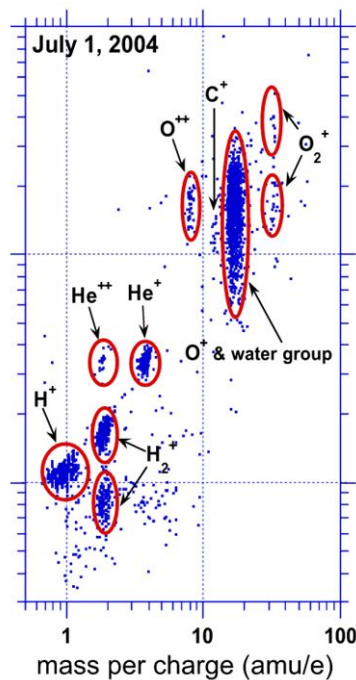


Figure 1.5: Magnetospheric ion composition in the energy range 83-220 keV/e measured by Cassini/MIMI/CHEMS during Saturn Orbit Insertion on July 1, 2004. Adapted from Blanc et al. (2015).

1.2.3.3 The plasma populations

The plasma filling Saturn’s magnetosphere exhibits various densities and energies from a few electron-volts (eV) to several MeV. The “cold” plasma, also known as the “thermal” plasma and characterized by particles with energy up to a few 100 eV, dominates the plasma density in the inner magnetosphere ($< 6 R_S$). This population is not present beyond $15 R_S$ (Schippers et al. 2008) and its equatorial plasma density peaks between 4 and $5 R_S$, thus between Enceladus and Tethys’ orbits (Persoon et al. 2013). Furthermore, the water group ions are centrifugally confined in the equatorial plane (Thomsen et al. 2010). On the basis of different observations, it has been concluded that the source of this plasma population is located in the inner magnetosphere. For instance, the observed increase of both the ion velocity and temperature with distance from Saturn rules out the existence of an inward adiabatic transport from outer magnetospheric regions (Sittler et al. 2006, Wilson et al. 2008).

The plasma at higher energies, between 0.1 and 1 keV, can be referred as “suprathermal”, even though this term is sometimes given for other energy ranges. The suprathermal plasma population is present mainly beyond $9 R_S$ and is still observed in the outer magnetosphere, beyond $15 R_S$ (Schippers et al. 2008). The source of the suprathermal electrons is thought to be located in the middle or outer magnetosphere and they might diffuse inward by flux tube interchange (see Section 1.2.4.3) with outward drifting cold plasma (Rymer et al. 2007, 2008). During the inward motion, the particles undergo an adiabatic heating.

Saturn’s magnetosphere also contains energetic electrons and ions which constitute

the dominant contribution in the total plasma pressure although their density is much lower (Sergis et al. 2007). The “hot” plasma, with energies ranging from 1 keV to 100 keV, is mainly found in the ring current and the plasma sheet mentioned in Section 1.2.2 (Krupp et al. 2005).

The very energetic particles (>100 keV up to tens of MeV) populate mainly the radiation belts, observed already during the first flyby’s of Saturn (e.g. Fillius and McIlwain (1980), Vogt et al. (1982)). Similar to the Van Allen radiation belts around the Earth, Saturn’s radiation belts are a population quasi-symmetric in local time⁶ of charged high-flux particles trapped by the magnetic field (Paranicas et al. 2008). The ionic radiation belts extend from the magnetic field lines connecting the planet to the outer edge of the main rings (at $2.27 R_S$ in the equatorial plane) to the field lines connected to Tethys’ orbit (at $4.89 R_S$), as represented in Figure 1.6. In other words, the radiation belts are between the L-shell ($L = 2.27$ and $L = 4.89$), the L-shell of a magnetic field line being approximately the ratio between the radial distance of the field line in the equatorial plane and the planet radius. The MeV ions in the radiation belts are continuously absorbed by the icy moons orbiting within them, namely Janus/Epimetheus, Mimas and Enceladus. The signature of the moon absorption is permanent drops of the count rates in the ion radial distribution at the L-shells corresponding to the moons (Paranicas et al. 2008, Krupp et al. 2009). These signatures are more important at Saturn because of the axisymmetry of the magnetic field (Roussos et al. 2007). Small intensity decreases are also observed at distances corresponding to the F Ring and the G Ring, revealing ion absorption by the ring material as well.

While the radiation belt population is relatively stable inward of Tethys’ L-shell ($L = 4.89$), a transient belt has been discovered near the orbit of the moon Dione, between 4.89 and $8 R_S$ (Roussos et al. 2008). This transient radiation belt can be observed for several months and appears in response to the arrival of solar wind shocks, also known as coronal mass ejections. On the contrary, the belts inside Tethys’ orbit remain unchangeable during enhanced solar wind activity, suggesting that Tethys and Dione isolate the inner belts by absorbing the inward energetic ions coming from the middle and outer magnetosphere (Roussos et al. 2008). However, the ionic radiation belts undergo a long-term modulation related to the solar wind cycle (Roussos et al. 2011).

It is suggested that the radiation belts are populated mainly through the cosmic ray albedo neutron decay (CRAND) process (Kollmann et al. 2013). The CRAND process (Cooper 1983, Blake et al. 1983) involves the production of high-energy neutrons (in addition to other various particles) by the interaction between GeV galactic cosmic rays and the planet’s atmosphere and rings. A tiny fraction (about 0.1%) of these high-energy neutrons decay and produce high-energy protons and electrons which can populate the radiation belts. Since less galactic cosmic rays can penetrate into Saturn’s magnetosphere when the solar activity is higher, the intensity of the ionic radiation belts follows the solar cycle (Roussos et al. 2011).

The Saturnian electron radiation belts exhibit much more complex structure and temporal variation than the ionic belts. KeV and MeV electron distributions show more

6. Local time (LT) refers to a planetary coordinate system fixed with the direction of the Sun: 12 h in local time (noon) corresponds to the longitude pointing to the Sun, 00 LT (midnight) points in the opposite direction, while 06 LT (dawn) and 18 LT (dusk) are perpendicular to the noon-midnight line, pointing respectively to the left and to the right with the Sun in the back.

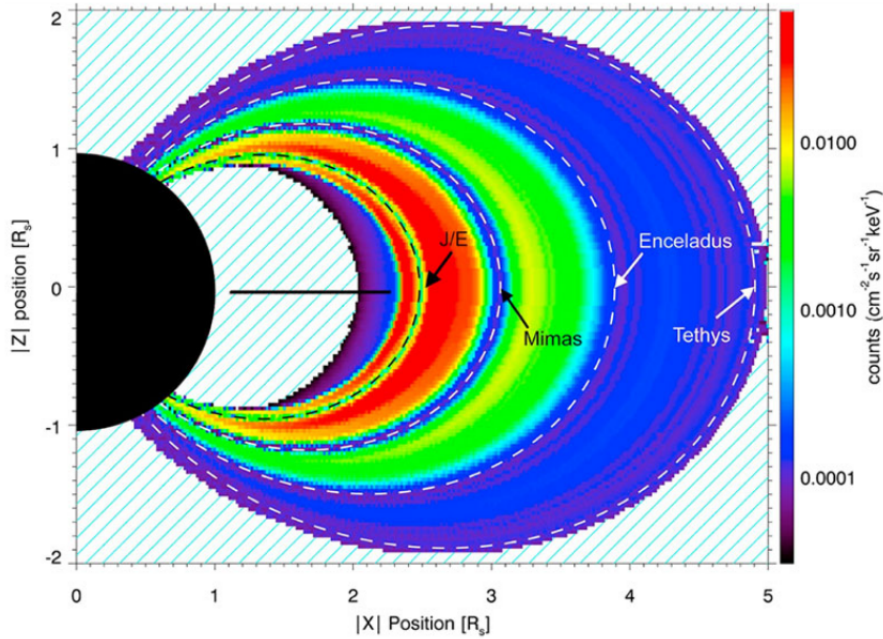


Figure 1.6: Differential flux map of the stable belts inside Tethys' L-shell of the 25-60 MeV/nuc ions, based on LEMMS data from 36 orbits. The L-shell of the various moons are indicated. The associated flux dropouts are visible as well as the small flux decrease at the L-shell of the G Ring. Hatched regions above the main rings have particle flux lower or equal to that of the color bar. From Roussos et al. (2008).

pronounced local time asymmetries especially in the noon-midnight direction (Paranicas et al. 2010a). This asymmetry is due to an electric field with a noon-to-midnight orientation (Andriopoulou et al. 2012, Thomsen et al. 2012, Wilson et al. 2013). Unlike the ions, the electrons are not confined within the moon L-shells and can then avoid moon absorption, preventing the intensity dropout at the moon L-shells (Roussos et al. 2014). For the same reason, electron belts are sensitive to the dynamics of the middle and outer magnetosphere (Krimigis et al. 2007). Roussos et al. (2014) argued that the source population of the radiation belt electrons resides in the ring current in the middle magnetosphere. The electrons in the seed population are adiabatically heated on their way to the radiation belts (Paranicas et al. 2010b).

The averaged electron intensity distribution in Saturn's magnetosphere is given in Figure 1.7 for five different energy ranges whose the mean energy is indicated in the inset panel. The high-energy electron population of the radiation belts are represented by the red line at L-shell < 6. Their sources in the middle magnetosphere are the populations at higher intensities but lower energy, noted from 1 to 3. The source sustaining the large intensities of the middle magnetosphere population is still unknown. It is natural to think that this source is located in the outer magnetosphere. However, at large L-shells, the magnetosphere is mainly populated by low energy particles and at MeV energies, the averaged electron intensities are roughly constant at the background level, as shown by the lower orange line in Figure 1.7 (Kollmann et al. 2011). Nevertheless, remarkable high-intensity MeV electrons have been observed in the outer magnetosphere during the Cassini mission. These MeV electron injections, which could be a source for the middle

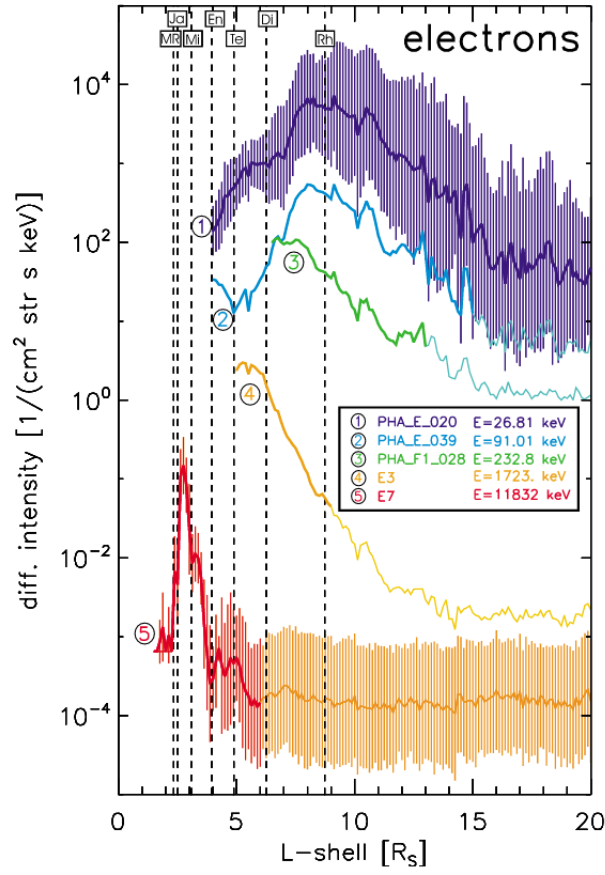


Figure 1.7: Long-term average of differential intensities of electrons as a function of L-shell. The error bars show the standard deviation of the averages. A variety of representative LEMMS channels is shown in different colors and their mean energies are indicated. Dashed lines mark the outer edge of the main rings and the orbits of several moons (Janus, Mimas, Enceladus, Tethys, Dione and Rhea). From Kollmann et al. (2011).

magnetosphere population, and hence for the radiation belts, are characterized by quasi-periodic flux enhancements. These pulsed electron events will be depicted in Section 1.4 and explicitly described in Chapter 3.

1.2.3.4 Plasma β

The plasma β is the ratio of thermal pressure over magnetic pressure:

$$\beta = \frac{nk_B T}{B^2 / \mu_0}$$

with n the number density, k_B the Boltzmann's constant, T the temperature, B the magnetic field and μ_0 the vacuum permeability. In the inner magnetosphere, where the magnetic field is strong, the plasma β is below the unity and is as low as 0.1 at $5 R_S$ (Sergis et al. 2017). The plasma β becomes greater than 1 from $8 R_S$ in the nightside and from $10 R_S$ in the dayside. Hence, beyond 8-10 R_S , the plasma pressure dominates the magnetic pressure. At farther distances, in the ring current, the plasma β generally ranges between

3 and 10 (Sergis et al. 2010, 2017). The plasma β adjacent to the magnetopause is slightly lower than in the ring current while large plasma β is encountered in the magnetosheath where it can exceed 50 (Masters et al. 2012a).

1.2.4 Magnetospheric dynamics

1.2.4.1 Motion of charged particles in an electromagnetic environment

The classical motion of a plasma in an electromagnetic field is briefly explained in this section. In a uniform magnetic field, the charged particles follow a helical path around the field line. This gyration motion, also called the cyclotron motion, is characterized by the radius of the helix, known as the gyroradius, the cyclotron radius or the Larmor radius. The gyroradius r_g depends on the particle mass m and charge q , the magnetic field intensity B and the particle velocity component perpendicular to the field v_{\perp} as follows:

$$r_g = \frac{mv_{\perp}}{qB} \quad (1.2)$$

The gyroradius of electrons is then smaller than the the proton gyroradius. The cyclotron frequency of the gyromotion of a given particle depends only on the magnetic field strength:

$$f_c = \frac{qB}{2\pi m} \quad (1.3)$$

Another important frequency characterizing a plasma is the so-called plasma frequency. A plasma is quasi-neutral: the number of positive and negative charges in the ionized gas are roughly equal in the stationary state. If an external force disturb this quasi-neutrality, the electrons, more mobile than the ions, move to restore the charge neutrality. Because of their inertia, the electrons move farther than the equilibrium position and start to oscillate around this position at a specific frequency which is the plasma frequency:

$$f_{pe} = \frac{1}{2\pi} \sqrt{\frac{n_e e^2}{m_e \epsilon_0}} \quad (1.4)$$

where n_e is the electron number density, e is the electric charge, m_e is the electron mass and ϵ_0 is the vacuum permittivity.

The angle between the velocity vector of the particle and the magnetic field is called the pitch angle α of the particle:

$$\alpha = \arctan\left(\frac{v_{\perp}}{v_{\parallel}}\right) \quad (1.5)$$

Hence, particles moving along the field lines have a pitch angle of 0° or 180° .

Generally, planetary magnetospheres include electric fields perpendicular to the magnetic field. The presence of the electric field leads to a drift of the cyclotron motion in a direction perpendicular to the magnetic field and to the electric field. This electric drift is known as the $\mathbf{E} \times \mathbf{B}$ drift since its velocity is given by

$$\vec{v}_E = \frac{\vec{E} \times \vec{B}}{B^2} \quad (1.6)$$

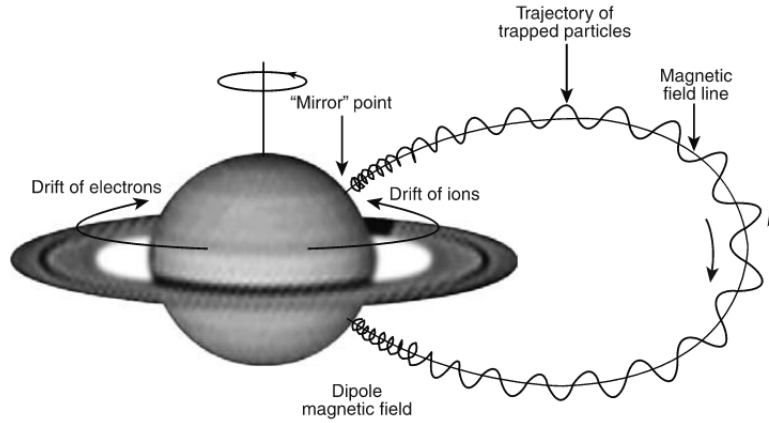


Figure 1.8: Schematic illustrating classical plasma motion along magnetic field lines around Saturn. Adapted from Rymer et al. (2007).

This velocity being charge-independent, electrons and ions drift in the same direction.

Another particle drift arises from the non-uniformity of the magnetic field. Indeed, the gradient of the magnetic field intensity induces a gradient drift which can be expressed as:

$$\vec{v}_\nabla = \frac{mv_\perp^2}{2qB^3}(\vec{B} \times \nabla \vec{B}) \quad (1.7)$$

This drift is perpendicular to the field and its gradient and is consequently in the azimuthal direction around a planet (see Figure 1.8). It is noteworthy that the electron and proton drifts are in opposite direction due to the charge dependence.

Finally, particles experience a curvature drift induced by the curvature of the magnetic field lines:

$$\vec{v}_c = \frac{mv_\parallel^2}{qR_c^2 B^2}(\vec{R}_c \times \vec{B}) \quad (1.8)$$

where R_c is the local radius of curvature. The curvature drift is also in the azimuthal direction and oppositely directed for ions and electrons. Both the gradient and the curvature drifts are energy dependent: a larger velocity of the particle implies an increased drift.

Some physical quantities, called adiabatic invariants, are conserved along the path of a charged particle in an electromagnetic environment. One of these quantities is the magnetic moment of the particle in gyromotion:

$$\mu = \frac{mv_\perp^2}{2B} = \frac{mv^2 \sin^2 \alpha}{2B} \quad (1.9)$$

using the pitch angle α . Because of the conservation of the magnetic moment, if a particle encounter an increased magnetic field, its perpendicular velocity must increase as well. The total energy of the particle being constant, its parallel velocity decreases. When the parallel velocity reaches zero, the particle cannot continue to stronger magnetic field region and is forced to go back in the opposite direction. The point where $v_\parallel = 0$ is called the magnetic mirror point. This magnetic mirroring leads to a bouncing motion of the particles between the mirror points of each hemisphere (see Figure 1.8). At the mirror point, the pitch angle $\alpha_m = 90^\circ$. Therefore, using the conservation and the definition of

the magnetic moment (Equation 1.9), the intensity of the magnetic field at the mirror point B_m can be determined from the magnetic field intensity (B_i) and the pitch angle (α_i) at any position along the particle's trajectory:

$$B_m = \frac{B_i}{\sin^2 \alpha_i} \quad (1.10)$$

The particles can be lost if their mirror point is located in the atmosphere. For any particle, a critical pitch angle exists above which the particle will be lost in the atmosphere. The so-called loss cone is defined by this critical pitch angle which can be easily calculated at the equatorial plane:

$$\alpha_{\text{loss cone}} = \arcsin \left(\sqrt{\frac{B_{\text{equator}}}{B_{\text{surface}}}} \right) \quad (1.11)$$

Finally, a plasma can host various kinds of waves including the Alfvén waves which will be invoked in this thesis. The Alfvén waves propagate along the magnetic field lines and oscillate in the transverse direction. The propagation speed of these noncompressional waves, the so-called Alfvén velocity, is $v_A = B / \sqrt{\mu_0 \rho}$ with B the magnetic field intensity, ρ the plasma mass density, and μ_0 the vacuum permeability. The Alfvén waves have the particularity to be able to carry currents.

1.2.4.2 Plasma corotation

Particles in the upper layer of Saturn's atmosphere can be ionized by the solar UV light, creating the ionosphere. The resulting ions move by following the motion of the magnetic field lines in the ionosphere. However, as the atmosphere rotates with the planet, collisions between the atmospheric neutrals and the ions drag the ionosphere towards planetary rotation. The magnetic field lines, frozen in the plasma, are then pulled toward corotation, eventually driving the corotation of the magnetospheric plasma. However, this azimuthal circulation of the plasma in the magnetosphere competes with plasma convection driven by the solar wind (Brice and Ioannidis 1970). Hence, the corotating region, which is called plasmasphere, and the magnetosphere-ionosphere coupling sustaining the corotation varies from one magnetosphere to the other. At Earth, the plasmasphere is limited to a few Earth radius from the planet (Mauk et al. 2009). At Jupiter, which is a fast rotator with an important plasma source and a strong magnetic field, the plasmasphere extends to the magnetopause. Therefore, Jupiter has a rotationally-driven magnetosphere while the Earth's magnetosphere is solar-wind driven. Cassini measurements of the plasma flow inside Saturn's magnetosphere have revealed that the corotation flow is dominant up to $20 R_S$ and until the magnetopause ($22\text{-}27 R_S$) on the dayside (McAndrews et al. 2009, Thomsen et al. 2010). Saturn's magnetosphere is then rotationally-driven like Jupiter.

Inside the plasmasphere, the corotating plasma is not everywhere in rigid corotation, i.e. in rotation at the same velocity as the planet. The plasma flow is slowed down when new plasma produced by ionization of Enceladus ejecta is added to the flow. Moreover, the outward motion of the magnetospheric plasma leads to a decrease of its angular velocity. These two effects are usually referred to as "mass-loading". Finally, the corotating plasma undergoes collisions with the neutrals. These three processes at Saturn cause a

lag of plasma compared to the rigid corotation (Wilson et al. 2008, Mauk et al. 2009). Hence, at Saturn, in-situ measurements have revealed that the plasma flow subcorotates with velocities from 50% to 70% of the full corotation over the L-shell range from 6 to 16, according to the study by Thomsen et al. (2010), and from 70% to 85% according to a previous study by Wilson et al. (2008). In the inner magnetosphere, the plasma subcorotation is more important in the vicinity of Enceladus' orbit ($\sim 4 R_S$) compared to shorter and farther distances (Wilson et al. 2009). This velocity decrease is likely due to the mass-loading of plasma from charge exchange interactions in the Enceladus torus. It appears that the plasma is in rigid corotation only inside $3 R_S$ (Wilson et al. 2009). In the outer nightside magnetosphere, the azimuthal velocity remains roughly constant beyond $25 R_S$ at $\sim 60\%$ of full corotation (Kane et al. 2008, McAndrews et al. 2009, Achilleos et al. 2010).

1.2.4.3 Plasma injections

An injection is a general term to denote a discrete population of energized particles in an environment of lower energy plasma. Various magnetospheric dynamics can trigger injections of plasma in Saturn's magnetosphere. The main injection processes are explained in this section.

The plasma produced from Enceladus material is loaded in the inner magnetosphere and is entrained by the planetary rotation. The centrifugal force confines the plasma in the equatorial plane and can lead to flux tube interchange motion induced by the so-called centrifugal interchange instability (Hill 1976). In a centrifugally-driven environment like in Saturn's plasma sheet beyond $2 R_S$ (Arridge et al. 2011), a flux tube mass content close to the planet higher than at further distances is an unstable configuration. This is equivalent to placing a dense fluid above a less dense fluid in a gravitational field. Hence, the centrifugal instability leads to a spontaneous motion of the flux tubes: the most loaded flux tubes will interchange with the less loaded flux tubes located further out. This flux tube interchange motion results in an inward transport of hot tenuous plasma coupled with an outward transport of cold dense plasma, as sketched in Figure 1.9a (Hill et al. 2005, Burch et al. 2005). The inward hot plasma motion is faster than the plasma outflow (Chen et al. 2010). This hot plasma injection has a narrow longitudinal extent, resembling a finger sinking in the dense plasma population (Hill et al. 2005, Liu et al. 2010). However, it is still unclear if injections are extended fingers or "bubbles", i.e. isolated flux tubes (Blanc et al. 2015).

The inward hot plasma motion undergoes gradient and curvature drifts, which are variable with charge and energy (see Section 1.2.4.1). Consequently, the particles arrive at the spacecraft at different times and an ion/electron energy dispersion is observable on energy-time spectrograms, as shown as example in Figure 1.9b (Hill et al. 2005, Mauk et al. 2005, Paranicas et al. 2007). The opposite drift of electrons and ions creates V-shaped structures on the spectrograms, with the left (right) leg of the V formed by the injection of hot ions (electrons). A statistical study of the injection/dispersion events revealed that they occur mainly between $L = 6.5$ and $L = 9$ (Chen et al. 2010, Kennelly et al. 2013). Chen and Hill (2008) found that the plasma injections cluster in the prenoon local time sector while Kennelly et al. (2013) argued that the interchange motion preferentially takes place in the postnoon and midnight sectors. This mismatch might stem

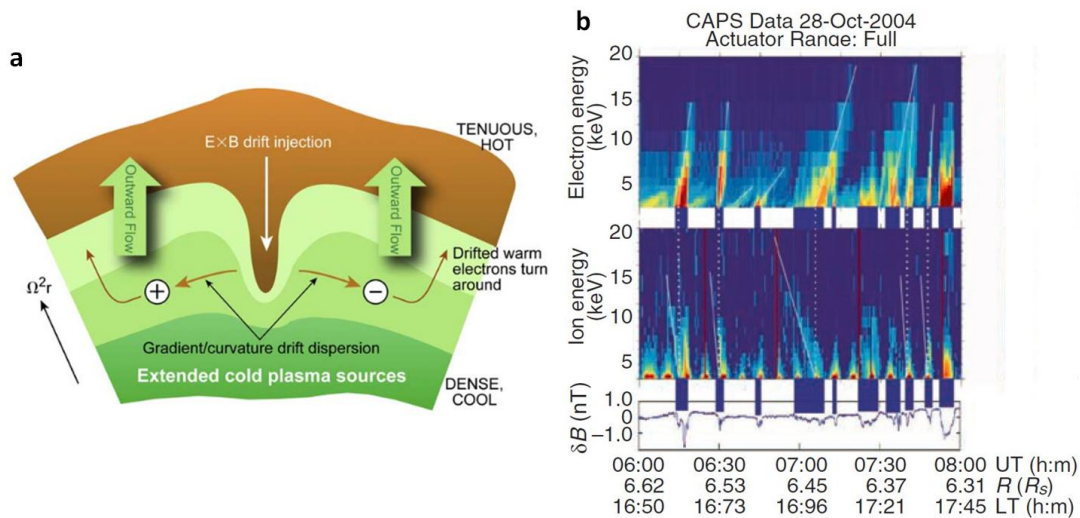


Figure 1.9: (a) Schematic of an interchange motion between hot tenuous plasma and cold dense plasma. From Rymer et al. (2008). (b) Example of interchange motion signatures on linear energy-time spectrograms of electrons (top) and ions (middle) from the Cassini/CAPS instruments. The bottom panel shows simultaneous magnetic field magnitude measurements from the MAG instrument, after subtracting a cubic polynomial fit. From Mauk et al. (2009), adapted from Hill et al. (2005).

from an inaccuracy in the plasma azimuthal velocity profile used by Chen and Hill (2008). Interchange events have also a signature in the magnetic field (André et al. 2007) and in the radio emissions (Rymer et al. 2009b, Kennelly et al. 2013).

The aforementioned injections triggered by centrifugal instabilities are observed mainly at low energies, have a limited size ($< 1 R_S$) and survive less than one Saturn rotation (Hill et al. 2005). Another type of injections involves high-energy particles, mainly electrons (> 100 keV). These injections have a larger size and subsist during one or more Saturn rotations (Mauk et al. 2005, Paranicas et al. 2007, 2010b). These large-scale injections have a similar V-shaped signature in the energy-time spectrograms as the centrifugally driven injections, except that they exhibit increased dispersion due to their longer survival time. The large-scale injections have been found to preferentially occur in the nightside and morning sector (Müller et al. 2010).

The large-scale energetic injections are associated with emissions of energetic neutral atoms (ENA) rotating from midnight to dawn. The ENA are produced by charge exchange between the injected ion flux and the neutral cloud in the Saturnian magnetosphere. Hence, the ENA emission gives information about the parent ion population. The location of the ENA emissions produced by the ion injections are in agreement with a source region of the injections residing in the midnight-to-dawn local time sector, between 15 and 20 R_S (Mitchell et al. 2005, 2009b). These injections are likely generated by the dipolarization of the magnetic field lines and the formation of plasmoids in the magnetotail, which will be explained in Section 1.2.4.4 (Bunce et al. 2005b, Hill et al. 2008, Mitchell et al. 2009b).

1.2.4.4 Magnetospheric convection and magnetic reconnection

The convection of flux tubes in planetary magnetospheres can be described by two different cycles: the Dungey cycle (Dungey 1961) and the Vasyliūnas cycle (Vasyliūnas 1983).

The Dungey cycle is a solar-wind driven convection pattern which is represented in Figure 1.10. When the interplanetary magnetic field (IMF) is oppositely directed to the planetary magnetic field lines in the nose of the magnetosphere, both magnetic fields can merge through the process of magnetic reconnection. Hence, the reconnection process changes the topology of two adjacent and antiparallel magnetic fields. Reconnection is also responsible for locally energizing plasma particles by releasing energy stored in the magnetic field. At the dayside magnetopause, closed planetary field lines which link the two hemispheres (in green in Figure 1.10) reconnect with the draped IMF in the magnetosheath (in blue), forming a “X-line” (in the grey rectangle), and become open (in red). These newly open field lines connect the ionosphere of the planet to the IMF. Dragged by the solar wind, they convect towards the nightside in the lobes. In the magnetotail, the open field lines are stretched and compressed to the equatorial plane. In the tail plasma sheet, in the grey rectangle in Figure 1.10, a second reconnection can occur between northern and southern open field lines. This magnetotail reconnection creates a new closed field line connected to the planet (in green) and convecting towards it. This process is also known as dipolarization because the produced closed field lines are more dipolar than the stretched field lines prior to the reconnection. In the opposite direction, the reconnection process expels out of the tail an interplanetary field line (in blue) or a plasmoid, which is a closed magnetic loop structure. The closed field line moving in the tail toward the planet can eventually convect to the dayside and hence a new cycle can begin.

This Dungey cycle is initiated if the IMF is antiparallel to the planet magnetic field. At the Earth, this condition is valid if the IMF is southward while at Saturn, a northward IMF is necessary since the two planets have oppositely aligned magnetospheric fields. In case of a northward IMF at Earth and a southward IMF at Saturn, the dayside reconnection site is shifted towards high latitudes where the open field lines of the lobe regions are opposite to the IMF. In that case, the reconnection involves only open field lines and no open flux is added in the magnetosphere (Gosling et al. 1991, Onsager and Fuselier 1994). In both cases, magnetosheath plasma, i.e. particles originating from the solar wind, can enter the magnetopause through the reconnection process. These particles can then flow inside the cusp region (Section 1.2.2) and eventually reach the ionosphere (e.g. Smith and Lockwood (1996), Cargill et al. (2005)).

The two-dimensional description of the Dungey cycle given above is simplified. Reconnection can occur at multiple locations at the same time, in a quasi-steady or bursty regime, and with various spatial scales (Fuselier and Lewis 2011). A reconnection can happen even if the magnetic field lines are not perfectly antiparallel and the east-west component of the IMF (B_y) plays also a significant role in the location of the reconnection site (Fuselier et al. 2011).

The importance of reconnection at Saturn’s magnetopause is subject of debate. The process of reconnection can occur at the magnetopause depending on the plasma β conditions (Section 1.2.3.4) on both sides of the magnetopause. Observations at Earth (Trenchi

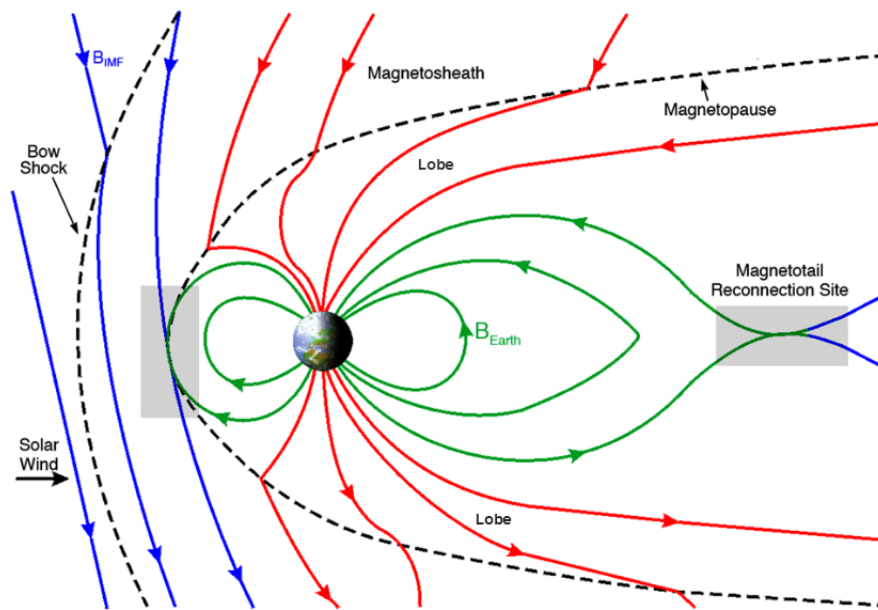


Figure 1.10: Sketch of the Dungey cycle on a noon-midnight meridian plane at the Earth's magnetosphere. From Fuselier and Lewis (2011), adapted from Hugues (1995).

et al. 2008) and theory (Swisdak et al. 2003, 2010) indicate that low plasma β values and small β gradient across the magnetopause boundary favor the triggering of reconnection. At Saturn, the typical value of the plasma β appears to be high in Saturn's magnetosheath (Masters et al. 2012a). Consequently, dayside magnetopause reconnection is thought to be not as common at Saturn as in the terrestrial case. Modeling the magnetopause conditions, Desroche et al. (2013) argues that the reconnection on the magnetopause dawn flank is even inhibited. However, dynamics at Saturnian magnetopause can differ from the terrestrial magnetopause. For instance, unlike at Earth, the magnetopause location is not strongly influenced by the IMF orientation (Lai et al. 2012). Furthermore, observational evidence of magnetopause reconnection has been reported (Huddleston et al. 1997, McAndrews et al. 2008, Lai et al. 2012, Fuselier et al. 2014). Transient structures in the auroral emissions have been attributed to magnetopause reconnection as well, as described later in Section 1.3.2 (Radioti et al. 2011, 2013b, Badman et al. 2013). Finally, crossings by Cassini of the cusp region revealed signatures of pulsed dayside reconnection at low latitude and in the lobe regions (Jasinski et al. 2014, 2016b). Nevertheless, it seems unlikely that magnetopause reconnection is a major driver of magnetospheric dynamics at Saturn (Masters et al. 2014).

In the rotationally-driven magnetospheres, another plasma transport cycle is dominant: the Vasyliūnas cycle (Vasyliūnas 1983) which is basically solar wind independent. In Jupiter's and Saturn's dayside magnetosphere, the flux tubes are highly mass-loaded due to the internal plasma sources, Io and Enceladus respectively. These flux tubes, as they rotate around the planet towards the nightside, are stretched out by centrifugal forces. This is represented by the meridional cuts (1) and (2) in Figure 1.11. Eventually, the flux tubes are so stretched that they pinch off through a reconnection along a X-line in the magnetotail (meridional cut (3)). Similarly to the Dungey cycle, dipolarization occurs and plasmoids are released tailwards (meridional cut (4)). The flux tubes depleted by the tail

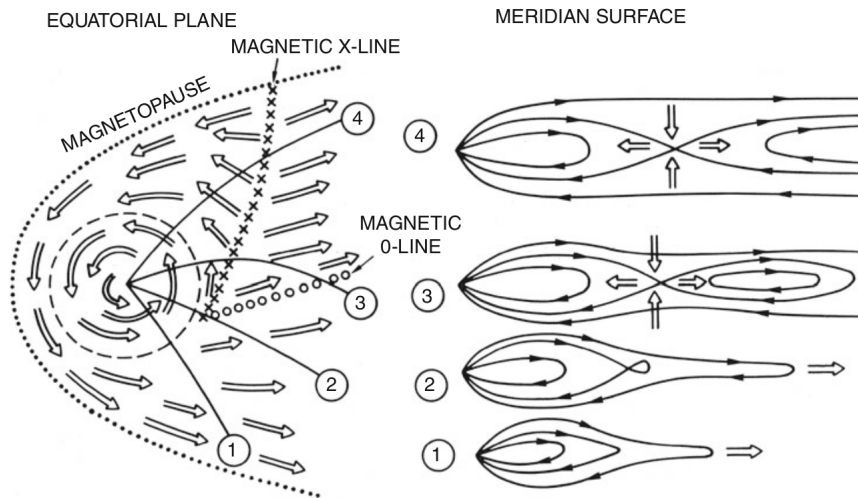


Figure 1.11: Schematic showing the mass loading and release process which are part of the Vasyliūnas cycle. The equatorial plane is shown on the left and meridional cuts (with the Sun to the left in both views) on the right. The magnetic X-line and O-line are drawn. Illustration from Bagenal (2013), adapted from Vasyliūnas (1983).

reconnection return to the dayside magnetosphere, via dawn, where they will be mass-loaded again. Then, a new cycle can start. While the Earth magnetosphere presents only the Dungey cycle and the Vasyliūnas cycle dominates the plasma transport in the Jovian magnetosphere, both cycles likely play an important role in Saturn's magnetosphere as suggested by Cassini observations (e.g. Jackman et al. (2011)) and theory (Cowley et al. 2004b, Badman and Cowley 2007).

The nightside reconnection has an important effect on the magnetotail plasma dynamics. The plasmoids escaping down the tail have a signature in both the magnetic field (e.g. Jackman et al. (2011), Jackman et al. (2014)) and the plasma data (Hill et al. 2008). Towards the planet, the dipolarization of reconnected field lines have also a magnetic field signature (Bunce et al. 2005b, Russell et al. 2008, Jackman et al. 2015) and contributes to large-scale injections of energized plasma in the middle and inner magnetosphere (Mitchell et al. 2005, 2009b, Thomsen et al. 2015). The position of the tail reconnection X-line varies between 25 and 40 R_S , as estimated on basis of magnetic field measurements (Jackman et al. 2014, Smith et al. 2016) and magnetohydrodynamic (MHD) simulations (Zieger et al. 2010, Jia et al. 2012).

1.2.4.5 Kelvin-Helmholtz instability at the magnetopause

In addition to magnetic reconnection, another process at the magnetopause is responsible of the entry of magnetosheath particles into the magnetosphere: the Kelvin-Helmholtz (K-H) instability. The K-H instability occurs at the interface between two fluids with a flow velocity shear across the interface. This viscous interaction generates waves propagating along the interface, which can evolve in vortices. Saturn's magnetopause, which is the boundary between magnetospheric and magnetosheath plasma flows, has been revealed to be K-H unstable, not only on its dawn flank where the flow shear is higher but also on its dusk flank (Galopeau et al. 1995, Masters et al. 2009, 2012b). Indeed, sur-

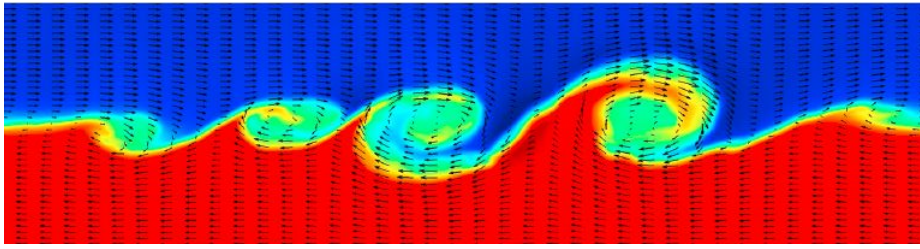


Figure 1.12: MHD simulation of Kelvin-Helmholtz vortices propagating along the magnetopause. The magnetosheath is in blue, the magnetosphere is in red. Adapted from Ma et al. (2014).

face waves generated by K-H instability have been detected on both the dawn and dusk flanks of the Kronian magnetopause (Masters et al. 2009, Cutler et al. 2011, Masters et al. 2012b). Kelvin-Helmholtz vortices have been also detected in the planetward vicinity of the Kronian magnetopause (Masters et al. 2010, Wilson et al. 2012), in a region of mixed magnetosheath and magnetospheric plasma adjacent to the magnetopause, called “boundary layer” (Masters et al. 2011a,b). Magnetopause K-H vortices simulated by MHD are visible in Figure 1.12.

Magnetopause models have confirmed that K-H instability can be encountered everywhere along the dayside magnetopause (Desroche et al. 2013, Delamere et al. 2013). K-H vortices growing in the prenoon and subsolar regions are likely transported towards the postnoon sector, explaining the relatively high frequency of K-H signatures on the dusk flank of the magnetopause (Delamere et al. 2013, Ma et al. 2015). Models show also that K-H activity could be a more important process for the magnetospheric dynamics than the magnetopause reconnection (Delamere et al. 2011).

1.3 Auroral processes at Saturn

The magnetospheric electrons traveling along the magnetic field lines can precipitate into the high-latitude upper atmosphere. Collisions between these electrons and the atmospheric species lead to ionization, dissociation and excitation of the neutral gas. These interactions produce auroral emissions at different wavelengths, from the radio to the X-rays (see the review by Badman et al. (2015)). Since the incident electrons come from various magnetospheric regions, the auroral emissions provide a picture of the magnetospheric processes all around the planet and therefore constitute a valuable tool to investigate the plasma dynamics.

In this thesis, only the ultraviolet (UV) auroral emissions at Saturn will be considered. The UV aurorae result from the radiative de-excitation of the excited H_2 molecules and H atoms (Bhardwaj and Gladstone 2000, Gustin et al. 2012). The UV aurorae consists of a spatially and temporally variable ring of emissions around Saturn’s pole in addition to several sporadic auroral structures. The main components of the Saturnian auroral UV emissions will be described in the following paragraphs and are schematically represented in Figure 1.13. Further details can be found in Grodent (2015).

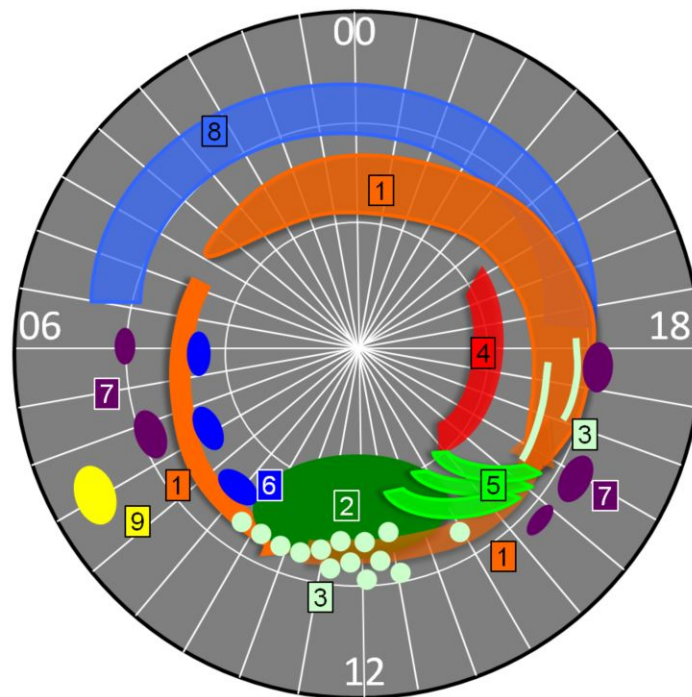


Figure 1.13: Sketch of the main UV auroral components discussed in the text and displayed on a polar map with parallels and meridians every 10° and oriented with the direction of the Sun (12 h LT) toward the bottom of the sketch. Adapted from Grodent (2015).

1.3.1 The main auroral emission

The ring of auroral emissions rotating around the magnetic poles is referred to as the main oval or the main emission (indicated by “1” in Figure 1.13). Actually, the main oval is not a closed structure but exhibits a spiral shape with various structures of different sizes separated by discontinuities (Gérard et al. 2004, Grodent et al. 2005). Nevertheless, the term “oval” is often used to denote this emission.

Theoretical approaches suggested that Saturn’s main emission is produced by the upward field-aligned currents driven by the flow shear at the boundary between the near-corotating closed magnetic field lines and the highly sub-corotating open field lines at higher latitude (Cowley et al. 2004a,b). Simultaneous observations of the aurorae and Cassini in-situ measurements have later confirmed this close relation between the main emission and the open-closed field line boundary (OCFLB) (Bunce et al. 2008, Talboys et al. 2009a). Because of this close relation, the main emission is strongly controlled by the solar wind conditions. An increase of the solar wind dynamic pressure results in a brightening of Saturn’s aurora (Clarke et al. 2005, Crary et al. 2005, Clarke et al. 2009) and a contraction of the main oval (Grodent et al. 2005, Badman et al. 2005, 2014). During quiet solar wind conditions, Saturn’s aurora can almost disappear (Gérard et al. 2006).

Hence, the ionospheric region enclosed by the main auroral ring contains the footprints of open field lines. The surface of this “open” region, which is usually referred to as the polar cap, varies with the amount of open flux content in the magnetosphere and

consequently with the rates of Dungey-type reconnection at the magnetopause and in the magnetotail (Badman et al. 2005, 2014). Recent studies have revealed that the OCFLB actually lies from 1 to 2° poleward of the upward field-aligned currents producing the main auroral emission in the nightside (Talboys et al. 2011, Jinks et al. 2014) and dawnside (Meredith et al. 2014, Belenkaya et al. 2014).

The main auroral oval rotates with the planet at approximately 70% of the rigid corotation (Grodent et al. 2005). In addition, the entire oval is revealed to oscillate by 1-2° in the prenoon-premidnight direction (Nichols et al. 2008, 2010b). This oscillation might be induced by a rotating external magnetospheric current system (Provan et al. 2009, Andrews et al. 2010). The oscillation of the main oval will be discussed further in Section 7.2.1.

The main emission can display small-scale auroral spots around local noon and isolated narrow arcs in the dusk sector, marked by “3” in Figure 1.13 (Grodent et al. 2011). Grodent et al. (2011) suggested that the spot structures are the signature of Kelvin-Helmholtz vortices at the magnetopause (see Section 1.2.4.5). Meredith et al. (2013) proposed an alternative explanation for these auroral patches observed simultaneously in both hemispheres: they may be produced by field-aligned currents associated with second harmonic Alfvén waves (Section 1.2.4.1) propagating through the equatorial plasma. Regarding the duskside arcs, they are tentatively explained by inhomogeneities in the equatorial plasma flow generating upward field-aligned currents (Grodent et al. 2011).

A faint partial ring (marked by “8” in Figure 1.13) is present in the nightside sector, equatorward of the main auroral emission (Grodent et al. 2010). This outer emission could be produced by a downward warm electron flow associated with a large-scale current system and whose the dayside counterpart is directed upward (Schippers et al. 2012). Equatorward of the main emission, the auroral footprint of the moon Enceladus has been identified by Pryor et al. (2011). Enceladus’ footprint is an isolated spot (indicated by “9” in Figure 1.13) produced by field-aligned electron beams resulting from the local interaction between Enceladus’ plume and the surrounding plasma (see the review by Simon et al. (2015)).

1.3.2 Auroral signatures of dayside reconnection

The cusp region and the associated magnetopause reconnection (see Section 1.2.4.4) leave also a signature in the auroral emissions (region “2” in Figure 1.13). Similarly to the cusp aurora at Earth (Milan et al. 2000, Frey et al. 2002, Fuselier et al. 2002), Saturn’s auroral cusp footprint presents two distinct morphologies fixed in local time: a diffuse spot around local noon, poleward of the main emission, and an intensification of the main emission in the same local time sector (Gérard et al. 2004, 2005). Bunce et al. (2005a) proposed a conceptual model accounting for both morphologies of the cusp auroral signature at Saturn. In case of northward directed interplanetary magnetic field (IMF), they argued that reconnection at the low-latitude dayside magnetopause generates twin vortical flows in the magnetosphere and in the ionosphere in the vicinity of the OCFLB. These vortices give rise to field-aligned currents which cause the intensity enhancement of the main emission near noon. During southward IMF conditions, reconnection takes place at high latitude, in the lobes. The twin vortical flows are then reversed in sense, as well as the associated field-aligned currents. These currents are located poleward of the

OCFLB and produce an auroral spot poleward of the main oval in the noon local time sector. According to the sign of the B_y component of the IMF, the cusp aurora is located in the prenoon or postnoon sector. This conceptual model is supported by observations of Saturn's aurora with the Hubble Space Telescope (HST) while Cassini was upstream of the Kronian magnetosphere, measuring the solar wind parameters and the IMF properties (Gérard et al. 2005, Meredith et al. 2014).

Bunce et al. (2005a) mentioned that reconnection at the magnetopause can be pulsed, causing a pulsed variation of the cusp aurora intensity. At Earth, the dayside magnetopause reconnection is also occasionally pulsed, generating the so-called flux transfer events, i.e. twisted flux tube magnetic structures (Russell and Elphic 1978, Wild et al. 2001). The Kronian cusp auroral emission and the associated magnetopause reconnection are the subject of Chapter 5.

The main emission can exhibit an intensity enhancement around noon which gradually gives birth to an elongated auroral structure moving towards the nightside (emissions “5” in Figure 1.13). This elongated structure has one extremity attached to the main oval while the other is convecting polewards, constituting a bifurcation of the main emission (Radioti et al. 2011, Badman et al. 2013). While the bifurcations deviate from the open-closed field line boundary towards the polar cap, the main emission moves to lower latitudes, increasing the polar cap size. The polar cap increase is evidence of opening of the flux and equals the area covered by the bifurcations. Consequently, it is suggested that the bifurcations are associated with dayside reconnection (Radioti et al. 2011). Several bifurcations can be observed revealing bursty reconnection at the magnetopause (Radioti et al. 2011, Badman et al. 2013). Furthermore, multiple brightenings within the bifurcations have been reported (Radioti et al. 2013b, Mitchell et al. 2016). These consecutive brightenings may reveal multiple magnetopause reconnection along the same flux tube (Radioti et al. 2013b), as suggested for the corresponding auroral structures at Earth (Fasel et al. 1993). Alternatively, shear flow in the magnetodisk, possibly driven by K-H instabilities, could generate the auroral bifurcations at Saturn (Radioti et al. 2013b). In that case, the bifurcations are associated with closed magnetic field lines and the multiple brightening may result from bouncing of Alfvén waves along the field lines (Kan et al. 1996).

1.3.3 Auroral signatures of tail reconnection

The reconnection in the magnetotail described in Section 1.2.4.4 is responsible for different auroral structures observed in the midnight-to-noon local time sector (“6” in Figure 1.13). The inward motion of closed flux tubes following the dipolarization causes a diversion of a dusk-to-dawn current in the tail (McPherron et al. 1973). Jackman et al. (2013) suggested that this diversion results, through associated field-aligned currents, in emission of small-scale auroral spots located slightly poleward of the main emission in the nightside. The observation by Jackman et al. (2013) of the small auroral spots was followed by a large brightness increase of Saturn's dawn aurorae and enhancement of ENA emissions in the midnight-to-dawn region at 15-20 R_S (Mitchell et al. 2009b). The ENA emission enhancement is generated by plasma injections triggered by tail reconnection, as already invoked in Section 1.2.4.3. Similar enhanced auroral activity in the dawn sector have been also reported by Nichols et al. (2014) and Radioti et al. (2016). Nichols et al. (2014) argued that their observations reflect the so-called solar wind-induced storms, namely an

auroral intensification associated with magnetotail reconnection induced by solar wind compression (Dungey-type tail reconnection). In another set of observations, Radioti et al. (2016) identified an auroral dawn enhancement suggested to be caused by internally driven tail reconnection (Vasyliūnas-type), as the estimated open flux amount remained constant.

Additionally, Radioti et al. (2014) identified an auroral arc extending from the night-side oval through the polar cap region (“4” in Figure 1.13). This rare nightside polar arc, very similar to the terrestrial transpolar auroral arc (e.g. Frank et al. (1982), Milan et al. (2005)), is likely associated with flux closure in the magnetotail (Dungey-type reconnection) during a period marked by the absence of dayside reconnection and Vasyliūnas-type tail reconnection (Radioti et al. 2014).

1.3.4 Auroral signatures of injections

The injections of anisotropic energetic electrons enhance the generation of whistler-mode waves (see Section 1.3.5) (Bolton et al. 1997, Xiao et al. 2003). The waves can scatter the electrons leading to the precipitation of some of them into the ionosphere and subsequently to the production of the auroral signature of injections (Mauk et al. 2002, Radioti et al. 2013a). Alternatively to this electron scattering process, auroral spots could be generated by pressure-driven electric currents flowing along the boundaries of the plasma injection cloud (Kivelson and Russell 1995, Mauk et al. 2002, Radioti et al. 2013a).

Transient isolated auroral features are occasionally observed on the equatorward edge of the dayside main emission (“7” in Figure 1.13). Based on HST auroral observations combined with quasi-simultaneous in situ measurements of Cassini, it has been suggested that these transient auroral spots are the signatures of energetic particle injections in the magnetosphere (Radioti et al. 2009). Cassini observations of the auroral spots together with simultaneous ENA emission enhancements, signature of injections (Section 1.2.4.3), have been studied in the context of this scenario (Radioti et al. 2013a). Based on a simulation of the temporal evolution of the auroral counterpart of a typical injection, Radioti et al. (2013a) confirmed that the auroral spots behave like an ionospheric signature of injections. However, the region where the injection is generated is unclear.

Additionally, large-scale (12-15 R_S) injections, which host strong corotation velocity gradients, could produce a spiral-shaped auroral signature in the ionosphere (Radioti et al. 2015). These auroral spirals, identified by Radioti et al. (2015), consist of detached swirling features propagating from predawn to noon.

1.3.5 Auroral hiss

The electron beams traveling along the magnetic field lines connected to the aurorae produce another kind of emissions in the radio wavelength domain. These radio emissions, so-called auroral hiss, are generated at high latitude by the interaction between the electron beams, mainly moving upward, and the plasma (Maggs 1976, Ergun et al. 2003, Kopf et al. 2010). The auroral hiss is a broadband electromagnetic plasma wave emission propagating in the whistler mode, as it propagates above the proton cyclotron frequency and below both the electron plasma frequency and the electron cyclotron frequency (see

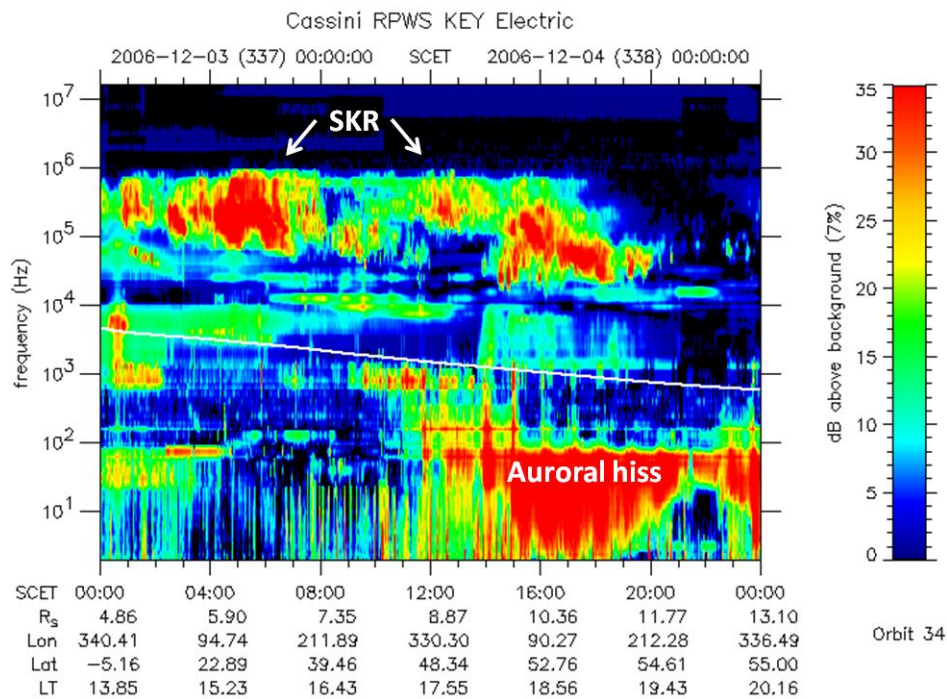


Figure 1.14: Typical Cassini/RPWS electric field spectrogram showing the auroral hiss emission and the Saturn Kilometric Radiation (SKR). The white line indicates the electron cyclotron frequency. Adapted from the NASA Planetary Data System.

Section 1.2.4.1). At Saturn, it is generally found beneath about 100 Hz (Gurnett et al. 2009b).

A typical frequency-time spectrogram acquired by Cassini/RPWS is given as an example in Figure 1.14. The auroral hiss is observed at low frequencies below the electron cyclotron frequency indicated by the white line. On the spectrogram, intense radio emissions can be observed at higher frequencies. These emissions are the Saturn Kilometric Radiation (SKR) which are emitted at frequencies ranging from 20 kHz to 1 MHz (e.g. Kurth et al. (2009), Ye et al. (2016) and references therein).

1.4 Periodicities in Saturn's magnetosphere

Various periodic phenomena have been discovered in Saturn's magnetosphere throughout its exploration by the Voyagers probe and Cassini. Evidence of solar wind-related periodicities characterised by ~ 26 -days or ~ 13 -days period are observed in the flux of electrons (Carbary et al. 2009, Carbary and Rymer 2017) and energetic ions (Carbary et al. 2013), as well as in the Saturn Kilometric Radiation (Desch and Rucker 1983). In addition to these long periodicities, the planetary rotation modulates a wide variety of magnetospheric observations. These planetary periodicities are the subject of intense investigation and are briefly described in the next section. Furthermore, several phenomena exhibit a period close to one hour. These hourly periodicities will be described in Section 1.4.2 and constitute the main topic of this thesis.

1.4.1 Planetary period oscillations

Numerous observations in Saturn's magnetosphere display periodicities at approximately the planetary rotation rate (~ 10.7 h) which is roughly inferred by tracking atmospheric features. These phenomena, called "planetary period oscillations" (PPO), involve bursts of Saturn Kilometric Radiation (SKR), magnetic field, plasma, energetic neutral atoms and auroral emissions (see the review by Carbary and Mitchell (2013)). The discovery of these periodicities was a surprise since the axisymmetry of the internal magnetic field of Saturn, without tilt nor offset (Section 1.2.1), would prevent the magnetosphere from being modulated by a "wobbling" of the magnetic field like at Earth and Jupiter.

While the SKR period was thought to be the best indicator of Saturn's internal rotation rate, long-term analysis revealed that it varies over time by $\sim 1\%$ per year, dismissing a connection with the underlying planetary rotation (e.g. Galopeau and Lecacheux (2000), Kurth et al. (2008), Lamy (2011)). Furthermore, SKR emissions display two distinct periods, one for each hemisphere (Gurnett et al. 2009a). Dual periodicities at the SKR frequencies are also observed in the auroral hiss (Gurnett et al. 2009b, Ye et al. 2010), in the magnetic field (Andrews et al. 2010, Provan et al. 2012, Andrews et al. 2012) and in the energetic electron data (Carbary et al. 2009). Both the northern and southern oscillation periods show a temporal variation: while the northern component (~ 10.6 h) was shorter than the southern one (~ 10.8 h) from 2004 to 2007, the dual periodicities became equal after Saturn's equinox in 2009 and more variable afterwards without clear trend until 2015 when the north SKR rotation started to slow down again (Lamy 2011, Provan et al. 2014, Fischer et al. 2015, Ye et al. 2016).

The source of the planetary period oscillations remains uncertain and several models have been proposed to account for Saturn's magnetospheric periodicities (see review by Carbary and Mitchell (2013)). Observations of the magnetic field oscillations have led to the development of an empirical model involving dual rotating perturbation magnetic fields generated by a field-aligned current system rotating at the SKR period of the corresponding hemisphere (Andrews et al. 2010, 2012, Provan et al. 2012, Hunt et al. 2015). The rotating current system is responsible for the oscillation of the main auroral oval identified by Nichols et al. (2008) (Provan et al. 2009, Nichols et al. 2010b). The intensity of the auroral emissions is also modulated by the magnetospheric oscillation period of each hemisphere (Nichols et al. 2010a, Badman et al. 2012b, Lamy et al. 2013). It is also noteworthy that, because of the internal magnetic field and plasma oscillations, the magnetopause location oscillates as well at the planetary period, over distances of $1-3 R_S$ (Clarke et al. 2006, 2010).

1.4.2 Hourly periodicities

In addition to the periodic phenomena related to the planetary rotation, shorter periodicities have been detected in the magnetosphere of Saturn already during the Voyager flybys of the giant planet. During the outbound pass of its flyby, in the dawn sector and at intermediate southern latitude ($\sim -29^\circ$), Voyager 2 observed impulsive injections of electrons at energies from 0.35 to 2 MeV, as shown in Figure 1.15 (Schardt et al. 1985). The signature of these injections in the electron flux measurements was characterised by a rapid increase followed by a slower decay, forming a "sawtooth" structure. The injections

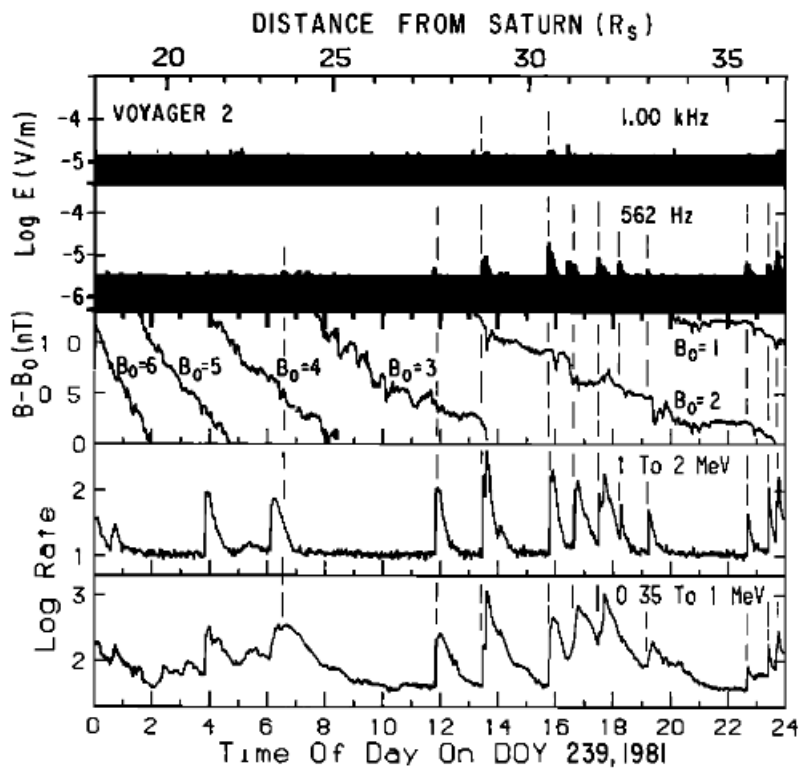


Figure 1.15: First observation of quasi-periodic injections of energetic electron fluxes in Saturn's magnetosphere by Voyager 2 in 1981. From top to bottom: plasma wave measurements at 1 kHz and 562 Hz, differenced magnetic field (with a constant B_0 chosen on short time intervals), count rate of electrons for the energy channels 1-2 MeV and 0.35-1 MeV. From Schardt et al. (1985).

repeated every 40 to 90 min, revealing a quasi-periodic phenomenon. Simultaneously to the quasi-periodic electron flux enhancements, sawtooth bursts were identified in the plasma wave measurements at frequencies ranging from 0.5 to 1 kHz, just above the local plasma electron frequency. Based on the time dispersion between the electron injection and a proton injection detected a couple of minutes later, Schardt et al. (1985) estimated that the plasma acceleration region was located in the magnetotail near the equator. However, the authors pointed out the unusual interplanetary configuration during the observations, with Saturn embedded in Jupiter's magnetotail. The observed injections could then be the manifestation of plasma release from the Jovian magnetotail.

Since Voyager 2 was a flyby mission, it was not until the Cassini mission that similar short-period phenomena have been observed again in Saturn's magnetosphere and reported in recent publications. Mitchell et al. (2009a) identified a pulsed particle acceleration event exhibiting quasi-periodic injections of electrons at energies from 200 keV to 1 MeV together with field-aligned beams of ions at energies of 30-200 keV (Figure 1.16). This injection event, characterized by a period of around one hour, was detected while Cassini was at intermediate latitude in the post-dusk sector of the magnetosphere, thus in a different region than the Voyager's event. Strikingly, in conjunction with the quasi-periodic energetic ion and electron flux enhancements, radio bursts were observed

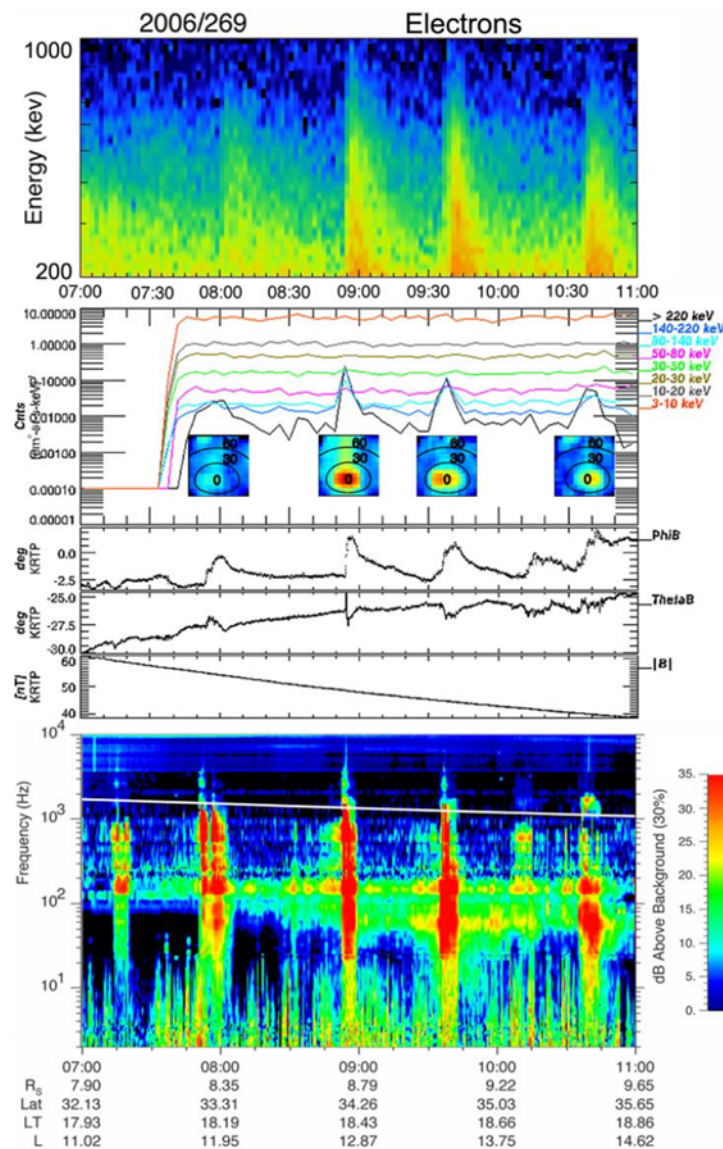


Figure 1.16: Cassini observations of a pulsed particle acceleration event on day 269 of 2006. From top to bottom: Cassini/MIMI/LEMMS electron spectrogram in the energy range 200 keV-1 MeV, Cassini/MIMI/INCA measurements of proton intensities for eight energy channels, Cassini/MAG measurements of the magnetic field angles and Cassini/RPWS plasma wave spectrogram. The white line on the bottom panel is the electron cyclotron frequency. From Mitchell et al. (2009a).

in the auroral hiss (Section 1.3.5), as well as fluctuations in the magnetic field. Mitchell et al. (2009a) suggested that these coincident observations are associated with a downward field-aligned current sheet in the auroral region, similarly to what is observed at Earth (Carlson et al. 1998). Downward current layers, carrying upward electron beams, have been also identified in Jupiter's magnetosphere (Mauk and Saur 2007) and at Saturn in the predawn and noon local time sectors (Saur et al. 2006).

A similar observation of coincident pulsations separated by approximately 60 min have been reported by Badman et al. (2012a) in the energetic particle fluxes, plasma wave

emissions and magnetic field measurements. This event was detected while Cassini was at high northern latitude around noon. The pulsed variations in the magnetic field are the signature of field-aligned currents associated with auroral bifurcation features (Section 1.3.2). Badman et al. (2012a) explained the injections of energetic electrons by scattering of upward electron beams carrying the downward component of the field-aligned current system. Badman et al. (2016) identified another event exhibiting ~ 60 min quasi-periodic pulsations in the magnetic field and radio emissions, associated with downward currents in the polar cap.

The aforementioned bifurcations of Saturn's main auroral emission are thought to be a signature of consecutive reconnection at the magnetopause (Radioti et al. 2011, Badman et al. 2013). Moreover, brightening of individual bifurcations with a periodicity of around one hour have been reported (Radioti et al. 2013b, Mitchell et al. 2016). By analogy with the observed brightening of the terrestrial auroral bifurcations (Fasel et al. 1993), Radioti et al. (2013b) suggested that the regular intensification of Saturn's bifurcations are caused by consecutive magnetopause reconnection along the same flux tube. During the time interval depicted by Mitchell et al. (2016), each bifurcation brightening was followed by an enhancement in the energetic electron flux, an intensity burst in the auroral hiss, a pulse in the magnetic field azimuthal component and a brightening in another auroral feature located in the polar cap, probably associated with the cusp region. The multi-instrument observation of these simultaneous quasi-periodic pulsations occur in the postnoon sector at high northern latitude and may be triggered by recurrent magnetopause reconnection.

Some quasi-periodic pulsations in the electron flux at slightly lower energies (10-500 keV) have been also identified while Cassini was crossing a plasma vortex structure in the prenoon sector close to the magnetopause (Masters et al. 2010). This vortex was associated with Kelvin-Helmholtz (K-H) instabilities at the magnetopause (see Section 1.2.4.5). Hence, in addition to bursty magnetopause reconnection, K-H instabilities along the magnetopause is another possible mechanism producing the quasi-periodic hourly pulsations in Saturn's magnetosphere.

Short periodicities have been also observed in the magnetosphere of Jupiter. During the Ulysses' flyby in 1992, energetic electron injections with a periodicity of around 40 min have been detected in the duskside of the magnetosphere at intermediate southern latitude (Simpson et al. 1992, McKibben et al. 1993, Zhang et al. 1995). The injected electrons were particularly energetic with energies from 1.5 MeV to beyond 16 MeV. In the Ulysses' measurements reproduced in the left panel of Figure 1.17, the electron pulsations exhibit a striking sawtooth shape, with a fast growth lasting only ~ 1 min, similarly to the electron pulsations observed in the Saturnian magnetosphere. Quasi-periodic ~ 40 -min radio bursts at frequencies from 1 to several hundreds of kHz have been also measured by Ulysses, some of them simultaneously to the electron pulsations (MacDowall et al. 1993, Desch 1994), and by the Galileo spacecraft in orbit around Jupiter between 1995 and 2003 (Hospodarsky et al. 2004). The Cassini instruments detected also some quasi-periodic ~ 40 -min pulsations (referred as "QP40") in the electron intensities during the Jupiter flyby in 2001 (Krupp et al. 2004). The QP40 source is thought to be located close to Jupiter, possibly in the auroral region. It has been revealed that the Jovian quasi-periodic radio emission bursts occur on average 8 min before the MeV electron pulsations (Desch 1994). This temporal shift suggests that the radio bursts are not generated by the energetic electrons. Finally, MacDowall et al. (1993) highlighted a positive correlation

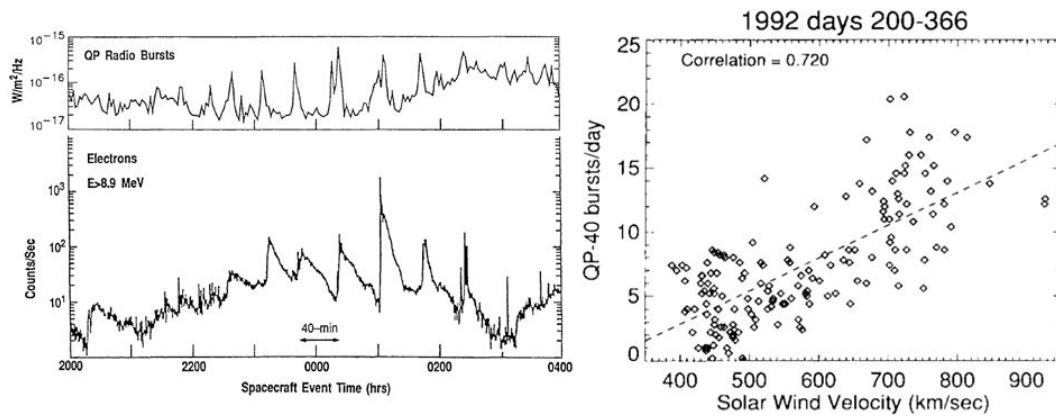


Figure 1.17: Left panel: Measurements during the Ulysses's flyby of Jupiter in 1992 of (top) the flux density of radio emissions at 8.1 kHz and (bottom) the count rate of electrons with energy >8.9 MeV. From Desch (1994). Right panel: Number of QP40 radio bursts per day as a function of the solar wind velocity at Jupiter during the Ulysses' flyby. From MacDowall et al. (1993).

between the number of QP40 radio bursts and the solar wind velocity at Jupiter (right panel in Figure 1.17). Finally, Gladstone et al. (2002) pointed out a ~ 45 -min brightening in an auroral X-Ray spot on Jupiter.

The observation of quasi-periodic injections of energetic electrons, as well as quasi-periodic radio bursts and auroral brightening, in both Jupiter's and Saturn's magnetosphere may suggest that they are generated by a fundamental dynamical process in outer planet magnetospheres. This fundamental process is still unknown and the aforementioned single-case studies give only a small insight of the hourly pulsations in Saturn's magnetosphere. The objective of this thesis is to survey the quasi-periodic hourly electron injections using Cassini measurements in order to investigate their origin and their significance. For the same purpose, a multi-instrument approach will help to improve our current understanding on the hourly pulsations observed in several datasets in Saturn's magnetosphere.

The survey and the statistical analysis of the quasi-periodic electron injections is described in Chapter 3. An investigation of coincident pulsed signatures in the plasma wave emissions and magnetic field is presented in Chapter 4. Chapter 5 is devoted to the analysis of hourly brightening identified in a high-latitude spot in Saturn's auroral emissions. The plasma environment during the pulsed events and the importance of magnetopause processes as trigger for the pulsations are discussed in Chapter 6. Finally, the last chapter, Chapter 7, presents ongoing work and perspectives. Before the presentation of the work carried out during this thesis, the Cassini mission and all the instruments used for the achievement of this PhD project will be described in Chapter 2.

2 The Cassini mission

2.1 Missions at Saturn before Cassini

Saturn has always aroused the curiosity of the humanity. But it is only in 1979, thanks to two decades of tremendous progress in space exploration, that humans were able to explore the Saturnian system from inside. This first encounter was achieved by Pioneer 11, only 21 000 km away from Saturn, and will be followed in 1980 by Voyager 1 and, one year later, by Voyager 2. These three flybys, whose trajectories are shown in Figure 2.1, provided a first good picture of the configuration of the magnetosphere surrounding Saturn. However, this picture covered only a few limited areas of the magnetosphere.

Since only an orbiting spacecraft allows a global and in-depth exploration of the planet, the *National American Space Agency* (NASA), together with the *European Space Agency* (ESA) started in the 80's the development of a mission devoted to the ringed planet, its environment and its moon Titan. The mission was named Cassini-Huygens, in honor of the two famous astronomers of the XVIIth century, the Italian/French Giovanni Domenico Cassini and the Dutch Christiaan Huygens. The latter was the first to observe Titan while the former discovered four Saturn's moons and a gap in the rings, the so-called Cassini division.

2.2 The Cassini-Huygens mission

The Cassini-Huygens space mission is composed of two parts: the Cassini orbiter and the Huygens probe destined to investigate Titan's atmosphere. The Cassini-Huygens couple was launched on October 15, 1997 from Cape Canaveral in Florida and traveled seven years through the solar system before reaching Saturn (Matson et al. 2002). After two gravity-assist flybys at Venus, one at the Earth and a last one at Jupiter, Cassini finally arrived at Saturn on July 1, 2004 and performed the *Saturn Orbit Insertion* (SOI) maneuver (solid line in Figure 2.1). On December 25, 2004, the Huygens probe was released and, 22 days later, landed on Titan after having performed in situ measurements throughout its descent in the atmosphere of the moon.

The initial four-year mission of Cassini ended in June 2008, but, given the immense success of the mission, it has been extended twice: the Equinox mission covers 27 additional months till September 2010, and was followed by the Solstice mission till September 2017. The names of the extended phases of the mission refer to Saturn's equinox which occurred on August 11, 2009 and to Saturn's solstice which will occur on May 25, 2017. In total, Cassini will have spent 13 years around Saturn, almost a half Saturnian year, achieving 295 orbits, 125 Titan's flybys, 23 Enceladus' flybys, as well as

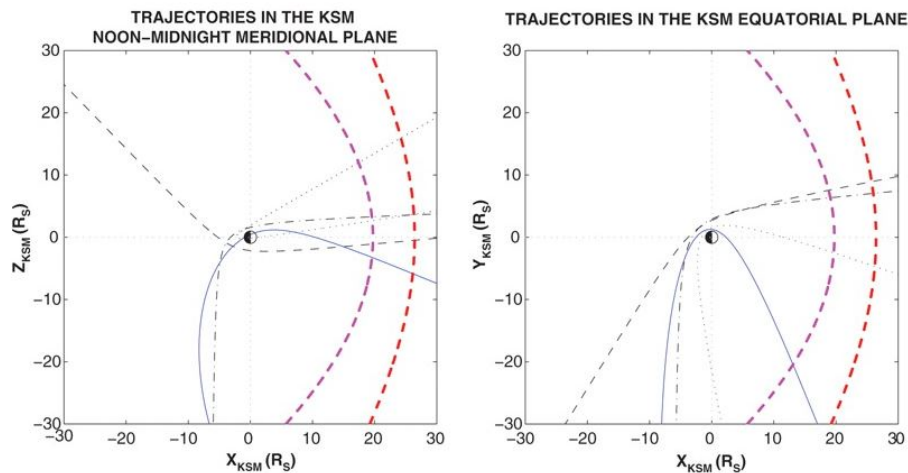


Figure 2.1: Trajectories of Pioneer 11 (dotted curve), Voyager 1 (dashed curve), Voyager 2 (dashed-dotted curve) and Cassini Saturn orbit insertion (solid line) through Saturn’s magnetosphere, projected in the noon-midnight meridional plane (left) and in the equatorial plane (right) in KSM coordinates. Nominal magnetopause (purple) and bow shock (red) are drawn according to the model of Slavin et al. (1983). From Dougherty et al. (2005).

several flybys of other moons. The last stage of the Solstice Mission, called the “Grand Finale”, consists of a series of orbits with the periapsis particularly close to the planet, as represented in Figure 2.2. In the first phase, between end of November 2016 and April 2017, Cassini will fly over the planet poles and graze the F-ring, the outer edge of the main rings. The spectacular second phase consists of 22 “proximal orbits” during which Cassini will dive between the planet and the inner edge of the main rings, at less than $1 R_S$ from Saturn’s surface. Finally, on September 15, 2017, the Cassini spacecraft will plunge into the atmosphere of Saturn, marking the end of the already successful Cassini mission.

The Cassini spacecraft is the largest interplanetary spacecraft built up to now, with a height of 6.8 m and a mass at launch of 2523 kg without the propellant and 5655 kg in total (Henry 2002). It is also the most complex interplanetary spacecraft, carrying no less than twelve instruments on board. All of them are listed in Table 2.1 and are represented in Figure 2.3. Six of them perform in-situ measurements of, e.g., the magnetic field and the plasma environment, and the six others are remote sensing instruments covering all the electromagnetic spectrum from the microwave wavelengths to the ultraviolet. Some instruments are composed of different subsystems and have multiple detectors. The instruments used during the thesis, listed in Table 2.3, are described in the following sections.

2.3 The Magnetosphere Imaging Instrument (MIMI)

One of the particle instruments on board the Cassini spacecraft is the *Magnetosphere Imaging Instrument* (MIMI). The MIMI instrument works as an in-situ particle detector as well as a remote sensing imager of the emissions of energetic neutral atoms (Krimigis et al. 2004). The instrument is composed of three independent sensors:

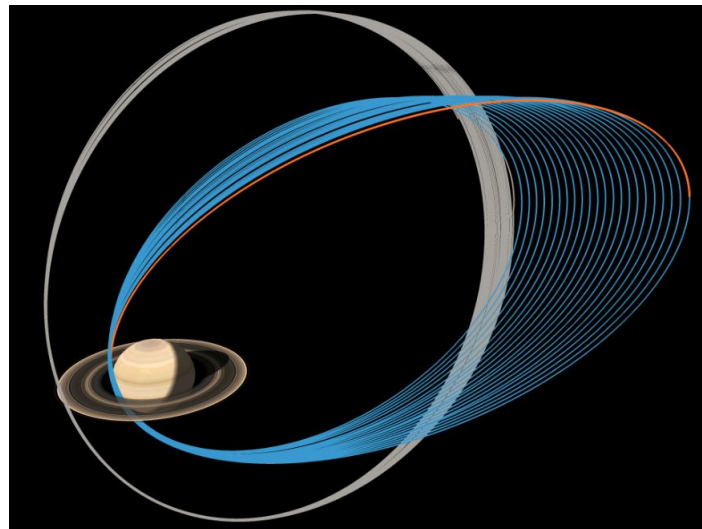


Figure 2.2: Trajectories of Cassini during the “Grand Finale” phase of the mission. The grey and the blue orbits represent respectively the F-ring and the proximal orbits. The orange orbit corresponds to the final plunge of Cassini into Saturn’s atmosphere. (Image courtesy of NASA/JPL-Caltech)

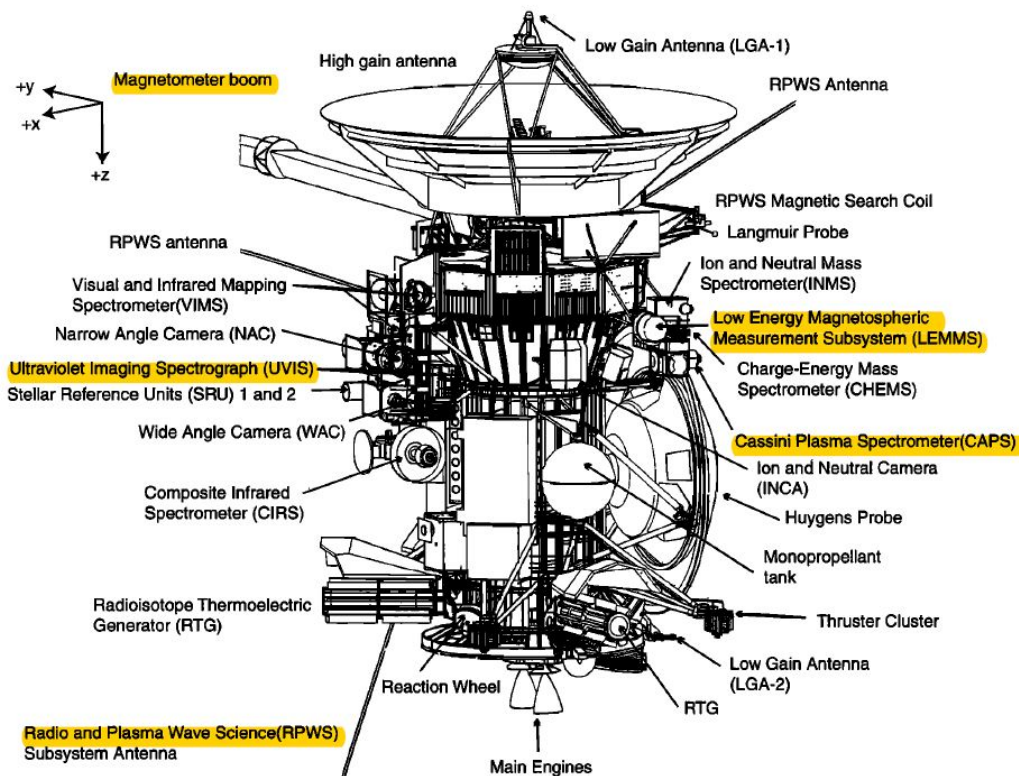


Figure 2.3: Sketch of the Cassini spacecraft with the instruments on board as well as the Huygens probe. The instruments or the sensors whose data have been used in the multi-instrument study presented in this thesis are highlighted. From Burton et al. (2001).

Instrument	Abbreviation
IN SITU	
Cassini Plasma Spectrometer	CAPS
Cosmic Dust Analyzer	CDA
Ion and Neutral Mass Spectrometer	INMS
Magnetometer	MAG
Magnetosphere Imaging Instrument	MIMI
Radio and Plasma Wave Science	RPWS
REMOTE SENSING	
Cassini Radar	RADAR
Composite Infrared Spectrometer	CIRS
Imaging Science Subsystem	ISS
Radio Science Subsystem	RSS
Ultraviolet Imaging Spectrograph	UVIS
Visible and Infrared Mapping Spectrometer	VIMS

Table 2.1: Instruments on board the Cassini spacecraft.

- The *Low-Energy Magnetospheric Measurement System* (LEMMS)
- The *Charge-Energy Mass Spectrometer* (CHEMS)
- The *Ion and Neutral Camera* (INCA)

The CHEMS sensor detects energetic ions in the energy range 2 to 220 keV per charge. CHEMS combines Time-of-Flight (TOF), energy and energy per charge measurements to determine the species and the charge state of the detected ions, which is useful to identify the sources of particles. The INCA sensor is designed to detect both ions and neutral particles, in the energy range from 5 keV to 3 MeV per nucleon. It can also perform global imaging of the energetic neutral atoms (ENAs) emitted from extended magnetospheric regions (Krimigis et al. 2004). Since no data from these two sensors are analyzed in the current work, no detailed description of them are presented here. On the contrary, the LEMMS detector, whose data have been widely used in this thesis, is described below.

2.3.1 LEMMS

General description

The *Low-Energy Magnetospheric Measurement System* (LEMMS) is made up of two detectors pointing in opposite direction and measuring ions and electrons: the *Low-Energy Telescope* (LET) and the *High-Energy Telescope* (HET). The double heads of the detector are visible on the picture in Figure 2.4. The LET has an aperture of 15° and detects ions with energy above 30 keV and electrons in the energy range 18 keV-1 MeV. The high-energy end has an opening angle of 30° and covers the energy range from 1.4 to several hundreds of MeV per nucleon for the ions and from 110 keV to energies greater than 10 MeV for the electrons.

In order to measure particles coming from all directions, the MIMI/LEMMS detector is mounted on a turntable platform which nominally rotates at a period of 86 sec. The data

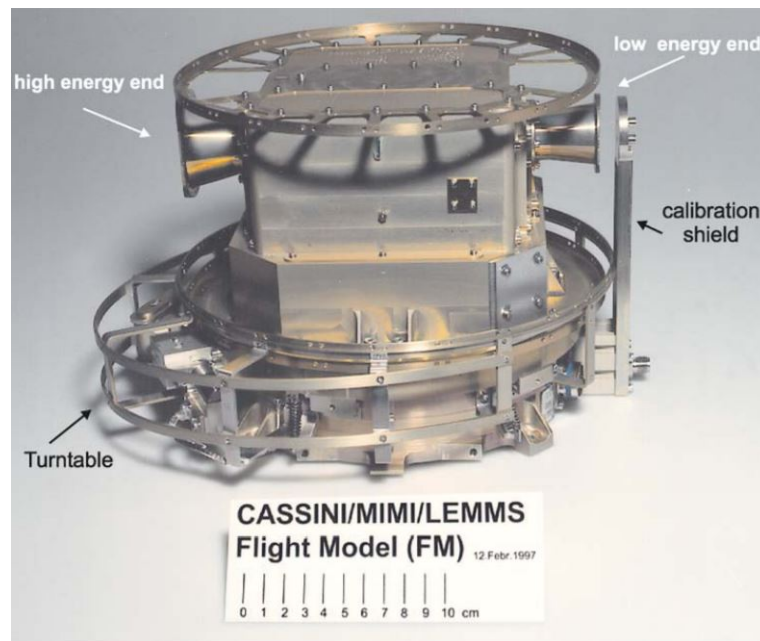


Figure 2.4: Flight model of the MIMI/LEMMS sensor. The double heads of the detector head surrounds the central electronic box which is mounted on the turntable platform, while the calibration shield is used to perform background measurements. From Krimigis et al. (2004).

were separated into 16 angular subsectors, providing an angular resolution of 22.5° and a time resolution of 86 sec (Krimigis et al. 2004). Unfortunately, on February 2, 2005, the scan platform malfunctioned, resulting in a fixed pointing of LEMMS after this date. Since then, only two directions are sampled at a given time (one per telescope). A better pitch-angle coverage can be achieved only during Cassini spins. However, the LEMMS rotation stop allowed the time resolution at a fixed pointing to be improved by a factor 16, at 5.3 sec. Then, to increase the signal-to-noise ratio, a longer averaging can be applied on the LEMMS data. In the following chapters, LEMMS data are averaged on 86 sec, namely the nominal rotation rate of LEMMS.

Measurement technique

The detection method of charged particles differs between the two telescopes of the LEMMS sensor. In the low-energy end, a magnetic deflection system separates electron and ions (Figure 2.5): the electrons are deflected towards the detectors E and F while the ions, because of their larger mass, are not significantly deviated by the magnet and continue straight until they strike the detectors A. The electron detectors E and F consists of three components: E1, F1 and a shared component E2/F2, as represented in the sketch of LEMMS in Figure 2.6. The specific components reached by a given electron depend on its incident energy. From the logic coincidences of detection of particles by the different components, the species and the energy of the incoming particle is derived. The coincidence method allows also to identify and reject the counts due to particles reaching the detectors under a non-nominal path. In the case of the ions, if their energy is high enough,

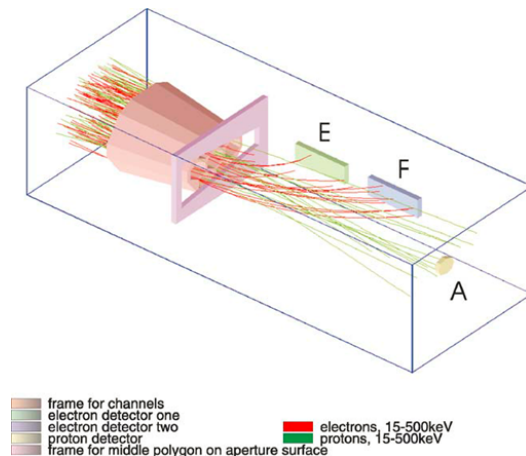


Figure 2.5: Simulated trajectories of electrons and ions in the MIMI/LEMMS Low-Energy Telescope. From Krimigis et al. (2004).

they are not absorbed by the detector A and continue their path until the B detector located behind. Electrons with high energy are not deflected enough so that they do not hit the detectors E and F but, if their energy exceeds 884 keV, reach the A detector like the ions. A gold absorber (marked by a C in Figure 2.6) prevents the particles penetrating the B detector to enter the High-Energy Telescope.

The HET is made up of a stack of five detectors D1, D2, D3a, D3b and D4 preceded by a thin aluminum foil which suppresses the incoming light and the flux of low-energy particles. As is the case for the detectors A and B and the coupled detectors E and F, the species and the energy of the incoming particles are derived from the logic coincidences of detection of particles by the five detectors. This coincidence technique enables to derive the so-called rate channels of MIMI/LEMMS. Each rate channel is defined by an energy passband and the combination of detection and no-detection by the different LEMMS detectors of the particles with energy included in this energy passband. In total, 57 rate channels are defined for LEMMS. The main ion channels are named from A0 to A8 (for the LET telescope) and from P1 to P9 (for the HET telescope). The main electron channels are C0 to C7 (LET) and E0 to E7 (HET). The energy passbands of the LEMMS channels are summarized in Krupp et al. (2009). A list of the rate channels used in this thesis and their corresponding energy passband is given in Table 2.2.

The E3 and the E4 channels have a similar energy bandwidth but their response with energy is very different. The E5 channel is an integral channel with no upper bound and has the same sensitivity as E4 for the lowest energy of the channel. Since most of the particles are detected in the lowest part of the energy bandwidth, there is not a big difference between the E4 and the E5 count rates.

For six rate channels, each of the 16 angular subsectors are subdivided into 8 microsectors improving the angular resolution (from 22.5° to 2.81°) and, after the failure of the LEMMS rotating platform, the time resolution from 5.3 to 0.67 sec. These six priority channels have been modified a few times throughout the mission. From the end of 2016 onwards, the priority channels are A3, C2, C5, E0, E4 and P7.

Every rate channel listed in Table 2.2 has a relatively large energy bandwidth. To increase the energy resolution, another type of data is available: the Pulse Height Analysis

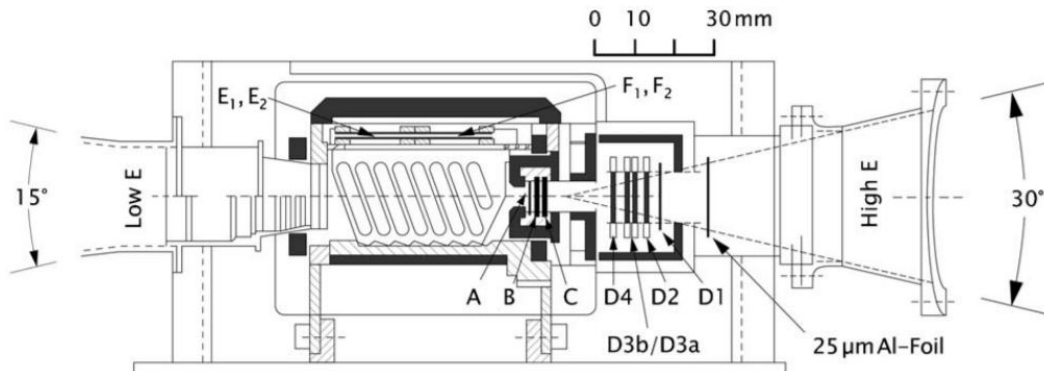


Figure 2.6: Side view of the MIMI/LEMMS double-ended detector, with the Low-Energy Telescope on the left and the High-Energy Telescope on the right. From Armstrong et al. (2009).

Telescope	Channel	Species	Energy (keV)
LET	C0	Electrons	18-40
LET	C1	Electrons	27-48
LET	C2	Electrons	41-60
LET	C3	Electrons	56-100
LET	C4	Electrons	92-183
LET	C5	Electrons	175-300
LET	C6	Electrons	265-550
LET	C7	Electrons	510-832
HET	E0	Electrons	110-365
HET	E1	Electrons	220-485
HET	E2	Electrons	340-1350
HET	E3	Electrons	600-4950
HET	E4	Electrons	790-4750
HET	E5	Electrons	>800
HET	E6	Electrons	1600-21000
HET	E7	Electrons	7000-20000
HET	P2	Ions	2280-4492

Table 2.2: Energy passbands for the ion and electron channels of MIMI/LEMMS used in this thesis. From Krupp et al. (2009).

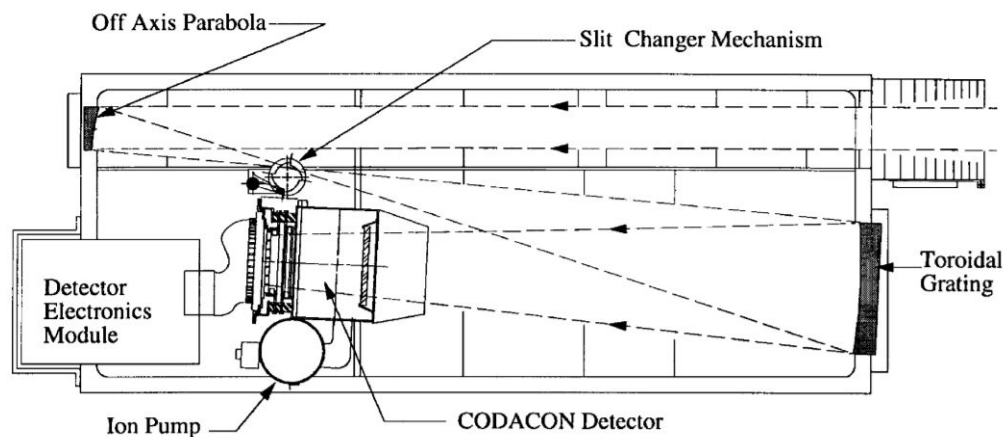


Figure 2.7: Optical design of the UVIS FUV telescope-spectrograph. From Esposito et al. (2004).

(PHA) data. The PHA data provide 64 energy channels for the A detector, 64 channels for the E detector and 64 others for the F detector.

2.4 The Ultraviolet Imaging Spectrograph (UVIS)

The *Ultraviolet Imaging Spectrograph* (UVIS) is a Cassini remote sensing instrument investigating mainly Saturn and Titan's atmospheres, the rings and the icy surfaces of the Kronian moons (Esposito et al. 2004). The UVIS instrument consists of two telescope-spectrographs, a high speed photometer and a hydrogen-deuterium absorption cell. The two spectrographs cover the wavelengths from 56 to 118 nm and from 111 to 191 nm, which correspond respectively to the extreme ultraviolet (EUV) and far ultraviolet (FUV).

Observations of Saturn's aurorae acquired with the FUV telescope-spectrograph are presented in Chapter 5. This telescope has an aperture of 20×20 mm. The incident light is deflected by an off-axis parabolic mirror of 100 mm focal length towards a toroidal grating (see Figure 2.7). Both the mirror and the grating are coated by aluminum and MgF₂. Between the mirror and the grating, the light crosses a slit which can have three dimensions: 75, 150 or 800 μm providing a field of view of 0.75, 1.5 and 8 mrad respectively. Finally, the diffracted light reaches the CODACON detector (for *Coded Anode Array Converter*) which is a photocathode counting and locating the photons. It has a two-dimensional format of 64 spatial pixels × 1024 spectral pixels.

In order to have 2D imaging of an interesting region, e.g. the auroral region, the Cassini spacecraft can slightly spin in the direction perpendicular to the UVIS slit so that the region of interest is swathed by the slit field-of-view. Once this region is getting outside the field-of-view, Cassini is going back to its initial pointing and a new scan can start. This observation procedure implies that the different rows of a UVIS image (a row corresponds to the UVIS slit FOV) are not acquired simultaneously. The time delay between the first and the last rows corresponds to the duration of a scan which lasts for a dozens of minutes. Because of this asynchronicity within the UVIS image, they are sometimes denoted by the term "pseudoimage".

2.5 The Radio and Plasma Wave Science (RPWS) instrument

The Cassini *Radio and Plasma Wave Science* instrument (RPWS) is designed to study the plasma waves, radio emissions, thermal plasma and dust in the Saturnian system (Gurnett et al. 2004). It includes three electric field antennas and three magnetic field antennas. A Langmuir probe measuring the local electron density and temperature is also part of the RPWS system. The three electric field antennas cover the frequency range from 1 Hz to 16 MHz. They consist of three 10 m long cylinders of about 3 cm in diameter pointing in nearly orthogonal directions. The magnetic antennas are orthogonal search coils mounted on a short boom. A coil is composed of 10 000 turns of thin wire around a 25 cm-long metal core. They cover the frequency range from 1 Hz to 12 kHz. Both types of antennas are used to determine if the detected plasma wave is electrostatic, i.e. without magnetic field component, or electromagnetic. The signals from the antennas are processed by five different receivers providing information about the properties of the plasma wave like, for instance, the frequency and the intensity.

2.6 The Magnetometer (MAG)

The Cassini spacecraft has a magnetometer (MAG) mounted on a 11 m-long boom to prevent measurement of electromagnetic signals produced by the spacecraft or by the instruments on board. The MAG instrument consists of a Fluxgate magnetometer (FGM), located half-way along the magnetometer boom, and, at the boom extremity, a vector helium magnetometer (V/SHM) that can operate in both vector and scalar modes (Dougherty et al. 2004). The two subsystems are complementary since FGM has a wide dynamical range while V/SHM has a low noise sensitivity (Arridge et al. 2011). Their complementary data also help to optimally remove the field perturbations induced by the spacecraft. Unfortunately, the V/SHM component stopped working in November 2005, leaving the FGM as the unique operational magnetometer system.

The orientation of the magnetic field given by the Cassini magnetometer combined with the pointing direction of the MIMI/LEMMS detector provides information about the pitch angle of the particles detected by LEMMS.

2.7 The Cassini Plasma Spectrometer (CAPS)

The *Cassini Plasma Spectrometer* (CAPS) is another instrument designed for the investigation of the plasma environment around Saturn (Young et al. 2004), but at lower energies compared to the MIMI instrument. It includes three subsystems: the *Electron Spectrometer* (ELS), the *Ion Mass Spectrometer* (IMS) and the *Ion Beam Spectrometer* (IBS). Since only measurements from ELS are presented in this thesis, a description of the two other sensors are not given here, but can be found in Young et al. (2004).

The ELS spectrometer detects electrons with energies from 0.6 eV to 28 keV. Hence, the CAPS/ELS together with the MIMI/LEMMS sensor provide a continuous coverage of all the energy spectrum of electrons between 0.6 eV and 21 MeV. The energy bandwidth of

Instrument	Purpose
MIMI/LEMMS	Detection and characterization of the quasi-periodic electron injections
RPWS	Detection of pulsed signatures of the electron injections in the radio emissions
MAG	Detection of pulsed signatures of the electron injections in the magnetic field
UVIS	Detection and characterization of pulsating auroral emissions
CAPS/ELS	Identification of magnetospheric environments

Table 2.3: Cassini instruments used in this thesis.

CAPS/ELS is divided in 63 logarithmically spaced energy levels with an energy resolution of $\Delta E/E \sim 0.17$ (Young et al. 2004, Lewis et al. 2010). The ELS detector is composed of a fan of eight adjacent anodes with an individual field-of-view of $5.2^\circ \times 20^\circ$. The total FOV of CAPS/ELS is then 5.2° in azimuth and 120° in elevation. The data provided by the central anodes (anodes 4 and 5) have a lower background count rate and suffer less from obscuration by parts of the spacecraft (Arridge et al. 2009). The CAPS/ELS data presented in this thesis have all been acquired with the anode 4. To extend the azimuthal FOV of CAPS, it is mounted on an oscillating platform which sweeps 208° in azimuth in about 4 min. In addition, from the CAPS/ELS measurements, different calculation methods allow to derive the electron moments, i.e., the electron temperature and density (Lewis et al. 2008, Arridge et al. 2009).

The CAPS instrument was switched off in June 2012 after it caused a series of electrical shorts to the spacecraft. It has been decided afterwards to not switch it on anymore.

3 Quasi-periodic hourly pulsations in the energetic electron fluxes

The magnetosphere of Saturn contains many periodic phenomena, some of them have been described in Section 1.4. Short periodicities of around one hour have been detected by several instruments on board Cassini. In particular, quasi-periodic energetic electron injections are observed in Saturn’s outer magnetosphere. These pulsed electron events are striking since they involve high intensities of MeV electrons in a region where MeV electron fluxes are generally at the instrument background level (Section 1.2.3.3). Their remarkable quasi-periodicity implies the existence of an impulsive trigger which is still unknown.

In order to increase our knowledge of this periodic phenomenon, this chapter¹ presents a survey of the quasi-periodic 1-hour injections of energetic electrons and a statistical study of their properties and their spatial distribution. In the first part of the chapter, an example of a quasi-periodic pulsed electron event is depicted.

3.1 Example of a quasi-periodic electron pulsed event

A typical example of a quasi-periodic injection of energetic electrons is given in Figure 3.1. This event was observed on days 129 and 130 of 2009 (May 9 and 10), when the Cassini spacecraft was in the post-dawn local time sector, $\sim 15 R_S$ away from Saturn and at mid-latitude in the southern hemisphere. The two right subpanels in Figure 3.1 indicate Cassini’s position (blue thick line) projected in the equatorial (x - y) plane (Figure 3.1g) and in the north-south (x - z) plane (Figure 3.1h), using the Saturn Equatorial coordinate system (SZS). In the SZS coordinate system, the z -axis is aligned with the planet’s rotation axis, the x -axis and the y -axis are in the equatorial plane towards the Sun and dusk, respectively. The orbit of Cassini, during the time interval covering half an orbit before and after the event, is drawn in green in Figure 3.1g and 3.1h. The orange curves represent two simulated magnetopause locations for two values of the solar wind dynamic pressure (2×10^{-3} and 4×10^{-2} nPa) using the model of Kanani et al. (2010). A red arrow indicates the subsolar latitude. In Figure 3.1g, Titan’s and Rhea’s orbit are indicated with the black circles (at 20.3 and $8.7 R_S$).

1. The main results presented in this chapter have been published in Palmaerts, B., Roussos, E., Krupp, N., Kurth, W. S., Mitchell, D. G., Yates, J. N., 2016a, Statistical analysis and multi-instrument overview of the quasi-periodic 1-hour pulsations in Saturn’s outer magnetosphere, *Icarus*, 271, 1-18.

Left panel in Figure 3.1 is a stack of time series plots of Cassini in-situ measurements. The differential intensities (in counts/(cm² sr s keV)) of electrons measured in the LEMMS HET channels E0 to E4 and E6 are transcribed in Figure 3.1a. The energy pass-bands of the electron channels are reminded in the bottom right corner. A frequency-time electric field spectrogram acquired with the RPWS instrument is given in Figure 3.1b. The white line represents the electron cyclotron frequency (see Section 1.2.4.1). The next three panels (c to e) show the Cassini magnetometer measurements of the three components of the magnetic field in spherical coordinates (azimuthal B_ϕ , radial B_r and polar B_θ). The azimuthal component is positive in the direction of corotation, the radial component is positive outward from Saturn and the polar component is positive southward. The strength of the radial component of the magnetic field being high in that region, small fluctuations are not distinguishable. Therefore, a third degree polynomial fit has been removed from the measurement and the resulting detrended radial component is given by the red line. Finally, the last plot (Figure 3.1f) represents the local pitch angle pointing of the LEMMS HET.

The electron pulsed event given as an example in Figure 3.1 can be divided in two parts: from 22 to 02 UT and from 02 to 06 UT. Cassini was rotating during the first part so that the LEMMS detector could measure electrons with a nearly entire pitch angle distribution (Figure 3.1e). In the second part of the event, Cassini's pointing was fixed and LEMMS detected energetic electrons with a pitch angle of $\sim 25^\circ$. From 00 UT onwards, four consecutive pulsed enhancements are observed in the E3 and E4 channels (green and orange lines in Figure 3.1a). Each pulsation is separated by around 60 min. Pulsed variations are also observed in phase in the lowest energy channels E0 to E2. At these energies, periodic narrow peaks are superimposed when Cassini is rolling. These peaks are correlated with the extreme values of the pitch angle and they reveal bidirectional electron beams aligned with the closed magnetic field lines (e.g. Saur et al. (2006)). Flux peaks in the E3 and E4 channels are also higher in the field-aligned direction (peaks at ~ 0030 and ~ 0130 UT). Hence, two different electron populations are mixed: the field-aligned electron beams and the ~ 1 -h pulsed electrons (see also the discussion in Section 3.5.4). After 02 UT, LEMMS points in a fixed direction. Two consecutive pulses separated by around 60 min are clearly visible in all the electron channels except E6 and two additional pulses are also distinguishable at ~ 04 and at ~ 05 UT. The electron intensity in the highest energy channel E6 peaks only once in the field-aligned direction, revealing an upward electron beam with an energy above 1.6 MeV. It is noteworthy that at these energies (above 500 keV), the electrons are relativistic. Other pulses in the E6 channel are likely below the detection limit.

The RPWS electric field spectrogram reveals periodic enhancements in the broadband plasma wave emissions. These enhancements are concomitant with the LEMMS electron pulsations during the main part of the time interval. Below the electron cyclotron frequency (f_{ce}), the radio emissions are electromagnetic waves propagating in the whistler mode. In this frequency range, the radio emissions are called auroral hiss (see Section 1.3.5). However, the two strongest broadband bursts, at ~ 0030 and ~ 0130 UT, extend to frequencies above f_{ce} , indicating an electrostatic mode, as discussed in Section 4.1.2.

Regarding the magnetic field, the azimuthal component (Figure 3.1c) exhibits strong fluctuations anti-correlated with the LEMMS electron pulsations: an enhancement of the electron flux coincides with a drop in the intensity of the B_ϕ component. The detrended

3.1 Example of a quasi-periodic electron pulsed event

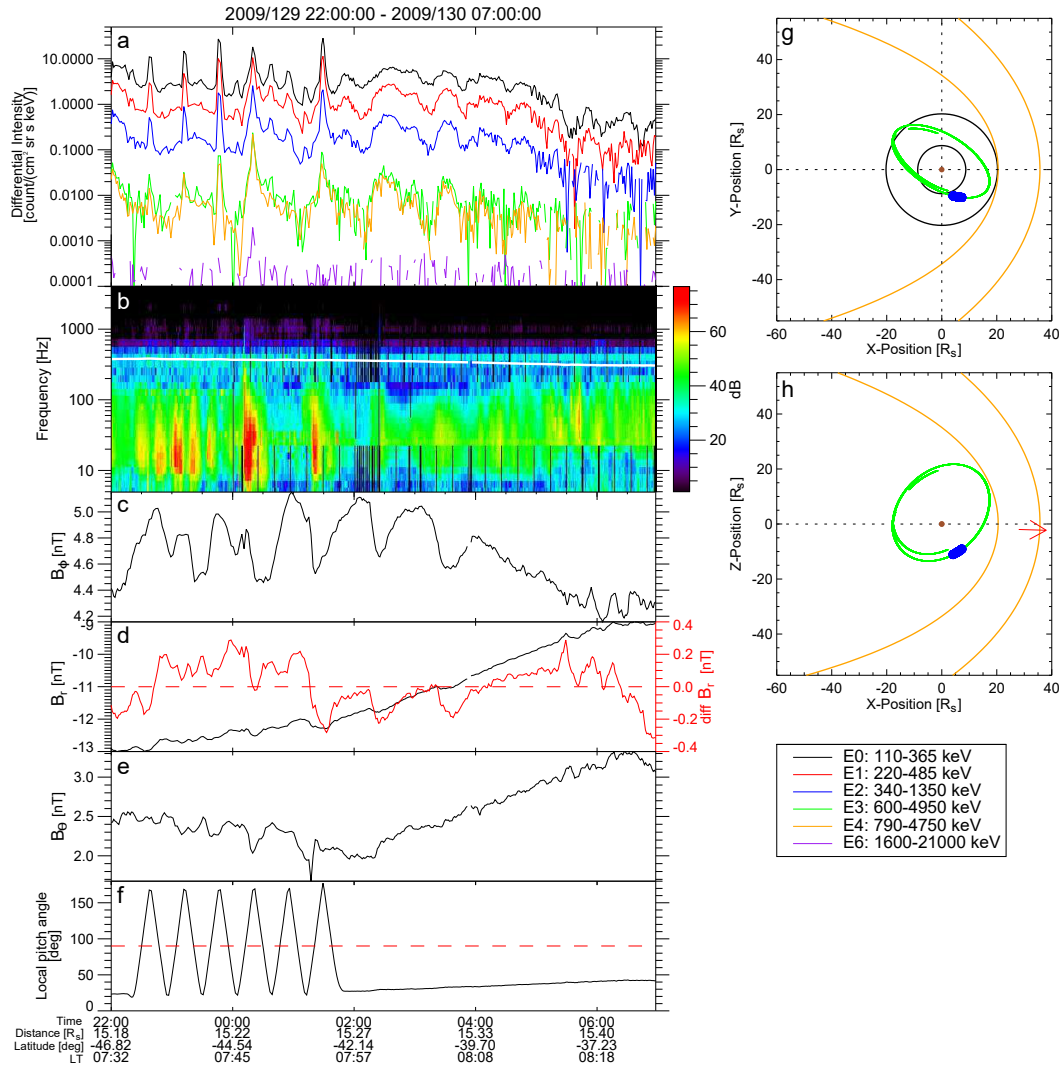


Figure 3.1: Quasi-periodic pulsed event observed on days 129 and 130 of 2009. The left panel is a stack of time series plots of (a) the differential intensities of energetic electrons from the LEMMS channels E0 to E4 and E6, (b) the RPWS electric field spectrogram, (c to e) the magnetic field components in spherical coordinates (B_ϕ , B_r and B_θ) measured by MAG and (f) the local pitch angle of the LEMMS HET. The white line on the RPWS spectrogram indicates the electron cyclotron frequency. The red line on the fourth panel is the detrended radial component of the magnetic field. Two subpanels on the right (g and h) indicate the location of Cassini during the event (blue line) along its orbit (green line), projected in the equatorial (x - y) plane and in the north-south (x - z) plane, using the Saturn Equatorial coordinate System (SZS). Titan and Rhea's orbits (at $20.3 R_S$ and $8.7 R_S$ respectively) are represented in the equatorial plane by black circles. Two simulated magnetopause locations are drawn in orange for two values of the solar wind dynamic pressure. The red arrow indicates the direction to the Sun. The energy passbands of the considered E-channels of LEMMS are given in the lower right corner. From Palmaerts et al. (2016a).

radial component (red line in Figure 3.1d) varies also in an anti-correlated way with the electron fluxes. Finally, some pulsations are also distinguishable in the B_θ component while Cassini was rolling but they are not correlated to the other pulsations. The concurrent hourly pulsations in the plasma wave and in the magnetic field will be tackled in Chapter 4.

3.2 Initial survey

The first global survey of the hourly pulsations observed in the Cassini/LEMMS electron flux measurements has been performed by Roussos et al. (2016). Their survey covers the period between June 28 of 2004 (180/2004), three days before Saturn Orbit Insertion, and May 7 of 2013 (124/2013). The selection of the pulsed events is based on the LEMMS electron data only, since no pulsations have been identified in the ion fluxes, and was achieved by manual inspection of the data. These events have been named “QP60” by Roussos et al. (2016) for “quasi-periodic 60-min”. In order to be included in the survey, an event had to exhibit a pulsed signal in one of the energetic channels E0 to E7 of LEMMS, i.e. at energies above 95 keV (see Table 2.2), and an interpulse period in the range between 40 and 80 min. The shape of the pulsations, in particular a sawtooth shape characterized by a rise time shorter than the decay time, was not a selection criteria. As a validating process for the selection, Roussos et al. (2016) applied a wavelet analysis on the LEMMS data. However, wavelet analysis can produce misleading periodicities due to data gaps or spacecraft rolls in the same period range. Their survey finally includes 543 QP60 events.

Roussos et al. (2016) mainly studied the spatial and spectral distribution of the quasi-periodic electron injections. They revealed that the QP60 injections can occur at various places in Saturn’s outer magnetosphere. However, a local time asymmetry in the occurrence rate appeared: most of the injections are observed in the dusk sector. Using the magnetic field model developed by Khurana et al. (2006), they also made the projection of the electron injection events along the field lines, towards the ionosphere or the equatorial plane. From this process, so-called “mapping”, it results that the duskside events are on closed field lines while most of the dawnside events are located on open field lines or map near the magnetopause.

Since the quasi-periodic electron pulsations occur globally, it is suggested that several processes are involved in the generation of the electron flux enhancements. However, no spatial discrepancies in the pulsation properties have been investigated, preventing any categorization of the events with their triggering process. In the following sections, results of a thorough analysis of the hourly electron pulsations properties are presented, based on a second review of these energetic events.

3.3 New survey of the hourly electron pulsations

The new survey of the quasi-periodic ~ 1 -h electron pulsations covers a 10-year period from the Saturn Orbit Insertion (on July 1st of 2004, day 183/2004) to July 1st of 2014 (183/2014), a period longer by 411 days than the one covered by Roussos et al. (2016). During this period, Cassini achieved 207 orbits around Saturn, traveling through most of

the magnetospheric regions, in the equatorial plane and up to $\sim 75^\circ$ of latitude. Cassini crossed magnetic field lines mapping to the magnetopause and at far distances in the magnetotail. Since Roussos et al. (2016) did not detect any pulsed electron injection in the inner magnetosphere with L-shell $< 8 R_S$, that inner region has not been considered in this survey.

The current survey was achieved using six electron rate channels of the LEMMS HET telescope: E0 to E4 and E6, covering an energy range from 110 keV to beyond 10 MeV. The LEMMS C-channels were not considered because, below 100 keV, pulsations are difficult to distinguish due to the mixing with other electron populations. Furthermore, Roussos et al. (2016) showed that any event detected below 100 keV appears also above that energy threshold. Moreover, Roussos et al. (2016) indicated that no pulsations have been identified in the E7 channel (> 7 MeV), likely because of the low sensibility of this channel. It was not necessary to include the E5 channel in the survey since it has a similar response as E4 (see Section 2.3.1).

The survey is based on a two-step detection method different from the one used by Roussos et al. (2016). The first step consists in a by-eye review of the LEMMS daily time series plots of the energetic electron fluxes to identify time intervals exhibiting pulsations separated by around 1 hour. Then, as a second step of the selection method, a Lomb-Scargle analysis is applied (using the fast algorithm developed by Press and Rybicki (1989)) to each event of the preliminary list in order to validate the manual selection. A pulsed event is selected if

1. at least two pulses are observed
2. pulses are present in at least one of the LEMMS E-channels
3. the mean interpulse period is in the range 40-90 min.

The first criteria indicates that events with only two pulses can be included in the survey, even if no periodicity can be inferred. However, the similar morphology of the pulsations and the time interval between the two intensity peaks suggest that they are generated by the same phenomenon as the longer events. The interpulse period range in the third criteria is not restrictive. Indeed, the preliminary manual selection as well as the Roussos et al. (2016) survey revealed a periodicity always included in this range. Periodic enhancements observed in the electron fluxes while Cassini was spinning at a period of around one hour were excluded from the list since electron flux variations can be induced only by the spacecraft motion.

The Lomb-Scargle analysis offers the advantage to be able to treat data gaps and unevenly sampled data. As an example, the Lomb-Scargle periodogram for the pulsed event on days 353 and 354 of 2009 is represented in Figure 3.2. The left panel gives the electron fluxes of the channels E0 to E4 and E6. The Lomb-Scargle algorithm was applied for each energy channel individually. The resulting periodogram is displayed on the right panel in Figure 3.2. The period is along the x -axis and the power spectral density (PSD) is given on the y -axis (in arbitrary units). The PSD for the different energy passbands is displayed with the same color as for the differential intensities. For the channels E0 to E4, the PSD peaks at a similar period around 1.15 h. By fitting the PSD peak with a gaussian curve and taking the Full Width at Half Maximum (FWHM), the inferred mean interpulse period for this event is 1.15 ± 0.07 h, i.e. 69 ± 4 min.

The selection resulted in a list of 720 quasi-periodic ~ 1 -h electron pulsation events

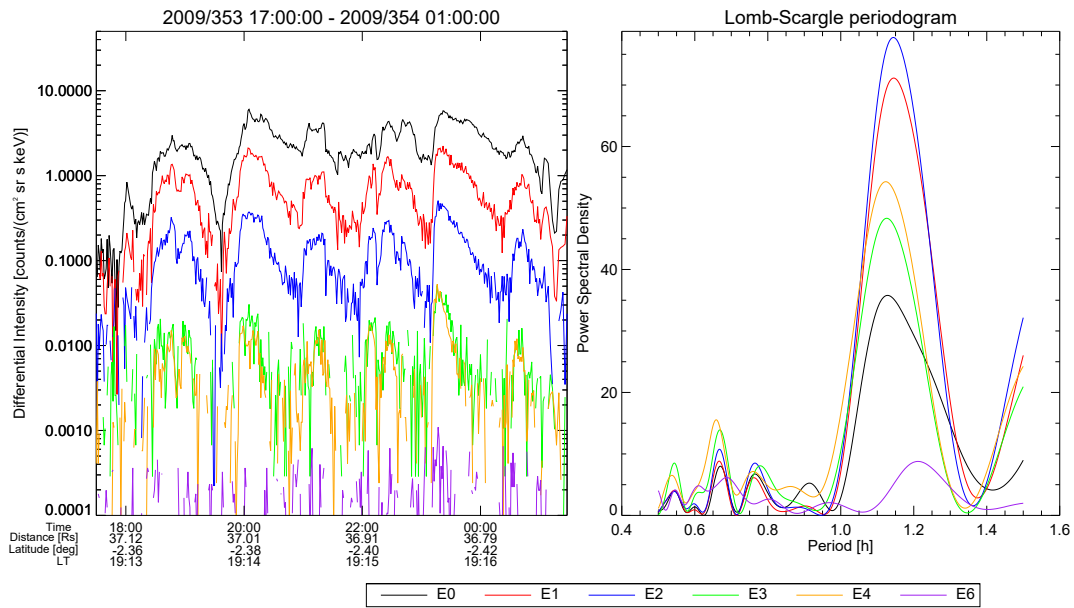


Figure 3.2: Quasi-periodic pulsed event observed on days 353 and 354 of 2009. Left panel: electron differential intensities of the LEMMS channels E0 to E4 and E6. Right panel: Lomb-Scargle periodogram showing the power space density (in arbitrary units) of the different channels. From Palmaerts et al. (2016a).

made up of at least two pulsations. This list is given in Appendix A.1. Compared to the first survey performed by Roussos et al. (2016), 123 additional events were identified. The longer period considered for the survey and the different selection method explain the larger number of events in the current survey. Moreover, this review includes time intervals without MAG data, contrary to the first survey.

The large number of pulsed electron injections reveals that this phenomenon is common in the magnetosphere of Saturn. The spatial distribution and the morphological properties of the ~ 1 -h pulsations will be analyzed on a statistical basis in the following sections.

3.4 Spatial distribution of the quasi-periodic electron injections

The quasi-periodic hourly electron pulsations described in the previous sections were detected in various regions of Saturn's magnetosphere, as shown in Figures 3.3 and 3.6. Figure 3.3 gives the spatial distribution of the pulsed events located at low latitudes, in the region within $2 R_S$ from the equatorial plane where the current sheet usually lies (Section 1.2.2). The green curves represent the orbits of Cassini in that region. Each event is represented by a colored dot. The color indicates the highest LEMMS energy channel at which pulsations are present, according to the periodogram provided by the Lomb-Scargle analysis. The percentage of events with the foreground pulsed signal in each channel is given in Table 3.1. The majority of the events (68%) exhibit pulsations up to at least 800 keV. The low percentage for the E3 channel is explained by its energy passband

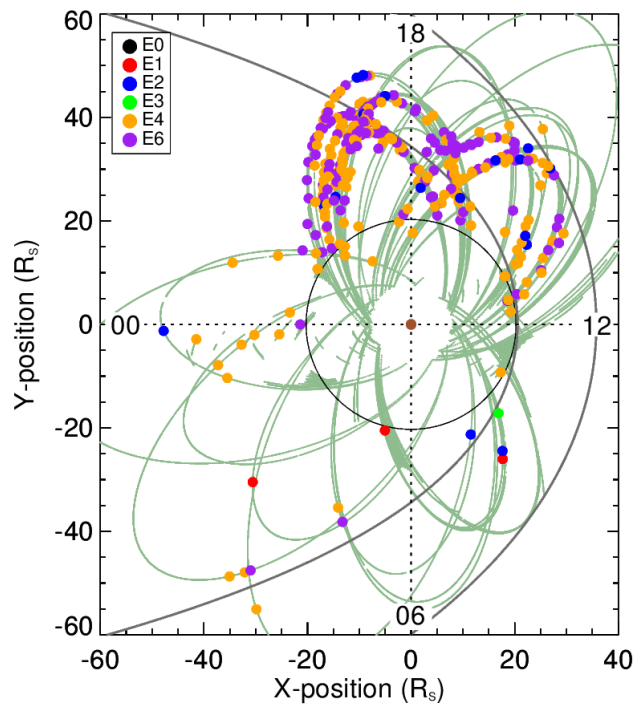


Figure 3.3: Location of the pulsed events (points) located within $2 R_S$ from the equatorial plane. The color of the points informs about the highest energy channel for which a pulsed signal is observed. The green curves indicate the orbits of Cassini within $2 R_S$ from the equatorial plane. Titan's orbit (black circle) and two simulated magnetopause locations (grey lines) are drawn, using the model of Kanani et al. (2010). From Palmaerts et al. (2016a).

Channel	Energy passband (keV)	Proportion of events
E0	110-365	0.1%
E1	220-485	2.1%
E2	340-1350	11.2%
E3	600-4950	0.8%
E4	790-4750	53.8%
E6	1600-21000	32.0%

Table 3.1: Energy passbands for the different MIMI/LEMMS electron channels used in this study and percentage of events with the foreground pulsed signal in the corresponding channel.

similar to the E4 energy passband. Hence, when pulsations are observed in E3, they are usually present in E4 as well.

Although the survey is longer and uses a different selection method, the spatial distribution of the equatorial events matches the spatial distribution inferred from the initial survey of Roussos et al. (2016). The large majority of the pulsed events occur in the outer magnetosphere, outside Titan's orbit (black circle at $20.3 R_S$). Some electron injections are identified close to the predicted magnetopause location (gray lines), while some other

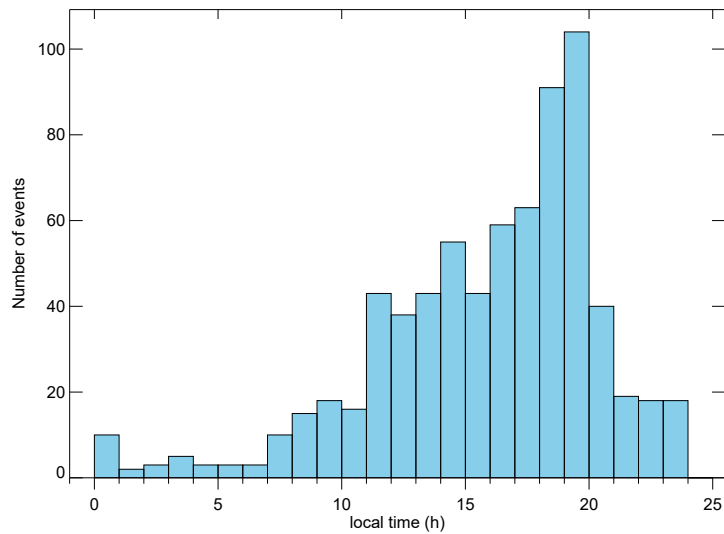


Figure 3.4: Distribution of the quasi-periodic electron pulsed events as a function of local time.

events are located deep inside the magnetosphere. They can be observed at all local times but the local time distribution of the events is strongly asymmetric with most of them encountered in the duskside of the magnetosphere (80% of the events), as shown by the histogram in Figure 3.4.

During the first 10 years of its mission, Cassini spent more time in the duskside of the magnetosphere so that the dawn-dusk asymmetry in the distribution could be due to the sampling. However, after the normalization of the number of events per local time bin by Cassini’s residence time in each bin, the dawn-dusk asymmetry remains. Figure 3.5 gives the averaged number of days separating two events in each local time bin, taking into account Cassini’s residence time in every individual local time bin. In the dusk magnetosphere, an event is observed every ~ 4 days of presence of Cassini while it is observed every 30-50 days in the dawnside.

Contrary to Figure 3.3, Figure 3.6 gives information about the latitudinal distribution of the quasi-periodic electron injections. The format is the same as in Figure 3.3 but the events are projected in a local time-latitude plane. It appears that a lot of electron pulsed events occur outside the low-latitude region, especially at dayside. In the dawnside of the magnetosphere, many of the pulsed events are encountered at high latitude, most of them in the southern hemisphere. The majority of the southern high-latitude events are very energetic, exhibiting a pulsed signal at energies above 1.6 MeV (purple dots). There is no corresponding energetic events at the northern dawn high-latitude region likely because Cassini was much further away from Saturn when it was orbiting in that region than in the corresponding region in the southern hemisphere. Furthermore, only few pulsed events are observed in the dawn equatorial plane. The absence of signatures of the dawn high-latitude pulsations in the equatorial plane suggests that these events reside on open magnetic field lines so that electrons do not reach the low latitudes.

In the following sections, the first in-depth analysis of the morphological properties of the hourly electron injections is presented.

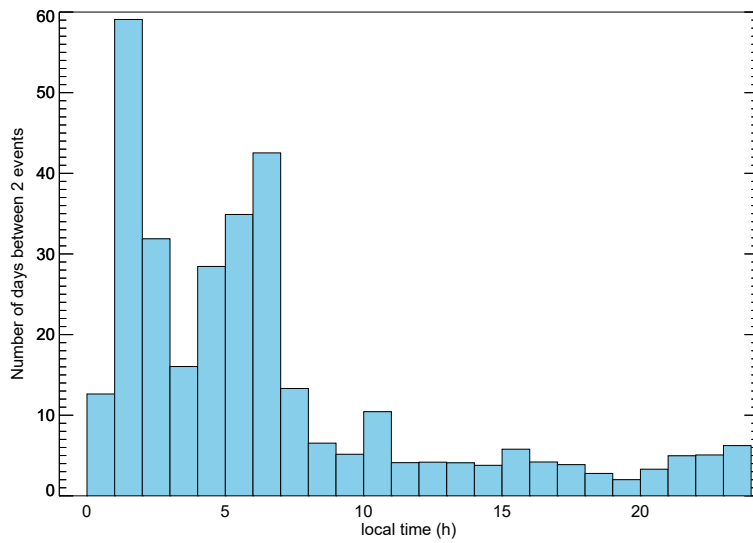


Figure 3.5: Average number of days between two quasi-periodic electron pulsed events as a function of local time, taking into account the total residence time of Cassini in each local time bin.

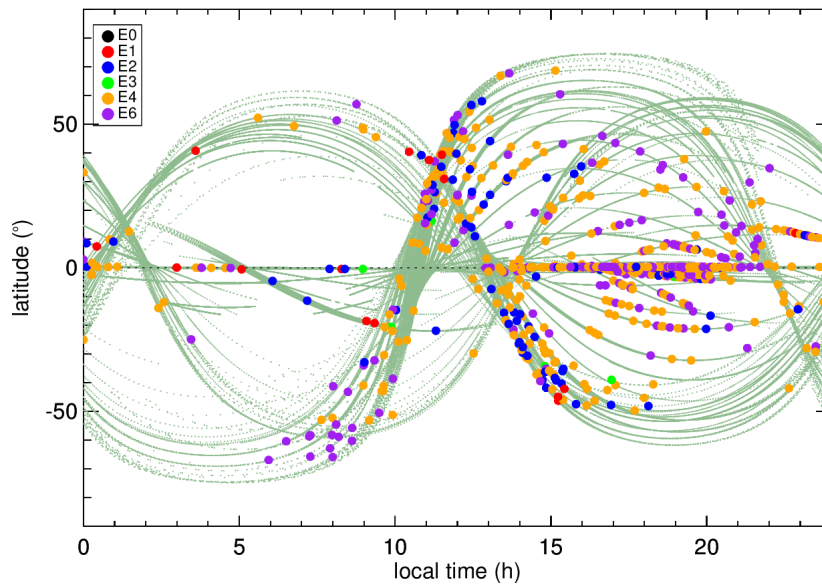


Figure 3.6: Location of the pulsed events (points) in a latitude-local time diagram. The color code is the same as in Figure 3.3. The green curves are the orbits of Cassini. From Palmaerts et al. (2016a).

3.5 Morphological properties of the hourly electron pulsations

The quasi-periodic ~ 1 -h electron pulsations occur in various regions of Saturn's outer magnetosphere. Based on the list of 720 events, a statistical analysis was performed to determine properties of this pulsed phenomenon and reveal any spatial discrepancies.

3.5.1 Interpulse period

The period commonly mentioned for the pulsed electron injections is one hour. However, no accurate spectral analysis of these events has been previously achieved. Using the Lomb-Scargle method like for the example in Figure 3.2, the periodicity was determined for every event and each LEMMS electron channel separately. The histograms in Figure 3.7 give the distribution of the interpulse period for the different energy channels. A gaussian fit is superimposed and the mean and the full width at half maximum (FWHM) are indicated on every subpanel. The interpulse period does not show any dependence with energy: the statistical mean varies only from 67 to 69 min between the different energy channels. By calculating the statistical distribution of the average pulsation periodicities throughout the different channels for each individual event, the overall interpulse duration is $\sim 1.14 \pm 0.16$ h or $\sim 68 \pm 10$ min. Hence, the typical periodicity of the quasi-periodic electron pulsations is somewhat longer than the 1-hour periodicity usually mentioned. However, for simplicity reasons, the notion of "1-hour periodicity" and "QP60" will continue being used throughout this manuscript. It should be noted that the period range of 40-90 min used for the selection of the pulsed events is validated a posteriori by the gaussian shape of the histograms: it is unlikely to detect pulsations with a periodicity outside this range. Furthermore, no temporal evolution of the interpulse period, for instance with Saturn's seasons, has been highlighted by the analysis.

The interpulse duration does not reveal any spatial discrepancies. In particular, no dependence with local time can be inferred, as illustrated in Figure 3.8. The left panel of Figure 3.8 indicates the average interpulse period at each local time. The pulsation period average is calculated over a local time bin whose the length is inversely proportional to the number of pulsed events identified in each bin. Hence, the local time bin length varies from 1 hour in LT for the interval 19-20 LT, where the event density is the highest, to 4 hour for the sector 1-2 LT which includes only two events. For most of the local time bins, a gaussian fit was applied on the distribution of the interpulse period, as shown for the bin 1315-1544 LT on the right panel of Figure 3.8. The gaussian mean is indicated by a red dashed line on the histogram and by black large dots for each local time bin on the left panel. The error bars represent the FWHM of the gaussian. The local time bin given in example is indicated in red. In the local time sector 2-5 LT, the sparsity of the pulsed events prevents from fitting a gaussian on the distribution of events. Therefore, for this particular region, the statistical mean and standard deviation of the interpulse periods were performed and are indicated by the gray large dots and error bars in Figure 3.8. The lower and upper dotted lines in the left panel of Figure 3.8 give the extreme values of the interpulse period for each bin. Within the error bars, no local time dependence of the interpulse period emerges from this statistical analysis. Hence, it is concluded that all

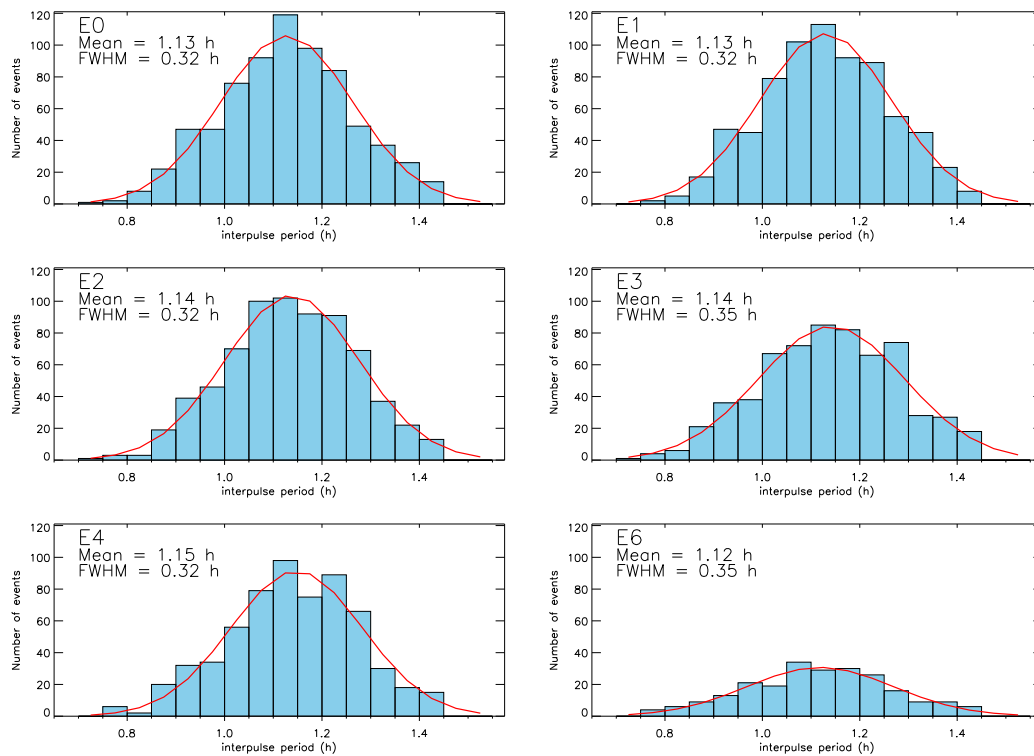


Figure 3.7: Histograms of the distribution of the interpulse period for each considered LEMMS energetic electron channel. The histograms are fitted by a gaussian (red curve). The mean and the full width at half maximum (FWHM) of the gaussian are indicated in the upper left corner. From Palmaerts et al. (2016a).

the electron pulsation events are characterized by a period close to 68 min although they occur in all local time sectors.

The analysis includes events made up of only two pulsations for which the periodicity is not well defined. However, excluding the events with less than 4 pulses does not change the results presented here. Furthermore, in order to obtain a result independent of the Lomb-Scargle method, the distribution of interpulse period has been also performed by dividing the duration of the quasi-periodic electron pulsed events by the number of pulses². This simple method gives a mean interpulse period of 64 ± 9 min, similar to the result obtained with the Lomb-Scargle method.

3.5.2 Number of pulses

The duration of a quasi-periodic electron injection, i.e. the time between the start of the rise of the first pulse to the end of the decay of the last pulse, is variable between events. As explained above, the shortest events are made up of only two pulses and consequently last only ~ 2 hours. However, particularly long events lasting almost 20 hours can occur, as illustrated in Figure 3.9. Hence, such long events survive during almost two entire rotation of Saturn.

². More accurately, the time between the first intensity peak and the last one is divided by the number of pulses reduced by 1.

3 Quasi-periodic hourly pulsations in the energetic electron fluxes

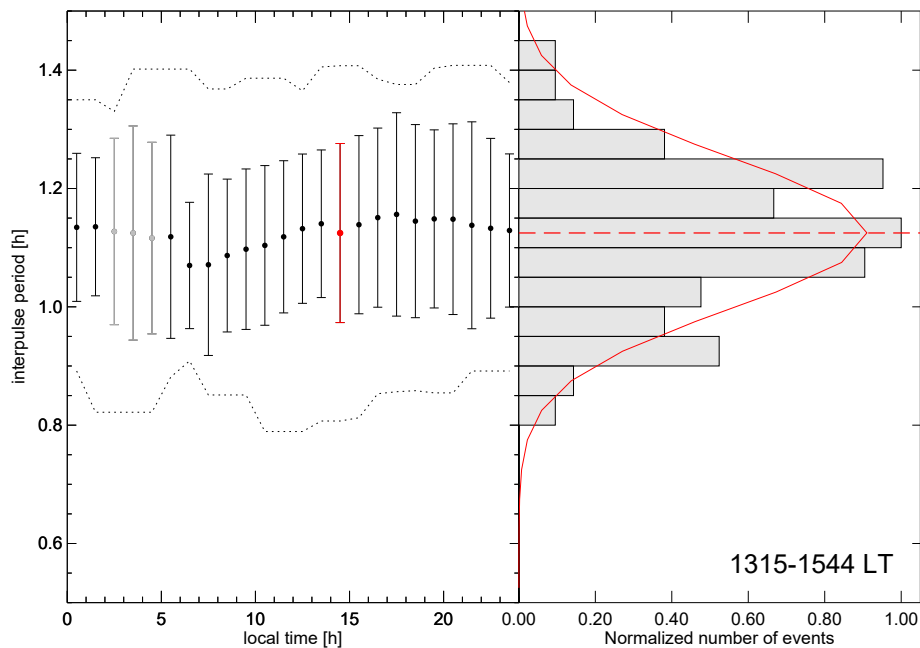


Figure 3.8: Left panel: Averaged interpulse period given every one hour in local time. The average is performed on a local time bin whose length depends on the number of events included in the bin. The error bars represent the FWHM of the gaussian fit of the histogram of the interpulse period distribution (black and red bars) or the standard deviation of the average (gray bars). The two dotted lines indicate the maximum and the minimum interpulse period encountered in each local time bin. Right panel: Normalized histogram of the interpulse period distribution for the local time bin 1315-1544 LT, whose the averaged interpulse period is highlighted in red on the left panel. The red line is a gaussian fit and the red dashed line indicates the mean of the gaussian. From Palmaerts et al. (2016a).

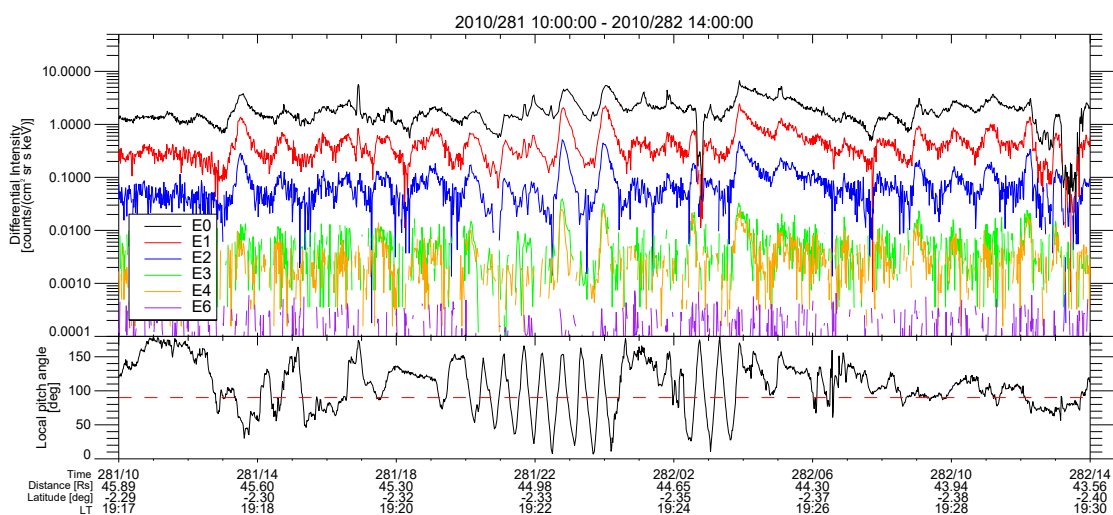


Figure 3.9: Quasi-periodic pulsed event observed on days 281 and 282 of 2010. Top panel: electron differential intensities of the LEMMS channels E0 to E4 and E6. Bottom panel: Local pitch angle of the LEMMS HET.

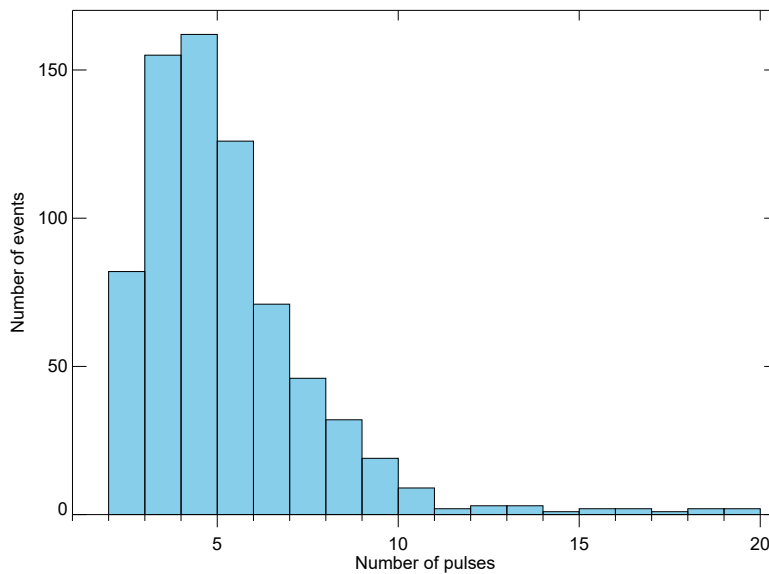


Figure 3.10: Histogram of the distribution of the number of pulsations per event. From Palmaerts et al. (2016a).

The distribution of the number of pulses per event is given by the histogram in Figure 3.10. Less than 8 pulses are observed for the majority of the quasi-periodic ~ 1 -h pulsations (90%) and the statistical average is 4.7 pulses per event. This study relies on the electron in-situ data collected by Cassini/LEMMS moving around Saturn. Hence, the duration of the event is not necessarily the duration of the phenomenon, but it can be the time interval during Cassini crosses the region of pulsations or maps into the electron acceleration region. The corotation velocity of the particles flowing around Cassini may also influence the event duration. However, in the low-latitude outer magnetosphere where Cassini travels slowly, the duration and the interpulse period does not reveal any correlation with the radial distance. Hence, these two characteristics are independent of the spacecraft velocity. Furthermore, the distribution of the number of pulses for the low-latitude events is similar to the one of the whole set of events, shown in Figure 3.10.

Similarly to what has been done for the interpulse period, an analysis of the dependence of the number of pulses with local time has been performed. The number of pulses averaged by local time bin is given in Figure 3.11. The length of each bin is determined by the number of events per bin, identically to the procedure for the interpulse period explained in the previous section. The black dots and the error bars in Figure 3.11 represent the statistical mean and standard deviation respectively. The dashed line indicates the largest number of pulses encountered in each 1-h LT bin and the dotted line gives the longest duration of the event in hours. Long events made up of more than 10 pulses are not encountered in the dawnside of the magnetosphere. However, it should be noted that most of the dawn events are located at high latitude and close to the planet where the magnetic field lines are crossed quickly by the Cassini spacecraft. As an illustration, 40 L-shells are crossed by Cassini during a high-latitude pulsed event on day 291/2008 while the L-shell variation is about one for an equatorial event with a similar duration (e.g. on day 284/2010). Apart from these long events, no local time trend can be inferred in the distribution of the number of pulsations. Finally, it is noteworthy that there is no clear

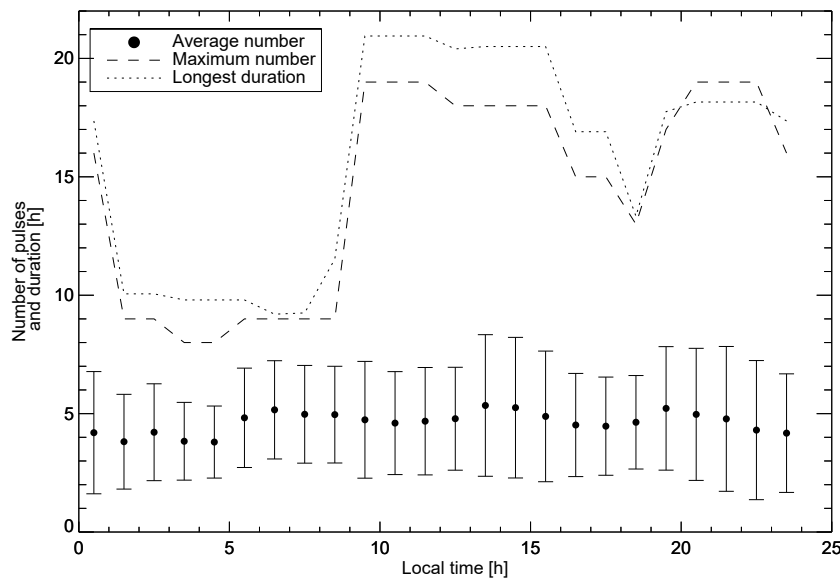


Figure 3.11: Averaged number of pulses per event given every one hour in local time. The average is performed on a local time bin whose length depends on the number of events included in the bin. The error bars represent the standard deviation of the average. The dashed line indicates the maximal number of pulsations encountered in each local time bin. The dotted line gives the longest duration (in hours) of the events.

correlation between the interpulse period and the number of pulses.

3.5.3 Morphology of the pulsations

The morphology of the QP60 pulsations can provide clues about the acceleration mechanism and the source of the pulsed energetic electrons. Therefore the morphology of each individual pulse in the LEMMS electron data has been investigated individually. The set of 720 quasi-periodic electron injections totals 3440 pulsations. One pulsation is counted if one peak is identified in at least one LEMMS E-channel. Most of the pulsations do not appear at all energies of the LEMMS HET. Except for one particular event discussed in Section 7.2.2, no energy dispersion is observed in the electron injection. Consequently, when flux enhancements are present at different energies, they are concomitant in the different LEMMS channels.

In total, by considering the energy channels separately, 13 338 pulsations were identified. Table 3.2 indicates the number of pulsations in each of the seven LEMMS channels considered. It appears that the number of pulses decreases with energy. Almost all pulsations ($\sim 96\%$) are present in the the energy range from 100 to 500 keV (E0-E1 channels). At higher energies (E2-E4 channels), pulsations are less frequent. At these energies, flux enhancements preferentially occur in the center of the event time interval, as defined by the pulsations in the lowest energy channel E0, than at the start or the end of the interval. This observation is illustrated in Figure 3.12 which gives, for each energy channel, the occurrence probability to observe the i^{th} flux pulse in an event made up of n pulses (n and i are determined by the pulsations in the E0 channel). Only events with 3 to 7 pulses were

3.5 Morphological properties of the hourly electron pulsations

Channel	Energy passband (keV)	Number of pulses	Percentage of sawtooth pulses
E0	110-365	3312	52%
E1	220-485	3291	60%
E2	340-1350	2914	64%
E3	600-4950	1890	68%
E4	790-4750	1775	75%
E6	1600-21000	156	89%

Table 3.2: Energy passbands for the different MIMI/LEMMS electron channels used in this study, total number of pulses and percentage of sawtooth pulses (rise rate shorter than 40% of the total duration of the pulse).

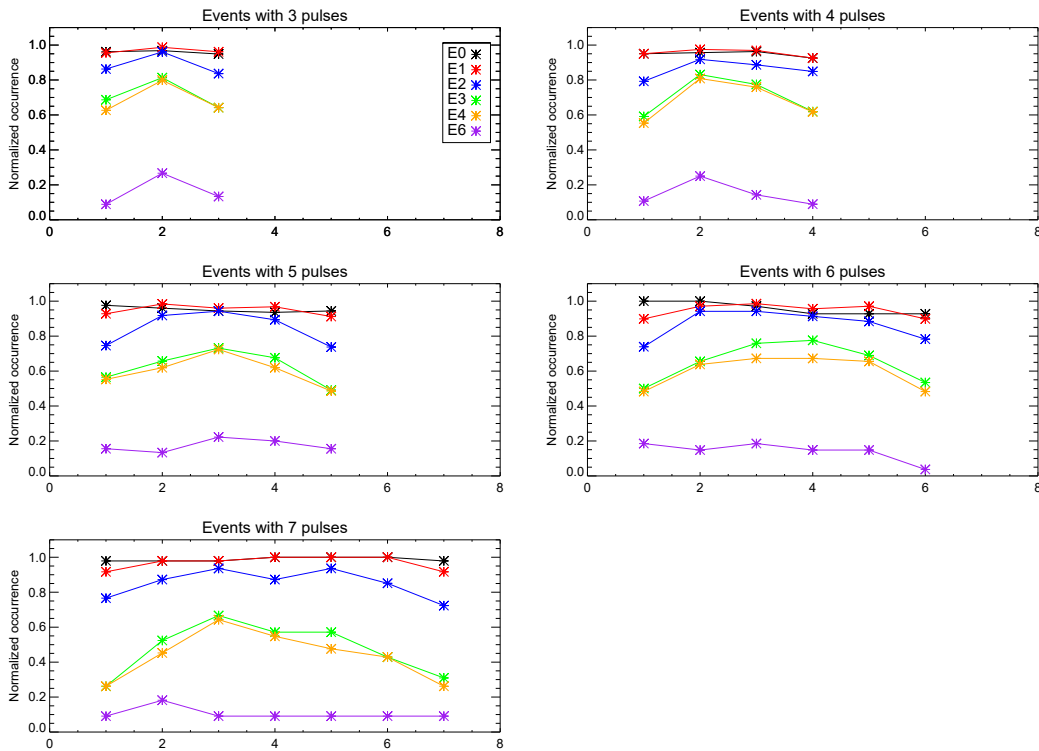


Figure 3.12: Normalized occurrence rate of each individual pulsation within a quasi-periodic pulsed event made up of 3 to 7 pulses, for the different LEMMS energy channels. The number of pulsations is defined in the E0 channel.

considered in order to have good statistics. For the channels E2 to E4, this probability is the highest around the center of the electron injection event. Hence, the first pulse in the E3 and E4 channel generally corresponds to the second pulse in the E0 channel and the last one is the second last one in the lowest energy channel.

Additionally, the highest peak intensities are generally encountered in the middle of the event time interval. These findings suggest that the process producing the electron flux pulsations is progressive: it requires time to accelerate electrons up to the highest energies at a flux exceeding the background signal of the detector and it starts to fade out in the last third of the event.

Only few pulsations (3.2%) are present in the highest energy channels (E3 to E6) without concurrent pulses at the lowest energy (E0-E1 channels). A mixing of different electron populations at lower energies may conceal the ~ 1 -h pulsations. Finally, the higher is the peak pulse in one channel, the higher are the corresponding pulses in the other channels.

The rise time and the decay time of every pulse have been investigated, as well as the rise and decay rates (e.g. the slopes of the pulse) by means of a linear fit (in a linear scale) from the pulse start to the peak and from the peak to the pulse end. The histograms in Figure 3.13 represent the distribution of the ratio between the growth and the decay times of the pulses for the different LEMMS channels. The mean values of the rise-over-decay ratio, indicated in the upper right corner of each panel, are all lower than the unity, indicating that the growth time is generally shorter than the decay time. It is noteworthy that the rise-over-decay ratio decreases with energy. It is found that on average, the rise time diminishes with energy while the decay time increases.

Similarly, the ratio between the rise rate and the decay rate of the pulses follows a log-normal distribution centered on a positive value, meaning that the growth rate is usually higher than the decay rate (in absolute value). Again, this ratio increases with energy. Hence, this statistical analysis of the morphology of the QP60 reveals that their most common shape is a fast growth followed by a slower decay. A rise time shorter than 40% of the full pulse duration or, similarly, a decay time longer than 60% of the pulse duration, characterize a “sawtooth” shape. The occurrence of sawtooth-shaped pulses increases with energy, from 52% in the E0 channel to 89% in the E6 channel, as listed in Table 3.2. The reverse shape (rise time longer than 60% of the pulse duration) is strictly speaking a sawtooth pattern too, but this designation will not be used hereafter for this morphology to avoid ambiguity. This morphology is encountered for 12% of the pulses in the E0 channel and this percentage decreases with energy to reach only 0.9% in the highest energy channel. The remaining pulses have a growth time comparable to the decay time (rise time between 40% and 60% of the pulse length).

No correlation has been found between the rise and decay rates of the electron flux enhancements and the interpulse period of an event nor the total number of pulses. However, the growth duration and the decay duration are longer when the interpulse period is longer. The latitude and local time dependence of the rise and decay rates is shown in Figure 3.14 for the E0 and E3 channels (upper and middle panels). The rates are averaged over $1 \text{ h} \times 20^\circ$ latitude bins. The number of pulses included in each bin is indicated in white. The lower panel in Figure 3.14 gives the latitudinal average of the rates for every energy channel separately. The local time distribution of the growth and decay rates of the electron pulsations is practically uniform except in the sector 06-09 LT where they are higher at all energies. As shown by the upper panels, these increased averaged rates in the morning originate from the high rates encountered at high southern latitudes ($\varphi < -30^\circ$) between 05 and 10 LT. In this magnetospheric region, most of the ~ 1 -h quasi-periodic electron events exhibit a foreground signal at energies above 1.6 MeV (see Figure 3.6). Higher rates are also found at high northern latitude between 17 and 20 LT. However, only a few pulses are included in that region.

The analysis of the pulsation morphology reveals that the growth and decay slopes of the pulsations are steeper if the peak intensity of the pulse is higher, as shown for the E1 and E4 channels in Figure 3.15. Every pulse is represented by a black cross and the

3.5 Morphological properties of the hourly electron pulsations

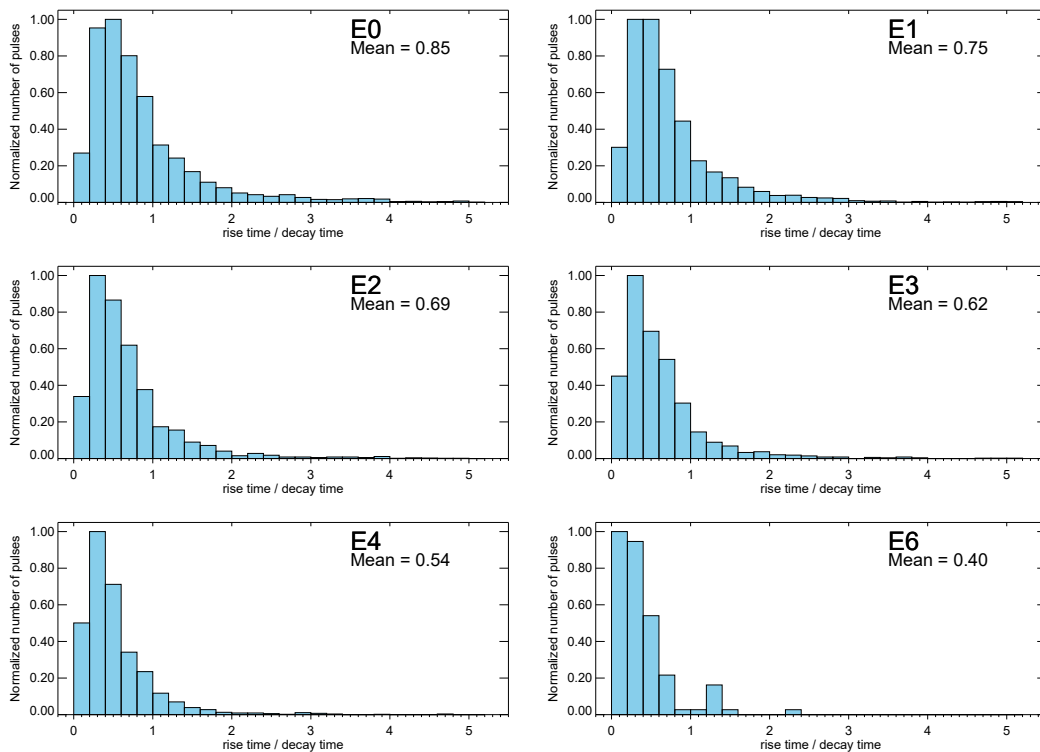


Figure 3.13: Normalized histograms of the distribution of the ratio between the rise time and the decay time of each pulse for each considered LEMMS electron energy channel. The average value of the ratio is indicated in the upper left corner. From Palmaerts et al. (2016a).

scattered distribution is fitted by a linear fit in the log-log scale (red line). For all the LEMMS channels, the slope of the fit is higher for the rise than for the decay. The fit slope increases with energy up to the E3 channel and then lower at higher energies, as shown in the bottom panels of Figure 3.15. It should be noted that a low number of pulses are observed in the E6 channel, making the fit less reliable. The correlation coefficient between the pulse rates and peak intensity, indicated on the left corner of the panels in Figure 3.15, varies between 0.71 and 0.84, indicating a significant correlation.

3.5.4 Pitch angle distribution of the pulsations

In this section, the pitch angle dependence of the periodic electron flux enhancements is investigated. As a reminder, the pitch angle indicates the angle between the magnetic field lines and the direction of the particle hitting the LEMMS detector. The isotropy of the pulsed energetic electrons can be known only when all pitch angles are covered, providing then the pitch angle distribution (PAD). The PADs are available only when LEMMS orientation is changing, thus when Cassini is spinning.

Information about the pitch angle distribution is available for 161 pulses from 78 different quasi-periodic ~ 1 -h electron injections. Three of them are visible at the beginning of the event depicted in Figure 3.1. In Roussos et al. (2016), the pitch angle dependence of an event is analyzed in detail. In that particular event shown in the upper panel of Fig-

3 Quasi-periodic hourly pulsations in the energetic electron fluxes

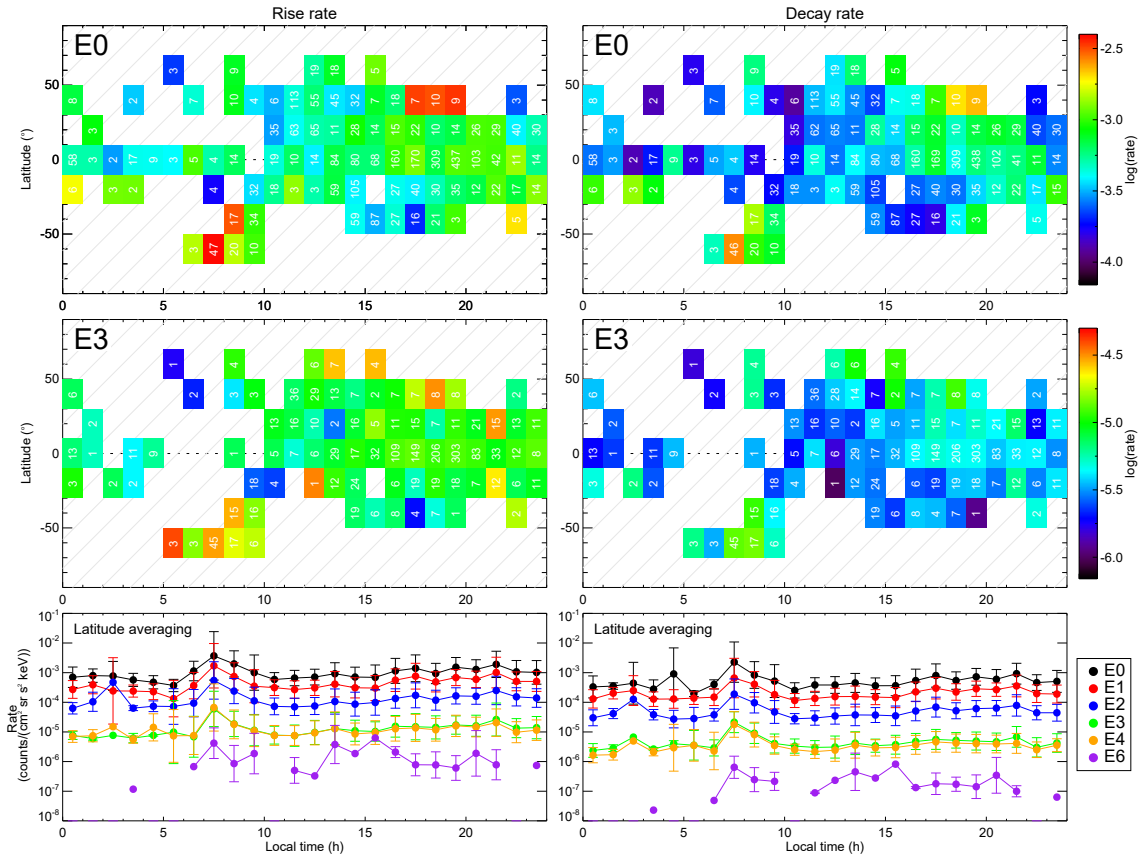


Figure 3.14: Upper and middle panels: Latitude-local time diagrams of the rise (left) and decay (right) rates of the pulses (absolute value of the slope of a beginning-to-peak and peak-to-end linear fit of the pulses) in the E0 (110-365 keV) and E3 channels (600-4950 keV), averaged over 1 h LT \times 20° latitude bins. The number of pulses included in each bin is indicated in white. Lower panels: Latitude average of the rise (left) and decay (right) rates binned on 1 h LT for each considered LEMMS electron channel. From Palmaerts et al. (2016a).

ure 3.16, periodic enhancements with a short periodicity are observed at lower energies (C0-E0 channels) in addition to clear \sim 1-h pulsations at energies above 790 keV (E4-E6 channels). These narrow peaks are in phase with the pitch angle variation (lower panel of Figure 3.16) caused by Cassini rolling. At intermediate energies (E2 channel), both periodic flux variations are mixed. The short-period flux peaks at low energy indicate the presence of a bidirectional electron beam along the field lines. The analysis by Roussos et al. (2016) revealed a quasi-isotropic PAD of the decay of the pulse.

The disentangling between the field-aligned electron and the \sim 1-h quasi-periodic electron populations is highlighted in the pulsed event which occurred on day 027 of 2008. This event is shown in the upper panel of Figure 3.17. In addition to the E-channels, a combination between the low energy electron channels C4, C5 and C7 is indicated. This combination, noted E0*, is calculated using the formula

$$E0^* = 0.1 \times C4 + 0.5 \times C5 - 0.25 \times C7$$

This combination of C-channels gives a pseudo-channel with an energy passband similar

3.5 Morphological properties of the hourly electron pulsations

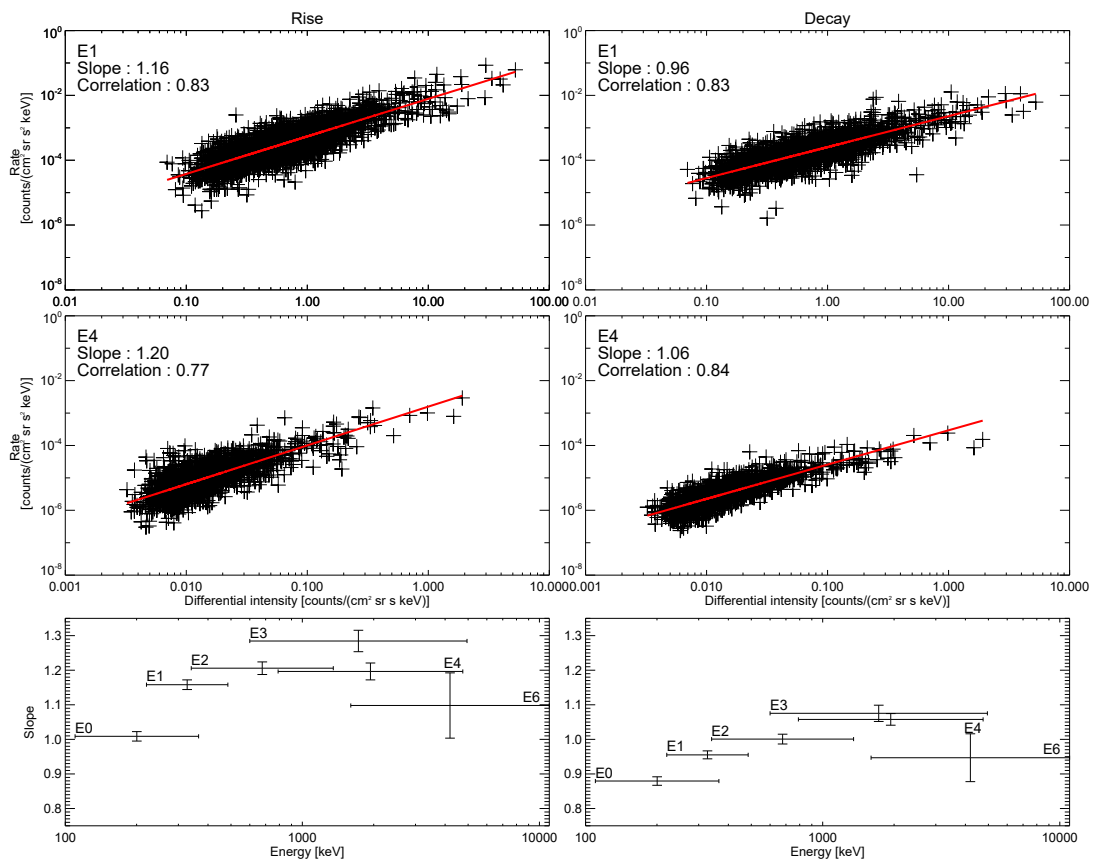


Figure 3.15: Upper and middle panels: Rise (left) and decay (right) rates for each pulse (in absolute value) in the E1 (220-485 keV) and E4 channels (790-4750 keV) as a function of the peak intensity of the pulse. A linear fit is plotted in red. The slope of the fit and the correlation coefficient are indicated in the upper left corner. Lower panels: Slope of the fit for each channel for the rise (left) and decay (right) rates. The vertical error bars are the 1-sigma uncertainty for the slope. From Palmaerts et al. (2016a).

as E0 but it measures electrons coming from the opposite direction and entering in the LEMMS LET telescope. Following the method described in Gurnett et al. (2010), the ratio between E0* and E0 indicates if LEMMS is located on open or closed field lines. On closed field lines, the flux of particles at a certain energy is the same in both directions because of the bouncing motion (Section 1.2.4.1), as illustrated in Figure 3.18. Hence, when the pointing of the two telescopes of LEMMS is aligned with the magnetic field lines (i.e. the pitch-angle is around 0° or 180°), the fluxes in E0 and in E0* are equivalent if Cassini crosses closed field lines and are significantly different on open field lines. In the bottom panel of Figure 3.17, the local pitch angles in the LEMMS HET (thick line) and LET (thin line) are indicated with a color scale giving respectively the intensity in the E0 and E0* channels. During the main part of the event, Cassini is rolling, providing a good pitch angle coverage.

During the event shown in Figure 3.17, three flux enhancements separated by around 60 min are detected between 0030 and 0300 UT. Three green rectangles are on top of these ~1-h pulsations. After 0300 UT, narrow peaks, indicated by short red lines, are

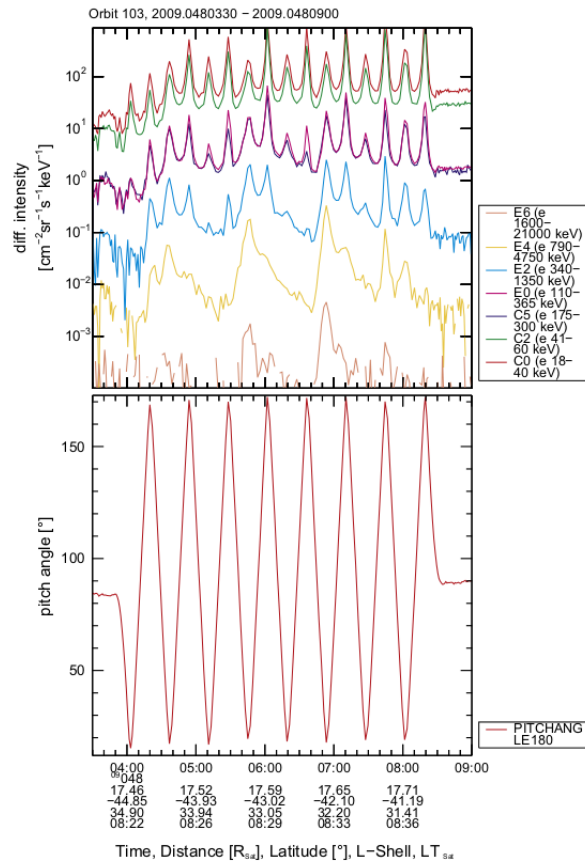


Figure 3.16: Quasi-periodic pulsed event observed on day 048 of 2009 in different LEMMS electron channels (top panel) and pitch angle of the LEMMS HET (bottom panel). From Roussos et al. (2016).

observed simultaneously with a pitch angle close to 0° . This observation, made in the northern hemisphere, reveals the presence of upward field-aligned electron beams similar to the beams reported by Saur et al. (2006). Hence, when HET is pointing in the field-aligned direction toward Saturn, a short but intense flux enhancement is detected in the E-channels. The same peaks appear in the E0* when the LET telescope is in the field-aligned direction toward the planet. Since the E0* and E0 fluxes do not peak simultaneously, it is revealed that LEMMS is on open field lines after 0300 UT.

Five narrow flux peaks are also present earlier in the interval, superimposed to the first two 1-hour pulsations. At that time, the field-aligned electron beams are bidirectional since they are observed at pitch angle of $\sim 0^\circ$ and $\sim 180^\circ$. Thus, Cassini resides on closed field lines between 0030 and 0215 UT. During the last 1-hour pulse at 0230 UT, LEMMS pointing is fixed and not in the field-aligned direction so that no narrow flux peak is detected. Like for the event presented in Figure 3.16, the field-aligned variations of the electron intensities are larger at low energies.

The event shown in Figure 3.17 and depicted in the previous paragraphs demonstrates the coexistence of two different electron populations: the hourly quasi-periodic relativistic electrons and the field-aligned electron beams. While the ~ 1 -h pulsations (green rectangles) stop after 0300 UT, the narrow field-aligned flux peaks (red lines) persist. It should

3.5 Morphological properties of the hourly electron pulsations

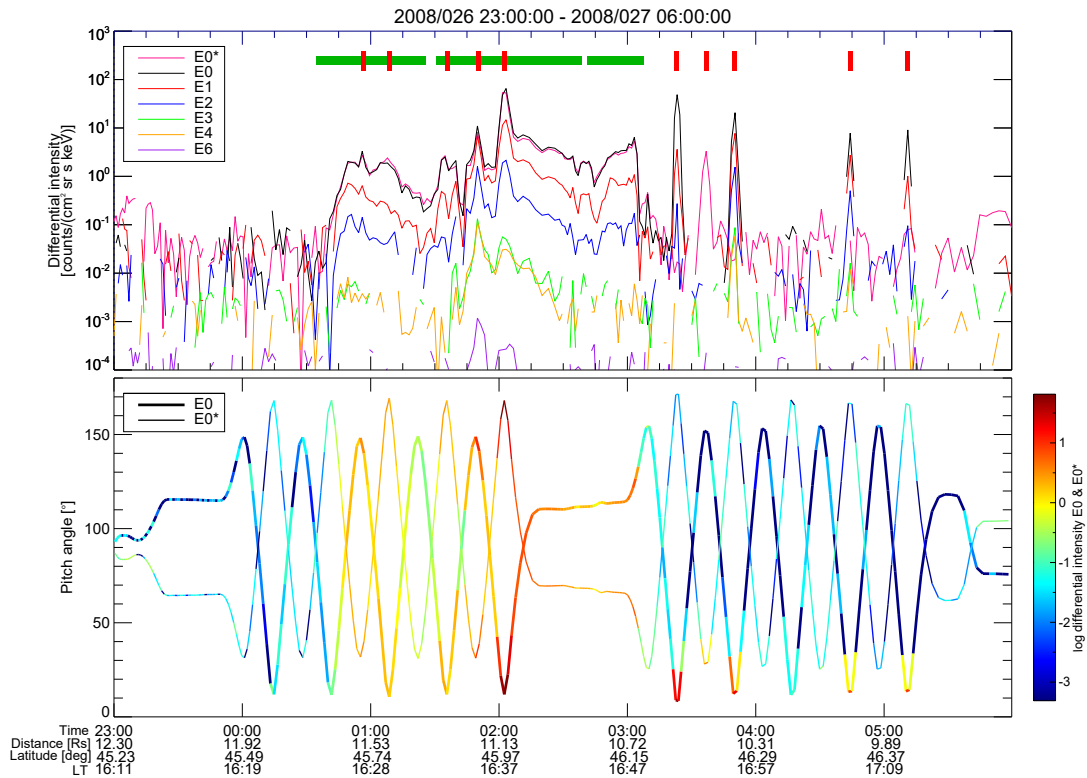


Figure 3.17: Upper panel: Quasi-periodic pulsed event observed on day 027 of 2008 mixed with a field-aligned electron beam population. Time series of the differential intensities of LEMMS electron channel E0 to E4, E6 and E0* (combination of C4, C5 and C7). The quasi-periodic pulsations are indicated by the green rectangles. Red lines point at the electron beams. Lower panel: Pitch angle pointing of the LEMMS HET (thick line) and LET (thin line). The colors indicate the intensity of the E0 and E0* channels. Adapted from Palmaerts et al. (2016a).

be also noted that Cassini is on closed field lines till 0300 UT and then is on open field lines, as indicated by the comparison between the E0* and E0 channels.

Using the set of 161 pulses with an available pitch angle distribution, a statistical analysis of the PAD of the hourly quasi-periodic electron pulsations has been achieved. Each pulse has been divided in three parts: the growth of the pulse, the peak (one single value per pulse) and the decay. The statistical PAD for each part in the E0 channel is shown in Figure 3.19. In order to conceal the flux level variations between different events, the intensity is normalized to the unity at the start of the pulse for the growth part and at the end of the pulse for the decay. The average distribution indicated by the black line is superimposed to the individual measurements (gray crosses). The growth and decay parts of the pulses exhibit a quasi-isotropic pitch angle distribution, in agreement with the single-case analysis for the decay performed by Roussos et al. (2016). For a few events, the PAD has a more field-aligned shape. Unlike the rise and decay phase, the PAD of the pulse peak intensity is mainly aligned with the magnetic field. This is explained by the mixing between the hourly pulsed electrons and the field-aligned electron beams which tends to increase the peak intensity of the ~1-h pulsations, especially at low

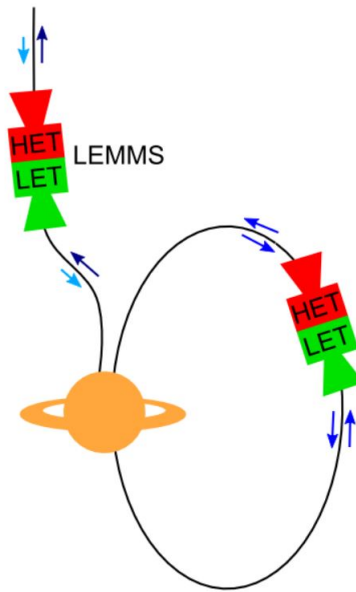


Figure 3.18: Illustration of the method described by Gurnett et al. (2010) to identify if Cassini is on open or closed field lines using Cassini/LEMMS instrument. On closed field lines, the flux of particles at a given energy is the same in both direction (blue arrows). Hence, when LEMMS is pointing in the field-aligned direction, the flux measured by HET and LET are the same. On open field lines, the particle flux is not the same toward the planet (light blue arrows) and backward the planet (dark blue arrows). Therefore, the measurement of particles at a given energy is not identical in the two LEMMS telescopes.

energies. At higher energies, the statistical PADs for the three parts of the pulses are similar.

Based on the $E0^*/E0$ ratio and the method of Gurnett et al. (2010), it appears that all the duskside field-aligned pulses but one are associated with closed field lines. The only exception is a high-latitude event on day 297/2008 occurring while Cassini was crossing open flux tubes during a brief time. This result is only valid in the dusk flank of the magnetosphere since only two dawnside events provide a pitch angle distribution.

3.6 Discussion

The ~ 1 -h quasi-periodic pulsations detected in the flux of the energetic electrons by the MIMI/LEMMS instrument on board Cassini have been thoroughly analyzed and described in this chapter. A total of 720 electron pulsed events have been identified over 10 years of observations, from the SOI till July 2014 (see Appendix A.1). The quasi-periodic pulsations occur in Saturn's outer magnetosphere and are characterized by a periodicity ranging from 40 to 90 min. The results reported in this chapter are in agreement with the results from the initial survey performed by Roussos et al. (2016), although the current survey is based on a different selection method and an extended observation period. Moreover, further investigation has been performed here providing with richer information about the morphological properties of the hourly electron pulsations, their pitch angle distribution and their spatial distribution.

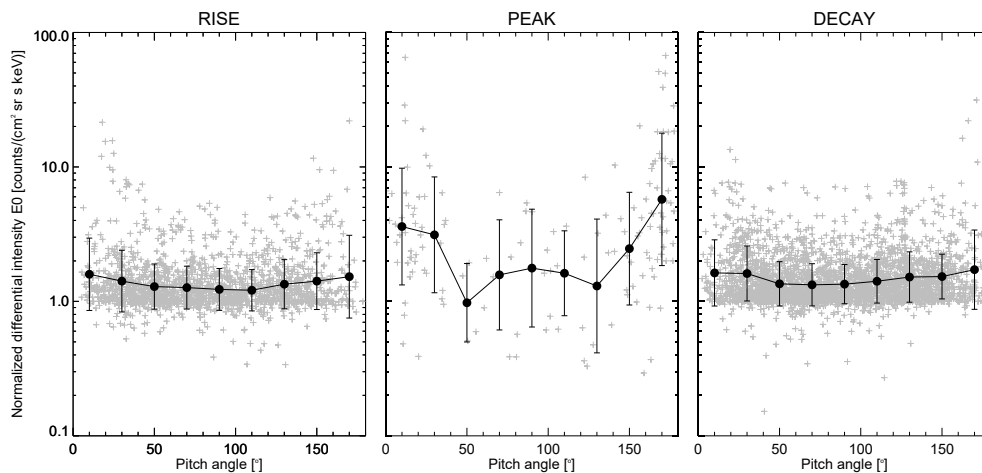


Figure 3.19: Pitch angle distribution of the rise (left), the peak (middle) and the decay (right) of the pulses for the E0 channel (110-365 keV). The intensity is normalized to one at the start of the pulse for the rise and at the end of the pulse for the decay. The intensity averaged on 20° pitch angle bins is drawn, as well as the standard deviation around the mean value. The pitch angle distribution of the peak is mainly field-aligned while the distribution of the rise and the decay phases is quasi-isotropic, except for a few events where it is also field-aligned. From Palmaerts et al. (2016a).

The quasi-periodic pulsations in energetic electron fluxes are observed in various regions of the Kronian magnetosphere, over a wide range of local times and latitudes. However, a local time asymmetry appears: when Cassini is in the dusk flank of the magnetosphere, a pulsed event is detected every ~ 4 days on average while the occurrence rate is one event every ~ 30 -50 days in the dawnside. Despite the global distribution of the electron pulsation events, the mean interpulse period of ~ 68 min does not show any trend with the local time, nor the duration of the events which is mostly ranging between 3 and 8 hours. The local time constancy of the pulsation morphological properties is unlikely compatible with a low-latitude source for the pulsed energetic electrons. Indeed, the low-latitude plasma dynamics present strong local time and temporal variations, as described in Section 1.2.4, which would create more spatial and temporal discrepancies than observed. Thus, the source of the electrons may be located in the high-latitude ionosphere or on magnetic field lines connected to the high latitudes. The local time independence of the pulsed event morphology indicates a common acceleration mechanism of the electrons for all the events.

However, the dawn-dusk asymmetry in the occurrence rate of the pulsed events suggests two distinct triggers for the electron acceleration. The observation frequency at dusk (1 event every ~ 4 days) is similar to timescales of internal processes in Saturn's magnetosphere (Rymer et al. 2013), whereas the frequency in the dawnside (1 event every ~ 30 -50 days) is closer to solar wind timescales. Hence, solar-wind induced storms triggering tail reconnection is a conceivable process for generating the dawnside events. The dusk-side events may be induced by internal plasma dynamics associated with the Vasyliūnas reconnection cycle (Section 1.2.4.4) or with multiple reconnection sites spread over the dusk sector. The existence of such dispersed reconnection sites at dusk has been sug-

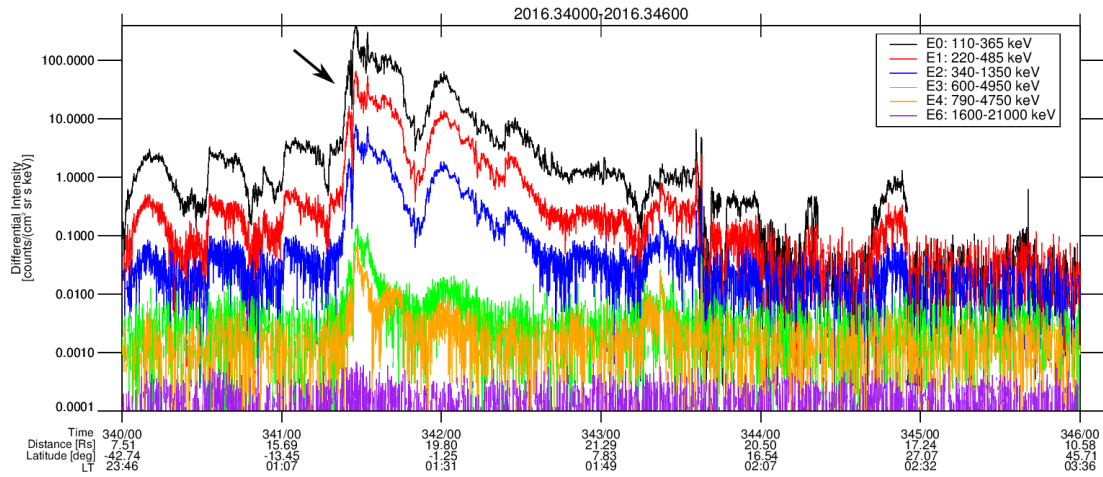


Figure 3.20: Strong acceleration event (arrow) detected by MIMI/LEMMS in the E0 to E4 channels while Cassini was in the postmidnight region.

gested by Delamere et al. (2015) after identifying in the MAG data the azimuthal bend back and bend forward of the magnetic field lines. The forward field line bending is related to empty flux tube transport following reconnection and can be then used as a tracer for reconnection. According to Delamere et al. (2015), many reconnection sites are distributed in the region where most of the quasi-periodic electron pulsations occur (15-21 LT). Moreover, in the Jovian magnetosphere, the source of pulsating X-ray auroral emissions is magnetically connected to the equatorial region extending from the prenoon to the postdusk sector (Kimura et al. 2016). In the same region, quasi-periodic bursts have been observed in the radio emissions, simultaneously with MeV electron pulsations (MacDowall et al. 1993, McKibben et al. 1993), as described in Section 1.4.2. Since most of the QP60 events are encountered between prenoon and postdusk, the same electron acceleration mechanism might take place at Jupiter and at Saturn. Finally, it cannot be excluded that Kelvin-Helmholtz instabilities at the magnetopause (Section 1.2.4.5) play a role in the generation of QP60 events, both at dawn and at dusk sides.

Recently, the MIMI/LEMMS sensor has detected particularly high flux of protons and energetic electrons in the post-midnight sector. This event, which started on day 341 of 2016, is shown in Figure 3.20. The large flux enhancement is apparent up to the E4 channel energy bandwidth (790-4750 keV), revealing a strong acceleration of electrons up to relativistic energies. The position of the event and the concurrent increase in the counts of magnetospheric ion species (O^+ , H_2^+ , O_2^+ , ...) measured by MIMI/CHEMS (see Section 2.3) are consistent with an acceleration caused by reconnection in the tail. It is then plausible that magnetic reconnection can energize the electrons up to MeV energies characterizing the hourly pulsed electron events.

The typical quasi-periodic electron pulsations present a sawtooth pattern: the growth time of the pulsations is shorter than the decay time. The sawtooth pattern characterizes also the 40-min energetic electron pulsations in the Jovian magnetosphere (Simpson et al. 1992). The sawtooth shape is more frequent as the energy increases. The statistical analysis of the rise and decay rates of the pulses reveals that the rates are larger at higher latitude. Energy dispersion of the electron flux in the LEMMS channels can be responsi-

ble of this observation. The signal rises and decays faster if all the electrons at the different energies within a channel arrive simultaneously. That happens when Cassini/LEMMS is closer to the electron source. Further away from the source, energy dispersion caused by drift motions (Section 1.2.4.1) has time to develop while the electrons at different energies are traveling till their detection by LEMMS: the most energetic electrons arrive first, softening the rise slope of the pulses. Hence, in addition to the local time constancy of the morphological properties, the higher growth and decay rate magnitudes at high latitude are consistent with a high-latitude acceleration region. The energy dispersion hypothesis can be validated by analyzing the MIMI/LEMMS “pulse-height-analysis” channels (see Section 2.3.1), which provide a higher energy resolution.

From the morphology analysis, a direct correlation has been revealed between the rise and decay rates and the peak intensity of the pulses. The slope of the rise/decay rate versus the peak intensity is the steepest in the E3 channel (Figure 3.15). At lower energies, the mixing of the pulsed electrons with other electron populations could smooth the pulses and thus the rise/decay rates. At higher energies, the noise level can affect the rate magnitudes.

The pitch angle distribution evolves along the pulsations, with a rather isotropic PAD for the growth and decay phases and an intensity peak generally pointing in the field-aligned direction (Figure 3.19), similarly to the electron beams depicted by Saur et al. (2006). Nevertheless, the event shown in Figure 3.17 illustrates that the quasi-periodic energetic electrons are distinct from the field-aligned electron beam population. In this particular event, the QP60 pulses (green rectangles) stop after ~ 03 UT whereas some field-aligned narrow peaks (red lines) survive. The field-aligned beams are unidirectional after ~ 03 UT and consequently they are residing along open field lines. The mixing between the pulsed electron population and the field-aligned population leads to an enhanced peak intensity of the hourly pulsations, especially at low energies. Therefore the field-aligned PAD of the pulsation peak (Figure 3.19) is due to this mixing between both electron populations.

Almost all the quasi-periodic electron injections reside on closed field lines, as revealed by using the method of Gurnett et al. (2010). In the study by Roussos et al. (2016), the mapping of the events based on a magnetic field model (Khurana et al. 2006) leads to the same conclusion for the duskside events. However, the authors stated that most of the dawn events reside either on open field lines or are located close to the open-closed field line boundary, such that their equatorial signature is located at large distances not sampled by Cassini. That may explain then the small number of QP60 detected in the dawnside equatorial plane. Due to the lack of pitch angle distribution at dawnside, only two dawn events have been considered in the analysis described here, such that no conclusion can be drawn for that local time sector. Hence, whether the ~ 1 -h electron pulsations observed at dawn are on closed or open field lines remains an outstanding question and will be discussed further in Chapter 5.

4 Coincident pulsations in the plasma wave and magnetic field

In the previous chapter, the hourly quasi-periodic electron pulsations have been thoroughly described. As already mentioned in Section 1.4.2, several studies have reported hourly pulsations in the magnetic field and in the plasma wave emissions simultaneously to pulsations in charged particle fluxes (e.g. Mitchell et al. (2009a), Badman et al. (2012a), Mitchell et al. (2016)). However, these studies are based on single events and the frequency of simultaneous pulsed signals in different Cassini observations and the mechanism generating them remain unknown. This chapter¹ describes the first statistical analysis of the signatures of the quasi-periodic ~ 1 -h electron injections (abbreviated in QP60) in the radio emissions and the magnetic field measurements.

4.1 Pulsed signatures in plasma wave data

The plasma wave data acquired by the RPWS instrument (described in Section 2.5) have been investigated for all the time intervals including pulsations in the energetic electron flux measured by LEMMS. Hence, the investigation is based on the list of the 720 pulsed events identified in the LEMMS data (see Chapter 3 and Appendix A.1). However, it should be noted that quasi-periodic radio bursts can be observed without corresponding electron pulsations in the LEMMS measurements. For example, intense bursts are present in the RPWS data on day 026/2008 while the electron fluxes are at the background level. On day 130/2008 too, Jinks et al. (2014) reported hourly pulsations in the auroral hiss (see Section 1.3.5) without LEMMS counterpart. Since the baseline of the current study is the hourly pulsations in the LEMMS energetic electron fluxes, a survey of all the RPWS quasi-periodic bursts has not been achieved here. Such a survey has been recently carried out by Carbary et al. (2016) and their findings will be discussed in section 4.3.

In the aforementioned studies revealing hourly pulsations in the plasma wave emissions, the pulsed signal has been always identified at low frequency, below 1.5 kHz. Therefore, the high frequency domain has not been considered in this survey.

1. The main results presented in this chapter have been published in Palmaerts, B., Roussos, E., Krupp, N., Kurth, W. S., Mitchell, D. G., Yates, J. N., 2016a, Statistical analysis and multi-instrument overview of the quasi-periodic 1-hour pulsations in Saturn's outer magnetosphere, *Icarus*, 271, 1-18.

4.1.1 Presence of pulsed signal in the radio emissions

The LEMMS pulsed electron events can be classified into three categories, depending on the presence of corresponding pulsed signature in the plasma wave data. An event is given as an example for each category in Figure 4.1. For 12% of the LEMMS events, the intensity of the radio emissions increases when the electron flux is enhanced (Figure 4.1a). These concomitant quasi-periodic radio bursts can extend over a wide range of frequencies (about two orders of magnitude) but are generally limited at frequencies lower than the electron cyclotron frequency (f_{ce} , indicated by a white line in Figure 4.1), in the auroral hiss. The event represented in Figure 3.1 belongs to this category. The second category includes the QP60 events with only one coincident pulse in the RPWS spectrogram. This pulse has a frequency extension limited at one order of magnitude (Figure 4.1b). This category made up of weak RPWS signatures includes 30% of the set of pulsed events. Finally, in most cases (58%), the plasma wave data do not exhibit any concurrent pulsed signature, like the one shown in Figure 4.1c.

Unlike the morphological properties of the electron pulsations, the spatial distribution of the three categories of radio signatures is not uniform. The spatial distribution is represented in the top panel of Figure 4.2, on a latitude-local time diagram similar to Figure 3.6. The color code indicates the category of each event: red for the QP60 with strong coincident signatures, green for the QP60 with weak signatures and blue for the events without RPWS signature. The analysis reveals that the strong coincident radio bursts (red dots) occur at all local times but mainly at high latitudes. It appears that strong coincident RPWS bursts are encountered where the electron cyclotron frequency is higher, as highlighted in the bottom panel of Figure 4.2 where the averaged f_{ce} for each event is given together with the category color. Since the electron cyclotron frequency is proportional to the magnetic field intensity (Section 1.2.4.1), coincident radio bursts are more probable to occur where the field strength is higher. No strong signatures have been identified between the end of 2009 and the beginning of 2012 because during this period the Cassini spacecraft was on low-latitude orbits. One exception has to be mentioned in mid-2010 when Cassini reached briefly a latitude of -22° . On the contrary, in 2008 and during the first half of 2009, Cassini was on high-latitude orbits close to the planet, with an intense magnetic field, favoring the strong signatures in the plasma wave data.

4.1.2 Characteristics of the signatures in the radio emissions

The first burst in a RPWS quasi-periodic pulsed signature can be occasionally observed before the first pulse in the LEMMS electron flux. The quasi-periodic radio bursts may also be observed over a longer time interval. Furthermore, for a small number of events, a continuous set of pulsations in the plasma wave emissions connects two distinct electron events, like in the example given in Figure 4.3. That implies a reduction of the total number of LEMMS events from 720 to 712 and an increase of the average number of pulses per event from 4.7 to 4.9. This modification in the list of events does not significantly affect the results of the statistical analysis reported in Chapter 3.

Simultaneous 40-min radio bursts and electron flux pulsations have been reported in Jupiter's magnetosphere, as previously mentioned in Section 1.4.2 (MacDowall et al. 1993). In addition to their longer period, Saturn's radio bursts differ from their equivalent

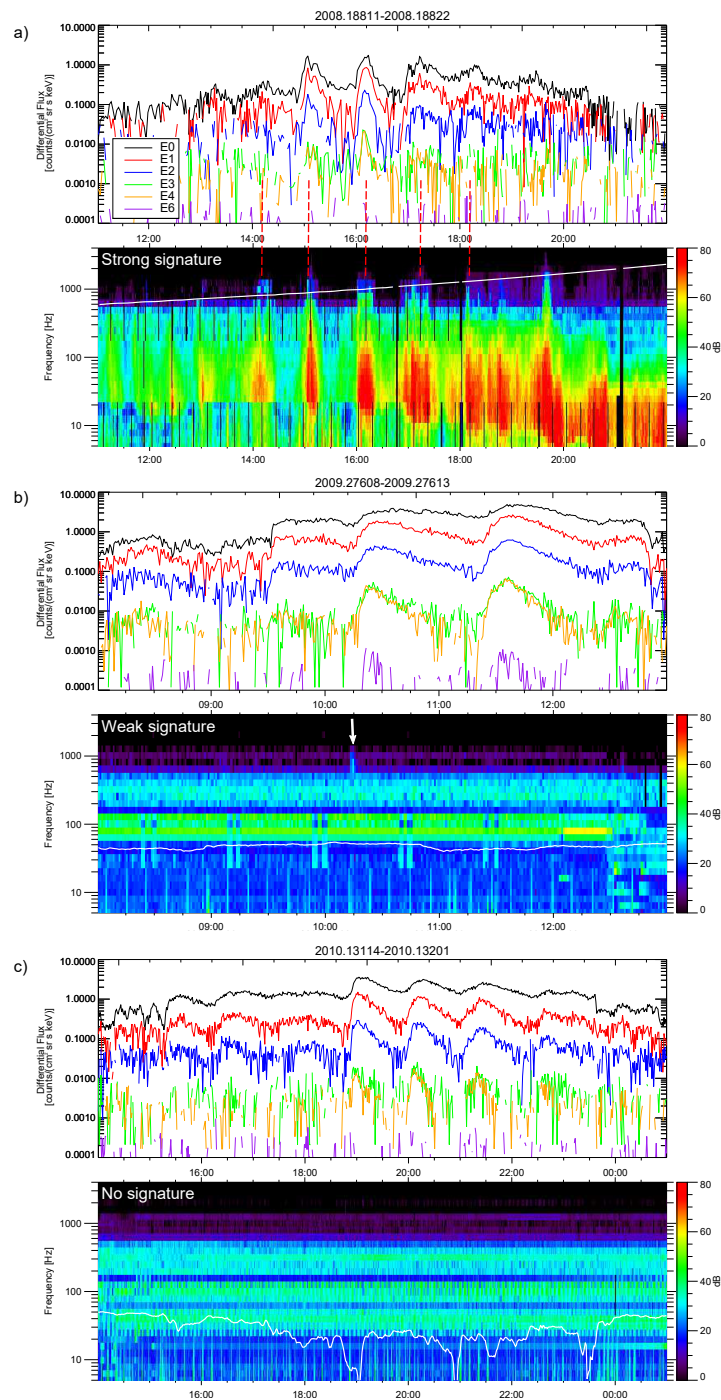


Figure 4.1: Examples of quasi-periodic electron events for each category of coincident signature in the plasma wave data. The differential intensities of energetic electrons from the LEMMS channels E0 to E4 and E6 are displayed above the concomitant RPWS electric field spectrogram. The white line on the RPWS spectrogram indicates the electron cyclotron frequency. (a) Event on day 188 of 2008 with strong coincident pulsations in the plasma wave data, (b) event on day 276 of 2009 with a weak coincident signature in the plasma wave data (indicated by the white arrow) and (c) event on day 131 of 2010 with no corresponding signature in the RPWS data.

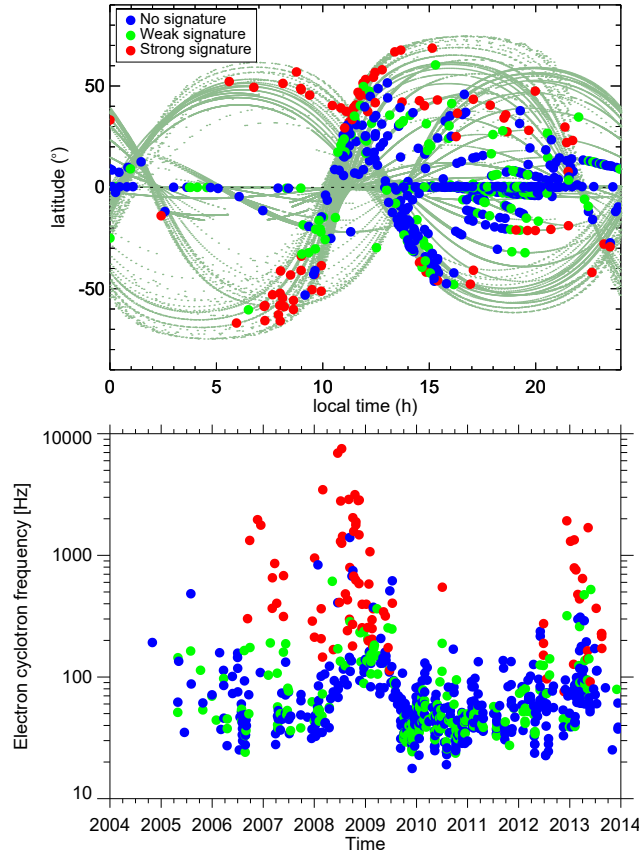


Figure 4.2: Top panel: Location of the pulsed events (points) detected by LEMMS in a latitude-local time diagram with the color indicating the presence of coincident signatures in plasma wave emissions (RPWS data above 5 Hz): red for strong multiple coincident pulsations, green for weak single pulse and blue for no concomitant signature. The green curves are the orbits of Cassini. Bottom panel: Averaged electron cyclotron frequency during each event as a function of the time. The color code is the same. From Palmaerts et al. (2016a).

at Jupiter by a longer duration: almost one hour while the Jovian radio bursts last only 5 to 10 minutes.

As already mentioned before, plasma wave pulsations always appear below the electron cyclotron frequency, in the auroral hiss emission frequency range. In the whole set of LEMMS events considered here, the lowest value of f_{ce} for an event with strong pulsed signatures in the plasma wave data is 84 Hz. One can consider that with a lower f_{ce} , the auroral hiss is not observable and no pulsations can be triggered. Nevertheless, for 418 time intervals with LEMMS pulsations, the electron cyclotron frequency exceeds 84 Hz but only 20% of them display coincident plasma wave pulsations. Hence the observation of the auroral hiss does not imply necessarily the observation of pulsations.

In almost 75% of the strong coincident signatures in the plasma wave emissions, the radio emission bursts extend to frequencies higher than the electron cyclotron frequency. This is apparent for the most intense radio burst at $\sim 00:30$ UT in the event represented in Figure 3.1, as well as in Figure 4.1a and Figure 4.3. Above the f_{ce} frequency, the

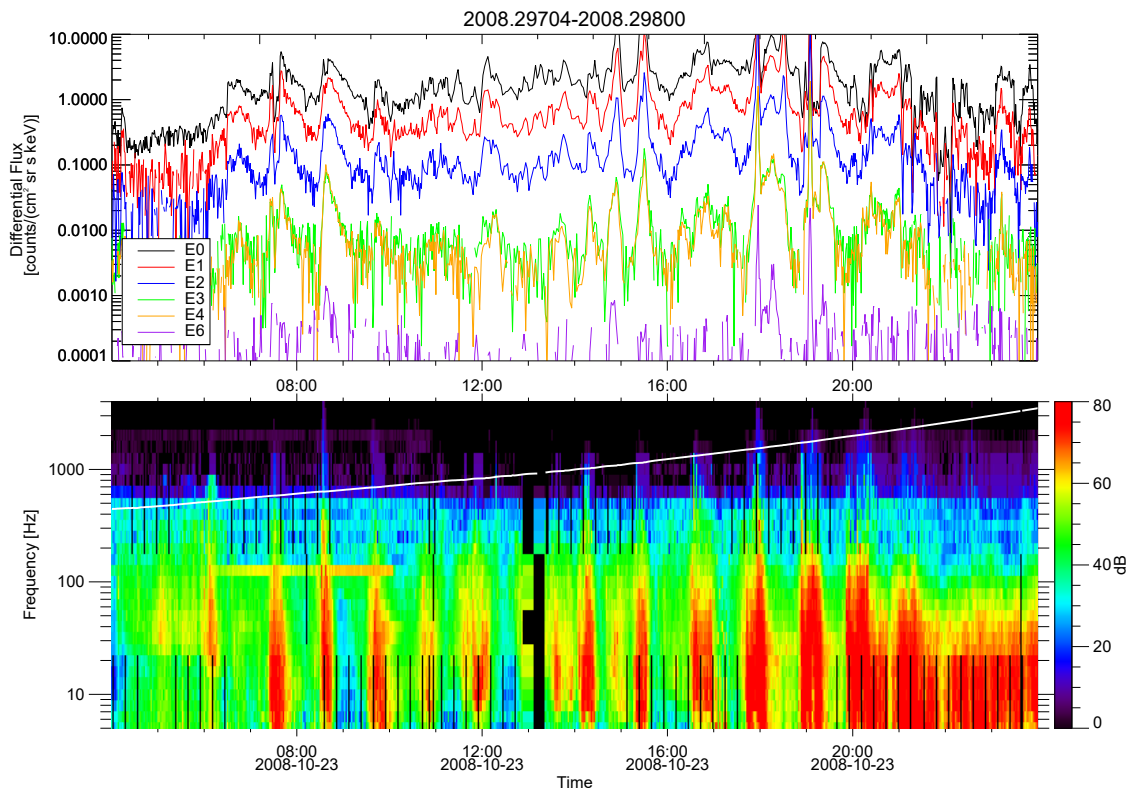


Figure 4.3: Example of two quasi-periodic electron events on day 297 of 2008 which are revealed to be connected by their coincident pulsed radio signatures. The differential intensities of energetic electrons from the LEMMS channels E0 to E4 and E6 are displayed above the simultaneous RPWS electric field spectrogram. The white line on the RPWS spectrogram indicates the electron cyclotron frequency.

auroral hiss and, consequently the whistler mode, does not exist. Hence, another mode prevails for the high frequency pulsations. An electrostatic mode is plausible since the observed extension of the pulsations at higher frequencies, running up from the bursts in the auroral hiss, is similar to the broadband electrostatic noise (BEN) reported at Earth and at Jupiter. In the terrestrial magnetosphere, the broadband electrostatic noise has been identified at high latitude (Gurnett and Frank 1977), at the edges of the plasma sheet in the magnetotail (Gurnett et al. 1976) and in the magnetopause current layer (Gurnett et al. 1979). In the former two cases, the BEN is connected with the field-aligned currents generated at the plasma sheet boundaries and its intensity is proportional to the auroral activity. In Jupiter’s magnetosphere, the same relation exists between the BEN and field-aligned currents connecting the ionosphere to the edges of the plasma sheet (Barbosa et al. 1981). It should be noted that the emissions above f_{ce} may be also explained by Doppler shift of the frequencies. The relative motion of the Cassini spacecraft and the surrounding plasma when the whistler-mode waves are in resonance with the local electron plasma frequency can indeed cause a Doppler shift (Kopf et al. 2010). In that case, the radio signal at high frequency could be below the electron cyclotron frequency in the plasma rest frame.

4.2 Pulsed signatures in the magnetic field

In the previous single-case studies of the 1-hour electron injections, the coincidence between the periodic electron flux enhancements and fluctuations in the magnetic field has been highlighted (Badman et al. 2012a, Mitchell et al. 2009a, 2016). This correlation with some components of the magnetic field can also be observed in Figure 3.1. However, Roussos et al. (2016) showed several examples of ~ 1 -h quasi-periodic electron events with no corresponding periodic variations of the magnetic field. In order to have a better knowledge of the occurrence of correlated periodic signatures in the magnetic field, the response of the three magnetic field spherical components (B_r , B_θ , B_ϕ) has been investigated for all the LEMMS electron events. The analysis has been performed after removing the overall trend of the magnetic field variation.

The analysis reveals that at least two coincident pulsations are observed in the radial component of the magnetic field (B_r) for 14% of the electron events, in the polar component (B_θ) for 11% of the events and 21% of the events exhibit simultaneous fluctuations in the azimuthal component (B_ϕ). Contrary to the signatures in the plasma wave emissions, the pulsed signatures in the magnetic field are uniformly distributed inside the magnetosphere. The distribution in the equatorial plane of the signatures in the B_ϕ , B_r and B_θ components is given in the upper panels of Figure 4.4. The orange dots represent the LEMMS events with at least two correlated fluctuations in the magnetic field. In addition, the lower panel of Figure 4.4 shows the distribution of the B_ϕ coincident signatures in a latitude-local time diagram. The red dots indicate the events with simultaneous pulsations in the electron fluxes, in the azimuthal component of the magnetic field and in the plasma wave emissions. At high latitude, the polar and the radial components could be meaningless since they are combinations of the mean field components. It would be interesting to convert B_r and B_θ into a more appropriate coordinate system, called the Mean Field-Aligned coordinate system (Kleindienst et al. 2009). This is beyond the scope of this study focused on the energetic electron pulsations.

4.3 Discussion

In this chapter, it has been shown that the quasi-periodic injections of relativistic electrons in Saturn's outer magnetosphere can have corresponding pulsed signals in other magnetospheric measurements. For most of the high-latitude pulsed electron events, the auroral hiss exhibits correlated strong bursts. The auroral hiss is a radio emission generated by electron beams traveling along magnetic field lines associated with the auroral emissions (Kopf et al. 2010). The existence of clear and simultaneous ~ 1 -h pulsations in the intensity of the auroral hiss at all local times suggests that the source of the pulsed phenomenon resides in the high-latitude magnetosphere and might be connected to the auroral region. The scenario of a high-latitude acceleration of the electrons is supported by the aforementioned previous studies of the 1-hour electron pulsations (Badman et al. 2012a, Mitchell et al. 2009a, Roussos et al. 2016). It is also consistent with the local time symmetry of the pulse morphology depicted in Chapter 3, as well as with the increased pulse growth and decay rates at high latitude.

It is noteworthy that many pulsed electron events are observed in a region with high

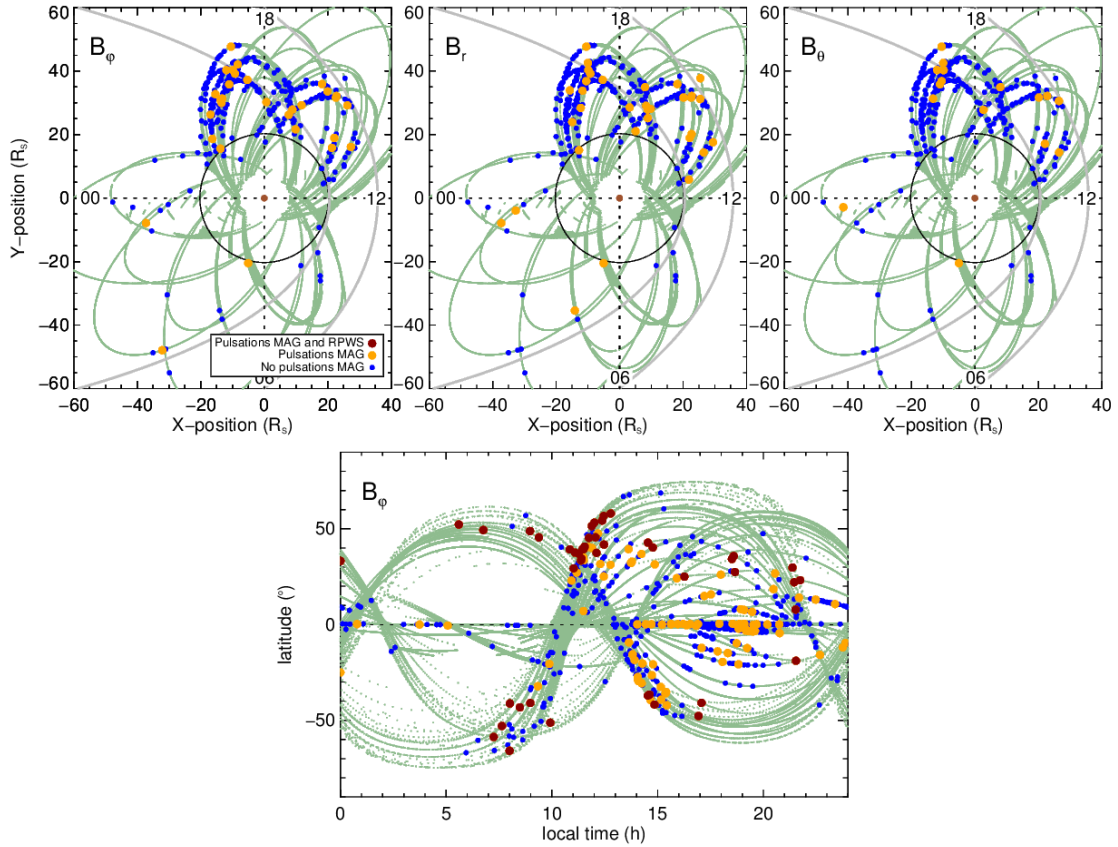


Figure 4.4: Top panels: Location of the pulsed events (points) detected by LEMMS and located within $2 R_S$ from the equatorial plane with the color indicating the presence of coincident signatures in the magnetic field data. For the events marked by an orange point, at least two coincident pulsations are observed in the B_ϕ (left panel), B_r (middle) or B_θ (right) component. Additionally to the pulsations in the MAG data, strong concomitant signatures are also observed in the plasma wave data for the events in red. The green curves are the orbits of Cassini. Titan's orbit (black circle) and two simulated magnetopause locations (gray lines) are drawn. Bottom panel: Location of the pulsed events (points) detected by LEMMS in a latitude-local time diagram with the same color code indicating coincident pulsations in the B_ϕ component of the magnetic field. From Palmaerts et al. (2016a).

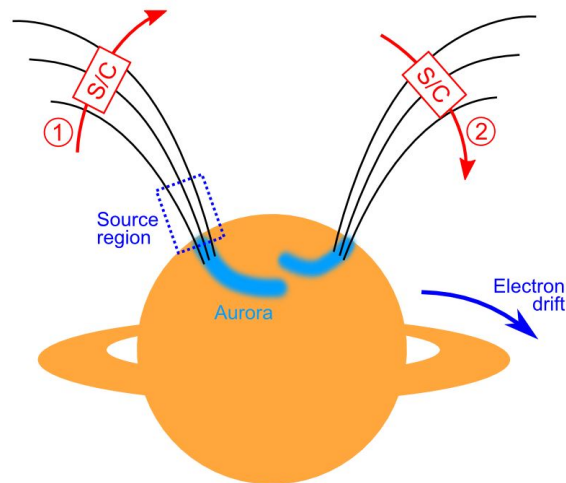


Figure 4.5: Sketch representing two observation situations of Cassini. In situation 1, the spacecraft is crossing magnetic field lines connected to the source of pulsed energetic electrons. Pulsations are observed in both the electron fluxes and the auroral hiss. In situation 2, Cassini is on field lines not connected to the source region. Auroral hiss is observed without pulsations. Pulsations can be detected by LEMMS if electrons have drifted from the source region.

f_{ce} but without corresponding quasi-periodic bursts in the plasma wave data (Figure 4.2). A pulsed signal is observed in the RPWS data likely only when the Cassini spacecraft is crossing magnetic field lines connected to the source of the pulsed energetic electrons. This is schematically represented in Figure 4.5. In the situation 1, Cassini is located on field lines mapping to the source region of the electrons and is detecting pulsations in the electron flux and in the auroral hiss. In the situation 2, the spacecraft is crossing flux tubes not connected to the electron source and the auroral hiss can be observed without pulsed intensity. Since the accelerated electrons are injected on closed field lines, they can drift and be observed away from the source region field lines, unlike the plasma waves. Therefore, pulsations in the LEMMS measurements can be identified also in the situation 2.

The investigation of simultaneous quasi-periodic fluctuations revealed that, for one event over five, correlated perturbations are identified in the azimuthal component of the magnetic field. Perturbations in B_ϕ are the signatures of the crossing by the spacecraft of currents aligned with the magnetic field lines. The field-aligned currents are part of a current system associated with transfer of momentum between the azimuthal plasma flow in the magnetosphere and the neutral atmosphere (Bunce et al. 2008, Talboys et al. 2009a). By Ampère's law, the currents of this magnetosphere-ionosphere current system produce magnetic field perturbations transverse to the field, i.e. in the azimuthal direction, such that the field lines are bent in a leading or lagging configuration, depending whether the magnetospheric azimuthal plasma flow is super- or subcorotational (Talboys et al. 2009b, 2011).

In previous single-case studies, the quasi-periodic hourly B_ϕ fluctuations have been associated with downward current regions connected to the auroral emissions (Badman

et al. 2012a, Mitchell et al. 2009a). This interpretation is consistent with the observation of coincident pulsations in the auroral hiss. The event in Figure 3.1 also exhibits quasi-periodic concurrent drops in B_ϕ revealing downward field-aligned currents. Nevertheless, for the majority of the quasi-periodic electron injections, no signatures are found in B_ϕ and consequently the downward currents cannot be invoked as a direct interpretation. Furthermore, following this scenario, B_ϕ signatures are expected to be observed only in the high-latitude regions connected to the auroral zone whereas they are also observed at low latitude (Figure 4.4). The relation between the electron pulsations and most of the concomitant magnetic field fluctuations remains thus unexplained.

In the RPWS data as well as in the magnetic field measurements, ~ 1 -h quasi-periodic pulsations can be observed without counterpart in the LEMMS energetic electron measurements. Since LEMMS remained the baseline instrument of the survey described here, no further investigation of the RPWS and MAG pulsed events has been achieved. Carbary et al. (2016) performed a survey of the ~ 1 -h quasi-periodic oscillations of the plasma wave at ~ 100 Hz measured by the RPWS instrument. They obtained similar results: the ~ 1 -h periodic events in the radio emissions are observed throughout the magnetosphere but preferably at high latitude, where the auroral hiss is observed. The mean period of the plasma wave pulsations is 65.3 ± 20.7 min, similar to the mean period of the LEMMS pulsations and this period does not show any correlation with local time or latitude. However, contrary to the present investigation of RPWS pulsations based on the LEMMS pulsed events, Carbary et al. (2016) noticed that, considering the distribution of events normalized by the spacecraft trajectory sampling, most of the RPWS pulsed events occur between dusk and midnight.

Carbary et al. (2016) explained the period of ~ 65 min observed in the radio emissions by the transit time of the Alfvén waves (Section 1.2.4.1) between the two hemispheres. The interhemispheric motion of Alfvén waves could possibly induce the ~ 1 -h interpulse period characterizing the electron pulsations described in Chapter 3. In the Earth's magnetosphere, it appears that the interhemispheric Alfvén wave transit time coincides with the typical 8-min time between two consecutive flux transfer events (Kuo et al. 1995, Bunce et al. 2004) which are generated by reconnection pulses at the magnetopause (Russell and Elphic 1978, Wild et al. 2001). Hence, if the hourly electron pulsations are triggered by magnetopause reconnection, the Alfvén transit timescale may determine the periodicity.

The Alfvén wave transit time depends on the plasma density. In their model, Carbary et al. (2016) obtained the particular period of ~ 65 min by considering only a water group W^+ plasma and at L-shells greater than $19 R_S$. By considering a plasma composed of protons H^+ , which are dominant in the outer magnetosphere (Thomsen et al. 2010), the calculated Alfvén wave transit time do not exceed 20 min. The interhemispheric Alfvén wave transit time has been also calculated by Roussos et al. (2016) using the K06 magnetic field model (Khurana et al. 2006). They could retrieve the period of ~ 60 min but they showed that this transit time varies significantly with the chosen value of the mean plasma density along the field line. Since the plasma density is not uniform in the magnetosphere (Thomsen et al. 2010), the Alfvén transit time is not constant throughout the magnetosphere unlike the relative constancy of the electron and plasma wave pulsation period. Furthermore, for any given plasma density, the transit time is different between distinct local time sectors (Roussos et al. 2016). Hence, the Alfvén wave transit time does not seem a plausible explanation for the periodicity of the electron injections.

However, using measurements by the Cassini magnetometer, Yates et al. (2016) interpreted the nature of Saturn's quasi-periodic ~ 1 -h fluctuations and their relation to the Alfvén waves differently. They found that the transverse magnetic field ~ 1 -h fluctuations at high latitude are organized in wave packets which recur periodically, following the northern magnetic oscillation phase described in Section 1.4 (Andrews et al. 2012, Provan et al. 2012). By means of a simple magnetospheric model, they argued that the observed magnetic pulsations represent second harmonic Alfvénic waves standing between the ionospheres of each hemisphere in the outer magnetosphere of Saturn. While the first harmonic, i.e. the transit time of Alfvénic waves between both hemispheres, decreases with radial distance because of its dependence with the plasma density, the second harmonic remains relatively constant beyond $15 R_S$. The temporal change of the density in the equatorial plasma sheet can explain why the period of the pulsations is not fixed at 60 or 68 min but oscillates around these values. Hence, the characteristic period of the electron pulsations and, by extension, of the hourly pulsations observed in Saturn's outer magnetosphere, might be induced by the second harmonic Alfvén waves. However, the mechanism producing the Alfvén waves is still unclear. Additionally, some pulsed electron events are located on open field lines (as discussed in Section 5.3.2) for which the Alfvén wave scenario does not apply. Consequently, the second harmonic Alfvénic wave timescale cannot be invoked as a global explanation for the 60-min characteristic period of the electron pulsations.

5 Pulsations in the polar cusp aurora

The analysis of the quasi-periodic hourly pulsations in the energetic electron fluxes and the concurrent pulsations in the auroral hiss provided some results suggesting a high-latitude source for the pulsed electrons. The source may also be connected to the auroral region and the associated processes. Therefore it is interesting to investigate whether there are pulsating auroral emissions at Saturn with a periodicity of around 1 hour. As depicted in Section 1.3, the auroral emissions provide information about the magnetospheric processes all around the planet. The electrons producing the auroral emissions are magnetically connected to these processes, and thus a variation in the magnetospheric dynamics could be transcribed, for instance, in a variation of the shape or the brightness of some auroral features. Furthermore, the auroral images provide a global view of the magnetospheric dynamics, contrary to the in-situ data for which a parameter is known only at a certain time and at a certain place. In-situ measurements do not allow to infer neither the spatial extension nor the lifetime of the pulsed electron region. A multi-instrument approach, in particular by using auroral imaging, would help to understand the mechanism triggering the electron hourly pulsations.

Previous studies have already reported some ~ 1 -h quasi-periodic pulsations in auroral structures called bifurcations, as mentioned in Section 1.4.2 (Radioti et al. 2013b, Mitchell et al. 2016). This chapter¹ is devoted to the analysis of another auroral feature, located poleward of the main emission in the dawnside, which exhibits also quasi-periodic hourly brightness pulsations.

5.1 Observation of an isolated polar auroral emission

In this chapter, images of Saturn's auroral emissions at Saturn are presented. These images have been obtained with the *Ultraviolet Imaging Spectrograph* (UVIS) on board the Cassini spacecraft (see Section 2.4), using the Far-UV channel (111-191 nm) of the instrument (Esposito et al. 2004). The auroral region was scanned by the narrow low-resolution slit, resulting in 64 spatial pixels of 1 mrad (along the slit) by 1.5 mrad (across the slit). All the UVIS observing sequences shown in this chapter have been acquired while Cassini was sufficiently distant from Saturn to allow a complete scan of the whole auroral region. As explained in Section 2.4, the scan through this region takes at least a dozens of minutes, so that the different rows of the obtained image suffer from a time

1. The main results presented in this chapter have been published in Palmaerts, B., Radioti A. Roussos, E., Grodent, D., Gérard, J.-C., Krupp, N., Mitchell, D. G., 2016b, Pulsations of the polar cusp aurora at Saturn, *Journal of Geophysical Research: Space Physics*, 121, 11,952-11,963.

delay compared to the first row. Following the method described by Grodent et al. (2011), the auroral “pseudoimages” are projected onto a polar plane fixed in local time which facilitates the tracking of the auroral features. In the projection procedure, it is assumed that the auroral emissions peak at 1100 km above the planet surface, in agreement with the observations (Gérard et al. 2009). Since the photometry is not preserved by the projection process, the aurora intensity indicated in the following figures can only be used as a proxy.

The polar projections of the 15 pseudoimages acquired by the UVIS spectrograph on day 128 of 2013 (8 May) are given in Figure 5.1. During this sequence, the southern hemisphere was observed by Cassini from a planetocentric latitude changing from -39.9° to -42.6° and an altitude decreasing from $19.7 R_S$ to $19.1 R_S$. The projections are displayed like if the auroral emissions are seen through the planet from the north pole. The direction of the Sun is toward the bottom of the projections. The sequence starts at 01:52 UT and ends more than five hours later, at 07:12 UT (time at the end of the acquisition of the last image). The acquisition duration of each image is ~ 21.5 min, for a total duration of 320 min. The top of each frame of Figure 5.1 gives information about the starting recording time as well as the elapsed time since the start of the sequence.

The trajectory of Cassini during the period covering two days before and after the UVIS observation time has been magnetically mapped to the ionosphere using the internal field model of Dougherty et al. (2005) combined with the ring current model of Bunce et al. (2007). For the mapping procedure, a magnetopause standoff distance of $22 R_S$ has been considered, as well as a half-thickness of the current sheet of $2.5 R_S$. The ionospheric footprint of the spacecraft trajectory is drawn in white on the enlarged first frame. The red part, near the letter “C” and present on each frame, indicates the mapped footprint of Cassini during the UVIS sequence.

The main auroral oval (see Section 1.3.1), albeit faint on the dawnside during the first hour, is apparent during the whole auroral observing sequence. A bright spot (circled in yellow on the first frame) is observed a few degrees in latitude poleward of the main oval before local noon. Although the spot size and brightness vary throughout the sequence, its position remains fixed.

In order to track the local time position and the brightness evolution of the polar auroral spot, a keogram has been built (upper panel of Figure 5.2). The keogram gives the intensity of the auroral emissions averaged over the colatitude range from 7° to 14° (indicated by dashed circles on the projections in Figure 5.1), as a function of local time and time along the sequence. In the keogram, the isolated auroral emission highlighted by the yellow circle in Figure 5.1 corresponds to the emission roughly static in local time at around 1030 LT. The keogram clearly shows that the brightness of this auroral spot pulses during the UVIS observation. At 13 LT, a particularly bright spot is visible in the keogram and in Figure 5.1 at 06:09 UT. Since this auroral feature is located at higher latitude and later in local time than the prenoon isolated auroral emission discussed here, it has not been considered in the present analysis.

In the lower panel of Figure 5.2, the brightness curve of the high-latitude auroral spot has been built by averaging the intensity between 9 and 12 LT corresponding to the local time sector containing the high-latitude spot (dashed lines on the keogram). A periodic brightening of this auroral structure is revealed with an intensity peak every three UVIS pseudoimages. That corresponds to a periodicity of ~ 65 min. Contrary to the pulsations in the LEMMS electron fluxes, the exact period of the auroral spot brightening cannot be

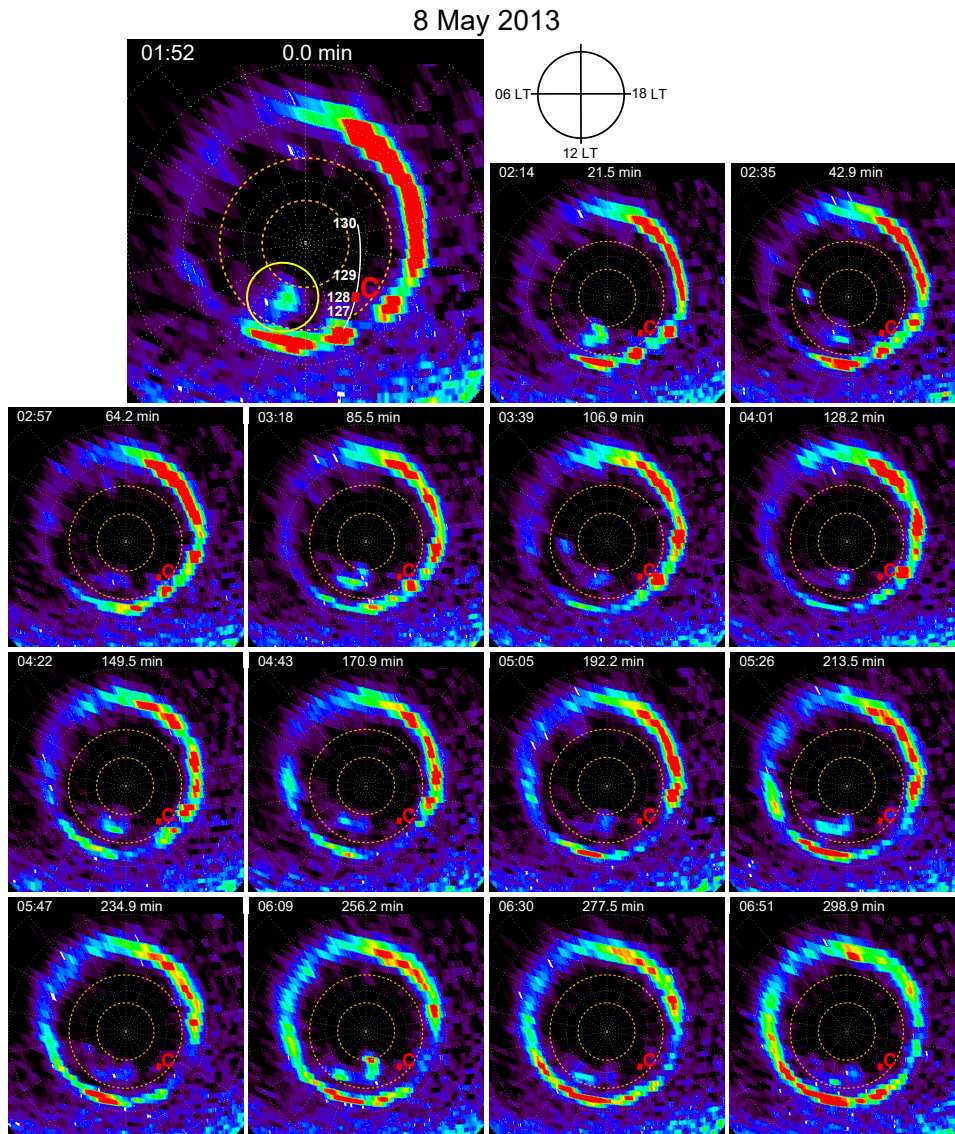


Figure 5.1: Sequence of polar projections of UVIS pseudoimages of the south FUV aurora, taken on May 8, 2013 (DOY 128) from 01:52 UT to 07:12 UT. The direction of the Sun (12 LT) is towards the bottom of the images and dusk (18 LT) to the right. The start of acquisition time in UT is given on the top of each frame as well as the elapsed time since the start of the sequence. On the first frame, the magnetically mapped Cassini trajectory is drawn in white for the period of four days around the UVIS sequence and the red part, close to the letter “C”, corresponds to the period covered by the UVIS sequence. The high-latitude auroral spot discussed in the text is surrounded by a yellow circle in the first frame. Dashed orange circles indicate the colatitude 7° and 14° , colatitude range used for the keogram in Figure 5.2. From Palmaerts et al. (2016b).

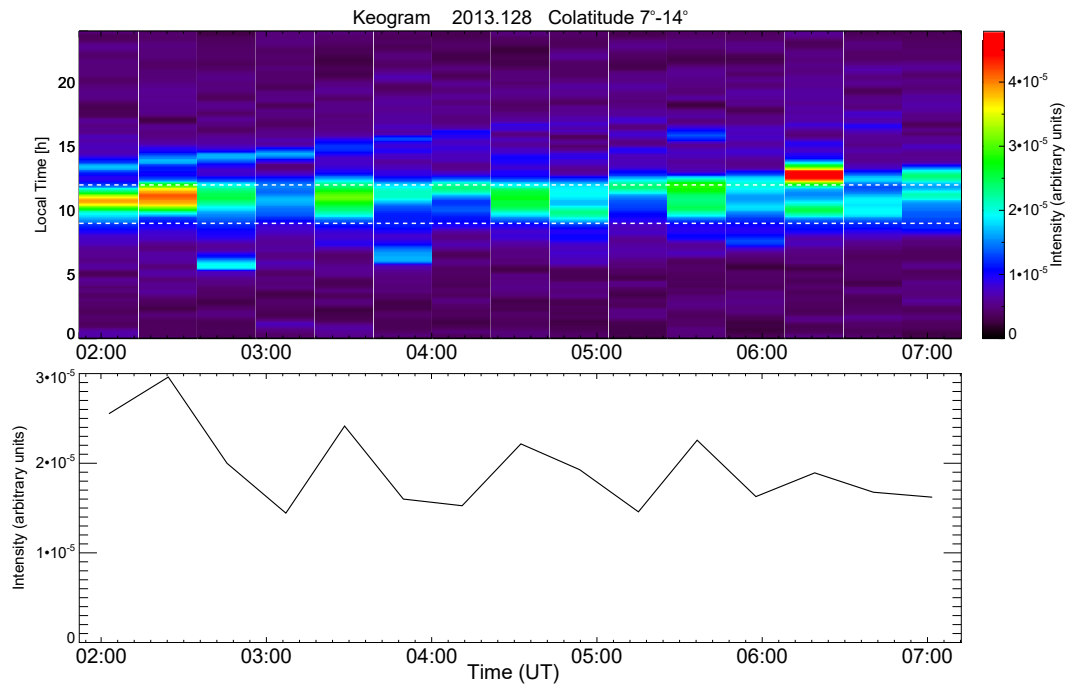


Figure 5.2: Upper panel: Keogram of intensity for the UVIS image sequence of May 8, 2013, as function of time and local time, built by averaging the brightness between 7° and 14° colatitude. Lower panel: Intensity average of the keogram between 9 and 12 LT (dashed lines drawn on the keogram). From Palmaerts et al. (2016b).

inferred due to the acquisition duration of every single UVIS image (21.5 min). However, it is worth to note that the inferred frequency of the brightening is smaller than the Nyquist frequency of the intensity sampling.

In order to constrain the properties and the frequency of the pulsating high-latitude auroral spot, other observations have been searched. The UVIS database includes only 15 auroral imaging sequences having an appropriate temporal resolution (at least three images per hour during the sequence) and duration (more than 90 min). Nevertheless, in addition to the observation depicted before, four other sequences with isolated polar emissions have been identified. For all the examples, the brightness of the auroral spot exhibits quasi-periodic variations. By taking into account the total duration of the 15 UVIS sequences, the inferred occurrence probability of the pulsating auroral spot is 29.6% for the images of the northern hemisphere aurorae and 22.7% for the southern aurora images.

In Figure 5.3, a snapshot of each of the four sequences is reproduced and the auroral spot is indicated by a yellow arrow. In all the cases, the isolated auroral emission is observed in the prenoon sector poleward of the main oval, in the latitude range from 79° to 87° . Its brightness evolution has been analyzed by means of a keogram as previously explained. It is noteworthy that, for these four sequences, the acquisition time for every single image is shorter than in the first example given in Figures 5.1 and 5.2 and thus provides a better sampling of the auroral spot intensity. The brightness curve is given on the right panels of Figure 5.3. In the long auroral imaging sequence acquired by

5.1 Observation of an isolated polar auroral emission

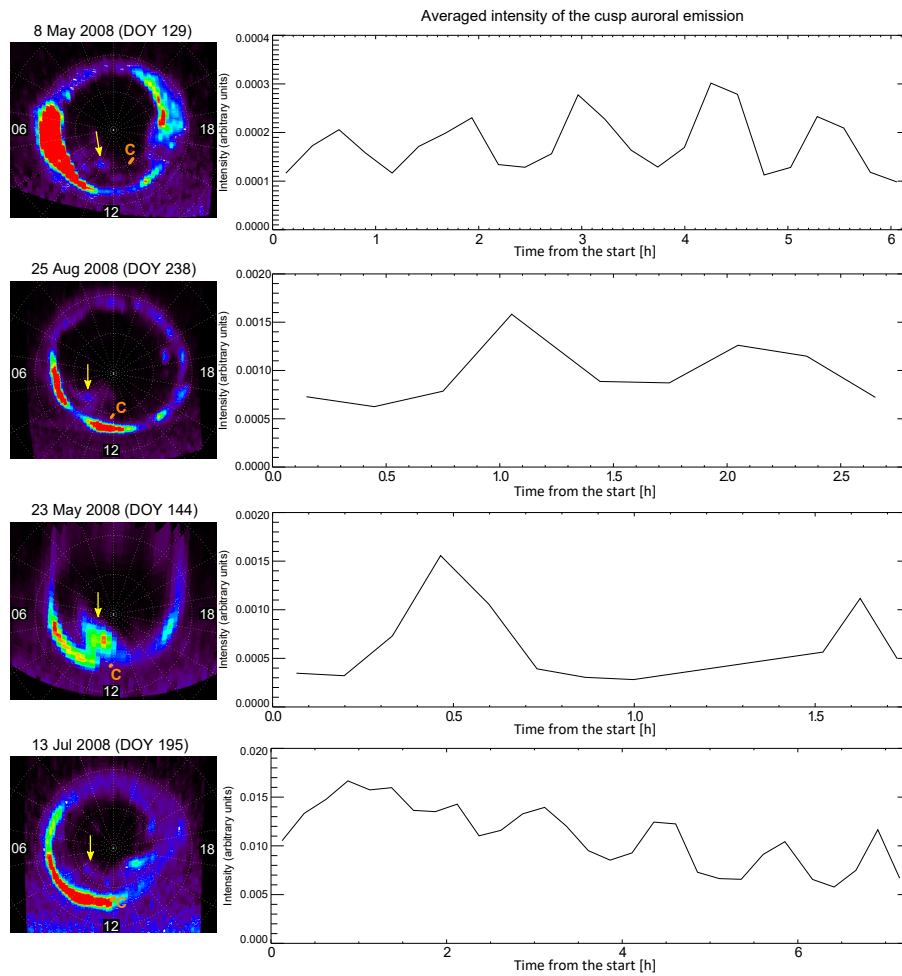


Figure 5.3: Four examples of UVIS observations of pulsating isolated polar emissions in the northern hemisphere. Left: Snapshots of the observation sequences with the polar auroral spot indicated by a yellow arrow. The magnetically mapped position of Cassini is indicated with an orange line, close to the letter “C”. Right: Brightness of the polar auroral spot along the sequence. From Palmaerts et al. (2016b).

UVIS on day 129 of 2008, the auroral spot pulses, as reported by Mitchell et al. (2016), with a periodicity of ~ 70 min. The second observation in Figure 5.3 was on day 238 of 2008 when the auroral spot pulses twice during a ~ 3 h-long UVIS sequence. The brightness peaks are separated by around 60 min. On day 144 of 2008, the intensity of the isolated auroral feature peaks twice, around 70 min apart. This observation presents the particularity that the auroral spot is connected to the main emission and its peak brightness is as high as the brightness of the main emission. The last example in Figure 5.3 was identified on day 195 of 2008. The auroral spot appears 2.5 hours after the start of the UVIS observation and directly starts pulsating. Simultaneously, in the dusk local time sector, a bifurcation is moving towards the nightside. From the five examples of isolated high-latitude auroral emissions identified, it can be concluded that the brightness of the spot varies with a periodicity ranging from 60 to 70 min.

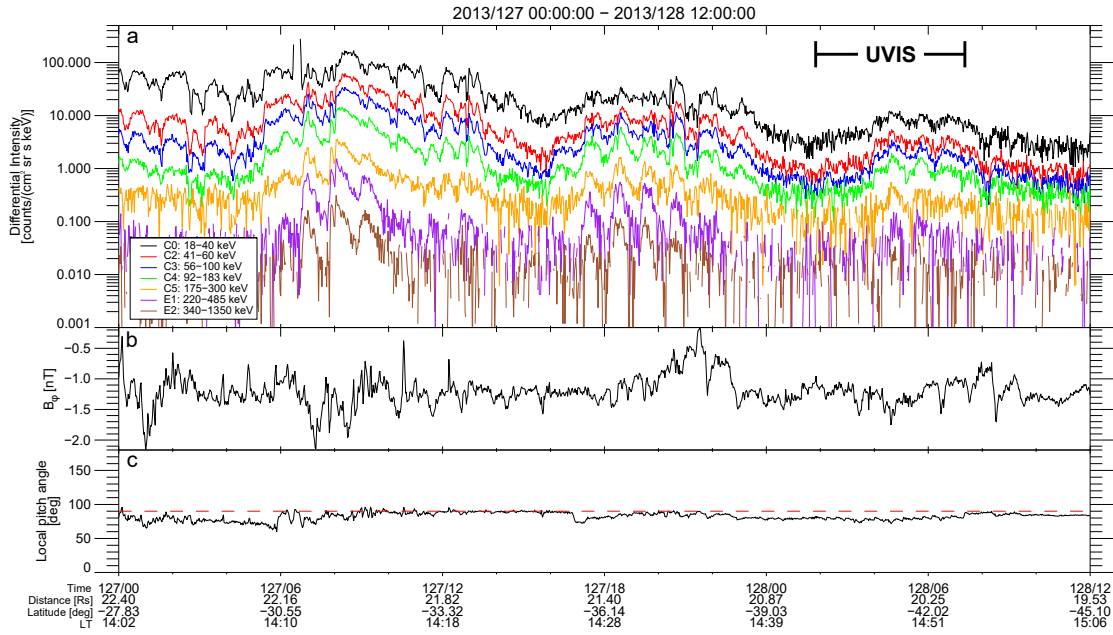


Figure 5.4: Cassini in-situ observations on days 127 and 128 of 2013. Time series plots of (a) the differential intensities of electrons from different Cassini/LEMMS channels between 18 and 1350 keV, (b) the azimuthal component of the magnetic field measured with Cassini/MAG, and (c) the local pitch angle of the particles entering the LEMMS High Energy Telescope. The time interval corresponding to the UVIS observation sequence presented in Figure 5.1 is indicated. From Palmaerts et al. (2016b).

5.2 In-situ measurements during auroral observations

While the auroral emissions were in the field-of-view of the UVIS spectrograph, the Cassini spacecraft was crossing magnetic field lines directly connected to the auroral region. Cassini instruments can thus provide information about these auroral flux tubes and the particles traveling along them. During the event reported by Mitchell et al. (2016), quasi-periodic fluctuations were observed in the magnetic field and the electron flux simultaneously to the brightness pulsations in the auroral emissions despite Cassini was not located on field lines directly connected to the pulsed auroral features. In the light of this previous study, the measurements of the electron flux and the magnetic field during the observations of the pulsating polar auroral spot are presented in this section.

The electron intensities have been analyzed using the MIMI/LEMMS measurements. Seven electron rate channels have been considered: C0, C2 to C5, E1 and E2 (see Table 2.2). The electron measurements in these channels are given in Figure 5.4a for the time interval from day 127 of 2013 at 00 UT till day 128 at 12 UT. The interval corresponding to the UVIS sequence presented in Figure 5.1 is indicated at the top of the panel. The second panel of Figure 5.4 presents the azimuthal component of the magnetic field measured by the Cassini magnetometer. Finally, the local pitch angle for the E-channel electrons (entering the LEMMS High Energy Telescope) is displayed in Figure 5.4c. The pitch angle of the C-channel electrons is the supplementary angle of the E-channel pitch angle ($PA_{LET} = 180^\circ - PA_{HET}$).

Simultaneously to UVIS observation of the pulsed auroral spot, pulsations are apparent in the electron intensities at energies from 18 keV to beyond 200 keV. A Lomb-Scargle analysis indicates that these pulsations have an interpulse period of 60 min, similar to the periodicity of the auroral spot brightening. The primary electrons precipitating in Saturn's ionosphere and producing the H₂ aurora in the region of the pulsed spot have an energy estimated between 6 and 50 keV (Gustin et al. 2017). This energy range corresponds to the LEMMS C0 and C2 channels in Figure 5.4. However, during UVIS observations, LEMMS was pointing perpendicularly to the field lines, as shown by the pitch angle in Figure 5.4c, implying that the detected pulsed electrons cannot be directly associated with the pulsed high-latitude auroral spot. Moreover, the magnetically mapped Cassini position in the ionosphere (indicated in Figure 5.1) shows that the flux tubes crossed by the spacecraft are not related to the aurora spot.

During the same time interval, the magnetic azimuthal component presents some sharp fluctuations with a 60-min periodicity too. As already explained in Section 4.3, B_ϕ perturbations can be the signatures of the crossing of field-aligned currents. It is worth to note that these field-aligned currents are not the main FAC connected to the main auroral emission. Furthermore, if the electrons carrying these FAC precipitate in the ionosphere, they do not produce the high-latitude auroral spot, as indicated by the mapped position of Cassini in Figure 5.4.

Before the UVIS observing sequence, some other regular enhancements in the electron fluxes have been detected by Cassini/LEMMS. They are organized in two groups of pulsations: the first one, on day 127, lasts from 05 UT to 10 UT, while the second set starts at 16 UT and ends at 23 UT. The mean interpulse period, derived by a Lomb-Scargle analysis, is 74 min for the first set and 63 min for the second set. These electron pulsations belong to the list of LEMMS quasi-periodic electron events described in Chapter 3.

During the other observations of the polar auroral spot shown in Figure 5.3, similar quasi-periodic pulsations in the electron flux and in B_ϕ measurements are detected by LEMMS and by MAG respectively, again with a periodicity of around one hour. With the same format as for Figure 5.4, in-situ data are displayed in Figure 5.5 for days 237 and 238 of 2008. Structured fluctuations are again present in the electron data during the UVIS observation time and they are preceded by some other ~ 1 -h pulsations. Likewise, presence of field-aligned currents at the Cassini location is revealed by B_ϕ fluctuations with a 58 min periodicity. However, like for the observation on day 128 of 2013, the detected electrons are perpendicular to the field and Cassini is not located on flux tubes directly connected to the pulsating aurora (see the Cassini ionospheric footprint on the UVIS snapshot on the second line in Figure 5.3). A ~ 1 -h quasi-periodic electron event is seen also on day 237 of 2008 starting at 16 UT. Regarding the polar spot observation on day 129 of 2008, ~ 1 -h pulsations have been reported in electron and magnetic field measurements by Mitchell et al. (2016). Some fluctuations can be also distinguished in in-situ measurements during the UVIS auroral imaging on day 144 of 2008, but gaps in LEMMS and MAG data do not allow a reliable analysis.

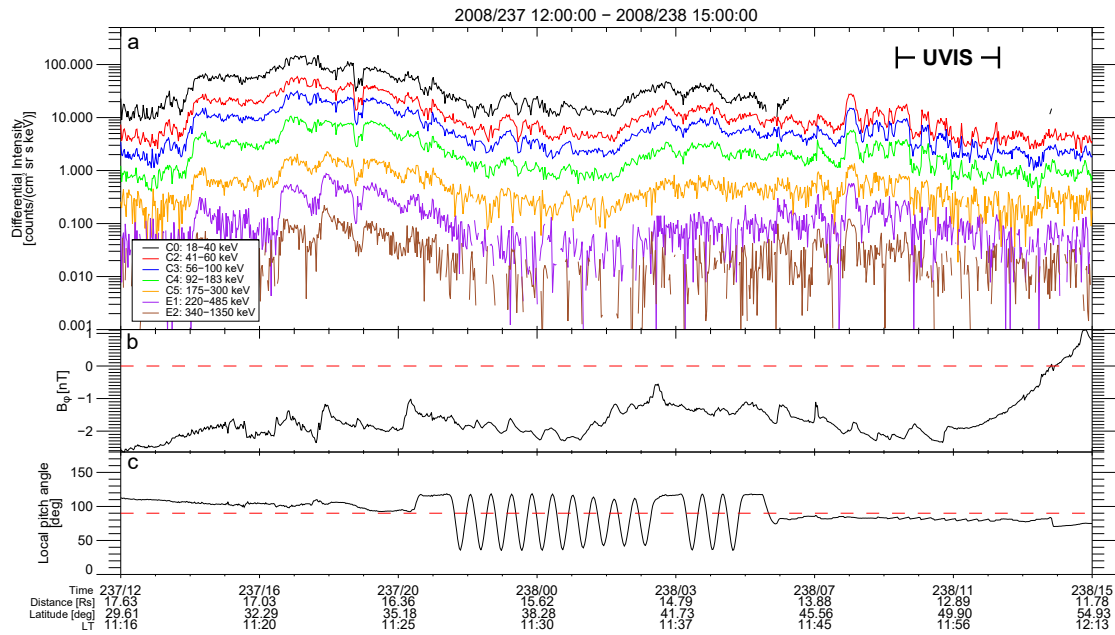


Figure 5.5: Cassini in-situ observations on days 237 and 238 of 2008. Time series plots of (a) the differential intensities of electrons from different Cassini/LEMMS channels between 18 and 1350 keV, (b) the azimuthal component of the magnetic field measured with Cassini/MAG, and (c) the local pitch angle of the LEMMS High Energy Telescope. The time interval corresponding to the UVIS observation sequence presented in Figure 5.3 is indicated. From Palmaerts et al. (2016b).

5.3 Discussion

5.3.1 Polar cusp aurora

In the previous sections, observations of an isolated auroral emission in the dawn-to-noon local time sector have been reported in both hemispheres using Cassini/UVIS auroral imaging. This auroral spot is located at high latitude, poleward of the main auroral emission. Except for the observation on day 144 of 2008 (see Figure 5.3), the polar auroral spot is separated from the main emission by a latitudinal shift exceeding the typical offset of $1\text{--}2^\circ$ between the main emission and the open-closed field line boundary (OCFLB) and fixed in local time, it is connected to open magnetic field lines. Similar auroral spots in the same ionospheric area have been previously reported on auroral images acquired with the Hubble Space Telescope (Gérard et al. 2004, 2005, Meredith et al. 2014, Grodent 2015). Gérard et al. (2005) associated this polar auroral spot with the cusp of Saturn’s magnetosphere (see Section 1.3.2). This association is in agreement with the model developed by Bunce et al. (2005a) where particle precipitation around noon and poleward of the OCFLB are induced by high-latitude lobe reconnection at the magnetopause with southward IMF, as described in Section 1.3.2. The isolated high-latitude auroral emission described in this chapter is then likely the ionospheric signature of the magnetospheric cusp and is thought to be related to high-latitude magnetopause reconnection in the lobe

regions.

As explained in Section 1.2.4.4, dayside magnetopause reconnection is possibly not as common at Saturn as at the Earth's magnetopause because of inappropriate plasma β conditions (Masters et al. 2012a). However, the investigation of the polar cusp aurora based on Cassini/UVIS data reveal that its occurrence probability is as high as 29.6% in the northern hemisphere and 22.7% in the southern hemisphere, suggesting that the lobe magnetopause reconnection might be more frequent than previously thought. Furthermore, models of magnetopause reconnection at Saturn indicate that this process is more likely to occur at high latitude (Desroche et al. 2013, Fuselier et al. 2014).

The magnetospheric cusp can be crossed by the Cassini spacecraft while it is moving on high-latitude orbits. The cusp leaves various observational signatures in the plasma and magnetic field measurements such as ion energy dispersion and diamagnetic effect. Arridge et al. (2016) and Jasinski et al. (2016b) analyzed a dozen of cusp plasma observations and the associated signature of magnetopause reconnection. Both studies concluded that reconnection at Saturn's magnetopause and plasma entry into the cusp can occur for various solar wind conditions. This independence with the upstream conditions could explain the relatively high occurrence probability of the polar cusp aurora at Saturn.

5.3.2 Pulsations of the high-latitude magnetopause reconnection

Unlike the HST auroral observation which cannot exceed 90 min, the Cassini/UVIS observing sequences allow to track the auroral dynamics over period of several hours. The UVIS observation of the intensity of the polar cusp aurora revealed quasi-periodic brightening with a periodicity ranging between 60 and 70 min. The brightening in the cusp aurora is indicative of a pulsed behavior of the high-latitude magnetopause reconnection in the lobes, as already suggested in the model of Bunce et al. (2005a). In the Earth's magnetosphere, pulsed reconnection at the dayside magnetopause triggers flux transfer events (FTE) and pulsed ionospheric flows (Russell and Elphic 1978, Provan et al. 1998, Wild et al. 2001). Contrary to the polar cusp aurora, FTEs at Earth are produced by low-latitude magnetopause reconnection between the IMF and closed field lines of the planetary magnetic field. Nevertheless, a connection exists at Earth between periodic bursts in the low-latitude magnetopause reconnection and brightening in the proton cusp aurora with an equivalent period (Fuselier et al. 2007). The typical timescale between consecutive FTEs at Earth, and consequently between reconnection bursts, is 8 min, but this time interval can range from 1 to 30 min (Kuo et al. 1995). A unique FTE has been identified in Saturn's magnetosphere at the low-latitude dayside magnetopause (Jasinski et al. 2016a). However, this is not a phenomenon frequent at Saturn as indicated by the fruitless search for FTEs performed by Lai et al. (2012). The quasi absence of Saturnian FTEs could be due to the plasma β conditions at the magnetopause which are inappropriate for a high reconnection rate (Masters et al. 2012a). Furthermore, magnetopause model developed by Desroche et al. (2013) indicates that reconnection is more viable at higher latitude while Lai et al. (2012) searched FTEs in the equatorial region.

Notwithstanding the rarity of FTEs, the bursty behavior of the reconnection at the Kronian magnetopause has been revealed by different indirect measurements. For instance, burst reconnection induces a stepped structure in the energy-time dispersion in the ion intensities. This signature has been regularly observed during Cassini cusp crossing

(Jasinski et al. 2014, 2016b, Arridge et al. 2016). Additionally, the bifurcations of the main auroral emission (Radioti et al. 2011) and their multiple brightenings provide another evidence of pulsed reconnection (Radioti et al. 2013b, Badman et al. 2013). The bifurcation brightenings are also present in the UVIS auroral sequence on day 129 of 2008 (Figure 5.3). Mitchell et al. (2016) determined that the brightening period is similar in the bifurcation and in the polar cusp aurora. However, the phase of the bifurcation brightness pulsations leads the cusp aurora pulsations by around 18 min. This delay could be explained if a pressure pulse or a wave traveling across the polar cap propagates the periodic pulsations from the dusk sector where the bifurcation resides, to the prenoon area containing the cusp spot.

As discussed in Section 5.2, simultaneously to the polar cusp aurora brightening, hourly periodic fluctuations are observed in the electron fluxes in the energy range from 18 keV to beyond 200 keV and in the azimuthal component of the magnetic field. Any direct relation between these pulsed electrons and the cusp spot brightening can be evaluated since the detected electrons are not in the field-aligned direction and the ionospheric footprint of Cassini during the observations do not match the polar cusp spot position. However, the periodicity range of these pulsations and the cusp aurora brightening is similar to the mean interpulse period (68 ± 10 min) of the quasi-periodic pulsations in the energetic electron (above 100 keV) fluxes analyzed in Chapter 3. This finding endorses the idea that the hourly quasi-periodic electron injections are connected to the auroral processes, as suggested in Chapter 4.

In particular, a subset of events is located at high southern magnetospheric latitudes ($\varphi < -40^\circ$) between 05 and 12 h in local time (Figure 3.6). These high-latitude dawn-side events occurred within $20 R_S$ from the planet and they present pulsations at energies beyond 1.6 MeV with high rise and decay rates (Figure 3.14). In order to have a comparison with the frequency of the pulsating cusp aurora, the occurrence probability of these high-latitude electron events has been calculated. For this purpose, it has been considered, for both hemispheres independently, the time spent by the Cassini spacecraft in the magnetospheric region mapping to the ionospheric region where the polar cusp aurora appears, i.e., between 06 and 12 LT and between the latitudes 79° and 87° (in absolute value). This magnetospheric region has been restricted to radial distances up to $20 R_S$, since no electron pulsations have never been observed at further distances at these high latitudes (Section 3.4). To perform the mapping, the magnetic field model of Dougherty et al. (2005) combined with the ring current model of Bunce et al. (2007) was used. Three different standoff distances of the magnetopause (18, 22, and $27 R_S$) have been considered. The resulting occurrence probabilities are listed in Table 5.1. Electron pulsations occur with an occurrence probability of 21 to 37% in the northern hemisphere and of 21 to 25% in the southern hemisphere. Hence, the probability to observe electron pulsations in the dawn high-latitude region mapping to the polar cusp aurora area is similar to the UVIS observation frequency of the polar cusp aurora itself. This result implies that the dawn high-latitude pulsed electrons are likely triggered by the same process responsible for the pulsating cusp auroral spot, namely the high-latitude magnetopause reconnection in the lobe regions.

The lobe magnetic reconnection being a process involving only open field lines, the relation between the pulsating cusp aurora and the dawn high-latitude pulsed electron events indicates that these electron events reside on open field lines. In Section 3.5.4, it has

	Magnetopause stand-off distance	Northern hemisphere (%)	Southern hemisphere (%)
Polar cusp emission		29.6	22.7
Pulsations in	18 R_S	21.6	21.8
energetic	22 R_S	27.0	23.5
electron fluxes	27 R_S	36.6	25.3

Table 5.1: Occurrence probability of the polar cusp emission in the UVIS auroral images and of the ~ 1 -h pulsations in the MIMI/LEMMS energetic electron fluxes in the magnetospheric region, within 20 R_S from the planet and mapping into the ionosphere in the cusp emission region (06-12 LT and 79-87° in latitude), using the internal magnetic field model of Dougherty et al. (2005) combined with the ring current model developed by Bunce et al. (2007).

been investigated whether the electron events are on open or closed field lines, based on the $E0^*/E0$ ratio method. It was concluded that all the duskside events except one are on closed field lines. However, no conclusion could be made for the dawnside events due to a lack of pitch angle distribution. The mapping of the quasi-periodic electron injections has been achieved by Roussos et al. (2016) using the magnetic field model of Khurana et al. (2006) which includes open magnetic field lines. The mapping indicated that the dawnside high-latitude electron pulsed events are located on open field lines, whatever value of the solar wind dynamic pressure was chosen for the mapping. Moreover, the ionospheric footprint of these events resides in the dawn-to-noon sector at higher latitude than the statistical poleward boundary of the main auroral emission, and thus in the ionospheric area where the polar cusp aurora is observed. The mapping towards the ionosphere of the dawn high-latitude events starts at high latitude and at short distance from the ionosphere where the magnetic field is dominated by the internal dipole field. For this reason, the mapping is weakly dependent on the magnetospheric model and its configuration and it is consequently reliable.

Another evidence that the dawnside high-latitude electron pulsations occur on open field lines is given by the plasma wave emissions and plasma electron data provided by the RPWS and CAPS/ELS instruments (see the Sections 2.5 and 2.7 for a description of these instruments). When Cassini moves above the polar cap and crosses open flux tubes, the auroral hiss observed by the RPWS instrument is more intense and its upper cutoff frequency is lower than in the closed field line region equatorward to the OCFLB (Gurnett et al. 2010, Jinks et al. 2014). The OCFLB is also clearly visible in the CAPS/ELS spectrograms of low-energy electrons: the outer magnetosphere region (closed field lines) is populated mainly by warm thermal electrons with energies in the range from 0.1 to 10 keV, while the lobe region (open field lines) is devoid of plasma at these energies (Talboys et al. 2011, Jinks et al. 2014). An example is illustrated in Figure 5.6 showing, from top to bottom, the MIMI/LEMMS electron fluxes, the RPWS electric field spectrogram and the CAPS/ELS electron spectrogram for a 19-hour time interval starting on day 298 of 2008 at 12 UT. At the start of the interval, Cassini is on closed field lines as shown by the warm electron populations (peak intensity at energy above 100 eV) and the weak radio emissions (below 50 dB). At $\sim 14:00$ UT, the spacecraft crosses the OCFLB and en-

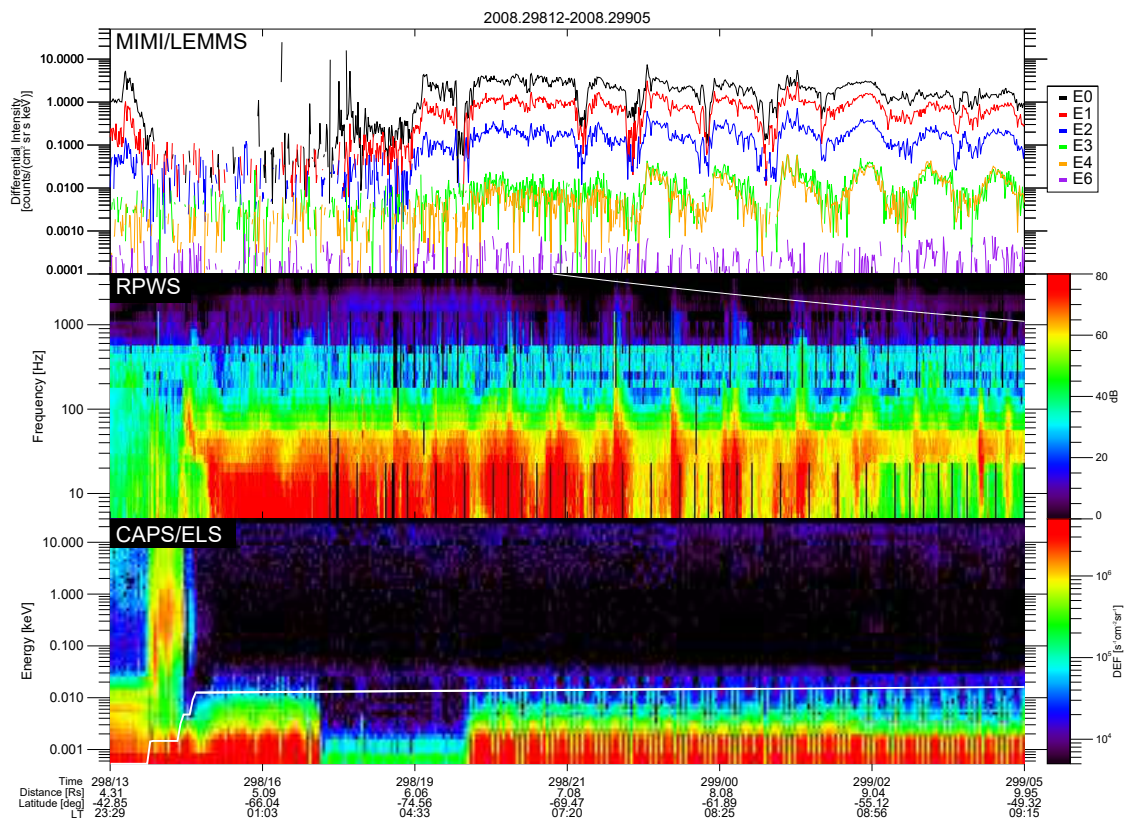


Figure 5.6: Multi-instrument time series plots between 12 UT on day 298 of 2008 and 05 UT on day 299. The upper panel gives the differential intensities of energetic electrons from the LEMMS channels E0 to E4 and E6, the middle panel is the RPWS electric field spectrogram and the bottom panel is the CAPS/ELS electron spectrogram of energy range 0.6 eV–20 keV. The white line on the RPWS spectrogram indicates the electron cyclotron frequency. The white line on the ELS spectrogram is the upper limit of the photoelectrons coming from the spacecraft.

ters into the lobe characterized by an absence of warm electrons and an intense auroral hiss. In the second part of the interval, ~1-h quasi-periodic pulsations are visible in the LEMMS electron data, simultaneously with pulsations in the auroral hiss, while Cassini is still in the dawn-to-noon sector of the open field line lobe region. Most of the dawnside high-latitude electron events have pulsed signatures in the auroral hiss (see Figure 4.2) and are observed in the lobe region, as revealed by the CAPS/ELS low energy electron spectrogram.

Hence, from the multi-instrument study performed in this thesis, it can be concluded that the quasi-periodic hourly electron pulsations occurring at high latitude in the dawn-to-noon local time sector reside on open field lines and are likely triggered by pulsed magnetopause reconnection in the lobe. The lobe reconnection also causes quasi-periodic brightening of the polar cusp aurora observed in the prenoon sector.

6 Electron pulsation triggering process at the magnetopause

In the previous chapter, the identification of hourly pulsations at the polar cusp aurora suggested bursty high-latitude lobe reconnection as a possible mechanism triggering the high-latitude dawnside pulsed electron events. This mechanism cannot be invoked for the events located at lower latitude since they reside on closed field lines and are not connected to the lobe regions. However, pulsed magnetopause reconnection at low latitude is a plausible scenario explaining the generation of the hourly electron injections. In this chapter, this scenario will be investigated and its validity will be discussed.

6.1 Survey of the magnetospheric environment during the energetic electron pulsations

In Section 5.3.2, it has been shown that the quasi-periodic hourly injections of energetic electrons can occur in the lobe regions along open field lines. Since the lobe electron events represent a minority of events, it is interesting to investigate the magnetospheric environment of all the other events located on closed field lines. The low-energy electron spectrograms provided by the CAPS/ELS instrument will be used again to determine the plasma environment.

The typical plasma environments encountered inside and around Saturn's magnetosphere described below are based on the categorization by Rymer et al. (2009a) of the magnetospheric environment during Titan encounters. This categorization has been adapted to also account for the magnetospheric regions away from Titan's orbit. An example of pulsed electron event is given for each category in Appendix B.

The center of the plasma sheet is characterized by a dense electron population with a maximum particle flux exceeding 3×10^5 counts/(s cm²sr) and peaking at energy above 120 eV (Rymer et al. 2009a). The plasma sheet at high latitude close to the lobes and at low latitude at radial distance farther than $25 R_S$ contains an electron population at similar energies as the central region of the sheet but at lower density: the maximum flux ranges from 5×10^4 counts/(s cm²sr) and 3×10^5 counts/(s cm²sr). This plasma environment is considered as "lobe-like" environment by Rymer et al. (2009a), although the density is actually higher than in the tail lobes which is almost devoid of plasma (e.g. Talboys et al. (2011) and Jinks et al. (2014)). Compared to the other environments, the magnetosheath contains lower energy and higher density population: the maximum flux of the magnetosheath population, made up of solar wind particles, peaks at energy below 120 eV and

Plasma environment	Number of events
Plasma sheet center	70
Plasma sheet	280
Lobes	22
Boundary layer	112
Bimodal	4

Table 6.1: Distribution of the quasi-periodic hourly electron injections in the different magnetospheric environments.

exceeds 1×10^6 counts/(s cm²sr) (Rymer et al. 2009a). Furthermore, the magnetosheath is generally characterized by a magnetic field weaker than in the magnetosphere but with a variability more important. The cusp contains similar electron population than the magnetosheath, but at slightly lower density (Arridge et al. 2016, Jasinski et al. 2016b). The boundary layer is a region of mixed magnetosheath and magnetospheric plasma along the planetward edge of the magnetopause (Masters et al. 2011a,b) or along the cusp boundaries (Arridge et al. 2016). It is characterized by a plasma population intermediate between the magnetosheath and the magnetosphere populations with a maximum flux at around 3×10^5 counts/(s cm²sr) and at energy ~ 100 eV. Finally, two distinct populations at different energies can be observed simultaneously, constituting a bimodal distribution.

6.1.1 Spatial distribution of the plasma environment

Since the CAPS/ELS instrument was switched off in June 2012, the survey of the plasma environment cannot be achieved for the whole list of hourly electron events. The magnetospheric environment could be reliably identified for 488 events. The number of events in each environment is given in Table 6.1.

The overall spatial distribution of the plasma environments shown in Figure 6.1 is consistent with what it is expected: the lobe events (blue dots) reside at high latitude, the pulsed electron events encountered in the dense central region of the plasma sheet (red dots) are those observed close to the planet at low latitude while the events occurring in the boundary layer (green dots) are found at large distances, close to the magnetopause. It is notable that no electron pulsations are found in the boundary layer adjacent to the cusp, but Cassini usually crosses this region in less than two hours (Arridge et al. 2016) preventing the identification of hourly flux enhancements. Most of the events are included in the plasma sheet category (orange dots) which mainly corresponds to intermediate latitude and radial distances. The extent of the plasma sheet electron population to high latitude is explained by the smaller effect of the centrifugal forces on the electrons, resulting in a reduced equatorial confinement compared to the ions. Finally, no events occur in the magnetosheath. If quasi-periodic pulsed electrons can escape the magnetosphere, for instance through a Kelvin-Helmholtz vortex (Section 1.2.4.5), their intensity is probably too low to be detected by MIMI/LEMMS.

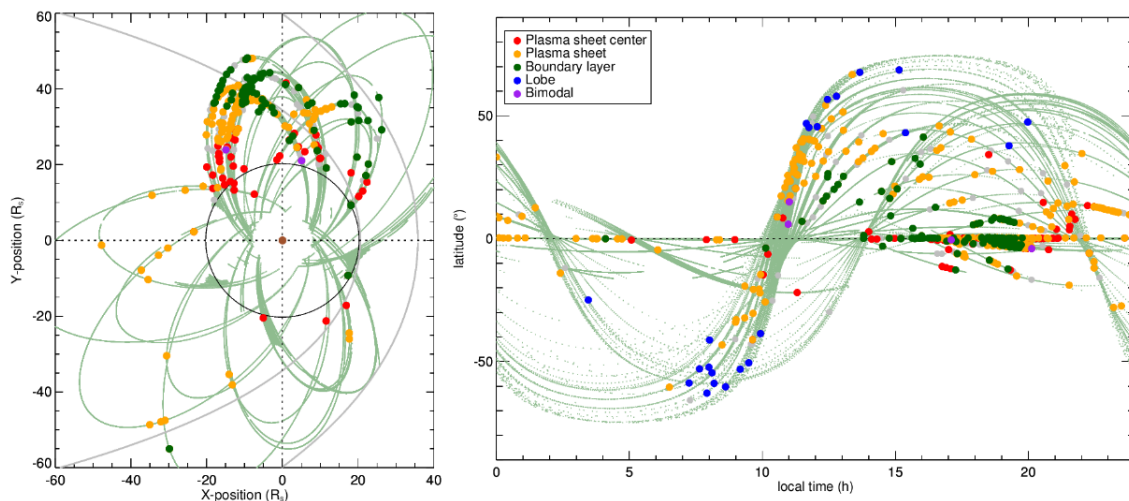


Figure 6.1: Spatial distribution of the plasma environments where quasi-periodic hourly electron pulsations are observed. Pulsed events (left) located within $2 R_S$ from the equatorial plane and (right) in a latitude-local time diagram. The color indicates the plasma environment. The gray dots are the events for which the plasma environment could not be determined. The green curves indicate the orbits of Cassini when CAPS data are available. Titan's orbit (black circle) and two simulated magnetopause locations (gray lines) are drawn, using the model of Kanani et al. (2010).

6.1.2 Evidence of electron events in the close vicinity of the magnetopause

The investigation of the plasma environment revealed that numerous QP60 events are encountered in the boundary layer along the inner side of the magnetopause. In this layer, magnetosheath particles originating from the solar wind are mixed with magnetospheric plasma. The magnetosheath particles can enter the magnetosphere through magnetic reconnection or Kelvin-Helmholtz vortices at the magnetopause.

When Cassini crosses the magnetopause, abrupt changes in the magnetic field and in the plasma environment are displayed in the in-situ measurements of the spacecraft. In this way, it is possible to determine the location of the magnetopause. Combined LEMMS and CAPS measurements revealed that many hourly electron pulsations occur close to the magnetopause.

The existence of hourly pulsations in the magnetosphere close to the magnetopause is illustrated in Figure 6.2. During one equatorial orbit in 2010, represented in the subpanel in Figure 6.2, the Cassini spacecraft crossed the magnetopause in the predusk sector (red cross), moved through the magnetosheath and crossed back the dusk flank of the magnetopause (red cross) eight days later. The magnetopause crossings (red dashed lines) are easily identifiable on the CAPS spectrogram: the magnetosheath electron population is denser and less energetic than the magnetospheric plasma although Cassini crossed a boundary layer on the inbound pass. On the LEMMS data in the upper panel of Figure 6.2, each pulse included in hourly pulsed electron events is indicated by a vertical blue line. It is apparent that hourly pulsations are observed in the close neighborhood of the inner side of the magnetopause. In particular, several consecutive pulsed electron events are

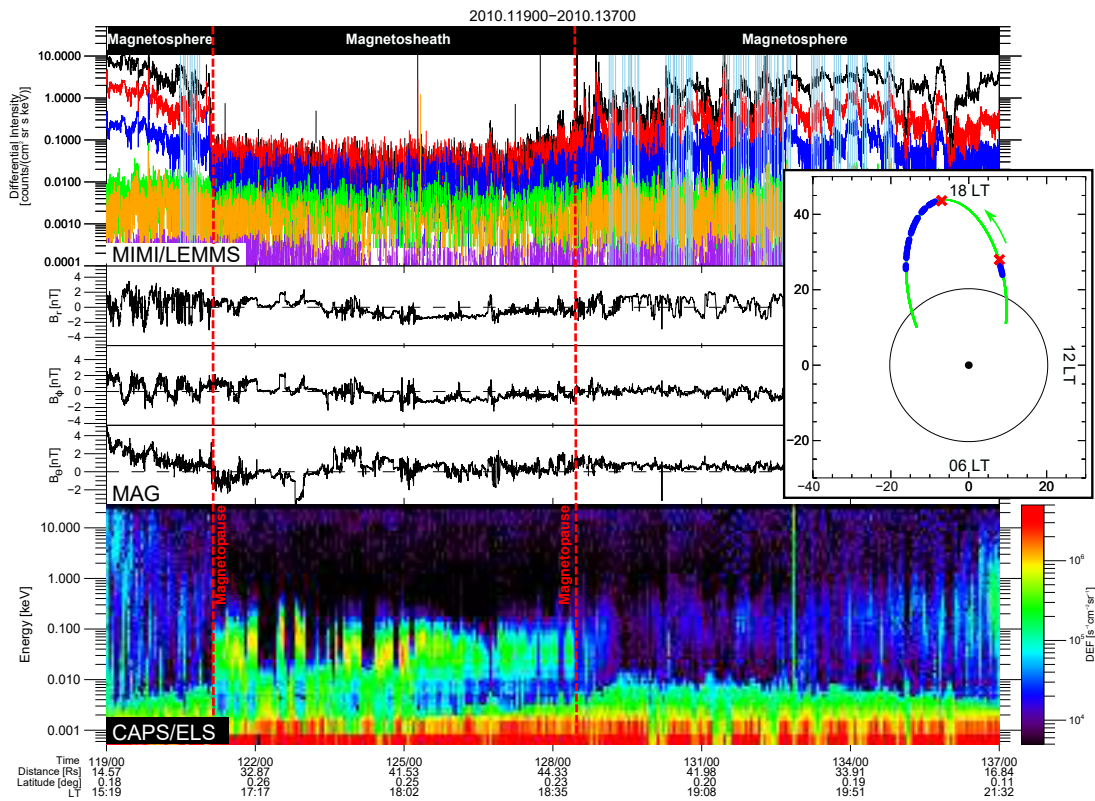


Figure 6.2: Evidence of quasi-periodic energetic electron injections close to the magnetopause during the time interval from day 119 to day 137 of 2010. Upper panel: Differential intensities of energetic electrons from the LEMMS channels E0 to E4 and E6. Each QP60 pulse is indicated by a vertical blue line. Middle panels: Magnetic field components in spherical coordinates (B_r , B_ϕ , B_θ) measured by Cassini/MAG. Bottom panel: CAPS/ELS electron spectrogram of energy range 0.6 eV-20 keV. The Cassini magnetopause crossings are indicated by the red dashed lines. Inset subpanel: Motion of Cassini during the observing time interval (green curve). The black dot represents Saturn and the black circle represents Titan's orbit. The QP60 pulses are indicated by blue dots and the magnetopause crossings by red crosses.

detected by MIMI/LEMMS along the inbound journey of Cassini, up to distances greater than $15 R_S$ from the magnetopause.

This example is not unique and in several low-latitude orbits in the dusk sector, the frequency of hourly electron pulsations was particularly high. The long event shown in Figure 3.9 provides another typical example.

From these observations and by analogy with the pulsed high-latitude magnetopause reconnection which could generate the high-latitude electron events on open field lines, magnetopause reconnection at lower latitude is thought to trigger electron pulsations on closed field lines akin to the Earth's magnetopause where bursts of reconnection produce the flux transfer events with a periodicity of around 8 min (see Section 5.3.2).

6.2 Study of the solar wind influence

The rate of magnetopause reconnection at Earth is strongly dependent on the IMF orientation but also varies with the solar wind velocity (Milan et al. 2012). Hence, provided that this coupling between dayside reconnection and solar wind speed exists at Saturn too, if the scenario of quasi-periodic electron injections generated by magnetopause reconnection is valid, then it is expected that we observe more electron pulsations during intervals of increased solar wind velocity or dynamic pressure.

At Jupiter, the daily number of quasi-periodic 40-min bursts observed in the radio emissions has been revealed to increase in phase with the arrival of faster solar wind (see Section 1.4.2 and Figure 1.17, MacDowall et al. (1993)). This correlation could be found thanks to the Ulysses spacecraft which, after its Jupiter flyby, continued measuring simultaneously the Jovian radio emissions and the solar wind velocity along its way back to the Sun.

Unfortunately, the investigation of such a correlation cannot be achieved directly at Saturn with the single Cassini spacecraft. Unlike at Jupiter where Ulysses could detect radio emissions outside the magnetosphere, the radio emissions with relevant hourly modulation have not been observed outside the Kronian magnetosphere. Hence, when the Cassini instrumentation detects hourly pulsations inside the magnetosphere, no direct measurements of the solar wind parameters are available. Reciprocally, when Cassini is outside the magnetosphere, the upstream solar wind conditions are known, but the pulsations are “invisible” to the spacecraft. Therefore, in order to find out if the quasi-periodic electron injections are influenced by the solar wind conditions, it is necessary to somehow estimate the solar wind parameters. Different methods have been used in this work and are explained in the next sections.

6.2.1 Magnetopause crossings

A first method to estimate the solar wind conditions consists in identifying the magnetopause position. At the magnetopause, the magnetic pressure and the thermal pressure approximately balance the dynamic pressure of the solar wind (see Section 1.2.2). Hence, the magnetopause location gives an indication on the solar wind ram pressure. As illustrated in Section 6.1.2, the Cassini magnetopause crossings leave a signature in the low-energy electron spectrogram as well as in the magnetic field. Using CAPS/ELS and MAG data, Pilkington et al. (2015) listed the magnetopause crossings from Saturn Orbit Insertion to October 2010 and from May 2012 to February 2013. In total, 1514 crossings are included in this list. The authors have also estimated for each crossing the solar wind dynamic pressure using two different methods. In the first method, the magnetospheric pressure is calculated at the magnetopause based on magnetometer and plasma (electron and suprathermal ion) data and the ram pressure is estimated assuming equilibrium between the two pressures. The second method consists in fitting an empirical magnetopause model through each crossing and finding the ram pressure satisfying the fit.

The pressure calculated by the first method is more realistic and gives more information about the dynamics occurring at the magnetopause at the time of the crossing. The second method has the advantage to be more stable to magnetopause instabilities such as

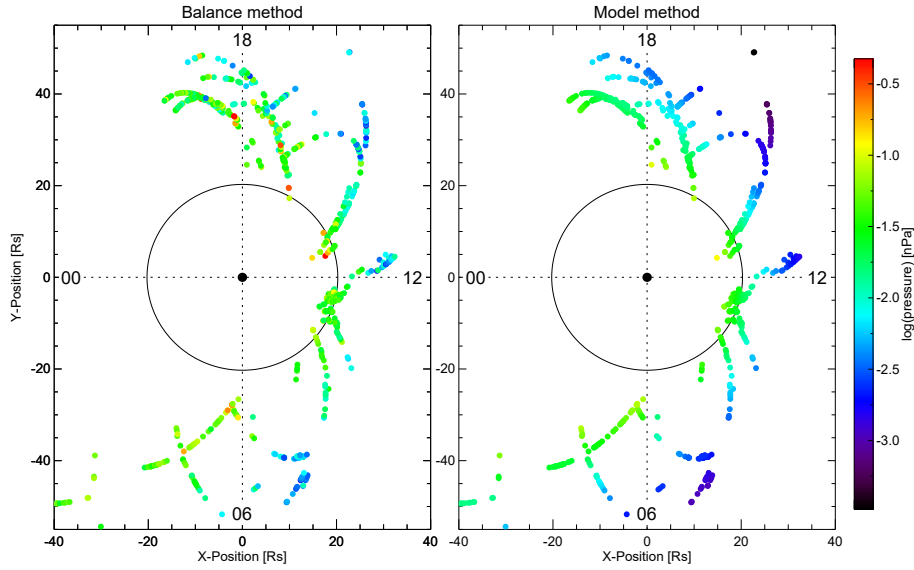


Figure 6.3: Distribution of the Cassini magnetopause crossings located within $2 R_S$ from the equatorial plane and provided by Pilkington et al. (2015) (covering the period from Saturn Orbit Insertion to late 2010 and from mid-2012 to early 2013). The color indicates the estimation of the solar wind dynamic pressure at each crossing using the balance between the dynamic pressure and the internal magnetospheric pressure (left panel) and an empirical magnetopause model (right panel). Titan’s orbit at $20.3 R_S$ is drawn.

Kelvin-Helmholtz instability. In Figure 6.3, all the magnetopause crossings provided by Pilkington et al. (2015) and located within $2 R_S$ from the equatorial plane are represented by dots with a color code giving the estimated solar wind dynamic pressure using the first method (“balance method”, left panel) and the second method (“model method”, right panel).

The estimation of the solar wind dynamic pressure obtained through the “balance method” can differ from the estimation coming from the “model method”, especially when instabilities are present at the magnetopause. A comparison between both methods is given in Figure 6.4. It is observed that the pressure estimated by the balance method is generally higher than the pressure given by the model method.

For the investigation of the solar wind effect on the hourly electron pulsations, a selection of 70 Cassini orbits containing at least one magnetopause crossing and one QP60 event has been achieved. These orbits are represented in Figure 6.5 on an equatorial projection (left) and on a noon-midnight meridian projection (right). In the next analyses, in order to have a reliable number of pulses occurring on a daily basis, only the pulsations observed before the first magnetopause crossing on the outbound trajectory and the ones observed after the last magnetopause crossing on the inbound trajectory have been considered, constituting a list of 1142 pulses.

In the present analysis, the estimated ram pressure is based on the measurements at the magnetopause crossings. Therefore, only the electron events located very close to the magnetopause can be taken into account in order to have a reliable investigation of the solar wind correlation. The solar wind conditions at the magnetopause may have significantly changed for the events detected much earlier or later than the crossing time.

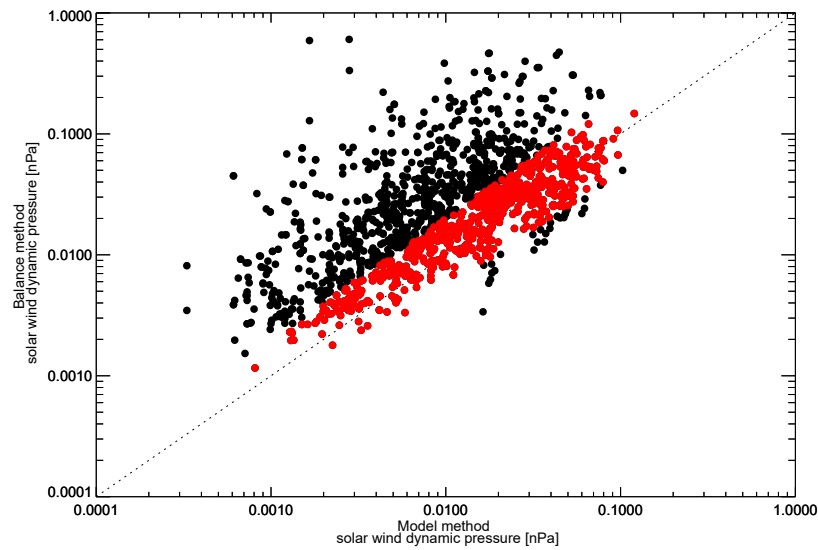


Figure 6.4: Comparison between the estimation of the solar wind dynamic pressure at the magnetopause crossings given by two different methods: using the balance between the dynamic pressure and the internal magnetospheric pressure and using an empirical magnetopause model. The red dots are the magnetopause crossings for which the two estimates do not differ from more than a factor of 2.

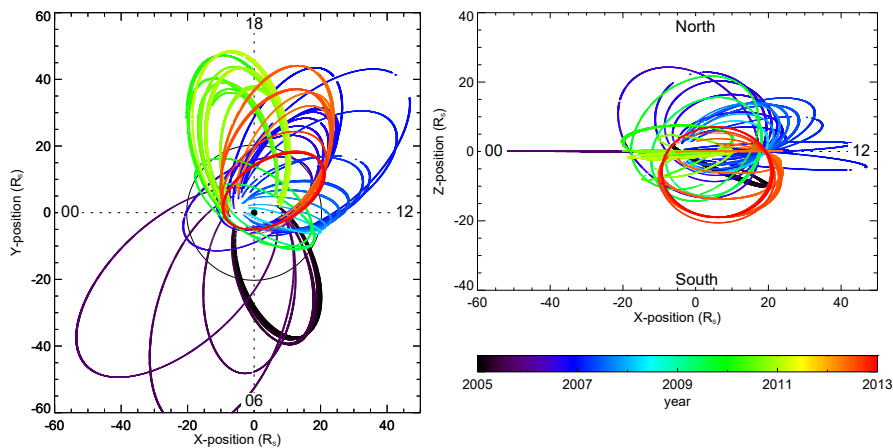


Figure 6.5: Cassini orbits considered in the investigation of the solar wind dependence, projected in the equatorial plane (left) and in the noon-midnight meridian plane (right). The color scale indicates the year of the orbit.

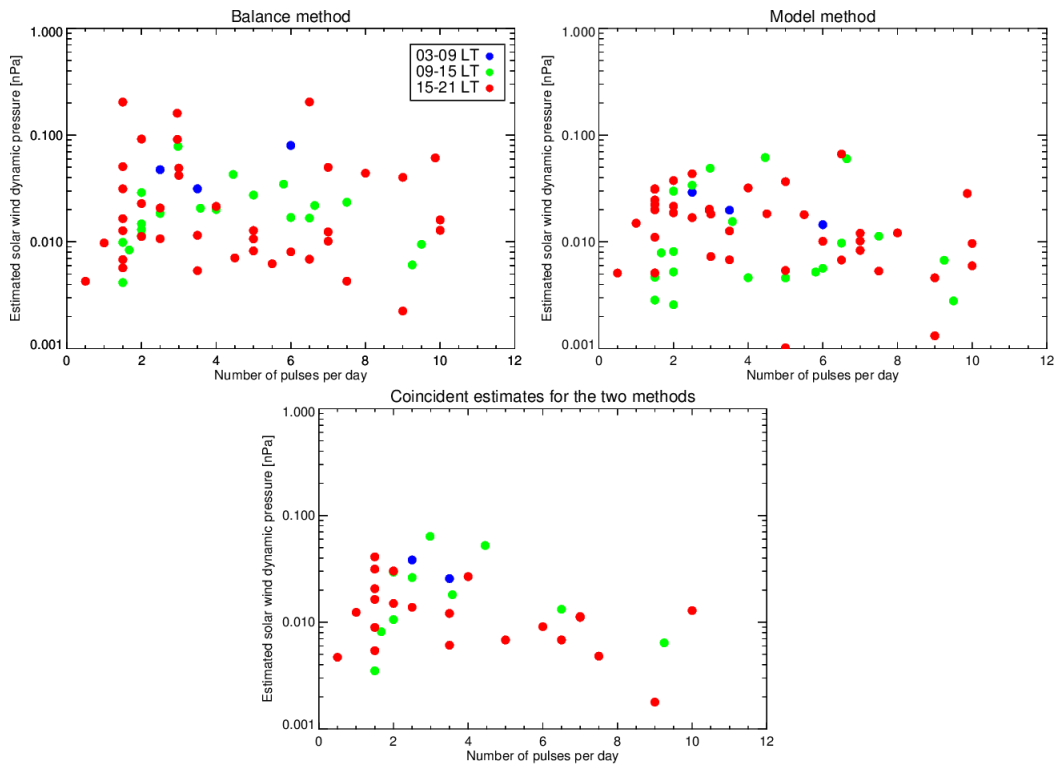


Figure 6.6: Daily number of hourly electron injections detected by MIMI/LEMMS within 2 days from the magnetopause compared to the estimation of the solar wind dynamic pressure. Upper left panel: Ram pressure estimated with the balance method. Upper right panel: Ram pressure estimated with the model method. Lower panel: Mean of the ram pressure estimates given by each method, considering only the estimates which do not differ between the two methods by more than a factor of 2.

Hence, the analysis is restricted to the pulses detected by Cassini/LEMMS within two days prior and after the magnetopause crossing.

Finally, taking into account these restrictions on the location of the QP60 events, scattered plots of the daily number of hourly electron injections as a function of the ram pressure estimates given by the two methods are given on the upper panels of Figure 6.6. The bottom panel in Figure 6.6 presents the same plot with an average of the estimates given by each method and considering only the estimates which do not differ between the two methods by more than a factor of 2 (red dots in Figure 6.4). In each panel, the three colors differentiate three local time sectors: the red, green and blue events are located in the local time quadrant 03-09 LT, 09-15 LT and 15-21 LT, respectively. Only three orbits analyzed are located in the morning sector, preventing any search of correlation. For the two other local time quadrants, it appears that no linear correlation between the number of pulses per day and the ram pressure is obvious in the data.

6.2.2 The mSWiM model

The Michigan Solar Wind Model (mSWiM) constitutes another tool to estimate the solar wind conditions at Saturn's magnetosphere. This one-dimensional MHD model prop-

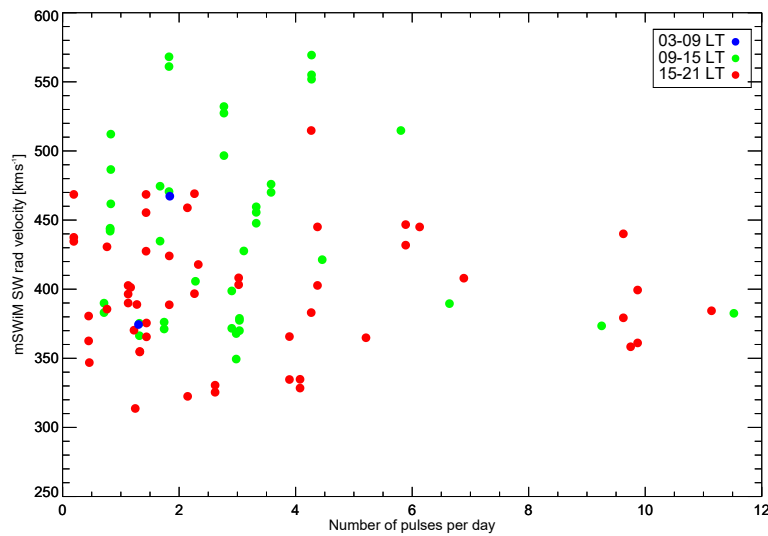


Figure 6.7: Daily number of hourly electron injections detected by MIMI/LEMMS within 8 days from the magnetopause compared to the radial solar wind velocity propagated from the Earth using the mSWiM model (Zieger and Hansen 2008).

agates the solar wind conditions measured by spacecraft around the Earth (ACE, SOHO, STEREO-A and STEREO-B) from 1 AU to 10 AU (Zieger and Hansen 2008). The SOHO and ACE satellites are on the Earth-Sun line while the STEREO spacecrafts are leading and following the Earth on its orbit. The most accurate predictions are obtained at the apparent opposition of the near-Earth spacecraft which measures the input solar wind parameters. Comparison between observations and mSWiM predictions showed that the model accuracy remains good within 75 days from apparent opposition and the uncertainty on the arrival time of solar wind shocks within this interval is 15 hours. When the position of Saturn is favorable with different Earth spacecraft, the model gives distinct results for each spacecraft. In that case, the propagated solar wind values are then averaged in the following analysis. Finally, the best predicted solar wind property is the radial velocity, followed by the IMF magnitude and the density. Consequently, only the propagated solar wind velocity will be used here.

Contrary to the previous method which is limited to the close vicinity of the magnetopause, the upstream conditions given by the mSWiM model are known at any time, as far as the geometry between Saturn and one of the Earth spacecraft is convenient. The investigation can then include more QP60 pulsations from the initial list of 1142 pulses. Figure 6.7 shows the daily number of hourly electron injections detected within 8 days from the magnetosphere compared to the daily-averaged mSWiM radial velocity. The events have been separated in three local time sectors of 6 hours: 03-09 LT (in blue), 09-15 LT (in green) and 15-21 LT (in red). Again, the dawn local time quadrant includes only two values preventing any investigation of a correlation with the solar wind. For the two others quadrant, no positive linear correlation can be found, contrary to what is observed at Jupiter.

However, the mSWiM propagation model suffers from an inaccuracy of 15 hours in the arrival time of the solar wind at Saturn. The correlation has then been analyzed after shifting the mSWiM time series from 15 hours backwards to 15 hours forwards, with step

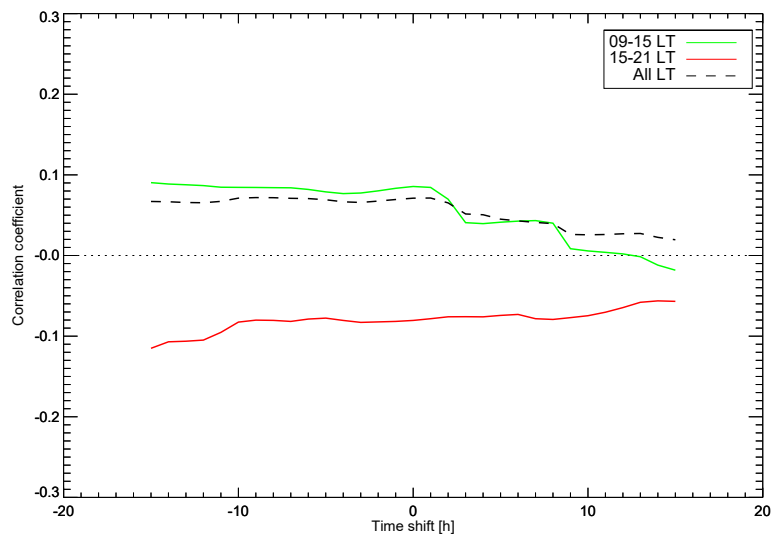


Figure 6.8: Correlation coefficient between the daily number of hourly electron injections and the mSWiM propagated solar wind velocity, as a function of the time lag applied on the mSWiM times series. The correlation coefficient was calculated for the events in the 09-15 LT sector (green line) and 15-21 LT sector (red line) and for both local time sectors together (dashed line).

of 0.1 hour. The calculated correlation coefficient is given as a function of the time shift in Figure 6.8, for the noon and the dusk sectors and for both local time sectors together. It results that the correlation coefficient is low for any time lag applied on the mSWiM velocity, indicating an absence of correlation. However, the arrival time shift is probably different for each event and further work could be done to refine this analysis.

CME detection

Finally, an indirect method enables the detection of solar coronal mass ejections (CME) at Saturn. The count rates in the LEMMS MeV ion channels, such as the P2 channel (2280-4492 keV, see Section 2.3.1), are typically at the background level when Cassini is outside the radiation belts. However, the arrival of a CME causes an enhancement of the MeV ion fluxes inside the magnetosphere since Saturn's magnetic field cannot shield the solar MeV ions of the CME (Roussos et al. 2008, 2011).

The daily number of electron injections in the vicinity of the magnetopause (8 days before and after a magnetopause crossing) has then be compared with the ion differential intensity in the P2 channel (Figure 6.9). During two out of the 70 orbits considered, a higher signal in the P2 channel reveal the arrival of a CME at Saturn. However, the averaged number of electron pulsations occurring every day along these orbits does not differ from the typical values during orbits with quiet solar wind conditions.

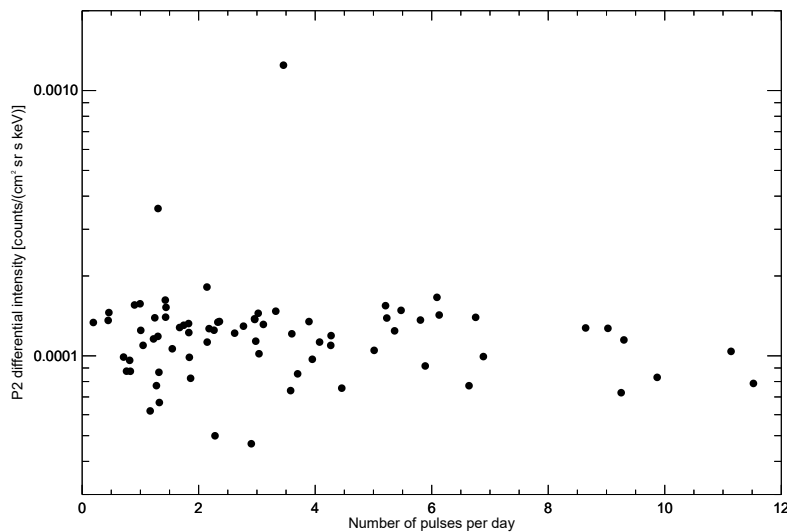


Figure 6.9: Daily number of hourly electron injections detected by MIMI/LEMMS within 8 days from the magnetopause compared to the differential intensity in the LEMMS ion P2 channel.

6.3 Discussion

In the first part of this chapter, the plasma environment where the hourly electron pulsations occur has been analysed based on the CAPS/ELS electron spectrogram. It has been shown that the pulsed electron events are encountered in various magnetospheric environments. While most of them are detected in the plasma sheet, some others were located in the boundary layer which is the region adjacent to the magnetopause where magnetospheric and magnetosheath plasma are mixed. The existence of electron pulsations in the magnetosphere so close to the magnetopause suggests that magnetopause processes may play a role in the generation of the hourly pulsations. In Chapter 5, pulsed magnetopause reconnection in the lobe regions has been proposed as a mechanism producing the high-latitude pulsed electron events residing on open field lines. Similar pulsed reconnection at the dayside low-latitude magnetopause could then trigger the quasi-periodic acceleration of the electrons. Bursty magnetopause reconnection is also the mechanism suggested for generating the auroral bifurcations in the duskside ionosphere (Radioti et al. 2011, Badman et al. 2013). These bifurcations have exhibited some brightening with a periodicity of around 60 min (Radioti et al. 2013b, Mitchell et al. 2016).

The solar wind conditions upstream of the magnetosphere influence the reconnection at the terrestrial magnetopause (Milan et al. 2012). Furthermore, a correlation between the number of quasi-periodic radio bursts and the solar wind velocity has been found at Jupiter (MacDowall et al. 1993). This correlation has motivated the investigation of such a solar wind influence on the occurrence of the hourly electron pulsations at Saturn. None of the three methods used in this investigation have revealed a linear correlation between the daily number of pulsations and the solar wind parameters. In the first method, the solar wind dynamic pressure is estimated based on the internal and external pressure equilibrium at the magnetopause and on the fitting of an empirical magnetopause model at the magnetopause crossing by Cassini. No correlation with the number of pulsations stood

out (Figure 6.6). The second method is based on a propagation model of the solar wind velocity from the Earth's orbit towards Saturn. This model suffers from an inaccuracy of 15 hours on the arrival time of the solar wind variations. However, the low correlation coefficient is not significantly modified by shifting this arrival time (Figure 6.8). Finally, the last method relies on the signature in the energetic ion fluxes of coronal mass ejections arrival at Saturn's magnetosphere. It has been shown that CME arrivals do not drive more hourly electron injections.

Contrary to what was achieved at Jupiter with the Ulysses mission and to what can be operated in Earth's magnetosphere thanks to multi-spacecraft observations, these three methods are not based on direct measurements of the solar wind parameters but only on estimations based on indirect measurements. This poor knowledge of the solar wind conditions at the time of the observations of the hourly pulsations could explain the lack of correlation.

Nevertheless, this lack of correlation with the solar wind can be added to a list of studies arguing that, surprisingly, the solar wind does not strongly influence the magnetosphere dynamics at Saturn. Neither the thickness of the low-latitude boundary layer, nor the position of the magnetopause show any Earth-like response to IMF orientation change (Masters et al. 2011a, Lai et al. 2012). Cassini crossings of the magnetospheric cusp have also revealed that high-latitude magnetopause reconnection and injection of plasma into the cusp occur for various solar wind conditions (Jasinski et al. 2016b).

While magnetopause processes are suggested to trigger the hourly electron injections, it cannot be excluded that Kelvin-Helmholtz activity at the magnetopause plays a significant role, possibly even more important than magnetopause reconnection. It has been shown that K-H instabilities are more frequent along the dusk flank of the magnetopause (Delamere et al. 2013, Ma et al. 2015) and it is precisely in the duskside of the magnetosphere that most of the pulsed electron events are encountered.

It is not conceivable that K-H instabilities can accelerate electrons at MeV energies. However, K-H vortices can induce reconnection by twisting and compressing the magnetic field lines as shown by observations at the Earth (Li et al. 2016) and simulations for the Earth (Pu et al. (1990), Nakamura et al. (2013) and references therein) and for Saturn (Fukazawa et al. 2007, Delamere et al. 2013). One type of magnetic reconnection caused by K-H instability is illustrated in Figure 6.10 (Delamere and Bagenal 2010). The high-latitude flanks of the magnetosphere are K-H stable while the equatorial magnetopause region is unstable. A vortex develops at low latitude, twisting a magnetosheath flux tube (in red) inside the magnetosphere. Reconnection can then occur at higher latitude (blue circles). The high-latitude reconnection could then energize the electrons up to relativistic energies. A high-latitude acceleration process for the electrons is in agreement with the conclusions of the analysis of the morphological properties of the hourly electron pulsations, suggesting a high-latitude source region (see Section 3.6). Furthermore, quasi-periodic pulsations in the electron intensities at energies from 10 to 500 keV have been identified by Masters et al. (2010) while Cassini was crossing a K-H plasma vortex structure in the low-latitude boundary layer. The authors considered that vortex-induced reconnection is a plausible mechanism to explain the electron flux increases detected during the vortex crossing. Finally, at Jupiter, some studies favored the presence of intermittent magnetic flux tube openings and closures in small-scale structures along the magnetopause rather than Dungey-type magnetopause reconnection (Delamere and

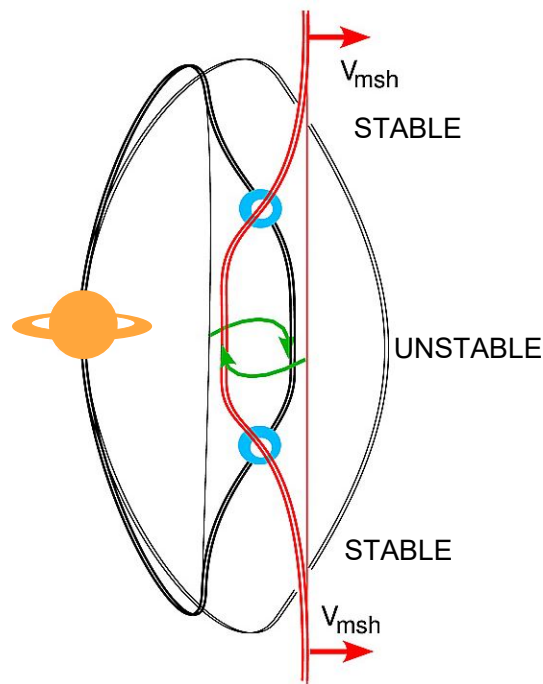


Figure 6.10: Sketch of Kelvin-Helmholtz-induced reconnection of flux tubes at the magnetospheric flanks. The reconnection takes place at the boundary (blue circles) between magnetically connected Kelvin-Helmholtz stable (at high latitude) and unstable (at low latitude) regions. Adapted from Delamere and Bagenal (2010).

Bagenal 2010, McComas and Bagenal 2007).

The multi-instrument study achieved in this chapter has revealed that hourly electron pulsations are encountered in the close proximity of the inner side of the magnetopause. This observation suggests that impulsive process at the magnetopause may generate the pulsations. It is still unclear if this magnetopause process is reconnection, Kelvin-Helmholtz instabilities or, more likely, K-H-induced magnetopause reconnection.

7 Conclusions and Perspectives

In this final chapter, the main findings of the thesis are presented as well as ongoing work and perspectives.

7.1 Conclusions

This thesis presents the first multi-instrument overview of the ~ 1 -h periodicities observed in Saturn's magnetosphere since the Voyager flybys. This multi-instrument study has been achieved in the frame of the Cassini mission which has been exploring Saturn's magnetosphere since 2004. The Cassini spacecraft contains several in-situ and remote sensing instruments providing numerous magnetospheric measurements and observations which have been widely used in this work.

The guiding line of the study achieved in this thesis was the investigation of the origin of the quasi-periodic ~ 1 -h pulsations observed in the energetic electron fluxes measured by the MIMI/LEMMS instrument. The hourly pulsed electron events are frequent, 720 events detected over 10 years, and occur globally in Saturn's outer magnetosphere. However, their spatial distribution is asymmetric with ten times more events on the duskside of the magnetosphere compared to the dawnside.

The results of this thesis indicate that the source of these energetic pulsed electrons is more likely located at high latitude given the local time independence of their morphology, for instance their mean interpulse period of 68 ± 10 min, and their higher growth and decay rate magnitudes at high latitude. The observation of strong bursts in the auroral hiss simultaneously to the electron flux pulsations reinforces this suggestion.

Additional results of the thesis suggest that the hourly pulsed electron events observed on the dawnside at high latitude are related to an auroral spot exhibiting quasi-periodic brightening with a period similar to the electrons. This auroral spot, located in the prenoon sector and poleward of the main auroral emission, is associated with the magnetospheric cusp. The polar cusp aurora is produced by magnetic reconnection at the magnetopause in the lobe regions. This reconnection process involves only open field lines. An analysis of the plasma environment has revealed that the high-latitude pulsed electron events in the dawn sector occur along open field lines in the lobe as well. It is then suggested that pulsed high-latitude magnetopause reconnection in the lobe triggers both the brightening of the polar cusp aurora and the high-latitude dawnside electron events.

Regarding the quasi-periodic hourly electron pulsations occurring at lower latitude on closed field lines, it has been highlighted for the first time that they can be encountered in the close vicinity of the magnetopause, in the boundary layer. Hence, it is thought that processes at the magnetopause trigger the electron pulsations. By analogy with the high-

latitude open field line events, bursty magnetopause reconnection can be invoked. The most plausible scenario for the electron acceleration is magnetic reconnection induced by Kelvin-Helmholtz instabilities at the low-latitude magnetopause. It is known that Kelvin-Helmholtz activity is enhanced on the dusk flank of the magnetosphere, which could explain the highest frequency of electron events in the dusk side. Furthermore, the K-H-induced magnetopause reconnection occur at higher latitude, in agreement with the suggestion of a high-latitude source for the pulsed electrons.

The main unanswered question remains the origin of the period of ~ 68 min. A possible explanation was proposed by Yates et al. (2016) based on magnetic fluctuations observed at high latitude. They argued that the hourly periodicities in the magnetic field are due to second harmonic Alfvén waves standing in Saturn’s outer magnetosphere between the two hemispheres. This second harmonic does not vary strongly with radial distance, similarly to the interpulse period of the hourly electron pulsations. Temporal variations of the plasma density in the plasma sheet could explain the fluctuations of the interpulse period around 68 min. However, it is still unclear how the Alfvén waves influence the reconnection burst periodicity at the magnetopause. Moreover, the Alfvén wave scenario cannot explain the ~ 1 -h periodicity of the electron pulsations occurring along open field lines.

7.2 Perspectives

Even though the aforementioned findings of this thesis brought forward the current understanding of the magnetospheric dynamics and pulsations at Saturn, they opened new questions to be addressed in the future. In order to complement these findings and validate the suggested scenarios, further analyses can be performed. A study about a pulsed motion of the main auroral emission has already started and is described in the next section. Some possible additional investigations are then suggested in the last section.

7.2.1 Pulsed oscillation of the main auroral emission

The extended distribution of hourly electron injections throughout Saturn’s outer magnetosphere and their pulsed signatures with no energy dispersion suggest that the hourly pulsations are produced at various places through a common global process. The auroral emissions provide a possible additional evidence that the ~ 1 -h pulsations at Saturn result from global magnetospheric dynamics. In this section, the first observation of a ~ 1 -h stepped oscillation of the main auroral emission is reported.

The main auroral emission at Saturn is roughly located at the boundary between open and closed field lines (see the description in Section 1.3.1). Using Hubble Space Telescope (HST) observations of the UV southern aurora in 2007 and 2008, Nichols et al. (2008) identified an oscillation motion of the center of the main auroral oval with a period of 10.75 h in 2007 and 10.79 h in 2008. This period is close to the periodicity of the southern oscillations in the Saturn Kilometric Radiation (SKR) power (Section 1.4.1). The oscillation of the oval center follows an eccentric ellipse of $1\text{-}2^\circ$ semi-major axis, oriented in the prenoon-premidnight direction. During the 2009 equinox HST campaign, centers of both northern and southern main emissions oscillate by $1\text{-}2^\circ$ in the dawn-dusk

direction (Nichols et al. 2010b). Nichols et al. (2010b) pointed out that the observed periodic motion is caused by the displacement of the entire oval rather than a periodic asymmetric expansion of the oval. The authors suggest that these auroral oscillations are induced by a rotating external magnetospheric current system. This current system produces rotating magnetic field perturbations associated with the observed planetary period oscillations (Provan et al. 2009, Andrews et al. 2010).

Bunce et al. (2014) reported throughout a 2h-long Cassini/UVIS imaging sequence a motion of the whole northern auroral main oval towards the premidnight sector at a rate of 1.1° in latitude per hour. Like in the previous studies, the latitudinal motion of the oval was consistent with the phase of the magnetosphere oscillations in the northern hemisphere at the time of the observations. Furthermore, using concurrent Cassini in-situ data, Bunce et al. (2014) argued that the field-aligned current system associated with the oscillating auroral oval is not static but also presents an oscillatory motion related to the magnetosphere oscillation phase.

During the Cassini/UVIS auroral imaging sequence on day 129 of 2008, a motion towards dayside of the main auroral oval is apparent. This motion does not seem to be continuous but jerky with increased displacement every hour. In order to analyze this motion, an elliptical fit has been applied to the main oval on the polar projections of all the UVIS pseudoimages of the sequence. This sequence is made up of 24 images and lasts for about 6 hours. The 24 fits of the main oval are displayed on the polar map on the left of Figure 7.1 with the Sun direction towards the bottom. The color scale enables the tracking of the main auroral emission position during the sequence. It is revealed that the auroral oval moves as a whole from the nightside towards the dayside. No significant change of the polar cap size is observed.

The crosses on the polar map indicate the center of the main oval inferred from the elliptical fits. A zoom on the center of the polar map is given on the right panel of Figure 7.1 where the motion of the oval center can be seen. A superimposed ellipse corresponds to the general displacement of the oval center. This ellipse is oriented along the premidnight-noon direction, at 30° from the noon-midnight meridian. This orientation of the oval center motion is similar to the orientation of the ellipses fitting the oval center motion inferred by Nichols et al. (2008) for 2007 and 2008 from HST observations. The two ellipses of Nichols et al. (2008) are drawn in red dashes in Figure 7.1. During the 2-h UVIS sequence analysed by Bunce et al. (2014), the main emission moved along the same orientation too, towards 21 LT.

The latitudinal displacement of the main emission has been further analyzed at noon and midnight. The temporal evolution of the main oval latitude at 12 LT and 0 LT is given on the top panels of Figure 7.2. The oval latitude decreases at noon and increases at midnight. The latitude variation can be fitted by a sinusoid with a period of 8.6 h at midnight and 10.5 h at noon, which is close to the typical planetary period (10.6-10.8 h). The latitudinal shift rate is close to 1° per hour, similar to the $1.1^\circ/\text{h}$ inferred by Bunce et al. (2014) from their observations. Thus, the main motion of the main emission in this current observation follow the auroral oscillation described previously by Nichols et al. (2008), Nichols et al. (2010b) and Bunce et al. (2014).

However, the latitude displacement of the oval exhibits fluctuations. Subtracting the sinusoidal fit to the latitude variation highlights these fluctuations which are quasi-periodic (middle panels in Figure 7.2). A Lomb-Scargle analysis revealed that the period

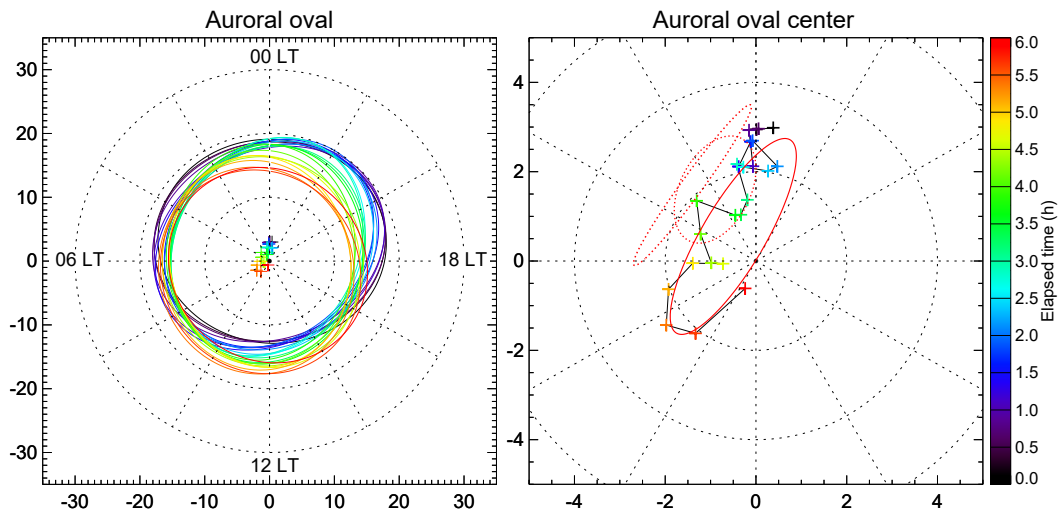


Figure 7.1: Motion of the main auroral oval during the Cassini/UVIS imaging sequence on day 129 of 2008. Left panel: Position on a polar map of the main oval determined by an elliptical fit for each of the 24 images. The direction of the Sun is towards the bottom. The parallels are drawn every 10° in latitude and the meridians every 2 h in local time. The color indicates the time from the start of the sequence. The center of the elliptical fits are indicated by the crosses. Right panel: Position of the elliptical fit center. The red thick ellipse superimposed gives the general motion of the auroral oval center. The two dashed red ellipses indicate the fit of the motion of the auroral oval center determined by Nichols et al. (2008) for 2007 and 2008 using HST images.

of these fluctuations is close to one hour (bottom panels of Figure 7.2). Hence, a ~ 1 -h stepped motion is superimposed to the oscillation of the main oval.

In the second part of another UVIS auroral sequence, on day 195 of 2008, the main auroral emission moves towards 10LT with some fluctuations. However, during this observing sequence, the main emission is well defined only in the morning, preventing an accurate fit of the main emission and thus making the analysis less reliable.

Further analysis needs to be carried out to validate this observation of this hourly pulsed oscillation of the main auroral oval. It is necessary to confirm that the fluctuations in the position of the oval are not due to instrumental or observational effects. If the observation is confirmed, since the whole auroral oval displays the hourly stepped motion, it suggests that these pulsations are generated by a global magnetospheric process. Opening of magnetic flux in the dayside causes an equatorward motion of the dayside arc of the main emission. Hence, pulsed dayside reconnection at the magnetopause could explain the stepped equatorward displacement of the oval in the dayside. However, a poleward motion of the nightside arc is induced by closure of the flux in the magnetotail (following the Dungey cycle explained in Section 1.2.4.4). Although no observational evidence of pulsed tail reconnection has been reported, it is not inconceivable that it is the case. The hourly quasi-periodic pulsed electron events in the midnight-to-dawn local time sector (Figure 3.3) could be triggered by pulsed tail reconnection. However, the existence of a direct connection between the reconnection bursts at the magnetopause and the ones in the tail is not obvious.

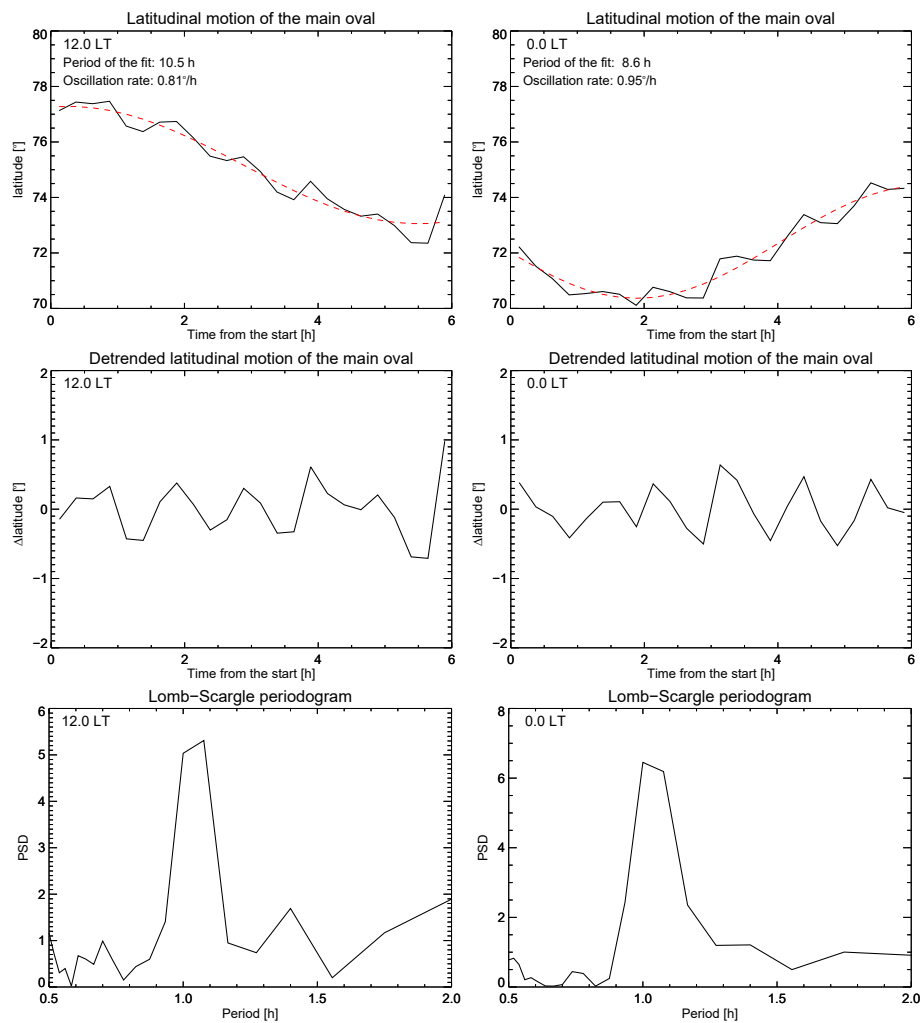


Figure 7.2: Latitudinal displacement of the main emission at 12 LT (left) and 0 LT (right) during the Cassini/UVIS imaging sequence on day 129 of 2008. Top panels: Evolution of the latitude of the main emission and fit by a sinusoid function (red dashed line). Middle panels: evolution of the latitude of the main emission detrended from the sinusoidal fit. Bottom panels: Lomb-Scargle periodogram of the detrended latitude evolution.

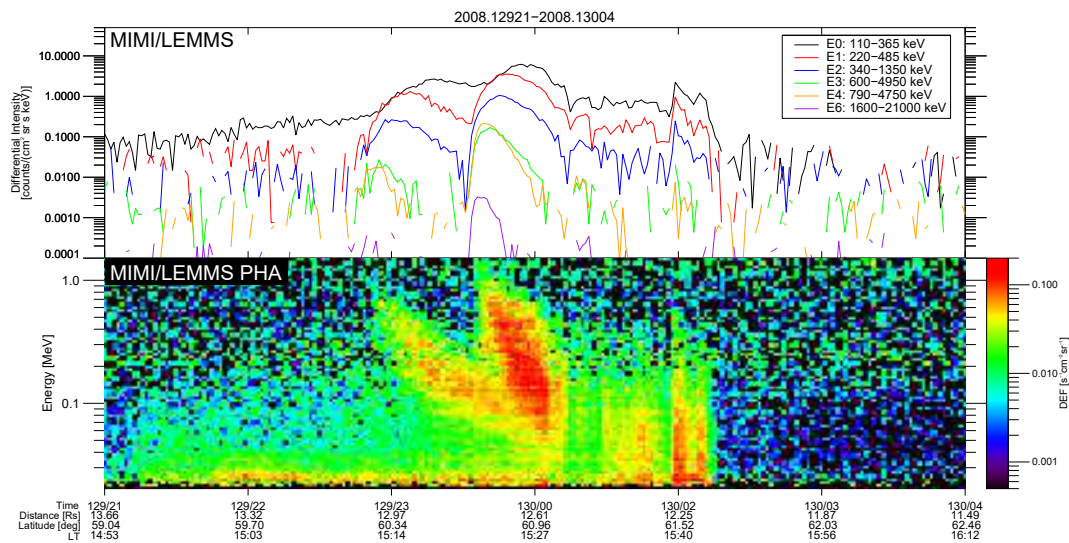


Figure 7.3: Pulsed electron injection on day 129 of 2008 exhibiting energy dispersion. Upper panel: differential intensities of energetic electrons from the MIMI/LEMMS channels E0 to E4 and E6. Lower panel: energetic electron energy-time spectrogram from the LEMMS Pulsed Height Analysis data.

7.2.2 Other perspectives

Energy-dispersion event

As mentioned in Section 3.5, the quasi-periodic hourly electron pulsations do not exhibit any dispersion in energy: the intensity peaks at the same time in each MIMI/LEMMS energy passband. This indicates that the electrons do not suffer from gradient or curvature drifts which lead to energy dispersion (see Section 1.2.4.1). This absence of energy dispersion can be explained by a short lifetime of the pulsed electrons, which means that the source of the electrons is close to the location where MIMI/LEMMS detects them, or by magnetic field curvature and gradient too small in the outer magnetosphere to generate significant drifts.

However, a peculiar pulsed electron event exhibits important energy dispersion. This event is shown in Figure 7.3 with the LEMMS electron differential intensities on the upper panel and an electron energy-time spectrogram from 64 energy channels of the LEMMS Pulse Height Analysis (PHA) data (Section 2.3.1). It can be seen on the spectrogram and in the electron fluxes that the most energetic electrons are detected before the electrons at lower energy. The slope of the energy dispersion on the LEMMS PHA spectrogram can be used combined with a magnetic field model to calculate the distance from the source. Once the position of the source is determined, it will be interesting to look at Cassini data in the source region in case the spacecraft has previously crossed this region. This analysis has not been done in this thesis.

Signature of Kelvin-Helmholtz activity

Up to now, only one observation of quasi-periodic electron pulsations together with a Kelvin-Helmholtz vortex has been reported (Masters et al. 2010). A new analysis of the

magnetic field data for all the electron events located in the boundary layer could result in the detection of twisted magnetic field topology, signature of K-H vortices. Coincident observations of K-H activity and hourly pulsed electrons would provide further arguments in favor of the suggested scenario, namely electron pulsations triggered by K-H-induced magnetopause reconnection.

Pulsed electron events deep inside the magnetosphere

In the nightside of the magnetosphere, some quasi-periodic hourly electron events are observed deep inside the magnetosphere, far away from the magnetopause (Figure 3.3). Since these events are energy dispersionless, it is not plausible that they are generated by magnetopause processes. For these events, a relation with the Vasyliūnas cycle is more likely. As discussed in Section 3.6, multiple reconnection sites spread over the dusk sector can be also invoked for triggering the pulsations deep inside the magnetosphere. These reconnection sites have been revealed by Delamere et al. (2015) after identifying in the Cassini/MAG data multiple reconnection-induced azimuthal forward bend of the magnetic field lines in the dusk sector. Following this scenario, similar forward bend signatures in the magnetic field measurements could be sought for these pulsed electron events.

Energy spectrum of the electron pulsations

In this thesis, the energy spectrum of the pulsed electrons has not been analysed. The calculation of the spectral index, i.e. the slope of the power spectrum, during the quasi-periodic electron pulsations could help to understand the acceleration mechanism. The spectral index is less negative when the electrons are accelerated. Hence, the evolution of the spectral index simultaneously to the quasi-periodic variation of the electron flux could indicate if the acceleration process is less efficient or interrupted during the decay phase of the electron pulsations. In case of bursty magnetopause reconnection, it is expected that there is no acceleration of electrons between two bursts.

Other Cassini datasets

The imaging of the energetic neutral atoms (ENA) emissions with the MIMI/INCA sensor could complement the multi-instrument study achieved in this thesis. The ENA emissions enable to remotely localize global plasma acceleration sites.

Furthermore, as stated in Chapter 4, the hourly pulsations observed in the magnetic field and in the radio emissions without counterpart in the LEMMS energetic electron data have not been considered in this thesis. Carbary et al. (2016) surveyed the quasi-periodic ~1-h bursts in the low-frequency radio emissions. For the magnetic field measurements, a survey and a statistical study as performed in this thesis has never been carried out. Likewise, there is no in-depth investigation of quasi-periodic hourly signal in the low-energy electrons or in the ion fluxes.

40-min pulsations in Jupiter's magnetosphere

Similar quasi-periodic energetic electron pulsations with a periodicity of 40 min have been reported in Jupiter's magnetosphere during the Ulysses and Cassini flybys (see Section 1.4.2). Data from the particle instrumentation on board the Galileo spacecraft (in orbit around Jupiter between 1995 and 2003) could be revisited in order to identify quasi-periodic enhancements in the electron flux. Furthermore, the current orbital mission Juno could provide a very good opportunity to study these electron pulsations at Jupiter. Juno spacecraft is traveling along polar orbits, flying closely over the poles in the dawn-to-noon local time sector. At Saturn, the most energetic hourly electron pulsations are found in that magnetospheric region.

Cassini F-Ring and Proximal orbits

Finally, since the start of the final phase of the mission in November 2016, the Cassini spacecraft is traveling along unprecedented orbits at short distances from Saturn (see Section 2.2). In particular, Cassini crosses high-latitude regions where the most energetic hourly electron pulsations have been observed. A preliminary list of potential pulsed electron events after July 2014 is provided in Appendix A.2. This list is based on an identification by-eye of the events and no further analysis has been applied on them yet. Undoubtedly, pulsed electron events detected during the "Grand Finale" will provide further information and could validate the conclusions of this thesis.

Appendix

A List of quasi-periodic hourly electron pulsed events

A.1 List of events used in this thesis: 1st July 2004 - 30rd June 2014

start time ['yyyy.dddhhmm']	end time ['yyyy.dddhhmm']	radial distance [R _S]	latitude [°]	local time [h]
2004.3040442	2004.3040812	20.2	-11.9	2.6
2005.1191925	2005.1192123	28.2	-18.5	9.1
2005.1200725	2005.1201040	25.5	-19.3	9.3
2005.1210034	2005.1210617	20.8	-20.5	9.9
2005.1261055	2005.1261522	29.4	-4.6	6.1
2005.1671112	2005.1671539	40.4	-11.5	7.2
2005.2120022	2005.2121153	21.2	-20.6	9.7
2005.2130729	2005.2131105	12.0	-21.9	11.3
2005.2160235	2005.2160625	21.1	-0.5	5.1
2005.2821607	2005.2821736	24.1	-0.4	9.0
2005.2982329	2005.2990338	31.5	-0.4	8.3
2005.2990533	2005.2991210	30.2	-0.4	8.4
2005.3640246	2005.3640639	38.1	-0.1	4.6
2005.3642028	2005.3642354	40.4	-0.1	4.7
2006.0292317	2006.0300414	62.6	-0.0	4.1
2006.0540102	2006.0540437	24.2	-0.4	7.9
2006.0631035	2006.0631331	43.2	0.1	3.0
2006.0820110	2006.0820248	23.5	0.3	23.6
2006.0830042	2006.0830600	30.3	0.3	0.3
2006.0830944	2006.0831900	33.0	0.3	0.5
2006.0841106	2006.0841557	38.1	0.3	0.8
2006.1071300	2006.1071846	60.0	0.0	3.6
2006.1081407	2006.1081857	57.7	0.0	3.7
2006.1082018	2006.1090606	56.7	0.0	3.8
2006.1450854	2006.1451123	28.9	0.4	22.2
2006.1461728	2006.1461939	36.5	0.4	22.7
2006.1821134	2006.1821958	14.3	0.1	20.1
2006.1830111	2006.1830450	18.4	0.2	20.9
2006.1831235	2006.1831632	22.1	0.3	21.4

A List of quasi-periodic hourly electron pulsed events

start time ['yyyy.dddhhmm']	end time ['yyyy.dddhhmm']	radial distance [R_S]	latitude [$^\circ$]	local time [h]
2006.1992051	2006.2000014	37.0	0.4	1.1
2006.2090846	2006.2091157	35.2	13.5	22.2
2006.2100348	2006.2100957	38.4	13.0	22.5
2006.2101332	2006.2101939	39.7	12.8	22.6
2006.2110121	2006.2110606	41.2	12.6	22.7
2006.2111255	2006.2111845	42.5	12.4	22.8
2006.2131822	2006.2132145	46.9	11.4	23.2
2006.2151333	2006.2151902	48.7	10.6	23.5
2006.2160218	2006.2160620	48.9	10.4	23.6
2006.2171046	2006.2171356	48.9	9.8	23.8
2006.2180736	2006.2181228	48.5	9.4	23.9
2006.2181828	2006.2182218	48.1	9.2	12.0
2006.2300922	2006.2301433	18.7	14.7	20.6
2006.2302127	2006.2310801	23.1	14.6	21.1
2006.2320021	2006.2320315	29.0	14.1	21.7
2006.2351744	2006.2361106	43.7	12.0	22.8
2006.2361938	2006.2362354	45.3	11.7	23.0
2006.2370320	2006.2370458	45.8	11.6	23.1
2006.2371446	2006.2371843	46.6	11.3	23.1
2006.2380011	2006.2380656	47.2	11.1	23.2
2006.2381421	2006.2381737	47.8	10.9	23.3
2006.2390135	2006.2390614	48.2	10.7	23.4
2006.2421710	2006.2421901	48.0	9.0	24.0
2006.2431339	2006.2431607	47.0	8.6	0.1
2006.2451013	2006.2451200	43.7	7.4	0.4
2006.2532215	2006.2540009	15.8	23.1	21.7
2006.2621222	2006.2621704	36.2	9.9	0.8
2006.2622208	2006.2630812	35.3	9.1	1.0
2006.2690752	2006.2691109	9.0	34.2	18.5
2006.2702307	2006.2710217	21.9	34.7	22.0
2006.2852038	2006.2852313	11.9	40.5	17.9
2006.2992338	2006.3000157	12.0	-24.9	3.5
2006.3250849	2006.3251427	8.2	43.4	17.1
2006.3442242	2006.3450203	26.1	12.6	1.5
2006.3481355	2006.3481640	8.5	-52.3	8.0
2007.0371644	2007.0372308	25.5	41.4	16.1
2007.0511927	2007.0512221	17.0	-29.8	12.5
2007.0650541	2007.0650747	13.8	-14.0	2.4
2007.0661231	2007.0661843	12.4	-58.2	8.0
2007.0830108	2007.0830452	11.0	-51.2	9.9
2007.0890413	2007.0890558	32.1	32.7	15.7
2007.0891719	2007.0891942	32.6	35.3	16.0
2007.0970743	2007.0971445	13.5	33.2	12.0
2007.1002355	2007.1010321	20.4	1.3	13.8
2007.1022108	2007.1030439	29.0	16.4	14.8

A.1 List of events used in this thesis: 1st July 2004 - 30rd June 2014

start time ['yyyy.dddhhmm']	end time ['yyyy.dddhhmm']	radial distance [R _S]	latitude [°]	local time [h]
2007.1030816	2007.1031108	30.0	18.2	14.9
2007.1031717	2007.1032234	31.2	20.3	15.1
2007.1041653	2007.1042114	33.1	24.3	15.4
2007.1061054	2007.1061232	34.7	30.3	15.9
2007.1080532	2007.1080813	34.0	35.9	16.6
2007.1081459	2007.1081659	33.5	37.0	16.7
2007.1230412	2007.1230918	36.2	24.2	15.9
2007.1231626	2007.1231912	36.0	25.2	16.0
2007.1330451	2007.1331451	23.3	2.8	14.0
2007.1350458	2007.1352237	32.4	9.3	14.8
2007.1450549	2007.1450758	19.4	26.1	18.0
2007.1451554	2007.1452210	15.3	27.4	18.7
2007.1460409	2007.1460853	11.0	28.1	19.7
2007.1582053	2007.1582329	31.6	12.8	16.5
2007.1600556	2007.1601117	25.6	14.5	17.0
2007.1601330	2007.1601810	23.9	14.9	17.2
2007.1610009	2007.1610624	20.9	15.7	17.5
2007.1611243	2007.1611607	17.5	16.6	17.9
2007.1690231	2007.1690446	36.7	0.8	15.1
2007.1730431	2007.1730715	36.2	1.2	16.0
2007.1761413	2007.1761743	24.2	1.7	17.1
2007.1810739	2007.1811358	24.9	-0.2	14.1
2007.1811711	2007.1812259	27.1	-0.1	14.3
2007.1841224	2007.1841736	39.2	-0.0	15.2
2007.1870733	2007.1870904	45.5	0.0	15.7
2007.1961438	2007.1961856	37.7	0.2	17.4
2007.1971107	2007.1980052	33.5	0.2	17.7
2007.2682105	2007.2690025	36.6	-6.1	16.6
2007.2690246	2007.2691941	34.0	-6.1	16.8
2007.2701542	2007.2702046	26.7	-6.2	17.3
2007.2710158	2007.2710704	24.0	-6.2	17.6
2007.3170242	2007.3170537	33.9	4.2	15.7
2007.3460958	2007.3461423	36.9	14.9	13.7
2007.3490356	2007.3492011	29.9	19.3	14.5
2007.3501258	2007.3501737	24.7	21.4	15.0
2007.3512313	2007.3520359	15.0	25.0	16.3
2007.3650626	2007.3651625	28.4	31.4	14.9
2008.0020650	2008.0021023	18.4	36.6	16.3
2008.0030353	2008.0031054	10.4	35.8	18.6
2008.0070204	2008.0070737	25.7	8.7	11.9
2008.0072254	2008.0080614	28.2	13.1	12.2
2008.0091840	2008.0092306	30.2	20.1	12.7
2008.0100519	2008.0101240	30.1	22.0	12.8
2008.0120942	2008.0121227	26.5	30.1	13.6
2008.0240901	2008.0241317	26.2	30.5	13.6
2008.0241709	2008.0242211	24.9	32.2	13.7
2008.0270029	2008.0270311	11.1	45.9	16.6

A List of quasi-periodic hourly electron pulsed events

start time ['yyyy.dddhhmm']	end time ['yyyy.dddhhmm']	radial distance [R_S]	latitude [$^\circ$]	local time [h]
2008.0301410	2008.0301716	24.1	6.5	11.7
2008.0320918	2008.0321237	29.1	15.4	12.3
2008.0321943	2008.0330121	29.7	17.3	12.4
2008.0342215	2008.0350625	29.2	25.4	13.0
2008.0361105	2008.0361602	25.7	31.3	13.6
2008.0361732	2008.0370129	24.5	32.9	13.8
2008.0370615	2008.0371321	22.2	35.5	14.1
2008.0491310	2008.0491702	21.1	36.8	14.2
2008.0492252	2008.0500904	17.9	40.3	14.8
2008.0552044	2008.0560003	26.4	16.9	12.0
2008.0570517	2008.0571049	27.0	25.1	12.5
2008.0582259	2008.0590358	23.9	35.6	13.1
2008.0591827	2008.0600215	20.5	42.1	13.7
2008.0611852	2008.0612109	6.7	47.5	20.0
2008.0751617	2008.0752004	23.1	7.0	11.5
2008.0781641	2008.0782332	26.9	26.5	12.5
2008.0791316	2008.0791701	25.7	31.2	12.8
2008.1071055	2008.1071342	24.4	25.4	12.0
2008.1080238	2008.1081040	23.6	31.6	12.3
2008.1081329	2008.1082038	22.7	35.4	12.5
2008.1091011	2008.1091827	19.9	44.1	13.0
2008.1180107	2008.1180555	23.0	34.3	12.4
2008.1292254	2008.1300047	12.9	60.4	15.3
2008.1361014	2008.1361637	19.9	30.7	11.9
2008.1362352	2008.1370506	17.8	37.4	12.1
2008.1431458	2008.1432018	21.7	22.6	11.6
2008.1681013	2008.1681750	6.5	-58.8	8.2
2008.1690342	2008.1690752	12.7	-25.2	10.4
2008.1691344	2008.1691859	15.7	-14.9	10.6
2008.1710611	2008.1711113	20.8	5.9	11.0
2008.1720907	2008.1721100	20.5	16.3	11.2
2008.1721724	2008.1722134	19.8	20.5	11.3
2008.1810246	2008.1810732	13.7	40.5	11.7
2008.1870615	2008.1871202	18.2	25.9	11.3
2008.1881251	2008.1881948	10.1	54.3	12.4
2008.1891846	2008.1892205	7.4	-50.5	9.5
2008.1961545	2008.1962040	5.9	-62.8	7.9
2008.1962317	2008.1970547	9.6	-38.6	9.9
2008.2021808	2008.2022227	9.4	56.7	12.4
2008.2081052	2008.2081535	18.0	26.3	11.3
2008.2140520	2008.2141042	20.0	15.0	11.0
2008.2211928	2008.2220040	19.8	17.5	11.0
2008.2231333	2008.2231635	13.6	46.9	11.9
2008.2360902	2008.2361305	19.9	15.5	11.0
2008.2371621	2008.2372032	16.5	34.5	11.4
2008.2380500	2008.2380834	14.0	45.3	11.8
2008.2471033	2008.2471308	7.5	-65.9	8.0

A.1 List of events used in this thesis: 1st July 2004 - 30rd June 2014

start time ['yyyy.dddhhmm']	end time ['yyyy.dddhhmm']	radial distance [R _S]	latitude [°]	local time [h]
2008.2520022	2008.2520359	18.1	27.1	11.2
2008.2521609	2008.2522354	15.0	40.7	11.6
2008.2542351	2008.2550236	9.3	-53.1	9.2
2008.2550452	2008.2550900	11.1	-42.9	9.6
2008.2551821	2008.2552121	14.7	-25.7	10.1
2008.2580014	2008.2580245	20.3	8.4	10.8
2008.2661209	2008.2661544	18.8	23.4	11.0
2008.2692123	2008.2700544	11.5	-41.1	9.6
2008.2740748	2008.2741628	17.0	32.2	11.2
2008.2741857	2008.2742349	15.3	39.4	11.5
2008.2770008	2008.2770137	8.3	-60.2	8.6
2008.2770801	2008.2771018	11.1	-42.9	9.6
2008.2821717	2008.2821945	12.1	53.2	12.0
2008.2830114	2008.2830421	9.3	66.8	13.4
2008.2911210	2008.2911809	7.5	-65.7	7.3
2008.2971602	2008.2972105	9.1	67.7	13.7
2008.2982219	2008.2990734	9.1	-55.8	8.6
2008.3140701	2008.3141613	8.1	-58.3	7.3
2008.3201554	2008.3202140	12.7	58.0	12.8
2008.3210323	2008.3210631	9.6	68.7	15.1
2008.3220649	2008.3221532	8.0	-58.7	7.2
2008.3261701	2008.3262320	18.4	30.7	11.2
2008.3271712	2008.3272154	14.7	49.7	11.9
2008.3310434	2008.3311311	16.3	-22.1	9.9
2008.3332015	2008.3341711	19.3	23.0	10.9
2008.3421449	2008.3422243	15.9	37.0	11.3
2008.3430252	2008.3430606	14.1	46.9	11.7
2008.3541755	2008.3542151	16.4	-30.4	9.6
2008.3551211	2008.3551902	18.7	-14.7	10.0
2008.3560221	2008.3560541	19.5	-6.3	10.2
2008.3562253	2008.3570429	19.5	8.8	10.6
2008.3650616	2008.3650902	19.5	-14.6	9.9
2009.0062001	2009.0070038	15.5	-54.6	8.1
2009.0101844	2009.0102228	18.7	20.9	10.8
2009.0170136	2009.0170338	17.2	-40.9	9.0
2009.0170933	2009.0171605	18.1	-32.2	9.3
2009.0210418	2009.0211157	16.8	39.4	11.5
2009.0251123	2009.0251335	13.6	-66.9	5.9
2009.0272104	2009.0280009	19.3	-16.3	9.8
2009.0291759	2009.0292111	18.9	17.4	10.7
2009.0300328	2009.0300837	18.2	25.7	11.0
2009.0330204	2009.0330502	9.4	29.7	21.4
2009.0380143	2009.0380628	19.7	-3.8	10.1
2009.0391341	2009.0391746	19.7	23.9	11.0
2009.0392019	2009.0392301	19.6	28.8	11.2
2009.0400121	2009.0400550	19.5	33.4	11.4
2009.0400955	2009.0401531	19.2	40.4	11.8

A List of quasi-periodic hourly electron pulsed events

start time ['yyyy.dddhhmm']	end time ['yyyy.dddhhmm']	radial distance [R _S]	latitude [°]	local time [h]
2009.0471414	2009.0472326	16.9	-53.0	7.6
2009.0480326	2009.0480828	17.6	-43.2	8.5
2009.0481343	2009.0481826	18.2	-34.0	9.0
2009.0521601	2009.0521929	18.9	45.6	12.1
2009.0560134	2009.0560356	14.1	22.1	21.5
2009.0570026	2009.0570233	13.6	-15.8	22.7
2009.0601427	2009.0601756	18.3	-32.9	9.0
2009.0641728	2009.0641954	18.8	47.5	12.2
2009.0830520	2009.0830820	16.3	-60.4	6.5
2009.0871710	2009.0872307	19.7	33.5	11.5
2009.0880120	2009.0880732	19.7	40.0	11.9
2009.0940711	2009.0941135	20.8	-5.9	22.3
2009.1031458	2009.1031908	20.8	44.9	12.2
2009.1032123	2009.1040050	20.9	48.8	12.6
2009.1091150	2009.1091643	21.1	7.9	21.8
2009.1101421	2009.1101615	20.1	-11.9	22.5
2009.1250819	2009.1250955	21.6	10.0	21.6
2009.1252015	2009.1252239	21.0	1.2	22.0
2009.1300009	2009.1300515	15.3	-41.2	8.0
2009.1340402	2009.1341554	22.9	51.5	13.0
2009.1402321	2009.1410616	22.3	13.2	21.5
2009.1430244	2009.1430816	16.4	-28.0	23.2
2009.1471011	2009.1471311	18.5	31.9	11.4
2009.1472050	2009.1472252	19.9	39.7	12.0
2009.1620127	2009.1620808	15.3	31.4	11.6
2009.1621028	2009.1622357	17.8	41.7	12.5
2009.1710209	2009.1710707	28.5	26.7	20.6
2009.1711157	2009.1711648	27.7	23.5	20.7
2009.1730256	2009.1730627	23.1	7.8	21.5
2009.1750223	2009.1750522	12.7	-27.4	23.5
2009.1831357	2009.1831650	33.2	37.8	19.3
2009.1890337	2009.1890943	22.9	5.1	21.6
2009.1900850	2009.1901224	16.2	-9.4	22.5
2009.1921756	2009.1922115	11.6	39.4	13.6
2009.1930037	2009.1930406	13.9	42.8	14.5
2009.1981115	2009.1981344	34.5	31.5	19.2
2009.2021108	2009.2021534	32.4	18.5	20.5
2009.2031930	2009.2040054	28.6	12.3	20.9
2009.2050335	2009.2050818	23.0	3.6	21.5
2009.2110607	2009.2111053	29.0	27.9	18.5
2009.2150853	2009.2151254	36.6	19.4	19.7
2009.2190102	2009.2190442	31.8	10.9	20.7
2009.2191219	2009.2191521	30.3	9.5	20.8
2009.2301227	2009.2301900	37.4	11.3	19.6
2009.2351609	2009.2351922	30.0	4.9	20.9
2009.2360249	2009.2360849	27.9	3.9	21.1
2009.2511644	2009.2512241	48.9	8.1	19.0

A.1 List of events used in this thesis: 1st July 2004 - 30rd June 2014

start time ['yyyy.dddhhmm']	end time ['yyyy.dddhhmm']	radial distance [R _S]	latitude [°]	local time [h]
2009.2520654	2009.2520911	48.7	7.9	19.1
2009.2530122	2009.2530333	48.3	7.6	19.2
2009.2531520	2009.2531748	47.8	7.4	19.3
2009.2551917	2009.2552351	44.2	6.4	19.7
2009.2570847	2009.2571149	40.3	5.4	20.0
2009.2580058	2009.2580510	38.0	4.9	20.2
2009.2651239	2009.2651704	22.9	11.9	16.3
2009.2740420	2009.2741428	48.5	8.5	18.7
2009.2751629	2009.2751933	48.7	8.0	18.9
2009.2760931	2009.2761252	48.5	7.7	19.0
2009.2761519	2009.2762104	48.3	7.6	19.1
2009.2771743	2009.2771919	47.4	7.2	19.3
2009.2780735	2009.2781112	46.6	6.9	19.4
2009.2782010	2009.2790123	45.7	6.6	19.5
2009.2791512	2009.2791937	44.2	6.2	19.6
2009.2830105	2009.2830800	33.2	3.7	20.5
2009.2831126	2009.2831534	31.4	3.3	20.6
2009.2911314	2009.2911651	33.8	0.4	18.2
2009.2920902	2009.2921308	36.4	0.4	18.5
2009.2990418	2009.2990846	40.2	0.4	19.8
2009.2991438	2009.2992131	39.4	0.3	19.9
2009.3001629	2009.3001933	37.1	0.3	20.2
2009.3011230	2009.3011654	34.4	0.3	20.4
2009.3111749	2009.3112213	37.6	0.4	18.5
2009.3180055	2009.3180527	40.5	0.4	19.8
2009.3221453	2009.3221717	25.2	0.2	21.1
2009.3281338	2009.3282144	30.2	0.4	17.9
2009.3291105	2009.3291301	33.4	0.4	18.2
2009.3302023	2009.3302346	37.8	0.4	18.5
2009.3311822	2009.3320008	39.9	0.4	18.7
2009.3320629	2009.3320859	40.6	0.4	18.8
2009.3330214	2009.3330520	41.7	0.4	19.0
2009.3331351	2009.3331801	42.1	0.4	19.1
2009.3340113	2009.3340632	42.3	0.4	19.2
2009.3341044	2009.3341503	42.4	0.4	19.3
2009.3341816	2009.3342048	42.4	0.4	19.3
2009.3350850	2009.3351541	42.2	0.4	19.4
2009.3351853	2009.3352312	42.0	0.4	19.5
2009.3360456	2009.3361549	41.5	0.4	19.6
2009.3370158	2009.3370736	40.5	0.4	19.8
2009.3502013	2009.3502313	37.3	-1.7	18.6
2009.3510229	2009.3510737	37.6	-1.7	18.7
2009.3511723	2009.3512044	37.9	-1.9	18.8
2009.3512202	2009.3520120	38.0	-1.9	18.9
2009.3520719	2009.3521325	38.0	-2.0	18.9
2009.3521855	2009.3530244	37.8	-2.2	19.1
2009.3530638	2009.3531044	37.5	-2.3	19.1

A List of quasi-periodic hourly electron pulsed events

start time ['yyyy.dddhhmm']	end time ['yyyy.dddhhmm']	radial distance [R_S]	latitude [$^\circ$]	local time [h]
2009.3531819	2009.3540323	36.8	-2.4	19.3
2009.3551108	2009.3560453	32.7	-2.9	19.7
2009.3560529	2009.3561553	30.7	-3.1	19.9
2009.3561716	2009.3570653	28.3	-3.3	20.1
2009.3620353	2009.3620659	21.7	-0.5	17.1
2009.3621543	2009.3622126	24.9	-2.3	17.4
2010.0010710	2010.0011011	36.3	-8.7	18.5
2010.0011531	2010.0011842	36.7	-9.1	18.6
2010.0020345	2010.0020754	37.2	-9.8	18.7
2010.0021413	2010.0022126	37.5	-10.4	18.8
2010.0041005	2010.0041321	36.9	-12.3	19.2
2010.0042000	2010.0042224	36.4	-12.7	19.3
2010.0050527	2010.0050839	35.8	-13.2	19.4
2010.0130727	2010.0131220	23.2	-0.4	17.2
2010.0140354	2010.0140912	27.7	-0.9	17.6
2010.0160057	2010.0160529	34.3	-1.7	18.2
2010.0161027	2010.0161558	35.2	-1.8	18.3
2010.0162037	2010.0162336	36.0	-1.9	18.4
2010.0170048	2010.0170501	36.3	-2.0	18.4
2010.0172156	2010.0172348	37.4	-2.2	18.6
2010.0182124	2010.0182354	38.0	-2.5	18.8
2010.0190217	2010.0190801	38.0	-2.5	18.9
2010.0191226	2010.0192233	37.9	-2.6	19.0
2010.0200204	2010.0200725	37.6	-2.8	19.1
2010.0220713	2010.0221208	33.8	-3.3	19.6
2010.0221730	2010.0222236	32.5	-3.4	19.7
2010.0230225	2010.0230905	31.2	-3.6	19.8
2010.0231950	2010.0232145	28.7	-3.8	20.0
2010.0381804	2010.0382054	37.4	0.0	19.7
2010.0391517	2010.0391927	35.2	0.0	19.9
2010.0400146	2010.0400527	33.8	0.1	20.0
2010.0401407	2010.0402006	31.9	0.1	20.2
2010.0410037	2010.0410419	30.2	0.1	20.3
2010.0411302	2010.0411709	27.9	0.1	20.5
2010.0420415	2010.0420609	24.8	0.1	20.8
2010.0470306	2010.0470733	25.0	-0.1	17.4
2010.0480208	2010.0480753	29.9	-0.1	17.8
2010.0520535	2010.0521030	39.9	-0.0	18.8
2010.0530150	2010.0530612	40.3	0.0	19.0
2010.0580027	2010.0580337	32.5	0.1	20.1
2010.0580639	2010.0581251	31.3	0.1	20.2
2010.0581646	2010.0582007	29.8	0.1	20.3
2010.0590032	2010.0590244	28.5	0.1	20.4
2010.0590757	2010.0591243	26.6	0.1	20.6
2010.0600039	2010.0600300	22.8	0.1	20.9
2010.0600630	2010.0600924	21.2	0.1	21.1
2010.0641550	2010.0642134	25.1	0.2	17.4

A.1 List of events used in this thesis: 1st July 2004 - 30rd June 2014

start time ['yyyy.dddhhmm']	end time ['yyyy.dddhhmm']	radial distance [R _S]	latitude [°]	local time [h]
2010.0690315	2010.0690920	39.3	0.3	18.7
2010.0762122	2010.0762344	27.3	0.3	20.5
2010.0770834	2010.0771002	24.9	0.3	20.7
2010.0871952	2010.0880046	40.2	0.3	18.9
2010.0900655	2010.0900959	39.5	0.3	19.3
2010.1141322	2010.1142332	28.4	0.1	20.3
2010.1201121	2010.1202159	26.6	0.3	16.8
2010.1290245	2010.1290645	44.0	0.2	18.8
2010.1290928	2010.1291816	43.7	0.2	18.9
2010.1300629	2010.1301949	42.6	0.2	19.1
2010.1311011	2010.1311347	41.1	0.2	19.2
2010.1311516	2010.1312338	40.4	0.2	19.3
2010.1320112	2010.1321009	39.4	0.2	19.4
2010.1321051	2010.1321951	38.4	0.2	19.5
2010.1330504	2010.1331203	36.2	0.2	19.7
2010.1331550	2010.1331950	34.7	0.2	19.8
2010.1332239	2010.1340351	33.7	0.2	19.9
2010.1340514	2010.1340819	32.8	0.2	20.0
2010.1341539	2010.1342147	30.7	0.2	20.1
2010.1400522	2010.1401628	22.3	0.7	16.3
2010.1451231	2010.1451733	37.6	5.7	17.9
2010.1452046	2010.1460002	37.8	5.9	18.0
2010.1460531	2010.1461122	37.8	6.1	18.1
2010.1461446	2010.1462343	37.7	6.4	18.2
2010.1481241	2010.1482135	35.5	7.5	18.6
2010.1492039	2010.1492327	32.5	8.2	18.9
2010.1562119	2010.1570051	25.4	0.2	16.6
2010.1570228	2010.1570710	26.7	0.1	16.7
2010.1572243	2010.1580030	30.1	-0.0	17.0
2010.1580822	2010.1581200	31.7	-0.1	17.1
2010.1590431	2010.1590729	34.2	-0.2	17.4
2010.1591552	2010.1592225	35.4	-0.3	17.5
2010.1600121	2010.1600709	36.1	-0.3	17.6
2010.1641437	2010.1642142	35.6	-0.8	18.6
2010.1650029	2010.1650904	34.5	-0.9	18.7
2010.1680621	2010.1680953	21.5	-1.4	19.9
2010.1732213	2010.1732358	30.1	-4.4	17.0
2010.1741036	2010.1741624	32.2	-5.4	17.2
2010.1741830	2010.1742355	33.1	-5.8	17.3
2010.1750020	2010.1750238	33.6	-6.1	17.3
2010.1752034	2010.1760142	35.6	-7.2	17.6
2010.1760303	2010.1760647	36.0	-7.5	17.6
2010.1830719	2010.1831237	26.0	-15.2	19.6
2010.1840627	2010.1840940	20.7	-16.7	20.1
2010.1850726	2010.1851138	11.9	-18.9	21.5
2010.1991736	2010.1991934	39.7	-3.3	19.2
2010.2020134	2010.2020340	32.4	-3.8	19.8

A List of quasi-periodic hourly electron pulsed events

start time ['yyyy.dddhhmm']	end time ['yyyy.dddhhmm']	radial distance [R_S]	latitude [$^\circ$]	local time [h]
2010.2022228	2010.2030304	28.3	-4.0	20.1
2010.2130405	2010.2130903	41.2	-2.1	17.9
2010.2140744	2010.2141343	42.8	-2.3	18.2
2010.2141950	2010.2150047	43.2	-2.4	18.2
2010.2170325	2010.2170813	43.2	-2.8	18.7
2010.2171057	2010.2171929	42.9	-2.9	18.7
2010.2180844	2010.2181858	41.7	-3.1	18.9
2010.2200634	2010.2201129	38.0	-3.4	19.3
2010.2220801	2010.2221408	30.5	-3.9	19.9
2010.2280621	2010.2281111	23.8	-0.3	16.4
2010.2281505	2010.2282150	26.2	-0.6	16.6
2010.2291159	2010.2291459	30.3	-1.0	16.9
2010.2301031	2010.2301440	34.3	-1.4	17.3
2010.2320535	2010.2320907	39.6	-1.9	17.7
2010.2382208	2010.2390353	41.1	-3.2	19.0
2010.2391204	2010.2392157	39.8	-3.3	19.1
2010.2410309	2010.2410805	35.5	-3.6	19.5
2010.2411504	2010.2412254	33.5	-3.8	19.7
2010.2420318	2010.2420924	31.6	-3.9	19.8
2010.2421155	2010.2421949	29.7	-4.0	20.0
2010.2530920	2010.2531230	41.6	-2.2	17.9
2010.2560630	2010.2561303	43.5	-2.8	18.5
2010.2640015	2010.2640534	20.8	-4.5	20.8
2010.2680424	2010.2681045	23.9	-0.3	16.3
2010.2690059	2010.2690945	29.3	-0.6	16.8
2010.2691152	2010.2691839	31.3	-0.8	17.0
2010.2770540	2010.2770947	48.8	-1.9	18.6
2010.2771119	2010.2771845	48.8	-1.9	18.7
2010.2780056	2010.2780847	48.8	-2.0	18.8
2010.2791644	2010.2792339	47.9	-2.1	19.0
2010.2801723	2010.2802139	46.8	-2.2	19.2
2010.2810129	2010.2810515	46.3	-2.3	19.2
2010.2811258	2010.2820218	45.1	-2.3	19.4
2010.2820321	2010.2821235	44.1	-2.4	19.5
2010.2821551	2010.2822218	43.0	-2.4	19.5
2010.2830115	2010.2831126	41.8	-2.5	19.6
2010.2831319	2010.2831928	40.7	-2.5	19.7
2010.2840046	2010.2840728	39.1	-2.6	19.8
2010.2840818	2010.2842005	37.6	-2.6	20.0
2010.2842338	2010.2850136	36.0	-2.7	20.1
2010.2860602	2010.2861100	30.1	-2.8	20.5
2010.2931320	2010.2932313	33.0	-1.0	17.0
2010.2940713	2010.2941810	36.3	-1.2	17.3
2010.2951630	2010.2952027	40.6	-1.4	17.6
2010.3020323	2010.3020837	49.1	-2.1	18.7
2010.3021938	2010.3022311	48.9	-2.1	18.8
2010.3041457	2010.3042045	47.1	-2.3	19.1

A.1 List of events used in this thesis: 1st July 2004 - 30rd June 2014

start time ['yyyy.dddhhmm']	end time ['yyyy.dddhhmm']	radial distance [R _S]	latitude [°]	local time [h]
2010.3060706	2010.3061256	44.1	-2.5	19.4
2010.3061705	2010.3062127	43.2	-2.5	19.5
2010.3250231	2010.3250605	44.2	-0.1	18.5
2010.3252303	2010.3260243	43.5	-0.1	18.7
2010.3261019	2010.3261405	42.9	-0.1	18.7
2010.3261635	2010.3262321	42.4	-0.1	18.8
2010.3270057	2010.3270437	42.0	-0.1	18.9
2010.3270701	2010.3271051	41.5	-0.1	18.9
2010.3271217	2010.3272125	40.8	-0.1	19.0
2010.3280159	2010.3280419	39.9	-0.1	19.1
2010.3280923	2010.3281511	38.9	-0.1	19.2
2010.3281731	2010.3282205	38.0	-0.1	19.2
2010.3290037	2010.3290537	37.1	-0.1	19.3
2010.3291154	2010.3291707	35.5	-0.1	19.4
2010.3291923	2010.3292351	34.5	-0.1	19.5
2010.3441450	2010.3442035	44.4	-0.1	18.3
2010.3460626	2010.3461330	43.6	-0.1	18.6
2010.3461605	2010.3462021	43.2	-0.1	18.7
2010.3462126	2010.3470206	43.0	-0.1	18.7
2010.3470459	2010.3470806	42.5	-0.1	18.8
2010.3471741	2010.3472347	41.5	-0.1	18.9
2010.3481209	2010.3481938	39.9	-0.1	19.0
2010.3492235	2010.3500503	35.8	-0.1	19.4
2010.3501153	2010.3501539	34.0	-0.1	19.5
2010.3501744	2010.3502350	32.9	-0.1	19.6
2011.0010749	2011.0010958	44.4	-0.1	18.4
2011.0031122	2011.0031752	41.6	-0.1	18.9
2011.0232206	2011.0240242	41.5	0.3	18.8
2011.0270212	2011.0270648	32.1	0.3	19.6
2011.0280919	2011.0281140	25.9	0.2	20.1
2011.0330414	2011.0330617	22.4	0.1	15.9
2011.0331533	2011.0331824	25.5	0.1	16.2
2011.0352121	2011.0352322	35.6	0.2	17.1
2011.0360847	2011.0361115	37.1	0.2	17.2
2011.0430305	2011.0430459	43.3	0.3	18.5
2011.0440728	2011.0441404	41.5	0.3	18.8
2011.0442101	2011.0442344	40.5	0.3	18.9
2011.0450726	2011.0451215	39.5	0.3	19.0
2011.0451629	2011.0452325	38.3	0.3	19.1
2011.0460210	2011.0460608	37.3	0.3	19.1
2011.0461257	2011.0462035	35.8	0.3	19.3
2011.0480033	2011.0480421	30.0	0.3	19.7
2011.0540106	2011.0540539	25.5	0.1	15.0
2011.0731833	2011.0732225	40.3	0.3	18.9
2011.0740354	2011.0740831	38.7	0.3	19.0
2011.0741442	2011.0741912	36.9	0.3	19.1
2011.0751844	2011.0760321	30.9	0.3	19.6

A List of quasi-periodic hourly electron pulsed events

start time ['yyyy.dddhhmm']	end time ['yyyy.dddhhmm']	radial distance [R _S]	latitude [°]	local time [h]
2011.0760344	2011.0760845	29.3	0.3	19.7
2011.0761105	2011.0762024	27.2	0.3	19.9
2011.0770110	2011.0770829	23.5	0.2	20.2
2011.0771638	2011.0771856	19.8	0.2	20.7
2011.0851604	2011.0860119	42.8	0.3	16.2
2011.1021709	2011.1022300	36.0	0.3	19.1
2011.1031402	2011.1032111	31.7	0.3	19.4
2011.1101609	2011.1102027	29.5	0.2	15.2
2011.1121206	2011.1121604	37.5	0.2	15.8
2011.1122145	2011.1130330	39.1	0.2	16.0
2011.1130903	2011.1131327	40.4	0.3	16.1
2011.1871613	2011.1872212	31.8	0.3	16.5
2011.1880157	2011.1880936	29.8	0.3	16.7
2011.2061704	2011.2062004	40.8	0.2	15.8
2011.2071828	2011.2080009	37.8	0.3	16.0
2011.2080152	2011.2080830	36.8	0.3	16.1
2011.2081809	2011.2082013	34.5	0.3	16.3
2011.2090427	2011.2090751	32.8	0.3	16.4
2011.2091000	2011.2091548	31.5	0.3	16.5
2011.2091720	2011.2092323	30.1	0.3	16.7
2011.2100138	2011.2100506	28.6	0.3	16.8
2011.2100653	2011.2101120	27.3	0.3	16.9
2011.2101312	2011.2101720	25.9	0.3	17.0
2011.2300556	2011.2301148	35.7	0.3	16.2
2011.2550656	2011.2551624	17.7	0.2	17.9
2011.2581300	2011.2581701	19.2	-0.0	12.9
2011.2641437	2011.2642132	39.9	0.2	15.1
2011.2660257	2011.2660748	40.2	0.2	15.4
2011.2670044	2011.2670641	39.7	0.2	15.6
2011.2670900	2011.2671221	39.4	0.2	15.6
2011.2681810	2011.2682342	37.1	0.2	16.0
2011.2700240	2011.2700535	33.6	0.2	16.3
2011.2900338	2011.2900752	23.2	0.1	17.2
2011.3010335	2011.3010744	40.4	0.2	15.2
2011.3120450	2011.3120844	21.2	0.0	13.1
2011.3121338	2011.3121927	23.8	0.1	13.3
2011.3131143	2011.3131601	28.5	0.1	13.8
2011.3142106	2011.3142352	33.8	0.1	14.2
2011.3150615	2011.3151116	35.1	0.1	14.4
2011.3190832	2011.3191147	40.5	0.2	15.3
2011.3311735	2011.3312032	30.1	0.1	13.9
2011.3320141	2011.3320720	31.7	0.1	14.0
2011.3391702	2011.3391859	38.2	0.2	15.8
2012.0070759	2012.0071346	27.2	-1.5	13.5
2012.0232339	2012.0240323	35.8	-1.4	17.1
2012.0251631	2012.0252028	27.7	-1.2	17.8
2012.0302058	2012.0302349	22.6	-1.4	13.0

A.1 List of events used in this thesis: 1st July 2004 - 30rd June 2014

start time ['yyyy.dddhmm']	end time ['yyyy.dddhmm']	radial distance [R_S]	latitude [$^\circ$]	local time [h]
2012.0310552	2012.0320216	27.1	-1.3	13.4
2012.0321438	2012.0322108	32.6	-1.1	13.9
2012.0330146	2012.0330446	34.3	-1.1	14.1
2012.0460922	2012.0461150	39.4	-0.3	16.7
2012.0471807	2012.0472008	34.7	-0.1	17.1
2012.0481608	2012.0482125	30.1	0.0	17.4
2012.0490341	2012.0490655	27.9	0.1	17.6
2012.0661630	2012.0662124	28.7	0.3	17.6
2012.0680620	2012.0680849	20.0	0.3	18.4
2012.0721307	2012.0721839	25.0	0.2	14.3
2012.0730912	2012.0731252	29.1	0.2	14.7
2012.0841358	2012.0841758	28.5	0.3	17.6
2012.0842247	2012.0850314	26.6	0.3	17.7
2012.0852030	2012.0852342	21.4	0.3	18.3
2012.1021913	2012.1022223	26.5	0.3	17.7
2012.1071101	2012.1071443	20.4	0.1	13.8
2012.1081213	2012.1081431	26.6	0.2	14.4
2012.1090608	2012.1091137	30.4	0.2	14.8
2012.1120953	2012.1121502	38.9	0.3	15.6
2012.1140625	2012.1141002	40.4	0.3	16.0
2012.1150524	2012.1150745	40.3	0.3	16.2
2012.1152320	2012.1160325	39.7	0.3	16.4
2012.1161031	2012.1161229	39.2	0.3	16.5
2012.1172049	2012.1172258	36.6	0.3	16.8
2012.1180559	2012.1180914	35.6	0.3	16.9
2012.1181634	2012.1182216	34.2	0.3	17.0
2012.1210722	2012.1211057	22.3	0.3	18.1
2012.1350241	2012.1350643	37.6	0.3	16.6
2012.1351251	2012.1351749	36.6	0.3	16.8
2012.1440959	2012.1441254	28.0	-3.0	14.5
2012.1522002	2012.1522225	32.0	-11.3	16.8
2012.1530501	2012.1531050	30.5	-11.7	16.9
2012.1531513	2012.1532234	28.7	-12.2	17.1
2012.1540140	2012.1540914	26.8	-12.7	17.3
2012.1541149	2012.1542059	24.3	-13.3	17.5
2012.1550022	2012.1550901	21.3	-14.0	17.8
2012.1551632	2012.1551845	17.5	-14.9	18.3
2012.1552130	2012.1560011	15.9	-15.2	18.6
2012.1762025	2012.1762325	32.6	-20.4	18.6
2012.1780148	2012.1780713	26.2	-21.1	19.3
2012.1781140	2012.1782042	23.3	-21.3	19.6
2012.1782131	2012.1790500	20.6	-21.3	20.0
2012.1791008	2012.1791901	16.5	-20.7	20.7
2012.1931934	2012.1940023	47.9	-15.9	16.9
2012.1942049	2012.1950322	47.2	-16.6	17.1
2012.1971623	2012.1972342	42.6	-18.5	17.6

A List of quasi-periodic hourly electron pulsed events

start time ['yyyy.dddhhmm']	end time ['yyyy.dddhhmm']	radial distance [R_S]	latitude [$^\circ$]	local time [h]
2012.1990856	2012.1991258	38.1	-19.5	18.1
2012.2000744	2012.2001301	34.4	-20.2	18.4
2012.2010753	2012.2011209	30.0	-20.8	18.8
2012.2011954	2012.2012242	27.5	-21.0	19.1
2012.2132035	2012.2140228	42.7	-21.7	16.2
2012.2141311	2012.2141820	43.2	-22.7	16.4
2012.2150224	2012.2150650	43.3	-23.4	16.5
2012.2220548	2012.2221352	29.2	-31.7	18.9
2012.2230541	2012.2230844	24.8	-32.2	19.5
2012.2420640	2012.2421256	34.2	-30.5	18.2
2012.2492010	2012.2492348	23.9	-4.1	14.0
2012.2500230	2012.2501142	26.0	-6.2	14.2
2012.3190718	2012.3191337	24.8	-9.9	14.0
2012.3200326	2012.3201026	27.9	-16.0	14.4
2012.3210144	2012.3210548	30.3	-20.8	14.8
2012.3211141	2012.3211553	31.2	-22.8	14.9
2012.3260926	2012.3261832	31.3	-40.9	17.1
2012.3341932	2012.3350002	22.3	-6.6	13.7
2012.3350553	2012.3351043	23.8	-11.2	13.9
2012.3450630	2012.3451414	8.3	49.3	6.8
2012.3460756	2012.3461406	14.1	22.9	12.0
2012.3530209	2012.3530355	27.5	-42.2	16.2
2012.3631527	2012.3632140	27.8	-26.4	14.7
2012.3640318	2012.3640847	28.2	-29.7	15.0
2012.3650158	2012.3650457	28.5	-35.2	15.4
2013.0060201	2013.0060840	9.4	48.2	9.0
2013.0112215	2013.0120230	28.5	-32.6	15.1
2013.0230028	2013.0230304	25.5	-16.9	14.1
2013.0231020	2013.0231447	26.5	-20.4	14.3
2013.0272341	2013.0280256	25.6	-47.7	16.9
2013.0321701	2013.0322146	9.3	48.8	9.0
2013.0322316	2013.0330316	10.8	40.4	10.4
2013.0351006	2013.0351824	23.2	-9.3	13.6
2013.0352357	2013.0361436	25.3	-16.2	14.0
2013.0361933	2013.0370348	26.8	-21.6	14.3
2013.0370533	2013.0371003	27.4	-24.1	14.5
2013.0371328	2013.0380958	28.0	-28.5	14.8
2013.0381037	2013.0382315	28.5	-32.9	15.1
2013.0390028	2013.0390828	28.5	-35.9	15.4
2013.0441446	2013.0441721	11.0	-29.3	23.5
2013.0481419	2013.0481720	22.0	-7.8	13.5
2013.0490616	2013.0490913	23.6	-15.5	13.8
2013.0511326	2013.0512022	25.3	-37.2	15.1
2013.0512343	2013.0520401	25.0	-40.3	15.3
2013.0580602	2013.0581107	12.5	37.5	11.1
2013.0581255	2013.0581438	13.6	30.9	11.6
2013.0642232	2013.0650238	23.7	-47.9	16.1

A.1 List of events used in this thesis: 1st July 2004 - 30rd June 2014

start time ['yyyy.dddhhmm']	end time ['yyyy.dddhhmm']	radial distance [R _S]	latitude [°]	local time [h]
2013.0700921	2013.0701127	13.2	33.5	11.4
2013.0701402	2013.0702321	14.9	23.8	11.9
2013.0710133	2013.0710741	16.9	14.1	12.4
2013.0711635	2013.0712123	19.4	3.2	12.9
2013.0721057	2013.0721636	22.0	-7.9	13.4
2013.0722252	2013.0730501	23.2	-13.8	13.7
2013.0730911	2013.0731530	24.1	-18.5	13.9
2013.0740513	2013.0741040	25.1	-26.4	14.3
2013.0750317	2013.0750750	25.4	-34.2	14.8
2013.0751250	2013.0752237	25.2	-38.4	15.1
2013.0830615	2013.0830848	17.6	11.0	12.6
2013.0852111	2013.0860018	24.8	-23.3	14.1
2013.0870525	2013.0870918	25.4	-35.2	14.8
2013.0871703	2013.0872201	25.2	-39.3	15.2
2013.0880143	2013.0880652	24.8	-42.2	15.4
2013.0911855	2013.0912320	12.7	-42.0	22.6
2013.0990507	2013.0990913	20.8	-39.1	14.7
2013.1031542	2013.1031959	12.7	35.2	11.5
2013.1040035	2013.1040447	14.7	25.2	12.0
2013.1070351	2013.1070856	22.6	-21.5	13.8
2013.1071751	2013.1072025	22.4	-27.3	14.1
2013.1080304	2013.1080715	22.0	-31.7	14.3
2013.1081251	2013.1082109	21.2	-37.4	14.6
2013.1182339	2013.1190115	19.2	-46.3	15.2
2013.1262031	2013.1262222	22.5	-26.5	14.0
2013.1270549	2013.1270954	22.1	-31.2	14.2
2013.1271555	2013.1272225	21.2	-37.1	14.5
2013.1280410	2013.1280721	20.3	-41.8	14.9
2013.1311819	2013.1312340	9.0	56.9	8.8
2013.1350651	2013.1351520	22.4	-15.7	13.5
2013.1351551	2013.1352251	22.6	-19.6	13.7
2013.1360006	2013.1360758	22.6	-23.5	13.8
2013.1361541	2013.1361949	22.3	-29.6	14.1
2013.1371254	2013.1371604	20.8	-39.4	14.7
2013.1451245	2013.1451627	23.0	-25.9	14.0
2013.1452241	2013.1460150	23.2	-30.6	14.2
2013.1460859	2013.1461704	23.2	-36.6	14.6
2013.1462108	2013.1470440	23.0	-42.3	15.0
2013.1470725	2013.1471120	22.7	-46.0	15.4
2013.1510146	2013.1510845	12.6	-25.0	12.0
2013.1710335	2013.1710641	22.8	-44.9	15.2
2013.1781409	2013.1781826	17.5	17.6	12.1
2013.1801836	2013.1802309	22.4	-18.2	13.5
2013.1811305	2013.1812003	23.1	-28.6	14.1
2013.1891747	2013.1891950	14.4	39.2	10.8
2013.1912232	2013.1920029	20.9	-7.4	13.1
2013.1930625	2013.1930825	23.1	-27.6	14.1

A List of quasi-periodic hourly electron pulsed events

start time ['yyyy.dddhhmm']	end time ['yyyy.dddhhmm']	radial distance [R_S]	latitude [$^\circ$]	local time [h]
2013.1950017	2013.1950534	24.9	-47.5	15.8
2013.2271813	2013.2272109	20.2	52.2	5.6
2013.2281526	2013.2281838	19.0	51.3	8.1
2013.2290229	2013.2290647	18.6	45.5	9.4
2013.2292313	2013.2300237	18.6	29.3	11.0
2013.2552110	2013.2552338	20.8	-12.4	13.3
2013.3050211	2013.3050502	61.2	-10.2	23.9
2013.3361715	2013.3362103	20.1	-36.3	14.8
2013.3442324	2013.3450117	38.8	-11.9	23.8
2013.3450817	2013.3451248	39.5	-9.7	23.9
2013.3461714	2013.3462244	41.6	-2.5	0.3
2014.0040454	2014.0040800	18.7	-46.3	16.4
2014.0041543	2014.0041849	19.4	-49.7	17.7
2014.0321348	2014.0322146	22.9	18.7	11.2
2014.0332306	2014.0340110	19.5	-3.9	12.5
2014.0350831	2014.0351136	16.4	-35.8	14.9
2014.0360821	2014.0361030	16.8	-48.1	18.1
2014.0502144	2014.0502318	48.0	40.7	3.6
2014.0670958	2014.0671646	14.5	-40.5	16.1
2014.0672136	2014.0680242	14.4	-45.3	18.0
2014.0710205	2014.0711008	25.5	1.7	0.3
2014.0972244	2014.0980043	17.9	-7.3	12.7
2014.0982301	2014.0990910	13.1	-34.0	15.7
2014.0991513	2014.0991926	12.4	-40.6	18.3
2014.1000227	2014.1002036	14.2	-27.9	21.3
2014.1002334	2014.1010446	16.6	-14.3	23.0
2014.1340739	2014.1341219	15.2	-19.5	13.6
2014.1341649	2014.1342149	13.6	-29.8	14.8
2014.1350436	2014.1351022	12.6	-39.0	16.9
2014.1361954	2014.1370041	16.8	-13.4	23.0
2014.1662041	2014.1670328	13.7	-42.6	16.8
2014.1681805	2014.1682052	17.3	-14.4	22.9
2014.1691507	2014.1692156	21.4	2.9	12.0

A.2 Preliminary list of events from July 2014 to April 2017

The events listed here, which have occurred between July 2014 and the end of the Cassini F-ring orbits (April 22, 2017), have not been analyzed and may not fulfill the selection criteria described in Section 3.3.

start time ['yyyy.dddhh']	end time ['yyyy.dddhh']	radial distance [R _S]	latitude [°]	local time [h]
2014.19902	2014.19906	15.0	-45.9	18.7
2014.19911	2014.19915	15.1	-41.0	20.2
2014.23202	2014.23207	17.1	-24.7	22.2
2014.23210	2014.23215	17.9	-17.1	22.7
2014.23309	2014.23315	21.2	2.2	19.1
2014.26115	2014.26123	16.1	-26.0	13.7
2014.26201	2014.26212	14.5	-36.8	15.0
2014.26313	2014.26318	14.4	-34.3	20.8
2014.26410	2014.26419	17.7	-11.7	22.9
2014.26501	2014.26505	20.0	-1.7	23.6
2014.27113	2014.27121	44.8	32.7	3.0
2014.29219	2014.29300	19.3	6.2	11.1
2014.34105	2014.34111	17.4	-1.1	11.6
2014.35602	2014.35609	55.2	24.4	3.2
2015.00305	2015.00309	41.3	28.5	5.8
2015.00801	2015.00806	17.2	16.9	9.2
2015.01302	2015.01307	28.9	5.2	0.5
2015.01309	2015.01315	30.6	6.0	0.6
2015.04407	2015.04413	25.2	1.3	17.8
2015.07507	2015.07512	19.0	-0.6	23.0
2015.07622	2015.07701	29.1	-0.1	0.3
2015.09104	2015.09111	51.1	-0.3	3.2
2015.09407	2015.09411	44.9	-0.3	3.8
2015.09600	2015.09606	39.3	-0.3	4.2
2015.09721	2015.09801	31.4	-0.3	4.9
2015.10316	2015.10407	22.8	-0.1	23.5
2015.10607	2015.10611	35.6	-0.1	0.8
2015.11615	2015.11619	53.3	-0.2	2.8
2015.11621	2015.11702	53.2	-0.2	2.8
2015.11817	2015.11900	51.7	-0.3	3.1
2015.14217	2015.14222	37.0	-0.4	4.2
2015.15219	2015.15300	32.4	-0.4	2.0
2015.16421	2015.16501	24.5	-0.4	5.5
2015.17220	2015.17302	36.1	-0.5	2.4
2015.19507	2015.19511	44.2	-0.5	3.2
2015.21607	2015.21612	43.3	-0.5	3.0
2015.21719	2015.21802	44.9	-0.5	3.3
2015.21904	2015.21907	45.3	-0.5	3.6
2015.22214	2015.22223	41.8	-0.5	4.3
2015.23310	2015.23315	29.4	-0.4	1.6

A List of quasi-periodic hourly electron pulsed events

start time ['yyyy.dddhh']	end time ['yyyy.dddhh']	radial distance [R_S]	latitude [$^\circ$]	local time [h]
2015.24221	2015.24303	44.3	-0.4	3.9
2015.24405	2015.24409	42.5	-0.4	4.2
2015.24514	2015.24518	39.5	-0.4	4.5
2015.25306	2015.25310	16.8	-0.4	13.3
2015.25317	2015.25323	20.4	-0.4	0.6
2015.25404	2015.25420	24.7	-0.4	1.1
2015.25417	2015.25420	26.3	-0.4	1.3
2015.27118	2015.27121	20.2	-0.4	6.4
2015.27614	2015.27618	26.2	-0.7	3.2
2015.29914	2015.29917	20.1	-0.4	6.4
2016.01818	2016.01905	32.8	1.0	3.8
2016.01905	2016.01909	33.6	1.1	3.9
2016.04316	2016.04321	22.7	15.9	6.8
2016.04400	2016.04405	20.7	16.3	7.1
2016.05206	2016.05211	39.5	11.5	4.5
2016.12318	2016.12322	18.9	18.4	11.7
2016.12403	2016.12409	16.1	14.0	12.4
2016.12515	2016.12521	8.4	-27.6	19.1
2016.12522	2016.12609	9.7	-26.1	21.9
2016.15513	2016.15518	18.4	11.6	13.0
2016.15704	2016.15708	10.3	-29.4	17.5
2016.15718	2016.15809	11.3	-30.8	22.3
2016.17901	2016.17907	18.6	15.0	12.9
2016.17912	2016.17917	16.3	6.7	13.6
2016.18016	2016.18021	11.3	-29.2	16.5
2016.18103	2016.18108	10.8	-41.9	19.0
2016.18117	2016.18122	11.9	-37.1	22.4
2016.18207	2016.18213	14.7	-20.9	0.5
2016.18512	2016.18519	29.5	19.8	3.6
2016.18804	2016.18810	37.2	31.5	4.8
2016.20219	2016.20301	19.6	17.9	12.6
2016.20306	2016.20314	17.0	9.3	13.3
2016.20405	2016.20412	12.5	-16.4	15.2
2016.20415	2016.20422	11.2	-31.2	16.7
2016.20516	2016.20520	11.9	-37.1	22.4
2016.21418	2016.21501	29.4	47.4	6.6
2016.21802	2016.21809	19.9	41.4	10.6
2016.21811	2016.21817	18.2	37.1	11.2
2016.22019	2016.22022	9.6	-44.0	17.7
2016.22120	2016.22201	13.2	-31.0	17.9
2016.22303	2016.22305	19.2	-3.4	1.8
2016.23018	2016.23100	15.4	51.1	9.5
2016.23217	2016.23223	8.1	-49.6	18.0
2016.23316	2016.23323	13.0	-31.1	6.4
2016.23921	2016.24002	24.7	41.9	4.6
2016.24011	2016.24021	23.4	46.6	5.3
2016.24022	2016.24103	22.5	48.9	5.7

A.2 Preliminary list of events from July 2014 to April 2017

start time ['yyyy.dddhh']	end time ['yyyy.dddhh']	radial distance [R _s]	latitude [°]	local time [h]
2016.24106	2016.24118	21.0	51.5	6.4
2016.24304	2016.24315	12.3	40.4	11.2
2016.24521	2016.24601	14.1	-25.8	0.5
2016.24717	2016.24800	22.0	7.3	2.2
2016.25507	2016.25515	11.8	37.5	11.5
2016.25810	2016.25815	17.1	-12.1	1.2
2016.26822	2016.26902	9.2	-52.9	20.7
2016.26912	2016.26918	12.6	-33.4	15.7
2016.27815	2016.27821	9.6	-46.9	23.0
2016.28109	2016.28114	21.9	8.4	2.1
2016.28812	2016.28823	12.4	-31.9	6.2
2016.29509	2016.29512	15.8	53.3	5.6
2016.29606	2016.29616	9.3	50.0	10.3
2016.29806	2016.29815	13.4	-27.0	0.5
2016.30717	2016.30721	12.0	-33.6	8.3
2016.30805	2016.30814	15.7	-17.2	1.0
2016.31407	2016.31412	16.6	51.3	5.1
2016.31415	2016.31419	15.0	54.8	5.9
2016.31501	2016.31514	11.2	56.2	8.6
2016.32314	2016.32321	9.0	59.3	6.3
2016.33301	2016.33306	10.6	-33.9	2.1
2016.33312	2016.33318	14.2	-20.1	0.8
2016.33917	2016.34000	5.4	-56.1	21.9
2016.34620	2016.34700	4.2	-61.1	19.9
2016.35121	2016.35203	18.0	24.9	2.4
2016.35419	2016.35509	14.1	-17.8	0.9
2016.36109	2016.36114	7.1	-45.2	23.5
2017.00122	2017.00203	4.8	60.7	8.3
2017.00209	2017.00214	5.1	-57.5	21.6
2017.00217	2017.00221	8.7	-36.5	9.8
2017.00823	2017.00905	6.0	61.1	6.3
2017.00917	2017.01006	8.7	-37.2	11.9
2017.01123	2017.01203	20.3	0.8	1.4
2017.01210	2017.01216	21.1	5.2	1.6
2017.01221	2017.01313	21.2	11.3	1.8
2017.01620	2017.01702	7.0	-45.8	23.3
2017.01711	2017.01716	12.8	-21.7	0.6
2017.01800	2017.01806	16.4	-11.4	1.0
2017.02322	2017.02401	5.2	-57.1	22.0
2017.02603	2017.02608	20.0	-0.5	1.3
2017.04119	2017.04123	21.3	11.0	1.7
2017.04205	2017.04209	20.9	14.6	1.8
2017.04223	2017.04302	19.2	21.5	2.1
2017.05006	2017.05009	18.8	22.5	2.1
2017.05300	2017.05304	9.8	-31.8	7.9
2017.06715	2017.06721	12.6	-22.0	0.4
2017.06801	2017.06807	15.5	-13.7	0.7

A List of quasi-periodic hourly electron pulsed events

start time ['yyyy.dddhh']	end time ['yyyy.dddhh']	radial distance [R_S]	latitude [$^\circ$]	local time [h]
2017.07406	2017.07413	7.5	-42.3	23.3
2017.07602	2017.07606	19.2	-3.1	1.1
2017.07611	2017.07617	20.3	0.9	1.2
2017.08109	2017.08203	9.3	-34.8	13.6
2017.09115	2017.09120	21.3	8.3	1.4
2017.09514	2017.09521	6.0	-51.2	22.3
2017.10500	2017.10505	20.0	-0.2	1.0
2017.10508	2017.10516	20.8	3.4	1.1
2017.11004	2017.11013	9.1	-35.0	22.2
2017.11019	2017.11023	13.7	-18.6	0.4

B Magnetospheric environment containing energetic electron pulsations

In Section 6.1, the various magnetospheric environments where the quasi-periodic hourly electron pulsations occur have been surveyed. In this appendix, the characteristics of each environment are given in Table B.1 and an example of pulsed electron event is given for each environment in the following figures. The environment categorization has been adapted from Rymer et al. (2009a) to also account for the magnetospheric regions away from Titan's orbit. All the figures present the LEMMS energetic electron intensities on the upper panel and the CAPS/ELS low-energy electron spectrogram on the lower panel. The white line indicates the upper energy boundary of the photoelectrons produced by the spacecraft when it is in sunlight (Lewis et al. 2008, Arridge et al. 2009).

Plasma environment	Maximum flux [counts s ⁻¹ cm ⁻² sr ⁻¹]	Energy at maximum flux [eV]	Figure
Plasma sheet center	$> 3 \times 10^5$	> 120	B.1
Plasma sheet	$5 \times 10^4 - 3 \times 10^5$	> 120	B.2
Lobe	$< 10^4$	no obvious maximum	B.3
Boundary layer	$\sim 3 \times 10^5$	~ 100	B.4
Bimodal	Plasma sheet and boundary layer populations combined		B.5

Table B.1: Characteristics of the different magnetospheric environments.

B Magnetospheric environment containing energetic electron pulsations

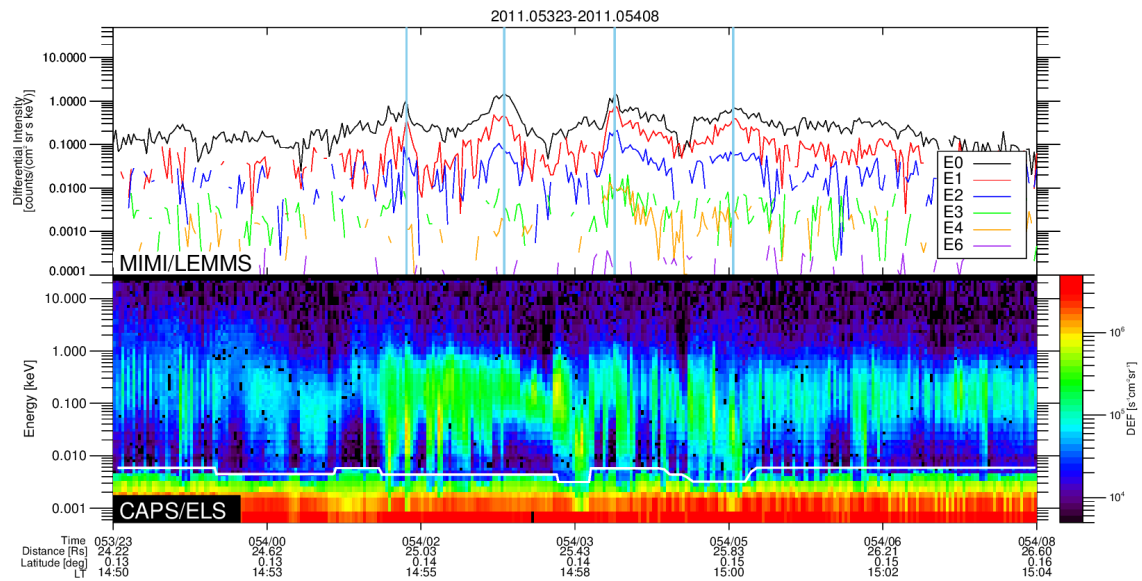


Figure B.1: Quasi-periodic hourly electron event on day 054 of 2011 observed in the central region of the plasma sheet. The upper panel gives the differential intensities of energetic electrons from the MIMI/LEMMS channels E0 to E4 and E6 and the lower panel is the CAPS/ELS electron spectrogram of energy range 0.6 eV-20 keV. Each hourly electron pulsation is indicated by a blue line centered on the intensity peak in E0. The white line on the ELS spectrogram is the upper limit of the photoelectrons coming from the spacecraft.

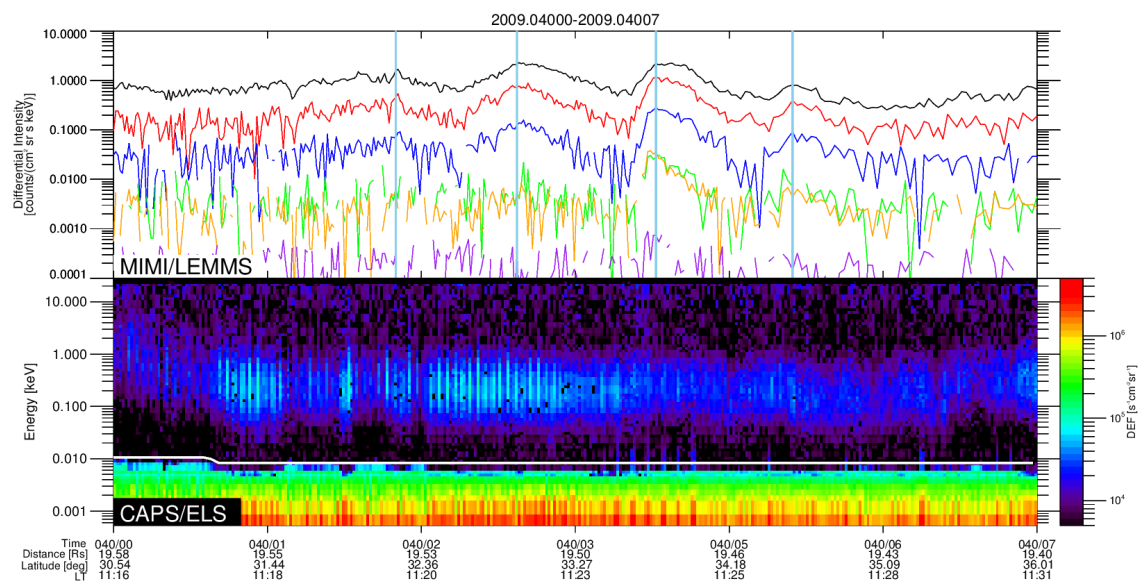


Figure B.2: Quasi-periodic hourly electron event on day 040 of 2009 observed in the plasma sheet. Same format as in Figure B.1.

B Magnetospheric environment containing energetic electron pulsations

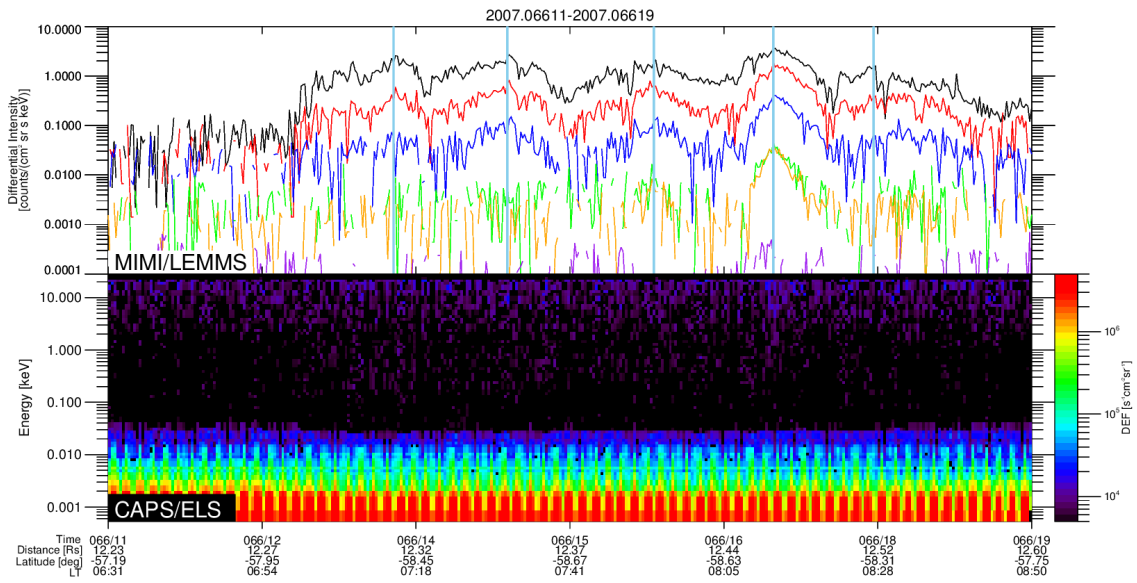


Figure B.3: Quasi-periodic hourly electron event on day 066 of 2007 observed in the lobe. Same format as in Figure B.1.

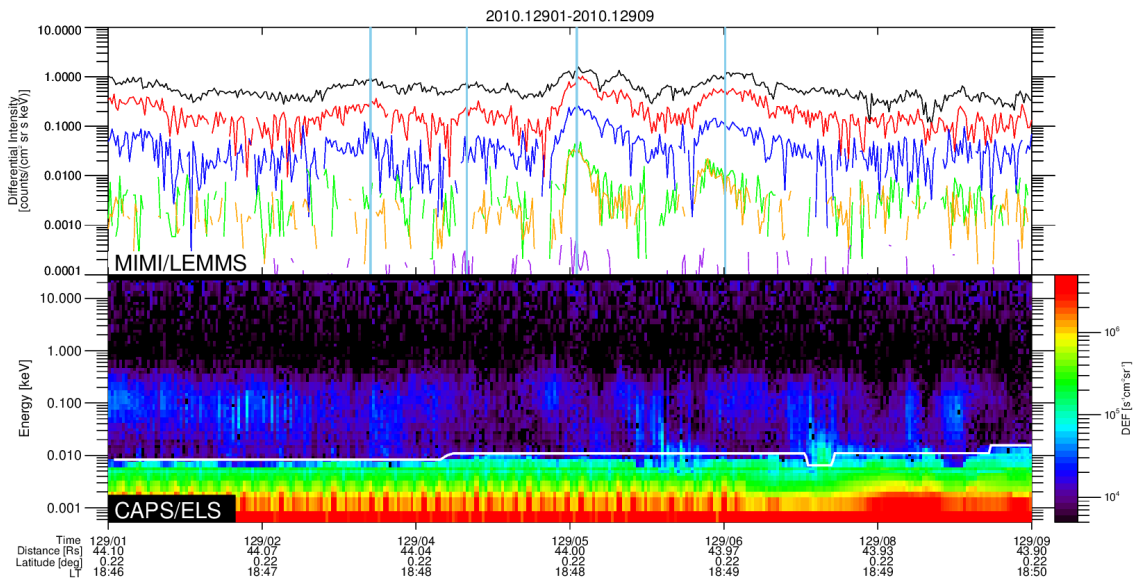


Figure B.4: Quasi-periodic hourly electron event on day 129 of 2010 observed in the boundary layer. Same format as in Figure B.1.

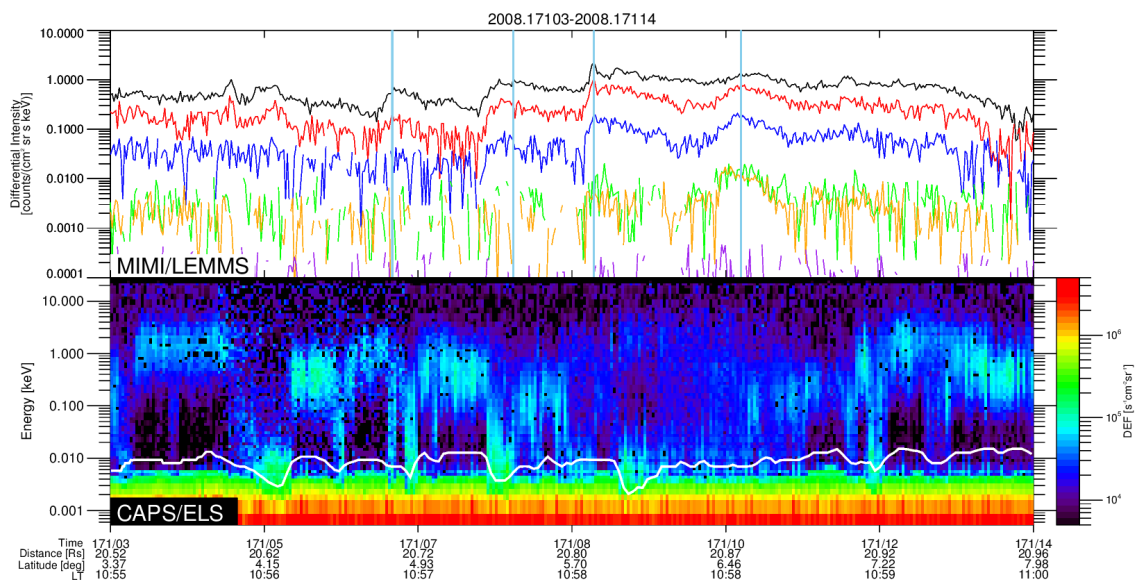


Figure B.5: Quasi-periodic hourly electron event on day 171 of 2008 observed in a bi-modal plasma environment. Same format as in Figure B.1.

Bibliography

- Achilleos, N., Arridge, C. S., Bertucci, C., Jackman, C. M., Dougherty, M. K., Khurana, K. K., Russell, C. T., 2008, Large-scale dynamics of Saturn's magnetopause: Observations by Cassini, *Journal of Geophysical Research*, 113, A11 209
- Achilleos, N., Guio, P., Arridge, C. S., 2010, A model of force balance in Saturn's magnetodisc, *Monthly Notices of the Royal Astronomical Society*, 401, 2349–2371
- André, N., Persoon, A. M., Goldstein, J., et al., 2007, Magnetic signatures of plasma-depleted flux tubes in the Saturnian inner magnetosphere, *Geophysical Research Letters*, 34, L14 108
- André, N., Blanc, M., Maurice, S., et al., 2008, Identification of Saturn's magnetospheric regions and associated plasma processes: synopsis of Cassini observations during orbit insertion, *Reviews of Geophysics*, 46
- Andrews, D. J., Coates, A. J., Cowley, S. W. H., Dougherty, M. K., Lamy, L., Provan, G., Zarka, P., 2010, Magnetospheric period oscillations at Saturn: Comparison of equatorial and high-latitude magnetic field periods with north and south Saturn kilometric radiation periods, *Journal of Geophysical Research*, 115, A12 252
- Andrews, D. J., Cowley, S. W. H., Dougherty, M. K., Lamy, L., Provan, G., Southwood, D. J., 2012, Planetary period oscillations in Saturn's magnetosphere: Evolution of magnetic oscillation properties from southern summer to post-equinox, *Journal of Geophysical Research: Space Physics*, 117, A12 252
- Andriopoulou, M., Roussos, E., Krupp, N., Paranicas, C., Thomsen, M., Krimigis, S., Dougherty, M., Glassmeier, K.-H., 2012, A noon-to-midnight electric field and night-side dynamics in Saturn's inner magnetosphere, using microsignature observations, *Icarus*, 220, 503–513
- Armstrong, T., Taherion, S., Manweiler, J., Krimigis, S., Paranicas, C., Mitchell, D., Krupp, N., 2009, Energetic ions trapped in Saturn's inner magnetosphere, *Planetary and Space Science*, 57, 1723–1731
- Arridge, C. S., Russell, C. T., Khurana, K. K., Achilleos, N., André, N., Rymer, A. M., Dougherty, M. K., Coates, A. J., 2007, Mass of Saturn's magnetodisc: Cassini observations, *Geophysical Research Letters*, 34, L09 108

- Arridge, C. S., Russell, C. T., Khurana, K. K., Achilleos, N., Cowley, S. W. H., Dougherty, M. K., Southwood, D. J., Bunce, E. J., 2008a, Saturn's magnetodisc current sheet, *Journal of Geophysical Research*, 113, A04 214
- Arridge, C. S., Khurana, K. K., Russell, C. T., Southwood, D. J., Achilleos, N., Dougherty, M. K., Coates, A. J., Leinweber, H. K., 2008b, Warping of Saturn's magnetospheric and magnetotail current sheets, *Journal of Geophysical Research*, 113, A08 217
- Arridge, C. S., Gilbert, L. K., Lewis, G. R., Sittler, E. C., Jones, G. H., Kataria, D. O., Coates, A. J., Young, D. T., 2009, The effect of spacecraft radiation sources on electron moments from the Cassini CAPS electron spectrometer, *Planetary and Space Science*, 57, 854–869
- Arridge, C. S., André, N., McAndrews, H. J., et al., 2011, Mapping Magnetospheric Equatorial Regions at Saturn from Cassini Prime Mission Observations, *Space Science Reviews*, 164, 1–83
- Arridge, C. S., Jasinski, J. M., Achilleos, N., et al., 2016, Cassini observations of Saturn's southern polar cusp, *Journal of Geophysical Research: Space Physics*, 121, 3006–3030
- Badman, S. V., Cowley, S. W. H., 2007, Significance of Dungey-cycle flows in Jupiter's and Saturn's magnetospheres, and their identification on closed equatorial field lines, *Annales Geophysicae*, 25, 941–951
- Badman, S. V., Bunce, E. J., Clarke, J. T., Cowley, S. W. H., Gérard, J.-C., Grodent, D., Milan, S. E., 2005, Open flux estimates in Saturn's magnetosphere during the January 2004 Cassini-HST campaign, and implications for reconnection rates, *Journal of Geophysical Research*, 110, A11 216
- Badman, S. V., Achilleos, N., Arridge, C. S., et al., 2012a, Cassini observations of ion and electron beams at Saturn and their relationship to infrared auroral arcs, *Journal of Geophysical Research*, 117, A01 211
- Badman, S. V., Andrews, D. J., Cowley, S. W. H., et al., 2012b, Rotational modulation and local time dependence of Saturn's infrared H_3^+ auroral intensity, *Journal of Geophysical Research*, 117, A09 228
- Badman, S. V., Masters, A., Hasegawa, H., Fujimoto, M., Radioti, A., Grodent, D., Sergis, N., Dougherty, M. K., Coates, A. J., 2013, Bursty magnetic reconnection at Saturn's magnetopause, *Geophysical Research Letters*, 40, 1027–1031
- Badman, S. V., Jackman, C. M., Nichols, J. D., Clarke, J. T., Gérard, J.-C., 2014, Open flux in Saturn's magnetosphere, *Icarus*, 231, 137–145
- Badman, S. V., Branduardi-Raymont, G., Galand, M., Hess, S. L. G., Krupp, N., Lamy, L., Melin, H., Tao, C., 2015, Auroral Processes at the Giant Planets: Energy Deposition, Emission Mechanisms, Morphology and Spectra, *Space Science Reviews*, 187, 99–179

- Badman, S. V., Provan, G., Bunce, E. J., et al., 2016, Saturn's auroral morphology and field-aligned currents during a solar wind compression, *Icarus*, 263, 83–93
- Bagenal, F., 2013, *Planets, Stars and Stellar Systems. Volume 3: Solar and Stellar Planetary Systems*, chap. Planetary Magnetospheres, pp. 251–307, Springer Science+Business Media Dordrecht
- Barbosa, D. D., Scarf, F. L., Kurth, W. S., Gurnett, D. A., 1981, Broadband Electrostatic Noise and Field-Aligned Currents in Jupiter's Middle Magnetosphere, *Journal of Geophysical Research*, 86, 8357–8369
- Belenkaya, E. S., Cowley, S. W. H., Meredith, C. J., Nichols, J. D., Kalegaev, V. V., Alexeev, I. I., Barinov, O. G., Barinova, W. O., Blokhina, M. S., 2014, Magnetospheric magnetic field modelling for the 2011 and 2012 HST Saturn aurora campaigns - implications for auroral source regions, *Annales Geophysicae*, 32, 689–704
- Bhardwaj, A., Gladstone, G. R., 2000, Auroral emissions of the giant planets, *Reviews of Geophysics*, 38, 295–353
- Blake, J. B., Hilton, H. H., Margolis, S. H., 1983, On the injection of cosmic ray secondaries into the inner Saturnian magnetosphere: 1. Protons from the CRAND Process, *Journal of Geophysical Research*, 88, 803–807
- Blanc, M., Andrews, D. J., Coates, A. J., Hamilton, D. C., Jackman, C. M., Jia, X., Kotova, A., Morooka, M., Smith, H. T., Westlake, J. H., 2015, Saturn Plasma Sources and Associated Transport Processes, *Space Science Reviews*, 192, 237–283
- Bolton, S. J., Thorne, R. M., Gurnett, D. A., Kurth, W. S., Williams, D. J., 1997, Enhanced whistler-mode emissions: Signatures of interchange motion in the Io torus, *Geophysical Research Letters*, 24, 2123–2126
- Brice, N. M., Ioannidis, G. A., 1970, The magnetospheres of Jupiter and Earth, *Icarus*, 13, 173–183
- Bunce, E. J., Cowley, S. W., Yeoman, T. K., 2004, Jovian cusp processes: Implications for the polar aurora, *Journal of Geophysical Research*, 109, A09S13
- Bunce, E. J., Cowley, S. W. H., Milan, S. E., 2005a, Interplanetary magnetic field control of Saturn's polar cusp aurora, *Annales Geophysicae*, 23, 1405–1431
- Bunce, E. J., Cowley, S. W. H., Wright, D. M., Coates, A. J., Dougherty, M. K., Krupp, N., Kurth, W. S., Rymer, A. M., 2005b, In situ observations of a solar wind compression-induced hot plasma injection in Saturn's tail, *Geophysical Research Letters*, 32, L20S04
- Bunce, E. J., Cowley, S. W. H., Alexeev, I. I., Arridge, C. S., Dougherty, M. K., Nichols, J. D., Russell, C. T., 2007, Cassini observations of the variation of Saturn's ring current parameters with system size, *Journal of Geophysical Research*, 112, A10 202

- Bunce, E. J., Arridge, C. S., Clarke, J. T., et al., 2008, Origin of Saturn's aurora: Simultaneous observations by Cassini and the Hubble Space Telescope, *Journal of Geophysical Research*, 113, A09 209
- Bunce, E. J., Grodent, D. C., Jinks, S. L., Andrews, D. J., Badman, S. V., Coates, A. J., Cowley, S. W. H., Dougherty, M. K., Kurth, W. S., Mitchell, D. G., Provan, G., 2014, Cassini nightside observations of the oscillatory motion of Saturn's northern auroral oval, *Journal of Geophysical Research: Space Physics*, 119, 3528–3543
- Burch, J. L., Goldstein, J., Hill, T. W., Young, D. T., Crary, F. J., Coates, A. J., André, N., Kurth, W. S., Sittler, E. C., 2005, Properties of local plasma injections in Saturn's magnetosphere, *Geophysical Research Letters*, 32, L14S02
- Burger, M. H., Sittler, E. C., Johnson, R. E., Smith, H. T., Tucker, O. J., Shematovich, V. I., 2007, Understanding the escape of water from Enceladus, *Journal of Geophysical Research*, 112, A06 219
- Burgess, D., 1995, Foreshock-shock interaction at collisionless quasi-parallel shocks, *Advances in Space Research*, 15, 159–169
- Burton, M. E., Buratti, B., Matson, D. L., Lebreton, J.-P., 2001, The Cassini/Huygens Venus and Earth flybys: An overview of operations and results, *Journal of Geophysical Research*, 106, 30 099–30 107
- Cao, H., Russell, C. T., Christensen, U. R., Dougherty, M. K., Burton, M. E., 2011, Saturn's very axisymmetric magnetic field: No detectable secular variation or tilt, *Earth and Planetary Science Letters*, 304, 22–28
- Carbary, J. F., Mitchell, D. G., 2013, Periodicities in Saturn's magnetosphere, *Reviews of Geophysics*, 51, 1–30
- Carbary, J. F., Rymer, A. M., 2017, Solar wind periodicities in thermal electrons at Saturn, *Journal of Geophysical Research: Space Physics*, 122, 150–155
- Carbary, J. F., Roelof, E. C., Mitchell, D. G., Krimigis, S. M., Krupp, N., 2009, Solar wind periodicity in energetic electrons at Saturn, *Geophysical Research Letters*, 36, L22 104
- Carbary, J. F., Roelof, E. C., Mitchell, D. G., Hamilton, D. C., 2013, Solar periodicity in energetic ions at Saturn, *Journal of Geophysical Research: Space Physics*, 118, 1891–1898
- Carbary, J. F., Kurth, W. S., Mitchell, D. G., 2016, Short periodicities in low-frequency plasma waves at Saturn, *Journal of Geophysical Research: Space Physics*, 121, 6562–6572
- Cargill, P. J., Lavraud, B., Owen, C. J., Grison, B., Dunlop, M. W., Cornilleau-Wehrin, N., Escoubet, C. P., Paschmann, G., Phan, T. D., Rezeau, L., Bogdanova, Y., Nykyri, K., 2005, Cluster at the Magnetospheric Cusps, *Space Science Reviews*, 118, 321–366

- Carlson, C. W., McFadden, J. P., Ergun, R. E., et al., 1998, FAST observations in the downward auroral current region: Energetic upgoing electron beams, parallel potential drops, and ion heating, *Geophysical Research Letters*, 25, 2014–2020
- Cassidy, T., Johnson, R., 2010, Collisional spreading of Enceladus' neutral cloud, *Icarus*, 209, 696–703
- Chen, Y., Hill, T. W., 2008, Statistical analysis of injection/dispersion events in Saturn's inner magnetosphere, *Journal of Geophysical Research*, 113, A07 215
- Chen, Y., Hill, T. W., Rymer, A. M., Wilson, R. J., 2010, Rate of radial transport of plasma in Saturn's inner magnetosphere, *Journal of Geophysical Research*, 115, A10 211
- Christon, S. P., Hamilton, D. C., DiFabio, R. D., Mitchell, D. G., Krimigis, S. M., Jontof-Hutter, D. S., 2013, Saturn suprathermal O_2^+ and mass-28⁺ molecular ions: Long-term seasonal and solar variation, *Journal of Geophysical Research: Space Physics*, 118, 3446–3463
- Christon, S. P., Hamilton, D. C., Mitchell, D. G., DiFabio, R. D., Krimigis, S. M., 2014, Suprathermal magnetospheric minor ions heavier than water at Saturn: Discovery of $^{28}M^+$ seasonal variations, *Journal of Geophysical Research: Space Physics*, 119, 5662–5673
- Christon, S. P., Hamilton, D. C., Plane, J. M. C., Mitchell, D. G., DiFabio, R. D., Krimigis, S. M., 2015, Discovery of suprathermal Fe^+ in Saturn's magnetosphere, *Journal of Geophysical Research: Space Physics*, 120, 2720–2738
- Clarke, J. T., Gérard, J.-C., Grodent, D., et al., 2005, Morphological differences between Saturn's ultraviolet aurorae and those of Earth and Jupiter, *Nature*, 433, 717–719
- Clarke, J. T., Nichols, J., Gérard, J.-C., et al., 2009, Response of Jupiter's and Saturn's auroral activity to the solar wind, *Journal of Geophysical Research*, 114, A05 210
- Clarke, K. E., André, N., Andrews, D. J., Coates, A. J., Cowley, S. W. H., Dougherty, M. K., Lewis, G. R., McAndrews, H. J., Nichols, J. D., Robinson, T. R., Wright, D. M., 2006, Cassini observations of planetary-period oscillations of Saturn's magnetopause, *Geophysical Research Letters*, 33, L23 104
- Clarke, K. E., Andrews, D. J., Arridge, C. S., Coates, A. J., Cowley, S. W. H., 2010, Magnetopause oscillations near the planetary period at Saturn: Occurrence, phase, and amplitude, *Journal of Geophysical Research*, 115, A08 209
- Colwell, J. E., Nicholson, P. D., Tiscanero, M. S., Murray, C. D., French, R. G., Marouf, E. A., 2009, Saturn from Cassini-Huygens, chap. The Structure of Saturn's Rings, pp. 375–412, Springer Science+Business Media
- Connerney, J. E. P., Acuña, M. H., Ness, N. F., 1981, Saturn's ring current and inner magnetosphere, *Nature*, 292, 724–726
- Connerney, J. E. P., Ness, N. F., Acuña, M. H., 1982, Zonal harmonic model of Saturn's magnetic field from Voyager 1 and 2 observations, *Nature*, 298, 44–46

- Cooper, J. F., 1983, Nuclear cascades in Saturn's rings: Cosmic ray albedo neutron decay and origins of trapped protons in the inner magnetosphere, *Journal of Geophysical Research*, 88, 3945–3954
- Cowley, S. W. H., Bunce, E. J., Prangé, R., 2004a, Saturn's polar ionospheric flows and their relation to the main auroral oval, *Annales Geophysicae*, 22, 1379–1394
- Cowley, S. W. H., Bunce, E. J., O'Rourke, J. M., 2004b, A simple quantitative model of plasma flows and currents in Saturn's polar ionosphere, *Journal of Geophysical Research*, 109, A05 212
- Cowley, S. W. H., Provan, G., Hunt, G. J., Jackman, C. M., 2017, Planetary period modulations of saturn's magnetotail current sheet: A simple illustrative mathematical model, *Journal of Geophysical Research: Space Physics*, 122, 258–279
- Cowling, T. G., 1933, The Magnetic Field of Sunspots, *Monthly Notices of the Royal Astronomical Society*, 94, 39–48
- Crary, F. J., Clarke, J. T., Dougherty, M. K., et al., 2005, Solar wind dynamic pressure and electric field as the main factors controlling Saturn's aurorae, *Nature*, 433, 720–722
- Cui, J., Yelle, R. V., Volk, K., 2008, Distribution and escape of molecular hydrogen in Titan's thermosphere and exosphere, *Journal of Geophysical Research*, 113, E10 004
- Cutler, J. C., Dougherty, M. K., Lucek, E., Masters, A., 2011, Evidence of surface wave on the dusk flank of Saturn's magnetopause possibly caused by the Kelvin-Helmholtz instability, *Journal of Geophysical Research*, 116, A10 220
- Cuzzi, J., Clark, R., Filacchione, G., French, R., Johnson, R., Marouf, E., Spilker, L., 2009, Saturn from Cassini-Huygens, chap. Ring Particle Composition and Size Distribution, pp. 375–412, Springer Science+Business Media
- De La Haye, V., Waite, J. H., Johnson, R. E., et al., 2007, Cassini Ion and Neutral Mass Spectrometer data in Titan's upper atmosphere and exosphere: Observation of a suprathermal corona, *Journal of Geophysical Research*, 112, A07 309
- Delamere, P. A., Bagenal, F., 2010, Solar wind interaction with Jupiter's magnetosphere, *Journal of Geophysical Research*, 115, A10 201
- Delamere, P. A., Bagenal, F., Dols, V., Ray, L. C., 2007, Saturn's neutral torus versus Jupiter's plasma torus, *Geophysical Research Letters*, 34, L09 105
- Delamere, P. A., Wilson, R. J., Masters, A., 2011, Kelvin-Helmholtz instability at Saturn's magnetopause: Hybrid simulations, *Journal of Geophysical Research*, 116, A10 222
- Delamere, P. A., Wilson, R. J., Eriksson, S., Bagenal, F., 2013, Magnetic signatures of Kelvin-Helmholtz vortices on Saturn's magnetopause: Global survey, *Journal of Geophysical Research: Space Physics*, 118, 393–404

- Delamere, P. A., Otto, A., Ma, X., Bagenal, F., Wilson, R. J., 2015, Magnetic flux circulation in the rotationally driven giant magnetospheres, *Journal of Geophysical Research: Space Physics*, 120, 4229–4245
- Desch, M. D., 1994, Jupiter radio bursts and particle acceleration, *The Astrophysical Journal Supplement Series*, 90, 541–546
- Desch, M. D., Rucker, H. O., 1983, The relationship between Saturn kilometric radiation and the solar wind, *Journal of Geophysical Research*, 88, 8999–9006
- Desroche, M., Bagenal, F., Delamere, P. A., Erkaev, N., 2013, Conditions at the magnetopause of Saturn and implications for the solar wind interaction, *Journal of Geophysical Research: Space Physics*, 118, 3087–3095
- DiFabio, R. D., Hamilton, D. C., Krimigis, S. M., Mitchell, D. G., 2011, Long term time variations of the suprathermal ions in Saturn's magnetosphere, *Geophysical Research Letters*, 38, L18 103
- Dougherty, M. K., Kellock, S., Southwood, D. J., et al., 2004, The Cassini Magnetic Field Investigation, *Space Science Review*, 114, 331–383
- Dougherty, M. K., Achilleos, N., Andre, N., et al., 2005, Cassini Magnetometer Observations During Saturn Orbit Insertion, *Science*, 307, 1266–1270
- Dougherty, M. K., Khurana, K. K., Neubauer, F. M., Russell, C. T., Saur, J., Leisner, J. S., Burton, M. E., 2006, Identification of a Dynamic Atmosphere at Enceladus with the Cassini Magnetometer, *Science*, 311, 1406–1409
- Dungey, J. W., 1961, Interplanetary Magnetic Field and the Auroral Zones, *Physical Review Letters*, 6, 47–48
- Ergun, R. E., Carlson, C. W., McFadden, J. P., Strangeway, R. J., Goldman, M. V., Newman, D. L., 2003, Fast auroral snapshot satellite observations of very low frequency saucers, *Physics of Plasmas*, 10, 454–462
- Esposito, L. W., Barth, C. A., Colwell, J. E., et al., 2004, The Cassini Ultraviolet Imaging Spectrograph Investigation, *Space Science Review*, 115, 299–361
- Fasel, G. J., Lee, L. C., Smith, R. W., 1993, A mechanism for the multiple brightenings of dayside poleward-moving auroral forms, *Geophysical Research Letters*, 20, 2247–2250
- Fillius, W., McIlwain, C., 1980, Very energetic protons in Saturn's radiation belt, *Journal of Geophysical Research*, 85, 5803–5811
- Fischer, G., Gurnett, D., Kurth, W., Ye, S.-Y., Groene, J., 2015, Saturn kilometric radiation periodicity after equinox, *Icarus*, 254, 72–91
- Fleshman, B. L., Delamere, P. A., Bagenal, F., 2010, Modeling the Enceladus plume-plasma interaction, *Geophysical Research Letters*, 37, L03 202

- Fortney, J. J., Nettelmann, N., 2010, The Interior Structure, Composition, and Evolution of Giant Planets, *Space Science Reviews*, 152, 423–447
- Fouchet, T., Moses, J. I., Conrath, B. J., 2009, Saturn from Cassini-Huygens, chap. Saturn: Composition and Chemistry, pp. 83–112, Springer Science+Business Media
- Frank, L. A., Craven, J. D., Burch, J. L., Winningham, J. D., 1982, Polar views of the Earth's aurora with Dynamics Explorer, *Geophysical Research Letters*, 9, 1001–1004
- Frey, H. U., Mende, S. B., Immel, T. J., Fuselier, S. A., Clafin, E. S., Gérard, J.-C., Hubert, B., 2002, Proton aurora in the cusp, *Journal of Geophysical Research*, 107, 1091
- Fukazawa, K., Ogino, T., Walker, R. J., 2007, Vortex-associated reconnection for northward IMF in the Kronian magnetosphere, *Geophysical Research Letters*, 34, L23 201
- Fuselier, S. A., Lewis, W. S., 2011, Properties of Near-Earth Magnetic Reconnection from In-Situ Observations, *Space Science Reviews*, 160, 95–121
- Fuselier, S. A., Frey, H. U., Trattner, K. J., Mende, S. B., Burch, J. L., 2002, Cusp aurora dependence on interplanetary magnetic field B_z , *Journal of Geophysical Research*, 107, 1111
- Fuselier, S. A., Petrinec, S. M., Trattner, K. J., Fujimoto, M., Hasegawa, H., 2007, Simultaneous observations of fluctuating cusp aurora and low-latitude magnetopause reconnection, *Journal of Geophysical Research*, 112, A11 207
- Fuselier, S. A., Trattner, K. J., Petrinec, S. M., 2011, Antiparallel and component reconnection at the dayside magnetopause, *Journal of Geophysical Research*, 116, A10 227
- Fuselier, S. A., Frahm, R., Lewis, W. S., Masters, A., Mukherjee, J., Petrinec, S. M., Sillanpaa, I. J., 2014, The location of magnetic reconnection at Saturn's magnetopause: A comparison with Earth, *Journal of Geophysical Research: Space Physics*, 119, 2563–2578
- Galopeau, P. H. M., Lecacheux, A., 2000, Variations of Saturn's radio rotation period measured at kilometer wavelengths, *Journal of Geophysical Research*, 105, 13 089–13 101
- Galopeau, P. H. M., Zarka, P., Quéau, D. L., 1995, Source location of Saturn's kilometer radiation: The Kelvin-Helmholtz instability hypothesis, *Journal of Geophysical Research*, 100, 26 397–26 410
- Gérard, J.-C., Grodent, D., Gustin, J., Saglam, A., 2004, Characteristics of Saturn's FUV aurora observed with the Space Telescope Imaging Spectrograph, *Journal of Geophysical Research*, 109, A09 207
- Gérard, J.-C., Bunce, E. J., Grodent, D., Cowley, S. W. H., Clarke, J. T., Badman, S. V., 2005, Signature of Saturn's aurora cusp: Simultaneous Hubble Space Telescope FUV observations and upstream solar wind monitoring, *Journal of Geophysical Research*, 110, A11 201

- Gérard, J.-C., Grodent, D., Cowley, S. W. H., Mitchell, D. G., Kurth, W. S., Clarke, J. T., Bunce, E. J., Nichols, J. D., Dougherty, M. K., Crary, F. J., Coates, A. J., 2006, Saturn's auroral morphology and activity during quiet magnetospheric conditions, *Journal of Geophysical Research*, 111, A12 210
- Gérard, J.-C., Bonfond, B., Gustin, J., Grodent, D., Clarke, J. T., Bisikalo, D., Shematovich, V., 2009, Altitude of Saturn's aurora and its implications for the characteristic energy of precipitated electrons, *Geophysical Research Letters*, 36, L02 202
- Gladstone, G. R., Waite, J. H., Grodent, D., et al., 2002, A pulsating auroral X-ray hot spot on Jupiter, *Nature*, 415, 1000–1003
- Gombosi, T. I., Armstrong, T. P., Arridge, C. S., Khurana, K. K., Krimigis, S. M., Krupp, N., Persoon, A. M., Thomsen, M. F., 2009, Saturn from Cassini-Huygens, chap. Saturn's Magnetospheric Configuration, pp. 203–254, Springer Science+Business Media
- Gosling, J. T., Thomsen, M. F., Bame, S. J., Elphic, R. C., Russell, C. T., 1991, Observations of reconnection of interplanetary and lobe magnetic field lines at the high-latitude magnetopause, *Journal of Geophysical Research*, 96, 14 097–14 106
- Grodent, D., 2015, A Brief Review of Ultraviolet Auroral Emissions on Giant Planets, *Space Science Reviews*, 187, 23–50
- Grodent, D., Gérard, J.-C., Cowley, S. W. H., Bunce, E. J., Clarke, J. T., 2005, Variable morphology of Saturn's southern ultraviolet aurora, *Journal of Geophysical Research*, 110, A07 215
- Grodent, D., Radioti, A., Bonfond, B., Gérard, J.-C., 2010, On the origin of Saturn's outer auroral emission, *Journal of Geophysical Research*, 115, A08 219
- Grodent, D., Gustin, J., Gérard, J.-C., Radioti, A., Bonfond, B., Pryor, W. R., 2011, Small-scale structures in Saturn's ultraviolet aurora, *Journal of Geophysical Research*, 116, A09 225
- Guillot, T., 2005, The Interiors of Giant Planets : Models and Outstanding Questions, *Annual Review of Earth and Planetary Sciences*, 33, 493–530
- Guillot, T., Atreya, S., Charnoz, S., Dougherty, M. K., Read, P., 2009, Saturn from Cassini-Huygens, chap. Saturn's Exploration Beyond Cassini-Huygens, pp. 745–761, Springer Science+Business Media
- Gurnett, D. A., Frank, L. A., 1977, A Region of Intense Plasma Wave Turbulence on Auroral Field Lines, *Journal of Geophysical Research*, 82
- Gurnett, D. A., Frank, L. A., Lepping, R. P., 1976, Plasma Waves in the Distant Magnetotail, *Journal of Geophysical Research*, 81
- Gurnett, D. A., Anderson, R. R., Tsurutani, B. T., Smith, E. J., Paschmann, G., Haerendel, G., Bame, S. J., Russell, C. T., 1979, Plasma Wave Turbulence at the Magnetopause: Observations From ISEE 1 and 2, *Journal of Geophysical Research*, 84

- Gurnett, D. A., Kurth, W. S., Kirchner, D. L., et al., 2004, The Cassini Radio and Plasma Wave Investigation, *Space Science Review*, 114, 395–463
- Gurnett, D. A., Lecacheux, A., Kurth, W. S., Persoon, A. M., Groene, J. B., Lamy, L., Zarka, P., Carbary, J. F., 2009a, Discovery of a north-south asymmetry in Saturn's radio rotation period, *Geophysical Research Letters*, 36, L16 102
- Gurnett, D. A., Persoon, A. M., Groene, J. B., Kopf, A. J., Hospodarsky, G. B., Kurth, W. S., 2009b, A north-south difference in the rotation rate of auroral hiss at Saturn: Comparison to Saturn's kilometric radio emission, *Geophysical Research Letters*, 36, L21 108
- Gurnett, D. A., Persoon, A. M., Kopf, A. J., Kurth, W. S., Morooka, M. W., Wahlund, J.-E., Khurana, K. K., Dougherty, M. K., Mitchell, D. G., Krimigis, S. M., Krupp, N., 2010, A plasma-like density boundary at high latitude in Saturn's magnetosphere, *Geophysical Research Letters*, 37, L16 806
- Gustin, J., Bonfond, B., Grodent, D., Gérard, J.-C., 2012, Conversion from HST ACS and STIS auroral counts into brightness, precipitated power, and radiated power for H₂ giant planets, *Journal of Geophysical Research*, 117, A07 316
- Gustin, J., Grodent, D., Radioti, A., Pryor, W., Lamy, L., Ajello, J., 2017, Statistical study of Saturn's auroral electron properties with Cassini/UVIS FUV spectral images, *Icarus*, 284, 264–283
- Hansen, C. J., Esposito, L., Stewart, A. I. F., Colwell, J., Hendrix, A., Pryor, W., Shemansky, D., West, R., 2006, Enceladus' Water Vapor Plume, *Science*, 311, 1422–1425
- Hedman, M. M., Gosmeyer, C. M., Nicholson, P. D., Sotin, C., Brown, R. H., Clark, R. N., Baines, K. H., Buratti, B. J., Showalter, M. R., 2013, An observed correlation between plume activity and tidal stresses on Enceladus, *Nature*, 500, 182–184
- Henry, C. A., 2002, An introduction to the design of the Cassini spacecraft, *Space Science Reviews*, 104, 129–153
- Hill, T., 1976, Interchange stability of a rapidly rotating magnetosphere, *Planetary and Space Science*, 24, 1151–1154
- Hill, T. W., Rymer, A. M., Burch, J. L., Crary, F. J., Young, D. T., Thomsen, M. F., Delapp, D., André, N., Coates, A. J., Lewis, G. R., 2005, Evidence for rotationally driven plasma transport in Saturn's magnetosphere, *Geophysical Research Letters*, 32, L14S10
- Hill, T. W., Thomsen, M. F., Henderson, M. G., et al., 2008, Plasmoids in Saturn's magnetotail, *Journal of Geophysical Research*, 113, A01 214
- Hospodarsky, G. B., Kurth, W. S., Cecconi, B., Gurnett, D. A., Kaiser, M. L., Desch, M. D., Zarka, P., 2004, Simultaneous observations of Jovian quasi-periodic radio emissions by the Galileo and Cassini spacecraft, *Journal of Geophysical Research*, 109, A09S07

- Hubbard, W. B., Burrows, A., Lunine, J. I., 2002, Theory of Giant Planets, *Annual Review of Astronomy and Astrophysics*, 40, 103–136
- Hubbard, W. B., Dougherty, M. K., Gautier, D., Jacobson, R., 2009, Saturn from Cassini-Huygens, chap. The Interior of Saturn, pp. 75–81, Springer Science+Business Media
- Huddleston, D. E., Russell, C. T., Le, G., Szabo, A., 1997, Magnetopause structure and the role of reconnection at the outer planets, *Journal of Geophysical Research*, 102, 24 289–24 302
- Huddleston, D. E., Russell, C. T., Kivelson, M. G., Khurana, K. K., Bennett, L., 1998, Location and shape of the Jovian magnetopause and bow shock, *Journal of Geophysical Research*, 103, 20 075–20 082
- Hugues, W. J., 1995, Introduction to Space Physics, chap. The magnetopause, magnetotail, and magnetic reconnection, pp. 227–287, Cambridge University Press
- Hunt, G. J., Cowley, S. W. H., Provan, G., Bunce, E. J., Alexeev, I. I., Belenkaya, E. S., Kalegaev, V. V., Dougherty, M. K., Coates, A. J., 2015, Field-aligned currents in Saturn’s northern nightside magnetosphere: Evidence for interhemispheric current flow associated with planetary period oscillations, *Journal of Geophysical Research: Space Physics*, 120, 7552–7584
- Jackman, C. M., Arridge, C. S., 2011, Statistical properties of the magnetic field in the Kronian magnetotail lobes and current sheet, *Journal of Geophysical Research*, 116, A05 224
- Jackman, C. M., Slavin, J. A., Cowley, S. W. H., 2011, Cassini observations of plasmoid structure and dynamics: Implications for the role of magnetic reconnection in magnetospheric circulation at Saturn, *Journal of Geophysical Research*, 116, A10 212
- Jackman, C. M., Achilleos, N., Cowley, S. W., Bunce, E. J., Radioti, A., Grodent, D., Badman, S. V., Dougherty, M. K., Pryor, W., 2013, Auroral counterpart of magnetic field dipolarizations in Saturn’s tail, *Planetary and Space Science*, 82-83, 34–42
- Jackman, C. M., Slavin, J. A., Kivelson, M. G., Southwood, D. J., Achilleos, N., Thomsen, M. F., DiBraccio, G. A., Eastwood, J. P., Freeman, M. P., Dougherty, M. K., Vogt, M. F., 2014, Saturn’s dynamic magnetotail: A comprehensive magnetic field and plasma survey of plasmoids and traveling compression regions and their role in global magnetospheric dynamics, *Journal of Geophysical Research: Space Physics*, 119, 5465–5494
- Jackman, C. M., Thomsen, M. F., Mitchell, D. G., et al., 2015, Field dipolarization in Saturn’s magnetotail with planetward ion flows and energetic particle flow bursts: Evidence of quasi-steady reconnection, *Journal of Geophysical Research: Space Physics*, 120, 3603–3617
- Jasinski, J. M., Arridge, C. S., Lamy, L., et al., 2014, Cusp observation at Saturn’s high-latitude magnetosphere by the Cassini spacecraft, *Geophysical Research Letters*, 41, 1382–1388

- Jasinski, J. M., Slavin, J. A., Arridge, C. S., Poh, G., Jia, X., Sergis, N., Coates, A. J., Jones, G. H., Waite Jr., J. H., 2016a, Flux transfer event observation at Saturn's dayside magnetopause by the Cassini spacecraft, *Geophysical Research Letters*, 43, 6713–6723
- Jasinski, J. M., Arridge, C. S., Coates, A. J., Jones, G. H., Sergis, N., Thomsen, M. F., Reisenfeld, D. B., Krupp, N., Waite Jr., J. H., 2016b, Cassini plasma observations of Saturn's magnetospheric cusp, *Journal of Geophysical Research: Space Physics*, 121, 12,047–12,067
- Jia, X., Hansen, K. C., Gombosi, T. I., Kivelson, M. G., Tóth, G., DeZeeuw, D. L., Ridley, A. J., 2012, Magnetospheric configuration and dynamics of Saturn's magnetosphere: A global MHD simulation, *Journal of Geophysical Research*, 117, A05 225
- Jinks, S. L., Bunce, E. J., Cowley, S. W. H., Provan, G., Yeoman, T. K., Arridge, C. S., Dougherty, M. K., Gurnett, D. A., Krupp, N., Kurth, W. S., Mitchell, D. G., Morroka, M., Wahlund, J.-E., 2014, Cassini multi-instrument assessment of Saturn's polar cap boundary, *Journal of Geophysical Research*, 119, 8161–8177
- Johnson, R., Luhmann, J., Tokar, R., Bouhram, M., Berthelier, J., Sittler, E., Cooper, J., Hill, T., Smith, H., Michael, M., Liu, M., Crary, F., Young, D., 2006a, Production, ionization and redistribution of O₂ in Saturn's ring atmosphere, *Icarus*, 180, 393–402
- Johnson, R. E., Smith, H. T., Tucker, O. J., Liu, M., Burger, M. H., Sittler, E. C., Tokar, R. L., 2006b, The Enceladus and OH Tori at Saturn, *The Astrophysical Journal*, 644, L137–L139
- Jurac, S., Richardson, J. D., 2005, A self-consistent model of plasma and neutrals at Saturn: Neutral cloud morphology, *Journal of Geophysical Research*, 110, A09 220
- Kan, J. R., Deehr, C. S., Lyu, L. H., Newell, P. T., 1996, Ionospheric signatures of patchy-intermittent reconnection at dayside magnetopause, *Journal of Geophysical Research*, 101, 10 939–10 946
- Kanani, S. J., Arridge, C. S., Jones, G. H., et al., 2010, A new form of Saturn's magnetopause using a dynamic pressure balance model, based on in situ, multi-instrument Cassini measurements, *Journal of Geophysical Research*, 115, A06 207
- Kane, M., Mitchell, D. G., Carbary, J. F., Krimigis, S. M., Crary, F. J., 2008, Plasma convection in Saturn's outer magnetosphere determined from ions detected by the Cassini INCA experiment, *Geophysical Research Letters*, 35, L04 102
- Kellett, S., Bunce, E. J., Coates, A. J., Cowley, S. W. H., 2009, Thickness of Saturn's ring current determined from north-south Cassini passes through the current layer, *Journal of Geophysical Research*, 114, A04 209
- Kellett, S., Arridge, C. S., Bunce, E. J., Coates, A. J., Cowley, S. W. H., Dougherty, M. K., Persoon, A. M., Sergis, N., Wilson, R. J., 2011, Saturn's ring current: Local time dependence and temporal variability, *Journal of Geophysical Research*, 116, A05 220

- Kempf, S., Beckmann, U., Schmidt, J., 2010, How the Enceladus dust plume feeds Saturn's E ring, *Icarus*, 206, 446–457
- Kennelly, T. J., Leisner, J. S., Hospodarsky, G. B., Gurnett, D. A., 2013, Ordering of injection events within Saturnian SLS longitude and local time, *Journal of Geophysical Research: Space Physics*, 118, 832–838
- Khurana, K. K., Arridge, C. S., Schwarzl, H., Dougherty, M. K., 2006, A model of Saturn's magnetospheric field based on latest Cassini observations, in *AGU Spring Meeting Abstracts*, P44A-01
- Kimura, T., Kraft, R. P., Elsner, R. F., et al., 2016, Jupiter's X-ray and EUV auroras monitored by Chandra, XMM-Newton, and Hisaki satellite, *Journal of Geophysical Research: Space Physics*, 121, 2308–2320
- Kivelson, M. G., Russell, C. T., 1995, *Introduction to Space Physics*, Cambridge University Press
- Kleindienst, G., Glassmeier, K.-H., Simon, S., Dougherty, M. K., Krupp, N., 2009, Quasiperiodic ULF-pulsations in Saturn's magnetosphere, *Annales Geophysicae*, 27, 885–894
- Kollmann, P., Roussos, E., Paranicas, C., Krupp, N., Jackman, C. M., Kirsch, E., Glassmeier, K.-H., 2011, Energetic particle phase space densities at Saturn: Cassini observations and interpretations, *Journal of Geophysical Research*, 116, A05 222
- Kollmann, P., Roussos, E., Paranicas, C., Krupp, N., Haggerty, D., 2013, Processes forming and sustaining Saturn's proton radiation belts, *Icarus*, 222, 323–341
- Kopf, A. J., Gurnett, D. A., Menietti, J. D., Schippers, P., Arridge, C. S., Hospodarsky, G. B., Kurth, W. S., Grimald, S., André, N., Coates, A. J., Dougherty, M. K., 2010, Electron beams as the source of whistler-mode auroral hiss at Saturn, *Geophysical Research Letters*, 37, L09 102
- Krimigis, S. M., Mitchell, D. G., Hamilton, D. C., et al., 2004, Magnetosphere Imaging Instrument (MIMI) on the Cassini Mission to Saturn/Titan, *Space Science Review*, 114, 233–329
- Krimigis, S. M., Sergis, N., Mitchell, D. G., Hamilton, D. C., Krupp, N., 2007, A dynamic, rotating ring current around Saturn, *Nature*, 450, 1050–1053
- Krupp, N., Woch, J., Lagg, A., Livi, S., Mitchell, D. G., Krimigis, S. M., Dougherty, M. K., Hanlon, P. G., Armstrong, T. P., Espinosa, S. A., 2004, Energetic particle observations in the vicinity of Jupiter: Cassini MIMI/LEMMS results, *Journal of Geophysical Research*, 109, A09S10
- Krupp, N., Lagg, A., Woch, J., et al., 2005, The Saturnian plasma sheet as revealed by energetic particle measurements, *Geophysical Research Letters*, 32, L20S03

- Krupp, N., Roussos, E., Lagg, A., et al., 2009, Energetic particles in Saturn's magnetosphere during the Cassini nominal mission (July 2004-July 2008), *Planetary and Space Science*, 57, 1754–1768
- Kuo, H., Russell, C. T., Le, G., 1995, Statistical studies of flux transfer events, *Journal of Geophysical Research*, 100, 3513–3519
- Kurth, W. S., Averkamp, T. F., Gurnett, D. A., Groene, J. B., Lecacheux, A., 2008, An update to a Saturnian longitude system based on kilometric radio emissions, *Journal of Geophysical Research*, 113, A05 222
- Kurth, W. S., Bunce, E. J., Clarke, J. T., et al., 2009, Saturn from Cassini-Huygens, chap. Auroral Processes, pp. 333–374, Springer Science+Business Media
- Lai, H. R., Wei, H. Y., Russell, C. T., Arridge, C. S., Dougherty, M. K., 2012, Reconnection at the magnetopause of Saturn: Perspective from FTE occurrence and magnetosphere size, *Journal of Geophysical Research*, 117, A05 222
- Lamy, L., 2011, Planetary Radio Emissions VII, chap. Variability of southern and northern periodicities of Saturn Kilometric Radiation, pp. 39–50, Austrian Academia of Sciences Press, Vienna, Austria
- Lamy, L., Prangé, R., Pryor, W., Gustin, J., Badman, S. V., Melin, H., Stallard, T., Mitchell, D. G., Brandt, P. C., 2013, Multispectral simultaneous diagnosis of Saturn's aurorae throughout a planetary rotation, *Journal of Geophysical Research: Space Physics*, 118, 4817–4843
- Lewis, G., Arridge, C., Linder, D., et al., 2010, The calibration of the Cassini-Huygens CAPS Electron Spectrometer, *Planetary and Space Science*, 58, 427–436
- Lewis, G. R., André, N., Arridge, C. S., Coates, A. J., Gilbert, L. K., Linder, D. R., Rymer, A. M., 2008, Derivation of density and temperature from the Cassini-Huygens CAPS electron spectrometer, *Planetary and Space Science*, 56, 901–912
- Li, W., André, M., Khotyaintsev, Y. V., et al., 2016, Kinetic evidence of magnetic reconnection due to Kelvin-Helmholtz waves, *Geophysical Research Letters*, 43, 5635–5643
- Liu, X., Hill, T. W., Wolf, R. A., Sazykin, S., Spiro, R. W., Wu, H., 2010, Numerical simulation of plasma transport in Saturn's inner magnetosphere using the Rice Convection Model, *Journal of Geophysical Research*, 115, A12 254
- Ma, X., Otto, A., Delamere, P. A., 2014, Interaction of magnetic reconnection and Kelvin-Helmholtz modes for large magnetic shear: 1. Kelvin-Helmholtz trigger, *Journal of Geophysical Research: Space Physics*, 119, 781–797
- Ma, X., Stauffer, B., Delamere, P. A., Otto, A., 2015, Asymmetric Kelvin-Helmholtz propagation at Saturn's dayside magnetopause, *Journal of Geophysical Research: Space Physics*, 120, 1867–1875

- MacDowall, R. J., Kaiser, M. L., Desch, M. D., Farrell, W. M., Hess, R. A., Stone, R. G., 1993, Quasiperiodic Jovian radio bursts: observations from the Ulysses Radio and Plasma Wave Experiment, *Planetary and Space Science*, 41, 1059–1072
- Maggs, J. E., 1976, Coherent generation of VLF hiss, *Journal of Geophysical Research*, 81, 1707–1724
- Masters, A., Achilleos, N., Bertucci, C., Dougherty, M., Kanani, S., Arridge, C., McAndrews, H., Coates, A., 2009, Surface waves on Saturn's dawn flank magnetopause driven by the Kelvin-Helmholtz instability, *Planetary and Space Science*, 57, 1769–1778
- Masters, A., Achilleos, N., Kivelson, M. G., et al., 2010, Cassini observations of a Kelvin-Helmholtz vortex in Saturn's outer magnetosphere, *Journal of Geophysical Research*, 115, A07 225
- Masters, A., Mitchell, D. G., Coates, A. J., Dougherty, M. K., 2011a, Saturn's low-latitude boundary layer: 1. Properties and variability, *Journal of Geophysical Research*, 116, A06 210
- Masters, A., Walsh, A. P., Fazakerley, A. N., Coates, A. J., Dougherty, M. K., 2011b, Saturn's low-latitude boundary layer: 2. Electron structure, *Journal of Geophysical Research*, 116, A06 211
- Masters, A., Eastwood, J. P., Swisdak, M., Thomsen, M. F., Russell, C. T., Sergis, N., Crary, F. J., Dougherty, M. K., Coates, A. J., Krimigis, S. M., 2012a, The importance of plasma β conditions for magnetic reconnection at Saturn's magnetopause, *Geophysical Research Letters*, 39, L08 103
- Masters, A., Achilleos, N., Cutler, J., Coates, A., Dougherty, M., Jones, G., 2012b, Surface waves on Saturn's magnetopause, *Planetary and Space Science*, 65, 109–121
- Masters, A., Fujimoto, M., Hasegawa, H., Russell, C. T., Coates, A. J., Dougherty, M. K., 2014, Can magnetopause reconnection drive Saturn's magnetosphere?, *Geophysical Research Letters*, 41, 1862–1868
- Matson, D. L., Spilker, L. J., Lebreton, J.-P., 2002, The Cassini/Huygens Mission to the Saturnian System, *Space Science Reviews*, 104, 1–58
- Mauk, B. H., Saur, J., 2007, Equatorial electron beams and auroral structuring at Jupiter, *Journal of Geophysical Research*, 112, A10 221
- Mauk, B. H., Clarke, J. T., Grodent, D., Waite, J. H., Paranicas, C. P., Williams, D. J., 2002, Transient aurora on Jupiter from injections of magnetospheric electrons, *Nature*, 415, 1003–1005
- Mauk, B. H., Saur, J., Mitchell, D. G., Roelof, E. C., et al., 2005, Energetic particle injections in Saturn's magnetosphere, *Geophysical Research Letters*, 32, L14S05

- Mauk, B. H., Hamilton, D. C., Hill, T. W., Hospodarsky, G. B., Johnson, R. E., Paranicas, C., Roussos, E., Russell, C. T., Shemansky, D. E., Sittler Jr., E. C., Thorne, R. M., 2009, Saturn from Cassini-Huygens, chap. Fundamental Plasma Processes in Saturn's Magnetosphere, pp. 281–331, Springer Science+Business Media
- McAndrews, H., Thomsen, M., Arridge, C., Jackman, C., Wilson, R., Henderson, M., Tokar, R., Khurana, K., Sittler, E., Coates, A., Dougherty, M., 2009, Plasma in Saturn's nightside magnetosphere and the implications for global circulation, *Planetary and Space Science*, 57, 1714–1722
- McAndrews, H. J., Owen, C. J., Thomsen, M. F., Lavraud, B., Coates, A. J., Dougherty, M. K., Young, D. T., 2008, Evidence for reconnection at Saturn's magnetopause, *Journal of Geophysical Research*, 113, A04 210
- McComas, D. J., Bagenal, F., 2007, Jupiter: A fundamentally different magnetospheric interaction with the solar wind, *Geophysical Research Letters*, 34, L20 106
- McKibben, R. B., Simpson, J. A., Zhang, M., 1993, Impulsive bursts of relativistic electrons discovered during Ulysses' traversal of Jupiter's dusk-side magnetosphere, *Planetary and Space Science*, 41, 1041–1058
- McPherron, R. L., Russell, C. T., Aubry, M. P., 1973, Satellite studies of magnetospheric substorms on August 15, 1968: 9. Phenomenological model for substorms, *Journal of Geophysical Research*, 78, 3131–3149
- Melin, H., Shemansky, D. E., Liu, X., 2009, The distribution of atomic hydrogen and oxygen in the magnetosphere of Saturn, *Planetary and Space Science*, 57, 1743–1753
- Meredith, C. J., Cowley, S. W. H., Hansen, K. C., Nichols, J. D., Yeoman, T. K., 2013, Simultaneous conjugate observations of small-scale structures in Saturn's dayside ultraviolet auroras: Implications for physical origins, *Journal of Geophysical Research: Space Physics*, 118, 2244–2266
- Meredith, C. J., Alexeev, I. I., Badman, S. V., Belenkaya, E. S., Cowley, S. W. H., Dougherty, M. K., Kalegaev, V. V., Lewis, G. R., Nichols, J. D., 2014, Saturn's dayside ultraviolet auroras: Evidence for morphological dependence on the direction of the upstream interplanetary magnetic field, *Journal of Geophysical Research: Space Physics*, 119, 1994–2008
- Milan, S. E., Lester, M., Cowley, S. W. H., Brittnacher, M., 2000, Dayside convection and auroral morphology during an interval of northward interplanetary magnetic field, *Annales Geophysicae*, 18, 436–444
- Milan, S. E., Hubert, B., Grocott, A., 2005, Formation and motion of a transpolar arc in response to dayside and nightside reconnection, *Journal of Geophysical Research*, 110, A01 212
- Milan, S. E., Gosling, J. S., Hubert, B., 2012, Relationship between interplanetary parameters and the magnetopause reconnection rate quantified from observations of the expanding polar cap, *Journal of Geophysical Research*, 117, A03 226

- Mitchell, D., Krimigis, S., Paranicas, C., et al., 2009b, Recurrent energization of plasma in the midnight-to-dawn quadrant of Saturn's magnetosphere, and its relationship to auroral UV and radio emissions, *Planetary and Space Science*, 57, 1732–1742
- Mitchell, D. G., Brandt, P. C., Roelof, E. C., et al., 2005, Energetic ion acceleration in Saturn's magnetotail: Substorms at Saturn?, *Geophysical Research Letters*, 32, L20S01
- Mitchell, D. G., Kurth, W. S., Hospodarsky, G. B., Krupp, N., Saur, J., Mauk, B. H., Carbary, J. F., Krimigis, S. M., Dougherty, M. K., Hamilton, D. C., 2009a, Ion conics and electron beams associated with auroral processes on Saturn, *Journal of Geophysical Research*, 114, A02 212
- Mitchell, D. G., Carbary, J. F., Bunce, E. J., Radioti, A., Badman, S. V., Pryor, W. R., Hospodarsky, G. B., Kurth, W. S., 2016, Recurrent pulsations in Saturn's high latitude magnetosphere, *Icarus*, 263, 94–100
- Müller, A. L., Saur, J., Krupp, N., Roussos, E., Mauk, B. H., Rymer, A. M., Mitchell, D. G., Krimigis, S. M., 2010, Azimuthal plasma flow in the Kronian magnetosphere, *Journal of Geophysical Research*, 115, A08 203
- Nakamura, T. K. M., Daughton, W., Karimabadi, H., Eriksson, S., 2013, Three-dimensional dynamics of vortex-induced reconnection and comparison with THEMIS observations, *Journal of Geophysical Research: Space Physics*, 118, 5742–5757
- Nichols, J. D., Clarke, J. T., Cowley, S. W. H., Duval, J., Farmer, A. J., Gérard, J.-C., Grodent, D., Wannawichian, S., 2008, Oscillation of Saturn's southern auroral oval, *Journal of Geophysical Research*, 113, A11 205
- Nichols, J. D., Cecconi, B., Clarke, J. T., Cowley, S. W. H., Gérard, J.-C., Grocott, A., Grodent, D., Lamy, L., Zarka, P., 2010a, Variation of Saturn's UV aurora with SKR phase, *Geophysical Research Letters*, 37, L15 102
- Nichols, J. D., Cowley, S. W. H., Lamy, L., 2010b, Dawn-dusk oscillation of Saturn's conjugate auroral ovals, *Geophysical Research Letters*, 37, L24 102
- Nichols, J. D., V.Badman, S., Baines, K. H., et al., 2014, Dynamic auroral storms on Saturn as observed by the Hubble Space Telescope, *Geophysical Research Letters*, 41, 3323–3330
- Onsager, T. G., Fuselier, S. A., 1994, *Solar System Plasmas in Space and Time*, chap. The location of magnetic reconnection for northward and southward interplanetary magnetic field, pp. 183–197, American Geophysical Union, Washington, D. C
- Palmaerts, B., Roussos, E., Krupp, N., Kurth, W. S., Mitchell, D. G., Yates, J. N., 2016a, Statistical analysis and multi-instrument overview of the quasi-periodic 1-hour pulsations in Saturn's outer magnetosphere, *Icarus*, 271, 1–18
- Palmaerts, B., Radioti, A., Roussos, E., Grodent, D., Gérard, J.-C., Krupp, N., Mitchell, D. G., 2016b, Pulsations of the Polar Cusp Aurora at Saturn, *Journal of Geophysical Research: Space Physics*, 121, 11,952–11,963

- Paranicas, C., Mitchell, D. G., Roelof, E. C., Mauk, B. H., Krimigis, S. M., Brandt, P. C., Kusterer, M., Turner, F. S., Vandegriff, J., Krupp, N., 2007, Energetic electrons injected into Saturn's neutral gas cloud, *Geophysical Research Letters*, 34, L02 109
- Paranicas, C., Mitchell, D., Krimigis, S., Hamilton, D., Roussos, E., Krupp, N., Jones, G., Johnson, R., Cooper, J., Armstrong, T., 2008, Sources and losses of energetic protons in Saturn's magnetosphere, *Icarus*, 197, 519–525
- Paranicas, C., Mitchell, D. G., Krimigis, S. M., et al., 2010a, Asymmetries in Saturn's radiation belts, *Journal of Geophysical Research*, 115, A07 216
- Paranicas, C., Mitchell, D. G., Roussos, E., Kollmann, P., Krupp, N., Müller, A. L., Krimigis, S. M., Turner, F. S., Brandt, P. C., Rymer, A. M., Johnson, R. E., 2010b, Transport of energetic electrons into Saturn's inner magnetosphere, *Journal of Geophysical Research*, 115, A09 214
- Persoon, A. M., Gurnett, D. A., Leisner, J. S., Kurth, W. S., Groene, J. B., Faden, J. B., 2013, The plasma density distribution in the inner region of Saturn's magnetosphere, *Journal of Geophysical Research: Space Physics*, 118, 2970–2974
- Pilkington, N. M., Achilleos, N., Arridge, C. S., Guio, P., Masters, A., Ray, L. C., Sergis, N., Thomsen, M. F., Coates, A. J., Dougherty, M. K., 2015, Internally driven large-scale changes in the size of Saturn's magnetosphere, *Journal of Geophysical Research: Space Physics*, 120, 7289–7306
- Porco, C., DiNino, D., Nimmo, F., 2014, How The Geysers, Tidal Stresses, And Thermal Emission Across The South Polar Terrain Of Enceladus Are Related, *The Astronomical Journal*, 148, 45
- Porco, C. C., Helfenstein, P., Thomas, P. C., et al., 2006, Cassini Observes the Active South Pole of Enceladus, *Science*, 311, 1393–1401
- Press, W. H., Rybicki, G. B., 1989, Fast algorithm for spectral analysis of unevenly sampled data, *The Astrophysical Journal*, 338, 277–280
- Provan, G., Yeoman, T. K., Milan, S. E., 1998, CUTLASS Finland radar observations of the ionospheric signatures of flux transfer events and the resulting plasma flows, *Annales Geophysicae*, 16, 1411–1422
- Provan, G., Cowley, S. W. H., Nichols, J. D., 2009, Phase relation of oscillations near the planetary period of Saturn's auroral oval and the equatorial magnetospheric magnetic field, *Journal of Geophysical Research*, 114, A04 205
- Provan, G., Andrews, D. J., Arridge, C. S., Coates, A. J., Cowley, S. W. H., Cox, G., Dougherty, M. K., Jackman, C. M., 2012, Dual periodicities in planetary-period magnetic field oscillations in Saturn's tail, *Journal of Geophysical Research: Space Physics*, 117, A01 209

- Provan, G., Lamy, L., Cowley, S. W. H., Dougherty, M. K., 2014, Planetary period oscillations in Saturn's magnetosphere: Comparison of magnetic oscillations and SKR modulations in the postequinox interval, *Journal of Geophysical Research: Space Physics*, 119, 7380–7401
- Pryor, W. R., Rymer, A. M., Mitchell, D. G., et al., 2011, The auroral footprint of Enceladus on Saturn, *Nature*, 472, 331–333
- Pu, Z. Y., Yei, M., Liu, Z. X., 1990, Generation of vortex-induced tearing mode instability at the magnetopause, *Journal of Geophysical Research*, 95, 10 559–10 566
- Radioti, A., Grodent, D., Gérard, J.-C., Roussos, E., Paranicas, C., Bonfond, B., Mitchell, D. G., Krupp, N., Krimigis, S., Clarke, J. T., 2009, Transient auroral features at Saturn: Signatures of energetic particle injections in the magnetosphere, *Journal of Geophysical Research*, 114, A03 210
- Radioti, A., Grodent, D., Gérard, J.-C., Milan, S. E., Bonfond, B., Gustin, J., Pryor, W., 2011, Bifurcations of the main auroral ring at Saturn: Ionospheric signatures of consecutive reconnection events at the magnetopause, *Journal of Geophysical Research*, 116, A11 209
- Radioti, A., Roussos, E., Grodent, D., Gérard, J.-C., Krupp, N., Mitchell, D. G., Gustin, J., Bonfond, B., Pryor, W., 2013a, Signatures of magnetospheric injections in Saturn's aurora, *Journal of Geophysical Research: Space Physics*, 118, 1922–1933
- Radioti, A., Grodent, D., Gérard, J.-C., Bonfond, B., Gustin, J., Pryor, W., Jasinski, J. M., Arridge, C. S., 2013b, Auroral signatures of multiple magnetopause reconnection at Saturn, *Geophysical Research Letters*, 40, 4498–4502
- Radioti, A., Grodent, D., Gérard, J.-C., Milan, S. E., Fear, R. C., Jackman, C. M., Bonfond, B., Pryor, W., 2014, Saturn's elusive nightside polar arc, *Geophysical Research Letters*, 41, 6321–6328
- Radioti, A., Grodent, D., Gérard, J.-C., Roussos, E., Mitchell, D., Bonfond, B., Pryor, W., 2015, Auroral spirals at Saturn, *Journal of Geophysical Research: Space Physics*, 120, 8633–8643
- Radioti, A., Grodent, D., Jia, X., Gérard, J.-C., Bonfond, B., Pryor, W., Gustin, J., Mitchell, D., Jackman, C., 2016, A multi-scale magnetotail reconnection event at Saturn and associated flows: Cassini/UVIS observations, *Icarus*, 263, 75–82
- Roussos, E., Jones, G. H., Krupp, N., Paranicas, C., Mitchell, D. G., Lagg, A., Woch, J., Motschmann, U., Krimigis, S. M., Dougherty, M. K., 2007, Electron microdiffusion in the Saturnian radiation belts: Cassini MIMI/LEMMS observations of energetic electron absorption by the icy moons, *Journal of Geophysical Research*, 112, A06 214
- Roussos, E., Krupp, N., Armstrong, T. P., Paranicas, C., Mitchell, D. G., Krimigis, S. M., Jones, G. H., Dialynas, K., Sergis, N., Hamilton, D. C., 2008, Discovery of a transient radiation belt at Saturn, *Geophysical Research Letters*, 35, L22 106

- Roussos, E., Krupp, N., Paranicas, C. P., Kollmann, P., Mitchell, D. G., Krimigis, S. M., Armstrong, T. P., Went, D. R., Dougherty, M. K., Jones, G. H., 2011, Long- and short-term variability of Saturn's ionic radiation belts, *Journal of Geophysical Research*, 116, A02 217
- Roussos, E., Krupp, N., Paranicas, C., Carbary, J., Kollmann, P., Krimigis, S., Mitchell, D., 2014, The variable extension of Saturn's electron radiation belts, *Planetary and Space Science*, 104, 3–17
- Roussos, E., Krupp, N., Mitchell, D. G., Paranicas, C., Krimigis, S. M., Andriopoulou, M., Palmaerts, B., Kurth, W. S., Badman, S. V., Masters, A., Dougherty, M. K., 2016, Quasi-periodic injections of relativistic electrons in Saturn's outer magnetosphere, *Icarus*, 263, 101–116
- Russell, C. T., Elphic, R. C., 1978, Initial ISEE magnetometer results: Magnetopause observations, *Space Science Reviews*, 22, 681–715
- Russell, C. T., Jackman, C. M., Wei, H. Y., Bertucci, C., Dougherty, M. K., 2008, Titan's influence on Saturnian substorm occurrence, *Geophysical Research Letters*, 35, L12 105
- Rymer, A., Mauk, B., Hill, T., et al., 2009b, Cassini evidence for rapid interchange transport at Saturn, *Planetary and Space Science*, 57, 1779–1784
- Rymer, A. M., Mauk, B. H., Hill, T. W., et al., 2007, Electron sources in Saturn's magnetosphere, *Journal of Geophysical Research*, 112, A02 201
- Rymer, A. M., Mauk, B. H., Hill, T. W., Paranicas, C., Mitchell, D. G., Coates, A. J., Young, D. T., 2008, Electron circulation in Saturn's magnetosphere, *Journal of Geophysical Research*, 113, A01 201
- Rymer, A. M., Smith, H. T., Wellbrock, A., Coates, A. J., Young, D. T., 2009a, Discrete classification and electron energy spectra of Titan's varied magnetospheric environment, *Geophysical Research Letters*, 36, L15 109
- Rymer, A. M., Mitchell, D. G., Hill, T. W., Kronberg, E. A., Krupp, N., Jackman, C. M., 2013, Saturn's magnetospheric refresh rate, *Geophysical Research Letters*, 40, 2479–2483
- Saur, J., Mauk, B. H., Mitchell, D. G., Krupp, N., Khurana, K. K., Livi, S., Krimigis, S. M., Newell, P. T., Williams, D. J., Brandt, P. C., Lagg, A., Roussos, E., Dougherty, M. K., 2006, Anti-planetward auroral electron beams at Saturn, *Nature*, 439
- Saur, J., Schilling, N., Neubauer, F. M., Strobel, D. F., Simon, S., Dougherty, M. K., Russell, C. T., Pappalardo, R. T., 2008, Evidence for temporal variability of Enceladus' gas jets: Modeling of Cassini observations, *Geophysical Research Letters*, 35, L20 105
- Schardt, A. W., Kurth, W. S., Lepping, R. P., MacLennan, C. G., 1985, Particle Acceleration in Saturn's Outer Magnetosphere: In Memoriam Alois Schardt, *Journal of Geophysical Research*, 90, 8539–8542

- Schippers, P., Blanc, M., André, N., et al., 2008, Multi-instrument analysis of electron populations in Saturn's magnetosphere, *Journal of Geophysical Research*, 113, A07 208
- Schippers, P., André, N., Gurnett, D. A., Lewis, G. R., Persoon, A. M., Coates, A. J., 2012, Identification of electron field-aligned current systems in Saturn's magnetosphere, *Journal of Geophysical Research*, 117, A05 204
- Sergis, N., Krimigis, S. M., Mitchell, D. G., Hamilton, D. C., Krupp, N., Mauk, B. M., Roelof, E. C., Dougherty, M., 2007, Ring current at Saturn: Energetic particle pressure in Saturn's equatorial magnetosphere measured with Cassini/MIMI, *Geophysical Research Letters*, 34, L09 102
- Sergis, N., Krimigis, S. M., Roelof, E. C., et al., 2010, Particle pressure, inertial force, and ring current density profiles in the magnetosphere of Saturn, based on Cassini measurements, *Geophysical Research Letters*, 37, L02 102
- Sergis, N., Jackman, C. M., Thomsen, M. F., Krimigis, S. M., Mitchell, D. G., Hamilton, D. C., Dougherty, M. K., Krupp, N., Wilson, R. J., 2017, Radial and local time structure of the Saturnian ring current, revealed by Cassini, *Journal of Geophysical Research: Space Physics*, 122, 1803–1815
- Shemansky, D., Liu, X., Melin, H., 2009, The Saturn hydrogen plume, *Planetary and Space Science*, 57, 1659–1670
- Shemansky, D. E., Matheson, P., Hall, D. T., Hu, H.-Y., Tripp, T. M., 1993, Detection of the hydroxyl radical in the Saturn magnetosphere, *Nature*, 363, 329–331
- Shue, J.-H., Chao, J. K., Fu, H. C., Russell, C. T., Song, P., Khurana, K. K., Singer, H. J., 1997, A new functional form to study the solar wind control of the magnetopause size and shape, *Journal of Geophysical Research*, 102, 9497–9511
- Simon, S., Roussos, E., Paty, C. S., 2015, The interaction between Saturn's moons and their plasma environments, *Physics Reports*, 602, 1–65
- Simpson, J. A., Anglin, J. D., Balogh, A., Burrows, J. R., Cowley, S. W. H., Ferrando, P., Heber, B., Hynds, R. J., Kunow, H., Marsden, R. G., 1992, Energetic Charged-Particle Phenomena in the Jovian Magnetosphere: First Results from the Ulysses COSPIN Collaboration, *Science*, 257, 1543–1550
- Sittler, E., Thomsen, M., Johnson, R., et al., 2006, Cassini observations of Saturn's inner plasmasphere: Saturn orbit insertion results, *Planetary and Space Science*, 54, 1197–1210
- Slavin, J. A., Smith, E. J., Gazis, P., Mihalov, J., 1983, A Pioneer-Voyager study of the solar wind interaction with Saturn, *Geophysical Research Letters*, 10, 9–12
- Smith, A. W., Jackman, C. M., Thomsen, M. F., 2016, Magnetic reconnection in Saturn's magnetotail: A comprehensive magnetic field survey, *Journal of Geophysical Research: Space Physics*, 121, 2984–3005

- Smith, E. J., Davis, L., Jones, D. E., Coleman, P. J., Colburn, D. S., Dyal, P., Sonett, C. P., 1980, Saturn's magnetosphere and its interaction with the solar wind, *Journal of Geophysical Research*, 85, 5655–5674
- Smith, H., Johnson, R., Sittler, E., Shappirio, M., Reisenfeld, D., Tucker, O., Burger, M., Crary, F., McComas, D., Young, D., 2007, Enceladus: The likely dominant nitrogen source in Saturn's magnetosphere, *Icarus*, 188, 356–366
- Smith, H. T., Johnson, R. E., Perry, M. E., Mitchell, D. G., McNutt, R. L., Young, D. T., 2010, Enceladus plume variability and the neutral gas densities in Saturn's magnetosphere, *Journal of Geophysical Research*, 115, A10 252
- Smith, M. F., Lockwood, M., 1996, Earth's magnetospheric cusps, *Reviews of Geophysics*, 34, 233–260
- Stanley, S., 2010, A dynamo model for axisymmetrizing Saturn's magnetic field, *Geophysical Research Letters*, 37, L05 201
- Stevenson, D. J., 1982, Reducing the non-axisymmetry of a planetary dynamo and an application to Saturn, *Geophysical & Astrophysical Fluid Dynamics*, 21, 113–127
- Sulaiman, A. H., Masters, A., Dougherty, M. K., 2016, Characterization of Saturn's bow shock: Magnetic field observations of quasi-perpendicular shocks, *Journal of Geophysical Research: Space Physics*, 121, 4425–4434
- Swisdak, M., Rogers, B. N., Drake, J. F., Shay, M. A., 2003, Diamagnetic suppression of component magnetic reconnection at the magnetopause, *Journal of Geophysical Research*, 108, 1218
- Swisdak, M., Opher, M., Drake, J. F., Alouani Bibi, F., 2010, The vector direction of the interstellar magnetic field outside the heliosphere, *The Astrophysical Journal*, 710, 1769–1775
- Talboys, D. L., Arridge, C. S., Bunce, E. J., Coates, A. J., Cowley, S. W. H., Dougherty, M. K., 2009a, Characterization of auroral current systems in Saturn's magnetosphere: High-latitude Cassini observations, *Journal of Geophysical Research*, 114, A06 220
- Talboys, D. L., Arridge, C. S., Bunce, E. J., Coates, A. J., Cowley, S. W. H., Dougherty, M. K., Khurana, K. K., 2009b, Signatures of field-aligned currents in Saturn's nightside magnetosphere, *Geophysical Research Letters*, 36, L19 107
- Talboys, D. L., Bunce, E. J., Cowley, S. W. H., Arridge, C. S., Coates, A. J., Dougherty, M. K., 2011, Statistical characteristics of field-aligned currents in Saturn's nightside magnetosphere, *Journal of Geophysical Research*, 116, A04 213
- Thomsen, M. F., Reisenfeld, D. B., Delapp, D. M., Tokar, R. L., Young, D. T., Crary, F. J., Sittler, E. C., McGraw, M. A., Williams, J. D., 2010, Survey of ion plasma parameters in Saturn's magnetosphere, *Journal of Geophysical Research: Space Physics*, 115, A10 220

- Thomsen, M. F., Roussos, E., Andriopoulou, M., Kollmann, P., Arridge, C. S., Paranicas, C. P., Gurnett, D. A., Powell, R. L., Tokar, R. L., Young, D. T., 2012, Saturn's inner magnetospheric convection pattern: Further evidence, *Journal of Geophysical Research*, 117, A09 208
- Thomsen, M. F., Mitchell, D. G., Jia, X., Jackman, C. M., Hospodarsky, G., Coates, A. J., 2015, Plasmapause formation at Saturn, *Journal of Geophysical Research: Space Physics*, 120, 2571–2583
- Thomsen, M. F., Jackman, C. M., Cowley, S. W. H., Jia, X., Kivelson, M. G., Provan, G., 2017, Evidence for periodic variations in the thickness of Saturn's nightside plasma sheet, *Journal of Geophysical Research: Space Physics*, 122, 280–292
- Trenchi, L., Marcucci, M. F., Pallochia, G., Consolini, G., Bavassano Cattaneo, M. B., Di Lellis, A. M., Rème, H., Kistler, L., Carr, C. M., Cao, J. B., 2008, Occurrence of reconnection jets at the dayside magnetopause: Double Star observations, *Journal of Geophysical Research*, 113, A07S10
- Tseng, W.-L., Ip, W.-H., Johnson, R., Cassidy, T., Elrod, M., 2010, The structure and time variability of the ring atmosphere and ionosphere, *Icarus*, 206, 382–389
- Vasyliūnas, V. M., 1983, *Physics of the Jovian magnetosphere*, chap. Plasma distribution and flow, pp. 395–453, Cambridge Univ. Press, New York
- Vogt, R. E., Chenette, D. L., Cummings, A. C., Garrard, T. L., Stone, E. C., Schardt, A. W., Trainor, J. H., Lal, N., McDonald, F. B., 1982, Energetic Charged Particles in Saturn's Magnetosphere: Voyager 2 Results, *Science*, 215, 577–582
- Waite, J. H., Combi, M. R., Ip, W.-H., et al., 2006, Cassini Ion and Neutral Mass Spectrometer: Enceladus Plume Composition and Structure, *Science*, 311, 1419–1422
- Wild, J. A., Cowley, S. W. H., Davies, J. A., et al., 2001, First simultaneous observations of flux transfer events at the high-latitude magnetopause by the Cluster spacecraft and pulsed radar signatures in the conjugate ionosphere by the CUTLASS and EISCAT radars, *Annales Geophysicae*, 19, 1491–1508
- Wilson, R. J., Tokar, R. L., Henderson, M. G., Hill, T. W., Thomsen, M. F., Pontius, D. H., 2008, Cassini plasma spectrometer thermal ion measurements in Saturn's inner magnetosphere, *Journal of Geophysical Research*, 113, A12 218
- Wilson, R. J., Tokar, R. L., Henderson, M. G., 2009, Thermal ion flow in Saturn's inner magnetosphere measured by the Cassini plasma spectrometer: A signature of the Enceladus torus?, *Geophysical Research Letters*, 36, L23 104
- Wilson, R. J., Delamere, P. A., Bagenal, F., Masters, A., 2012, Kelvin-Helmholtz instability at Saturn's magnetopause: Cassini ion data analysis, *Journal of Geophysical Research*, 117, A03 212
- Wilson, R. J., Bagenal, F., Delamere, P. A., Desroche, M., Fleshman, B. L., Dols, V., 2013, Evidence from radial velocity measurements of a global electric field in Saturn's inner magnetosphere, *Journal of Geophysical Research: Space Physics*, 118, 2122–2132

- Xiao, F., Thorne, R. M., Gurnett, D. A., Williams, D. J., 2003, Whistler-mode excitation and electron scattering during an interchange event near Io, *Geophysical Research Letters*, 30, 1749
- Yates, J. N., Southwood, D. J., Dougherty, M. K., et al., 2016, Saturn's quasiperiodic magnetohydrodynamic waves, *Geophysical Research Letters*, 43
- Ye, S.-Y., Gurnett, D. A., Groene, J. B., Wang, Z., Kurth, W. S., 2010, Dual periodicities in the rotational modulation of Saturn narrowband emissions, *Journal of Geophysical Research*, 115, A12 258
- Ye, S.-Y., Fischer, G., Kurth, W. S., Menietti, J. D., Gurnett, D. A., 2016, Rotational modulation of Saturn's radio emissions after equinox, *Journal of Geophysical Research: Space Physics*, 121, 11,714–11,728
- Young, D. T., Berthelier, J. J., Blanc, M., et al., 2004, Cassini Plasma Spectrometer Investigation, *Space Science Reviews*, 114, 1–112
- Zhang, M., McKibben, R. B., Simpson, J. A., Cowley, S. W. H., Staines, K., Anglin, J. D., Marsden, R. G., Sanderson, T. R., Wenzel, K.-P., 1995, Impulsive bursts of energetic particles in the high-latitude duskside magnetosphere of Jupiter, *Journal of Geophysical Research*, 100, 19 497–19 512
- Zieger, B., Hansen, K. C., 2008, Statistical validation of a solar wind propagation model from 1 to 10 AU, *Journal of Geophysical Research*, 113, A08 107
- Zieger, B., Hansen, K. C., Gombosi, T. I., Zeeuw, D. L. D., 2010, Periodic plasma escape from the mass-loaded Kronian magnetosphere, *Journal of Geophysical Research*, 115, A08 208

Publications

Refereed publications

- **B. Palmaerts**, A. Radioti, D. Grodent, E. Chané and B. Bonfond, 2014, Transient small-scale structure in the main auroral emission at Jupiter, *Journal of Geophysical Research: Space Physics*, 119, 9,931-9,938, doi:10.1002/2014JA020688
- **B. Palmaerts**, E. Roussos, N. Krupp, W. S. Kurth, D. G. Mitchell and J. N. Yates, 2016a, Statistical analysis and multi-instrument overview of the quasi-periodic 1-hour pulsations in Saturn's outer magnetosphere, *Icarus*, 271, 1-18, doi:10.1016/j.icarus.2016.01.025
- **B. Palmaerts**, A. Radioti, E. Roussos, D. Grodent, J.-C. Gérard, N. Krupp and D. G. Mitchell, 2016b, Pulsations of the polar cusp aurora at Saturn, *Journal of Geophysical Research: Space Physics*, 121, 11,952-11,963, doi:10.1002/2016JA023497
- **B. Palmaerts**, M. F. Vogt, N. Krupp, D. Grodent and B. Bonfond, in press (accepted in April 2016), Dawn-dusk asymmetries in Jupiter's magnetosphere in *Dawn-Dusk Asymmetries in Planetary Plasma Environments*, eds. S. Haaland, A. Runov and C. Forsyth, AGU/Wiley Book.
- B. Bonfond, J. Gustin, J.-C. Gérard, D. Grodent, A. Radioti, **B. Palmaerts**, S. V. Badman, K. K. Khurana and C. Tao, 2015a, The far-ultraviolet main auroral emission at Jupiter - Part 1: Dawn-dusk brightness asymmetries, *Annales Geophysicae*, 33, 1203-1209, doi:10.5194/angeo-33-1203-2015
- B. Bonfond, J. Gustin, J.-C. Gérard, D. Grodent, A. Radioti, **B. Palmaerts**, S. V. Badman, K. K. Khurana and C. Tao, 2015b, The far-ultraviolet main auroral emission at Jupiter - Part 2: Vertical emission profile, *Annales Geophysicae*, 33, 1211-1219, doi:10.5194/angeo-33-1211-2015
- E. Roussos, N. Krupp, D. G. Mitchell, C. Paranicas, S. M. Krimigis, M. Andriopoulou, **B. Palmaerts**, W. S. Kurth, S. V. Badman, A. Masters and M. K. Dougherty, 2016, Quasi-periodic injections of relativistic electrons in Saturn's outer magnetosphere, *Icarus*, 263, 101-116, doi:10.1016/j.icarus.2015.04.017

Conference proceedings

- **B. Palmaerts**, A. Radioti, D. Grodent, E. Chané and B. Bonfond, Transient small-scale structure in the main auroral emission at Jupiter, *European Planetary Science Congress (EPSC) 2014*, Cascais, Portugal, 7-12 September 2014 (Oral)
- **B. Palmaerts**, E. Roussos, N. Krupp, W. S. Kurth and M. K. Dougherty, Statistical analysis of the quasi-periodic relativistic electron injections in Saturn's magnetosphere, *Cassini PSG meeting #65*, Roma, Italy, 19-22 January 2015 (Oral)
- **B. Palmaerts**, E. Roussos, N. Krupp, W. S. Kurth, D. G. Mitchell and M. K. Dougherty, Statistical analysis and multi-instrument overview of the quasi-periodic 1-hour pulsations in Saturn's outer magnetosphere, *Magnetospheres of the Outer Planets (MOP) 2015*, Atlanta, USA, 01-05 June 2015 (Oral)
- **B. Palmaerts**, E. Roussos, N. Krupp, W. S. Kurth, D. G. Mitchell and M. K. Dougherty, Statistical analysis and multi-instrument overview of the quasi-periodic 1-hour pulsations in Saturn's outer magnetosphere, *European Planetary Science Congress (EPSC) 2015*, Nantes, France, 27 September-2 October 2015 (Poster)
- **B. Palmaerts**, E. Roussos, A. Radioti, N. Krupp, D. Grodent, W. S. Kurth and J. N. Yates, Multi-instrument overview of the 1-hour pulsations in Saturn's magnetosphere and auroral emissions, *European Geosciences Union General Assembly (EGU) 2016*, Vienna, Austria, 17-22 April 2016 (Invited oral)
- **B. Palmaerts**, E. Roussos, A. Radioti, N. Krupp, D. Grodent, W. S. Kurth and J. N. Yates, Multi-instrument overview of the 1-hour pulsations in Saturn's magnetosphere and auroral emissions, *Cassini MAPS meeting 2016*, Ann Arbor, USA, 11-13 May 2016 (Oral)
- **B. Palmaerts**, E. Roussos, A. Radioti, N. Krupp, D. Grodent, Multi-instrument overview of the 1-hour pulsations in Saturn's magnetosphere, *Deutsche Physikalische Gesellschaft (DPG) Frühjahrstagungen 2017*, Bremen, Germany, 13-17 March 2017 (Oral)
- N. Krupp, E. Roussos, M. Fränz, **B. Palmaerts**, F. Bagenal, R. Wilson and C. Paranicas, Global Flow Patterns in the Jovian Magnetosphere: Galileo/EPD and Galileo/PLS measurements, *European Planetary Science Congress (EPSC) 2014*, Cascais, Portugal, 7-12 September 2014 (Oral)
- E. Roussos, N. Krupp, D. G. Mitchell, **B. Palmaerts**, C. Paranicas, S. M. Krimigis, M. Andriopoulou, W. S. Kurth, S. V. Badman, A. Masters and M. K. Dougherty, 2016, Quasi-periodic injections of relativistic electrons in Saturn's magnetosphere, *European Planetary Science Congress (EPSC) 2014*, Cascais, Portugal, 7-12 September 2014 (Oral)

- D. Grodent, B. Bonfond, G. Gladstone, J.-C. Gérard, J. Gustin, A. Radioti, M. Dumont, **B. Palmaerts** and the Juno Science Team, Auroral emission at Jupiter, through Juno's UVS eyes, *Magnetospheres of the Outer Planets (MOP) 2015*, Atlanta, USA, 01-05 June 2015 (Oral)
- D. Grodent, B. Bonfond, A. Radioti, J. Gustin, J.-C. Gérard, M. Dumont and **B. Palmaerts**, Ultraviolet auroral emissions on giant planets, *European Space Weather Week 12*, Ostend, Belgium, 23-27 November 2015 (Oral)

Acknowledgements

If this thesis reports my work during the last three years, none of this would have been possible without the help and the support of many people. I have been really lucky to be well surrounded during all my PhD.

First, I would like to express my sincere gratitude to all my supervisors. I am grateful to Katerina Radioti for having talked to me about the possibility to apply for a doctoral thesis at the Max-Planck-Institute for Solar System Research (MPS) in Göttingen. It was definitely an excellent decision. It is also my collaboration with Katerina during my master thesis which made me want to start a scientific career. Since the start of my master thesis almost five years ago, my work has always highly benefited from her guidance. Katerina also suggested me to present my master thesis work in London in 2013 during the EPSC conference where I could meet my two future supervisors at MPS, Norbert Krupp and Elias Roussos.

I would like to thank Norbert Krupp and Elias Roussos for having accepted me in their research group and for having trusted me. By giving me the opportunity to participate in several international conferences and scientific meetings, Norbert enabled me to get into the scientific community of the magnetospheres of outer planets. His friendly personality definitely contributes to the pleasant environment of the plasma group at MPS. Elias has been very helpful throughout my PhD providing me the Cassini datasets, innumerable useful advices and an invaluable guidance. I benefited a lot from his impressive knowledge of the magnetospheres of Saturn and Jupiter.

Even being overworked, Denis Grodent always took time to supervise my work. With Katerina, he even traveled to Göttingen to attend my yearly IMPRS seminar and supervisor meeting. His constant enthusiasm for my results always gave me further motivation to keep improving the quality of my work. I am also grateful to him for allowing me to continue in this research field.

I would like to also thank Andreas Tilgner who cordially accepted to be my supervisor for the University of Göttingen and hence made possible the achievement of the beneficial joint PhD program between the universities of Göttingen and Liege.

During the three years of my PhD, I could benefit from the expertise of several people among the scientific community of my research field. Special thanks to Don Mitchell, Bill Kurth, Jaf Yates, Michelle Thomsen and Nathan Pilkington. Bertrand Bonfond as well, who, with his questions sometimes annoying but always so relevant, helped me to understand better my PhD topic.

Thanks also to Leonardo and Fabien for their friendship at MPS and to Maïté and Arnaud who have always kindly welcomed me in their office each time I was back at LPAP.

This thesis has been achieved in the frame of the IMPRS Solar System School at MPS

which provide a very good environment for doctoral studies. The IMPRS coordinator Sonja Schuh plays an important role in the success of the school. I would like to thank Sibylla at MPS and Angela at LPAP for their support for the administrative matters and to acknowledge the Max Planck Society and the German Space Agency DLR for their financial support.

J'aimerais aussi remercier ma famille et en particulier mes parents pour leur soutien indéfectible. Nul doute que sans eux, je ne serais pas là où j'en suis aujourd'hui. Désolé de n'être pas revenu plus souvent et pour de plus longues périodes en Belgique.

Por último, me gustaría agradecer a Azaymi. Su apoyo, atención y amor continuos hicieron mi vida más feliz y divertida durante esos tres años, a pesar de mi estrés ocasional y del trabajo importante necesario por un doctorado. Azaymi es mi más grande aficionada y me da mucha confianza en mí. Soy muy afortunado de compartir mi vida con ella.

Curriculum vitae

Name Benjamin Palmaerts
Date of birth 10.08.1990
Place of birth Ottignies-Louvain-la-Neuve, Belgium
Nationality Belgian

Education

2014-2017 PhD student, Georg-August-Universität Göttingen, Göttingen, Germany and Max-Planck Institute for Solar System Research, Göttingen, within the International Max Planck Research School for Solar System Science
2013-2017 PhD student, Université de Liège, Liege, Belgium
2011-2013 Master in Space Sciences, Université de Liège, Liege, Belgium
Master thesis: “Morphologie de l’émission aurorale UV principale de Jupiter en fonction du temps local”
2008-2011 Bachelor in Physics, Université catholique de Louvain, Louvain-la-Neuve, Belgium